# ABSTRACT

Title of Dissertation: FROM NANOMETERS TO LIGHT YEARS: EXPLORATION OF THE EARLY UNIVERSE WITH GAMMA-RAY BURSTS AND DEVELOPMENT OF PHOTONIC SPECTROGRAPHS FOR ASTRONOMY

Pradip Gatkine
Doctor of Philosophy, 2020

Dissertation Directed by: Professor Sylvain Veilleux
Department of Astronomy

Recent space- and ground-based studies of the circumgalactic medium (CGM) around nearby galaxies have revealed the dynamic interplay between the galaxy ecosystem and surrounding CGM using bright background quasars. In this thesis, we extend this investigation to higher redshifts by using the bright afterglows of gamma-ray bursts (GRBs) as background sources probing the CGM of their own host galaxies. We compiled a sample of 27 high-resolution (R $>$ 6000) rest-frame UV spectra of GRB afterglows in a redshift range ($2 \lesssim z \lesssim 6$); we call this the 'CGM-GRB sample'. We find stronger blue wings in high-ionization species (Si IV, C IV) compared to the low-ionization species (Si II, Fe II), indicative of the presence of ubiquitous warm outflows in the GRB hosts at high redshifts. Using kinematic models, we estimated typical values of CGM properties (for the sample) such as CGM mass ($10^{9.8}$ $M_\odot$) and outflow launch velocity (300 km $s^{-1}$). Further, by comparing our results with previous C IV absorption studies, we find a possible

CGM-galaxy co-evolution. Over the course of evolution of present-day galaxies with $M_* > 10^{10}$ $M_\odot$, the ratio of C IV mass in the CGM to the stellar mass remains fairly uniform, such that $\log(M_{CIV}/M_*) \sim -4.5$ within $\pm 0.5$ dex from $z \sim 4$ to $z \sim 0$, suggesting CGM-galaxy co-evolution.

Next, we embarked on a search for possible relations between the outflow properties and those of the host galaxies such as $M_*$, star formation rate (SFR), and specific SFR ($= SFR/M_*$). To estimate the total SFR, we first investigated the degree of dust obscuration in the massive GRB hosts in our sample by comparing radio- and UV-based star-formation rates. We inferred that the GRB hosts in our sample are not heavily dust obscured, and hence, their SFRs can be estimated reliably using the established dust-correction methods. For the outflow-galaxy correlations, we focused on three outflow properties − outflow column density ($N_{out}$), maximum outflow velocity ($V_{max}$), and normalized maximum velocity ($V_{norm} = V_{max}/V_{circ,halo}$, where $V_{circ,halo}$ is the halo circular velocity). We observe clear trends of $N_{out}$ and $V_{max}$ with increasing SFR in high-ion-traced outflows. These correlations indicate that these high-ion outflows are driven by star formation at these redshifts (in the mass range $\log(M_*/M_\odot) \sim 9 - 11$). We also, for the first time, observe a strong ($> 3\sigma$) trend of normalized velocity decreasing with halo mass and increasing with sSFR at high redshifts, suggesting that outflows from low-mass halos and high sSFR galaxies are most likely to escape and enrich the outer CGM and IGM with metals.

Thus, we demonstrate GRB afterglows as a method to uncover CGM-galaxy co-evolution and outflow-galaxy correlations at high redshifts, which constitute an important piece of the galaxy growth puzzle and cosmic metal enrichment.

Next, we set out to develop a new tool − an on-chip photonic spectrograph − which will eventually expand our investigation to the first galaxies in the universe ($z > 6$). Astrophotonics is the application of versatile photonic technologies to channel, manipulate, and disperse guided light to efficiently achieve various scientific objectives in astronomy in a miniaturized form factor. We used the concept of arrayed waveguide gratings (AWG) to develop an on-chip photonic spectrograph in the H band ($1.45 - 1.65\ \mu m$) with a moderate resolving power of ∼1500, a peak throughput of ∼23%, and a size of only 1.5 cm × 1.5 cm. Various practical aspects of implementing AWGs as astronomical spectrographs are also discussed, including a) the coupling of the light between the fibers and AWGs, b) cleaving at the output focal plane of the AWG to provide continuous wavelength coverage, and c) a multi-input AWG design to receive light from multiple single-mode fibers at a time and produce a combined spectrum.

Finally, we built a cross-dispersion setup which will orthogonally separate the overlapping spectral orders in the AWG and thus image the full spectrum on the detector. The AWG will be incorporated with this setup in the near future to get the spectrograph ready for our first on-sky test. The work conducted in this thesis is a crucial stepping stone towards building a high-throughput, miniaturized spectrograph for the next generation of ground-, balloon-, and space-based telescopes.

With the nano-scale fabrication on a chip, we are poised to unravel the mysteries of galaxies billions of light years away, making this thesis a truly *'Nanometers to Light Years'* journey.

# From Nanometers to Light Years: Exploration of the Early Universe with Gamma-ray Bursts and Development of Photonic Spectrographs for Astronomy

by

Pradip Gatkine

Dissertation submitted to the Faculty of the Graduate School of the
University of Maryland, College Park in partial fulfillment
of the requirements for the degree of
Doctor of Philosophy
2020

Advisory Committee:
Professor Sylvain Veilleux, Chair/Advisor
Professor Mario Dagenais, (Dean's Representative)
Professor Stuart Vogel
Dr. S. Bradley Cenko
Professor Andrew Harris

# Preface

This thesis has two clear focal points – exploring the galaxies in the early universe using Gamma-ray Bursts and development of a photonic spectrograph for augmenting and expanding these astronomical investigations in the future. Large parts of this thesis have been published in peer-reviewed journals and conference proceedings and presented at several international conferences. While chronologically, the instrumentation results come first, the thought process was always to develop the next-generation instrumentation and conduct the science investigation with existing instruments in tandem. Therefore, we present the scientific exploration first and then go on to describe our technological efforts to build new instrumentation as the next step to expand our scientific horizon.

In the following lists, I summarize the relevant published work that I led or contributed to through the journey of this thesis.

**Exploring the early universe**

1. **P. Gatkine**, S. Veilleux, A. Cucchiara, *The CGM-GRB Study I. Uncovering The CircumGalactic Medium around GRB hosts at redshifts 2–6*, The Astrophysical Journal, 884 66, 2019 [Chapter 2]

2. **P. Gatkine**, S. Vogel, S. Veilleux, *New Radio constraints on the obscured star formation rates of massive GRB hosts at* $z \sim 2 - 3.5$, The Astrophysical Journal, 897 9, 2020 [Chapter 3]

3. **P. Gatkine** et al. *The CGM-GRB Study II: Outflow-Galaxy Relations at* $z \sim 2 - 6$, Submitted to ApJ [Chapter 4]

**Photonic Instrumentation**

4. **P. Gatkine** et al. *Development of high-resolution arrayed waveguide grating spectrometers for astronomical applications: first results*, Proc. of SPIE Volume 9912, Article ID 991271, (2016) Link

5. **P. Gatkine** et al. *Arrayed waveguide grating spectrometers for astronomical applications: New results*, Optics Express, 25(15):17918−17935 (2017) [Chapter 5]

6. **P. Gatkine** et al. *Towards a multi-input astrophotonic AWG spectrograph*, Proceedings of SPIE Volume 10706, Article ID 1070656, (2018) Link [Chapter 6]

7. **P. Gatkine**, S. Veilleux, M. Dagenais, *Astrophotonic Spectrographs*, Applied Sciences, 9(2):290-307 (2019)

8. **P. Gatkine** et al. *Astro2020: Astrophotonics White Paper*, Bulletin of American Astronomical Society, 51g.285G, (2019) Link [Adapted in Chapter 1]

9. Y. Hu, Y. Zhang, **P. Gatkine** et al. *Characterization of low-loss waveguides using Bragg gratings*, IEEE Journal of Selected Topics in Quantum Electronics, 24(4):1-8 (2018) Link

10. T. Zhu, Y. Hu, **P Gatkine** et al. *Arbitrary on-chip optical filter using complex waveguide Bragg gratings*, Applied Physics Letters, 108 (101104):1-5 (2016) Link

11. T. Zhu, Y. Hu, **P. Gatkine** et al. *Ultrabroadband high-coupling-efficiency fiber-to-waveguide coupler using $Si_3N_4/SiO_2$ waveguides on Silicon*, IEEE Photonics Journal, 8(5):1-12 (2016) Link

# Dedication

*To my late grandfather and my parents*

*whose blessings are with me eternally :)*

# Acknowledgments

*I look at the sky and wonder about how things conspired*

*to make us and make us wonder about things!*

And in the same way, I wonder about how so many different individuals came together to make the journey of this thesis possible and in fact, cherishable.

First and foremost I'd like to thank my advisor, Professor Sylvain Veilleux. Coming from a mechanical engineering background, I was back to square one when I started graduate school in astronomy. Sylvain introduced me to the exciting world of astrophotonics and kick-started my journey. He always encourages and helps me to come up with new ideas, brings my attention to new research, and cautions me with the pitfalls. Thanks to him, I have been able to participate in numerous conferences around the world and gain valuable insights on many fronts. I want to thank him for giving me the freedom to work at my own pace, introducing me to new researchers, and supporting me every step of the way, often on very tight timelines. At times I have wondered how he manages to go through my drafts and make detailed comments so quickly.

I also want to offer my gratitude to Professor Mario Dagenais for assimilating me into his group at the Electrical and Computer Engineering (ECE) Department, guiding me through the projects in photonics, planting interesting questions in my mind, and helping learn valuable lab skills. With the collaborative work, challenging problems, and innovative approaches, I had a very enriching experience at the ECE

department. I am very thankful to my friends and colleagues in the ECE, who are always around to help, teach, and discuss as we tread our paths. I want to particularly thank Yiwen Hu, Tiecheng Zhu, Shengjie Xie, Jiahao Zhan, Yang Meng, and Yang Zhang. I also want to thank Meghna Sitaram who has been an excellent undergraduate collaborator in this work.

I thank my collaborators Nino Cucchiara and Dan Perley for providing me with research data, teaching me reduction techniques, and hosting me at their home institutions. I particularly thank Nino for helping me evacuate from the US Virgin Islands just before hurricane Irma. I also want to thank Chris Betters, Sergio Leon-Saval, and Joss Bland-Hawthorn for hosting me at the University of Sydney and helping me learn new photonic techniques that have been of great use in this research.

I am grateful to so many amazing people in the Astronomy department who made me feel welcome and were always ready to help with a smile. I thank Stuart who has been an excellent collaborator and teacher, and a kind mentor to me. I also extend my gratitude to Brad Cenko for his advice and support in my research and career. He taught me how to plan and observe at the Lowell Discovery Telescope. I highly appreciate his kindness and patience with me. I am thankful to Richard Mushotzky for the very enriching discussions as well as collaboration on the X-ray astronomy projects. Interactions with him − and many on an urgent basis − have always been a great help.

I had a very pleasant and enjoyable experience at the UMD Astronomy department, thanks to my wonderful friends. I thank my classmates, Dana, Amy, Zeeve,

Thomas, and Jonathan for keeping me company through this journey and helping me adjust to a new country. I appreciate Dana and Amy for their acts of kindness and arranging social gatherings to wind down every now and then. I am grateful to Krista, Vicki, Taro, John Capone, Arnab, Mahmuda, and Ashlee for their words of advice and frequent support which made my path much easier. Many thanks to Laura, Becca, Ginny, Sara, Ramsey, Tomas, Milena, Charlotte, and Vicente for the many fun times we shared at UMD.

In the end, I would like to send my heartfelt thanks to my parents, my late grandfather, and my siblings for always being there, through thick and thin. Thanks to their blessings, kindness, and sacrifices, I have been able to follow my dreams. This journey would not have been possible without the unconditional love and support that I received from my family.

Table of Contents

Preface ii

Dedication iv

Acknowledgements v

Table of Contents viii

List of Tables xii

List of Figures xiii

1 Introduction 1
1.1 Introduction . . . 1
1.1.1 Cosmic Metal Enrichment . . . 1
1.1.2 Missing Metals . . . 2
1.1.3 Importance of the Circumgalactic Medium . . . 3
1.1.4 A historical perspective on the CGM . . . 4
1.1.5 Different probes of the CGM . . . 5
1.1.6 Use of GRBs . . . 6
1.1.7 Key scientific questions . . . 8
1.2 Astrophotonics: A new tool in our toolkit . . . 9
1.2.1 Arrayed Waveguide Gratings . . . 11
1.2.2 AWG: New directions . . . 12
1.3 Thesis outline . . . 14
1.4 A summary of facilities . . . 15

2 Uncovering The Circumgalactic Medium around GRB hosts at redshifts 2−6 17
2.1 Introduction . . . 17
2.1.1 Methods to Probe the CGM . . . 19
2.1.2 The CGM-GRB Project . . . 20
2.2 The GRB Sample . . . 22
2.2.1 Sample Properties . . . 22
2.2.2 Selection Effects . . . 24
2.3 Methods . . . 25
2.3.1 Redshift Determination . . . 25
2.3.2 Spectroscopic Analysis . . . 26

2.4 Inferring Kinematics . . . 31
2.4.1 Median Plots . . . 31
2.4.2 Integrated Line Profiles . . . 32
2.4.3 Detection Fractions . . . 35
2.4.4 Kinematic Asymmetry . . . 36
2.4.5 Line Ratios . . . 38
2.5 Toy Model . . . 40
2.5.1 Line-of-sight Simulations: Setup . . . 40
2.5.2 Line-of-sight Simulations: Results . . . 46
2.6 CGM Mass Estimate . . . 48
2.6.1 Converting Column Densities into Mass . . . 49
2.6.1.1 Method . . . 49
2.6.1.2 Results . . . 52
2.6.1.3 Caveats . . . 54
2.6.2 CGM Mass Evolution with Redshift . . . 55
2.6.3 Comparison with Carbon Mass in the ISM . . . 60
2.7 Implications . . . 62
2.7.1 Outflows and Metal Enrichment . . . 62
2.7.1.1 Outflow Mass . . . 63
2.7.1.2 Mass Outflow Rate . . . 64
2.7.1.3 Mass Loading Factor and Energetics . . . 67
2.7.2 CGM-Galaxy Co-Evolution . . . 70
2.7.3 Existence of Inflows? . . . 73
2.7.4 Origin of O VI and N V: CGM vs Circumburst? . . . 76
2.8 Summary and Conclusions . . . 79

3 New radio constraints on the obscured star formation rates of massive GRB hosts at redshifts $2-3.5$ 85
3.1 Introduction . . . 85
3.2 Sample and observations . . . 89
3.2.1 Sample Selection . . . 89
3.2.2 VLA Observations . . . 90
3.3 Radio- and UV-based SFR . . . 92
3.3.1 Radio-based SFR . . . 92
3.3.2 Late-time afterglow emission . . . 94
3.3.3 SFR in each GRB host . . . 96
3.3.3.1 GRB 021004 . . . 96
3.3.3.2 GRB 080310 . . . 99
3.3.3.3 GRB 080810 . . . 99
3.3.3.4 GRB 121024A . . . 101
3.4 Discussion . . . 103
3.5 Summary . . . 105

4 Outflow-Galaxy Relations at $z \sim 2-6$ 108
4.1 Introduction . . . 108
4.2 Observations and Methods . . . 111
4.2.1 Optical Photometry . . . 111
4.2.2 Spitzer IRAC Photometry . . . 113
4.2.3 Stellar Mass . . . 115
4.2.4 Dust Correction . . . 117
4.2.5 Star formation rate . . . 118
4.3 Sample properties and analysis . . . 120
4.3.1 Comparison with star formation main sequence . . . 120
4.3.2 Blue-wing column density and outflows . . . 122
4.3.3 Inferring correlations and hypothesis testing . . . 123
4.4 Outflow correlations . . . 125
4.4.1 Outflow column density vs galaxy properties . . . 125
4.4.1.1 Blue-wing detection fraction . . . 125
4.4.1.2 $N_{out}$ vs SFR . . . 126
4.4.1.3 $N_{out}$ vs $M_*$ . . . 127
4.4.1.4 $N_{out}$ vs sSFR . . . 127
4.4.2 Outflow kinematics and galaxy properties . . . 130
4.4.2.1 Outflow $V_{max}$ vs SFR . . . 130
4.4.2.2 Outflow $V_{max}$ vs $M_*$ . . . 131
4.4.2.3 Outflow kinematics vs Halo mass . . . 132
4.4.2.4 Outflow $V_{max}$ vs sSFR . . . 133
4.4.3 Outflow $V_{norm}$ vs specific SFR . . . 134
4.4.4 Relation of O VI absorption with galaxy properties . . . 135
4.5 Discussion . . . 139
4.5.1 SFR-driven outflow . . . 139
4.5.2 Evidence for High-ion traced outflows . . . 142
4.5.3 Outflow Geometry . . . 143
4.5.4 Evolution with redshift . . . 144
4.6 Summary . . . 145

5 Arrayed waveguide grating spectrometers for astronomical applications 149
5.1 Introduction . . . 149
5.2 Arrayed waveguide gratings . . . 150
5.3 Methods . . . 153
5.3.1 Design . . . 153
5.3.2 Fabrication . . . 157
5.3.3 Characterization . . . 159
5.4 Results . . . 160
5.4.1 AWG #1: fiber-coupling taper . . . 162
5.4.2 AWG #1: annealing . . . 165
5.4.3 AWG #2: cleaving at the output FPR . . . 167
5.5 Polarization insensitivity . . . 173
5.6 Conclusions . . . 177

6 Towards an Integrated Photonic Spectrograph 179
6.1 An Integrated Photonic Spectrograph . . . 179
6.2 A Few-input AWG . . . 181
6.2.1 Design . . . 182
6.2.2 Simulation . . . 183
6.2.3 Simulation Results . . . 185
6.2.4 Experimental Verification . . . 186
6.3 Cross-dispersion setup . . . 186
6.3.1 Detector Characterization . . . 187
6.3.2 Cross-dispersion optics . . . 188
6.3.3 Future work: Integration with the AWG . . . 192

7 Summary and Future Work 194
7.1 GRB afterglows as probes of the CGM . . . 194
7.1.1 Summary . . . 194
7.1.2 Future Work . . . 196
7.2 Development of photonic spectrographs . . . 198
7.2.1 Summary . . . 198
7.2.2 Future Work . . . 199

A Methods for CGM-GRB Paper I 203
A.1 Voigt profile fitting using MCMC . . . 203
A.2 Line-of-sight simulation with toy model . . . 207

Bibliography 228

# List of Tables


1.1 Metal distribution in galaxy ecosystem . . . . . 3

2.1 Detection fractions in various kinematic regions . . . . . 36
2.2 Kinematic asymmetry in high and low ions . . . . . 38
2.3 Fit parameters of the spectra . . . . . 84
2.4 List of GRBs in the sample . . . . . 84

3.1 Summary of the VLA observations . . . . . 89
3.2 Summary of GRB host properties . . . . . 102

4.1 Summary of new observations of GRB hosts . . . . . 113
4.2 Summary of GRB host properties in the CGM-GRB sample . . . . . 121

5.1 Summary of the characteristics of the two AWGs. . . . . 154
5.2 Waveguide geometry for polarization independent design . . . . . 175

6.1 Summary of the AWG design . . . . . 183
6.2 Summary of the AWG simulations . . . . . 185

A.1 Typical values of the toy model parameters . . . . . 210

# List of Figures


1.1 Importance of the CGM . . . 2
1.2 Various Probes of the CGM . . . 7

2.1 CGM-GRB sample properties . . . 20
2.2 The median absorption line profiles of of the individual spectra . . . 28
2.3 Comparison of estimated total column densities with the literature . . . 30
2.4 The integrated column density profiles for the high- and low-ion species 33
2.5 The high- to low-ion line ratios as a function of velocity . . . 34
2.6 A schematic of the CGM toy model . . . 41
2.7 Integrated C IV column density from the toy model assuming $M_{CGM} = 10^{9.3} M_{\odot}$ . . . 43
2.8 Integrated C IV column density from the toy model assuming $M_{CGM} = 10^{9.8} M_{\odot}$ . . . 44
2.9 Integrated C IV column density from the toy model assuming $M_{CGM} = 10^{10.3} M_{\odot}$ . . . 45
2.10 CGM column densities and mass estimates for $z \sim 2 - 2.7$ . . . 58
2.11 CGM column densities and mass estimates for $z \sim 2.7 - 5.0$ . . . 59
2.12 Estimates of the minimum carbon mass in the CGM of the GRB hosts 62
2.13 The evolution of $M_{\rm CIV}/M_*$ as a function of redshift . . . 71

3.1 Contour maps of radio flux density of GRB hosts . . . 91
3.2 SFR limits as a function of observed radio flux density limits . . . 92
3.3 Temporal evolution of GRB radio flux density . . . 96
3.4 The GRB hosts in the context of SFR $- M_{\star}$ relation . . . 98
3.5 The comparison of radio-derived SFR with UV-derived SFR of GRB hosts . . . 106

4.1 Contamination-subtracted images of GRB fields from *Spitzer*-IRAC in 3.6 $\mu m$ band. . . . 114
4.2 Properties of the CGM-GRB sample host galaxies. . . . 117
4.3 Outflow column density vs Host-galaxy SFR . . . 128
4.4 outflow column density vs $M_*$ . . . 129
4.5 Outflow column density vs specific SFR . . . 129

4.6 Same as Figure 4.3, for the maximum outflow velocity, $V_{max}$ vs SFR. The horizontal dashed line in the panels shows the 100 km $s^{-1}$ level, which we treat as the threshold for outflow. . . . 136
4.7 Maximum outflow velocity, $V_{max}$ vs $M_*$ . . . 136
4.8 Normalized velocity, $V_{max}/V_{circ,halo}$ vs $M_{halo}$ . . . 137
4.9 Maximum outflow velocity ($V_{max}$) with specific SFR (= SFR / $M_*$) . . . 138
4.10 Normalized maximum velocity ($V_{max}/V_{circ,halo}$) with specific SFR (= SFR / $M_*$) . . . 138
4.11 correlations of the O VI-traced outflow with galaxy properties . . . 138
4.12 A schematic showing a biconical outflow as sampled by a GRB sightline. 145

5.1 Mode profiles of the waveguide . . . 156
5.2 CAD of AWG #1 . . . 158
5.3 Fabrication process . . . 159
5.4 Characterization setup . . . 161
5.5 Taper efficiency . . . 162
5.6 AWG throughput results . . . 164
5.7 Effect of annealing on AWG throughput . . . 167
5.8 CAD of AWG #2 without output waveguides . . . 169
5.9 Cleaved AWG results . . . 171
5.10 Achieving braodband polarization insensitivity . . . 177

6.1 Full setup of an integrated photonic spectrograph . . . 180
6.2 CAD of the multi-input AWG . . . 182
6.3 Simulation results . . . 184
6.4 Experimental Verification of Multi-input AWG . . . 187
6.5 Saturation characteristics . . . 189
6.6 Grating Disperser . . . 190
6.7 Blazed grating calculations . . . 191
6.8 Simulation results . . . 191
6.9 Simulation of chip to air illumination . . . 192
6.10 AWG-cross-dispersion schematic . . . 193

7.1 Photonic lantern and improvements in propagation loss . . . 200

A.1 A sample plot to show the parameter estimation using the MCMC-based method . . . 208
A.2 A sample plot to show the parameter estimation with an R $\sim$ 8000 spectrum (X-shooter) . . . 209
A.3 Overall simulation CIV kinematics with $\log(M_{CGM}/M_{\odot}) = 9.8$ . . . 210
A.4 Voigt profile fit for GRB 000926 . . . 214
A.5 Voigt profile fit for GRB 021004 . . . 214
A.6 Voigt profile fit for GRB 050730 . . . 215
A.7 Voigt profile fit for GRB 050820A . . . 215
A.8 Voigt profile fit for GRB 050922C . . . 216
A.9 Voigt profile fit for GRB 060607A . . . 216

A.10 Voigt profile fit for GRB 071031 . . . . . 217
A.11 Voigt profile fit for GRB 080310 . . . . . 217
A.12 Voigt profile fit for GRB 080804 . . . . . 218
A.13 Voigt profile fit for GRB 080810 . . . . . 218
A.14 Voigt profile fit for GRB 090926A . . . . . 219
A.15 Voigt profile fit for GRB 100219A . . . . . 219
A.16 Voigt profile fit for GRB 111008A . . . . . 220
A.17 Voigt profile fit for GRB 120327A . . . . . 220
A.18 Voigt profile fit for GRB 120815A . . . . . 221
A.19 Voigt profile fit for GRB 120909A . . . . . 221
A.20 Voigt profile fit for GRB 121024A . . . . . 222
A.21 Voigt profile fit for GRB 130408A . . . . . 222
A.22 Voigt profile fit for GRB 130606A . . . . . 223
A.23 Voigt profile fit for GRB 130610A . . . . . 223
A.24 Voigt profile fit for GRB 141028A . . . . . 224
A.25 Voigt profile fit for GRB 141109A . . . . . 224
A.26 Voigt profile fit for GRB 151021A . . . . . 225
A.27 Voigt profile fit for GRB 151027B . . . . . 225
A.28 Voigt profile fit for GRB 160203A . . . . . 226
A.29 Voigt profile fit for GRB 161023A . . . . . 226
A.30 Voigt profile fit for GRB 170202A . . . . . 227

# Chapter 1: Introduction

*In this chapter, I will summarize the motivation and the background for my PhD thesis.*

## 1.1 Introduction

### 1.1.1 Cosmic Metal Enrichment

The basic elements of life (Carbon, Oxygen, Nitrogen, Sulfur, etc) are formed in stars and their explosive deaths as supernovae. These elements (or metals) are dispersed across the whole universe since the formation of the first galaxies. Metals drive the cooling of clouds which eventually form stars, which further produce metals. The synthesis and distribution of metals among various components of the universe: stars, interstellar medium (ISM) of galaxies, circumgalactic medium (CGM) and intergalactic medium (IGM), is known as metal enrichment [Schindler and Diaferio, 2008, Hirschmann et al., 2013, Tumlinson et al., 2017]. The cosmic metal enrichment is a result of a complex interplay between gas coming into the galaxy (accretion flows), star formation in the galaxy and gas outflowing from the galaxy (outflows) in a cosmological context (Fig. 1.1). *Metal enrichment plays a*

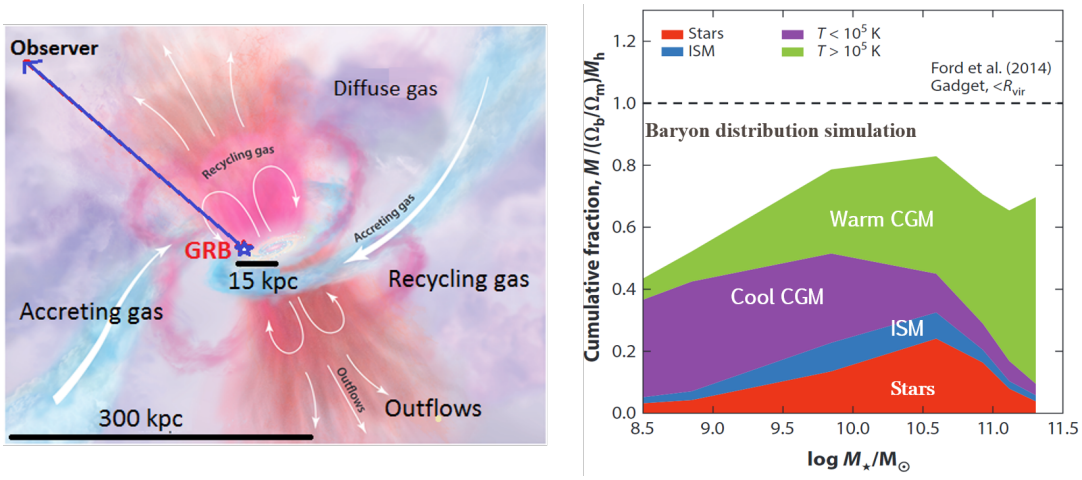


Figure 1.1: Left: A depiction of the galaxy ecosystem with its outflows, accretion flows and the CGM, which resides at the nexus of these processes. It shows how a GRB sightline samples the galaxy, CGM and various gas flows simultaneously. Right: Distribution of baryons in different components of the galaxy ecosystem at $z = 0$ in GADGET-2 simulations [Ford et al., 2014]. These results highlight the role of the CGM as a reservoir of metals and baryons. Both figures are adopted from [Tumlinson et al., 2017].

*key role in shaping the galaxy evolution and is therefore, vital for our understanding of the cosmic origins.*

### 1.1.2 Missing Metals

However, the history and mechanisms of metal enrichment of the universe remain poorly understood, primarily due to limited probes of galaxies, CGM and IGM (also called the galaxy ecosystem, as shown in Fig. 1.1) at high redshifts. The metal content of the universe as a function of cosmic time can be estimated, given the cosmic star formation history and the models of stellar nucleosynthesis. Even with liberal estimates, current observations have only accounted for ∼50% of the metals created in stellar processes [Peeples et al., 2014, Campana et al., 2015]. Resolving this discrepancy requires a comprehensive study of the metal content in galaxy ecosys-

Table 1.1: Metal distribution in galaxy ecosystem as % of total metals produced by star formation

| **Redshift →** | **z = 0** | **z = 2-3** |
|---|---|---|
| Metals in galaxies (ISM + stars) | ∼20-25 % | ∼10-15 % |
| Metals in CGM | ∼25 % | ∼19-34% (in highly ionized CGM) |
| Metals in IGM | ∼15 % | 15-30% |
| Metals in Ly-alpha absorbers | <5% | 5-20% |
| Method used | QSO sightlines | QSO sightlines |
| References | [Peeples et al., 2014], [Shull et al., 2014] | [Lehner et al., 2014], [Bouché et al., 2006] |

tems, extending to the dawn of galaxy formation ($z \sim 9$). Direct observations and spectroscopy of galaxies at high redshifts ($z > 5$) is extremely difficult and time-expensive, due to their large distances [Shapley, 2011], however, *gamma-ray bursts offer an attractive solution in this difficult quest.*

### 1.1.3 Importance of the Circumgalactic Medium

The CGM is loosely defined as diffuse gas surrounding the galaxies within dark matter halos (out to $100 - 300$ kpc). Figure 1.1 shows the vibrant ecosystem of a galaxy with its winds/outflows, accretion flows, and neutral hydrogen (H I) clouds. The CGM resides at the nexus of these interactions. The competition between these processes is thought to shape galaxies and drive their evolution.

Promising theoretical and observational studies about the missing metals problem suggest that the majority of the metals are stored in the CGM reservoirs around galaxies and/or expelled into the IGM [Oppenheimer and Davé, 2006, Shull et al., 2014]. As summarized in Table 1.1, it is evident that *the CGM is a major reservoir*

*of metals in the universe* and its contribution to cosmic metal budget evolves as a function of redshift. Therefore, probing the CGM is critical to test the theories of galaxy evolution and metal enrichment. Hence, we focus on measuring (a) the properties of the CGM as a function of redshift (b) CGM-galaxy relations and the governing feedback processes, and finally, (c) the mass of metals in CGM and its evolution with redshift.

### 1.1.4 A historical perspective on the CGM

One of the first propositions of the existence of a "galactic corona" (i.e. hot gas surrounding the Milky Way) was by [Spitzer Jr, 1956] to provide pressure confinement for observed cool interstellar clouds at high galactic latitudes. Soon after the discovery of quasars [Schmidt, 1963], their spectra, taken by state-of-the-art telescopes back then, revealed a wealth of information about the existence of such an extended reservoir of gas around other galaxies falling in the quasar sightlines. The number of intervening absorbers in the quasar spectra could not be accounted for with the visible size and number of galaxies in optical or radio wavelengths. This discrepancy prompted a new idea of the presence of tenuous gas extending several times the visible size of the galaxy itself. In a one-sentence abstract, [Bahcall and Wolf, 1968] wrote, *"We propose that most of the absorption lines observed in quasi-stellar sources with multiple absorption redshifts are caused by gas in extended halos of normal galaxies"*.

In the modern times, with the advent of telescopes such as the Keck telescopes and Hubble Space Telescope and the sensitive spectrographs thereon, the

observational studies of the CGM have grown exponentially. This has led to several important milestones, for instance, uncovering ubiquitous outflows in high-redshift galaxies [Shapley et al., 2003] or the discovery of systematic differences in the CGM of 'red-and-dead' galaxies versus the main-sequence galaxies at low redshifts (eg: [Tumlinson et al., 2011]).

### 1.1.5 Different probes of the CGM

As summarized in Fig. 1.2, there are multiple methods of studying the CGM depending on the redshift range and the mass of the galaxy of interest. The most widely used QSO sightline method uses a bright background QSO as a backlight to study the CGM composition and kinematics in absorption spectra. However, due to the small impact parameters ($< 300$ kpc) that are required to study the CGM, this method is most useful at low redshifts (see [Tumlinson et al., 2011, Werk et al., 2013, Borthakur et al., 2013, Bordoloi et al., 2014b] for example). A similar method is to use the star light of the galaxy itself as the background, hence, called 'down-the-barrel' observation. In this method, the impact parameter is unknown, but a much larger sample of galaxies can be constructed over a wide redshift range using this method (see [Martin, 2005, Kornei et al., 2012] for example). The galaxy star light can also be used as a backlight for studying a foreground galaxy's CGM [Steidel et al., 2010]. Strongly lensed galaxies can be used to study the CGM using multiple sightlines, thanks to the extended bright arcs resulting from gravitational magnification (eg: [Rigby et al., 2018]). All of these studies, however, are only

possible for galaxies that are UV-bright, and thereby, have high star formation rates. In addition, there is a significant challenge of subtracting the background galaxy's continuum itself, which can contaminate the results.

The emission-based observations offer the most direct probes of the CGM. For instance, X-ray maps allow direct imaging of the hot phase of the CGM (T $> 10^6$ K) for nearby massive galaxies and their intra-cluster medium (see [Li, 2020] for a full discussion). On the other hand, emission maps of lines such as Lyman-$\alpha$, H-$\alpha$, and C IV allow the study of low- and high-redshift ($z > 2$) CGM in emission using integral field units such as the Keck Cosmic Web Imager (see [O'Sullivan et al., 2020], for example). However, given the low surface brightness of the CGM, these methods are only suitable for the most massive galaxies (such as QSO hosts) or galaxies undergoing intense starbursts. Thus, the CGM of low-mass galaxies at high redshifts, which may significantly contribute to the cosmic meta enrichment, remains sparsely studied.

### 1.1.6 Use of GRBs

Long-duration gamma-ray bursts (GRBs) are bright flashes peaking in gamma rays and are thought to be associated with explosions of certain massive stars. The duration of prompt gamma-ray emission is measured in seconds but it is often accompanied by a bright and rapidly fading ($\sim$ 1-2 days) afterglow in X-ray, ultra-violet, and optical wavelengths. GRB afterglows have been detected from low redshift $\sim$0.01 out to redshift of 8.2 [Tanvir et al., 2009], thus probing all the way back to the first

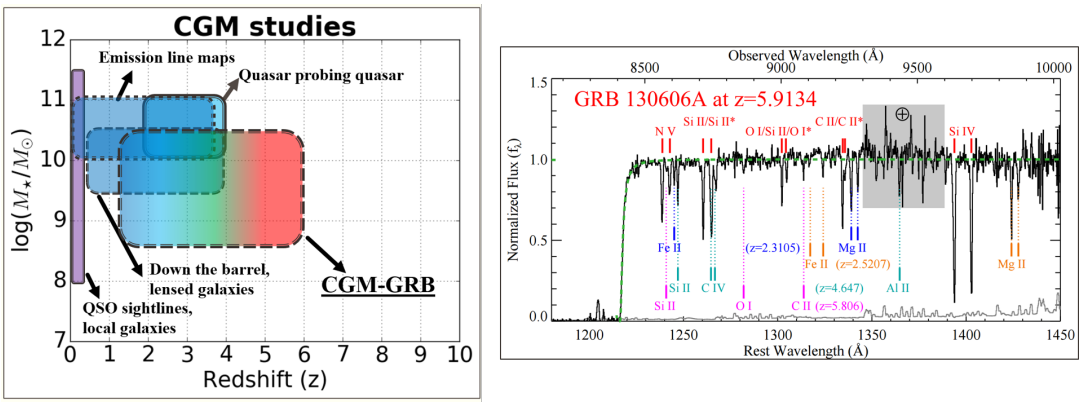


Figure 1.2: Left: A summary of most prominent methods of probing the CGM in the redshift-M$_*$ parameter space. Our GRB probe method is shown for comparison. The color in the boxes is to suggest the band in which the rest-frame UV gets redshifted (with purple = UV and red = optical R-band). Right: Example of a GRB afterglow ($z = 5.91$) spectrum probing a variety of intervening absorption systems shown in different colors as well as absorption corresponding to the host galaxy's ecosystem (shown in red). This figure is from [Chornock et al., 2013].

billion years of the universe (the era of formation of the first galaxies).

Since GRB afterglows are bright background sources, their spectra have absorption features produced by the intervening material along the line-of-sight (host galaxy ISM, CGM, and IGM). This presents an excellent opportunity to probe the metal content and physical conditions of the entire galaxy ecosystem. Thanks to the bright afterglow, it is also easy to localize the host galaxy and get its redshift. GRBs fade rapidly, making it possible to study the host galaxy component separately, in the absence of GRB. Hence, GRB sightlines offer the best chance to probe the metal-enrichment history of the universe.

Past observational efforts to trace the missing metals used quasar (QSO) sightline spectra to probe intervening CGM and IGM (see Table 1.1). In contrast to QSO sightlines, GRB sightlines have certain striking advantages: 1) GRBs happen within

their host galaxy. Hence GRB spectra contain signatures from the host galaxy as well as the associated CGM, which is crucial to draw inferences about the host galaxy ecosystem. 2) GRB discovery is based on gamma- and X-ray detection and hence, the GRB sample is largely unbiased with respect to host galaxy properties such as extinction. 3) The afterglow fades in 1-2 days, clearing the path for future deep observations of the host galaxy to study its global properties (imaging the whole galaxy and not just probing along the GRB sightline). 4) GRB hosts at $z > 2$ typically trace low-mass star-forming galaxies. These galaxies may play an important role in metal enrichment in the early universe due to their shallow potential wells. However, it is difficult to probe the CGM and outflows in this population by other methods described above.

### 1.1.7 Key scientific questions

In this thesis, we set out to use GRB afterglows and their low-mass, star-forming host galaxies over a broad redshift range ($z \sim 2 - 6$) to probe the production (through star formation) and distribution of metals in the host galaxy and its CGM (through outflows) and thereby, infer the mechanisms of cosmic metal enrichment. More specifically, we investigate the following key questions:

1. Can we measure galactic outflows in the GRB hosts? What is the nature of these outflows and the CGM in terms of their kinematics, composition, and ionization state?
2. What is the mass of metals in the CGM? Does it evolve with redshift? Can we estimate a timeline of the enrichment of the CGM?

3. How do the properties of the host galaxies such as stellar mass ($M_*$), star formation rate, and halo mass ($M_{halo}$) impact the outflows, and thereby, the transport of metals from the galaxy to the circum- and inter-galactic medium?

While the current instrumentation allows us to reach as far as $z \sim 6$ (1 billion years after Big Bang), the next-generation extremely large telescopes (ELTs) are required to understand the very first galaxies in the universe (at $z \sim 10$, or the first billion years of the universe). Astrophotonics is a new technique that will augment this scientific pursuit.

## 1.2 Astrophotonics: A new tool in our toolkit

Astrophotonics is the application of versatile photonic technologies to channel, manipulate, and disperse guided light from one or more telescopes to achieve scientific objectives in astronomy in an efficient way and a compact form factor. The developments and demands from the telecommunication industry have driven a major boost in photonic technology and vice-versa in the last ∼40 years.

The field of astrophotonics spans a wide range of technologies including: collecting astronomical light into guided channels (fibers/waveguides), manipulating the transport and reconfiguration of the light, and filtering/dispersing/combining the guided light. A combination of one or more of these functionalities has led to a wide spectrum of astrophotonic instruments. Just as radio astronomy finds its roots in radio communication, astrophotonics finds its roots in photonic / fiber-optic communication industry. The ongoing growth of photonics industry and astrophotonics

displays a strong parallel with the development of radio communication and radio astronomy, where each positively influenced the other.

The photonic platform of guided light in fibers and waveguides has opened the doors to next-generation instrumentation for both ground- and space-based telescopes in optical and near/mid-IR bands, particularly for the upcoming extremely large telescopes (ELTs). The key idea here is to leverage the ability of guiding the light in waveguides (using total internal reflection) to collapse the conventional optical setups into 2D “optical circuits". The large telescopes are pushing the limits of adaptive optics to reach close to a near-diffraction-limited performance. Photonic devices offer many advantages, thanks to the following key characteristics of photonic circuits:

1) With photonic lanterns, light can be coupled into single-mode waveguides/fibers giving a diffraction-limited performance. This means the most coherent slit width, which gives the minimal spectrograph configuration needed for a desired spectral resolution.

2) The light path can be controlled on a chip to a precision smaller the wavelength of the light (for UV, optical, IR).

3) Unlike conventional optics, there is no divergence of light with distance once it is guided in waveguides/fibers, thus eliminating the need for large optical elements to capture the light.

4) With the high-confinement-factor of on-chip waveguides, light path can be bent to create a photonic circuit with a very small form factor.

These advantages reduce the size of spectroscopic instrumentation and help

ameliorate several challenges such as thermal and mechanical stability, spiralling costs, and mass (in case of space-based instruments). This is particularly useful for large telescopes. The photonic devices are ideally suited for capturing the AO-corrected light and enabling exciting science cases such as characterizing exoplanet atmospheres and measuring the cosmological redshift, energetics, and chemistry of the earliest galaxies.

### 1.2.1 Arrayed Waveguide Gratings

The astronomical light guided in the single mode fibers can be dispersed in many ways, most of which are inherited from the telecommunication technique wavelength division multiplexing (WDM). This technique emerged from the need to increase the data density of the existing fiber-optic networks by using multiple wavelengths to carry multiple data packets simultaneously. Thus, a variety of photonic platforms were developed to combine different wavelengths (multiplex) and disperse them (de-multiplex).

Some of the photonic technologies particularly relevant for spectroscopy applications include: Arrayed Waveguide Gratings (AWG), Photonic Echelle Gratings (PEG), Photonic Fourier Transform Spectrographs (FTS). For each technique, we briefly discussed their relevance to astronomy, their underlying concept, fabrication methods, challenges, and their upcoming solutions in the context of astronomical spectroscopy in [Gatkine et al., 2019b]. Given the current paradigm of well-established design and fabrication techniques and the stringent throughput re-

quirements in astronomy, Arrayed Waveguide Grating technique is the best-suited option for low-/moderate-resolution astronomical spectroscopy.

### 1.2.2 AWG: New directions

AWG uses an on-chip phased array-like structure of waveguides to introduce progressive path lengths similar to a grating. The on-chip implementations are compact and easily stackable to create an IFU or multi-object spectrograph [Cvetojevic et al., 2012a, Harris and Allington-Smith, 2012, Gatkine et al., 2017]. The idea of the use of AWG for astronomical spectroscopy was first proposed by [Bland-Hawthorn and Horton, 2006] and an on-sky demonstration was conducted at the Anglo-Australian Telescope [Cvetojevic et al., 2012a]. This implementation used a commercial AWG based on $SiO_2$ platform.

Over the past few years, silicon nitride (SiN) platform has emerged as a new alternative to the conventional $Si/SiO_2$ platforms with its low loss in visible, near- and mid-IR wavelengths [Muñoz et al., 2017]. It is possible to achieve ∼90% on-chip throughput in photonic devices on SiN platform provided a tight process control is exercised in fabrication [Blumenthal et al., 2018]. Such control with nanoscale precision can be achieved using stable electron-beam / extreme-UV lithography.

We explored this direction of SiN platform with precision electron-beam lithography to build a high-throughput AWG for astronomical spectroscopy. Apart from improving the throughput on the chip itself, we also engineered waveguide tapers to achieve high-efficiency coupling between the fibers (carrying the light from tele-

scope to the chip) and the on-chip waveguides (feeding the light to the AWG). These developments are crucial to attain high end-to-end throughput for the spectrograph.

It is important to make certain adaptations to the conventional AWG designs due to requirements unique to spectroscopy (particularly, in astronomy). We explored various such adaptations including: 1) cleaving at the focal plane of the AWG to access continuous spectrum (instead of discretized sampling in a conventional AWG), 2) new ways of attaining polarization insensitivity, and 3) multi-input AWGs to receive the light from multiple single-mode fibers emanating from the photonic lanterns. Finally, to acquire the full spectrum on a detector, we built a cross-dispersion setup which will be used in the near future for integrating all of these elements − a photonic lantern, multi-input AWG, cross-dispersion setup, and the detector − to make the AWG spectrograph ready for an on-sky test.

For this thesis, we focused on astronomical H band (1.45 – 1.65 $\mu m$) for two reasons: 1) The UV/optical light from the stars in the earliest galaxies ($z > 6$) is redshifted to this waveband. 2) This waveband is widely used in telecommunication applications and hence, the material properties are well-known and various peripherals (eg: fibers, lasers, spectrum analyzers) are readily available.

Apart from my key work on AWGs, I also contributed to 1) development of waveguide tapers for an efficient coupling of light from a fiber to a SiN waveguide [Zhu et al., 2016b], 2) development of on-chip waveguide Bragg gratings for suppression of OH-emission lines [Zhu et al., 2016a], and 3) characterization of the propagation loss of a waveguide on a chip [Hu et al., 2018].

## 1.3 Thesis outline

This thesis has two focal points: 1) exploring the circumgalactic medium and outflows in the early universe ($z \sim 2-6$) using GRB afterlows, and 2) development of photonic spectrographs to enable the observations of GRB afterglows even beyond $z \sim 6$ and other astronomical pursuits.

The key questions that we will be addressing in this thesis are summarized in Sections 1.1.7 and 1.2.2. In chapter 2, we discuss the kinematics of the CGM around high-z star-forming galaxies derived using GRB afterglow spectra (in the CGM-GRB sample) and investigate any redshift evolution. Next, we set out to estimate the host galaxy properties ($M_*$, SFR) and explore their correlations with the CGM/outflow properties. Along that path, we first estimate the total SFR (obscured + unobscured) of massive GRB hosts in our sample using radio observations. This part is covered in chapter 3. Finally, we examine the correlations between the kinematic properties of the outflow and the host galaxy properties in chapter 4 to learn about the mechanisms of cosmic metal enrichment.

Next, we discuss our efforts on the development of photonic spectrographs using the promising technique of Arrayed Waveguide Gratings in chapter 5. In chapter 6, we summarize our work on two key aspects to make the spectrograph ready for deployment − multi-input AWG and cross-dispersion system. We conclude and outline the path for future work for both the science and instrumentation parts in chapter 7.

## 1.4 A summary of facilities

The work presented in this thesis is based on new as well as archival data obtained from several observatories. Each chapter discusses the relevant facilities in greater detail. Here we highlight the most important facilities that made this thesis possible.

First, we used the high-resolution GRB afterglow spectra from the Keck and Very Large Telescopes in Chapter 2. Most of these GRBs have been discovered and localized by NASA's *Neil Gehrels Swift Observatory*. Second, we used the photometry of the host galaxies of these GRBs obtained from the *Spitzer Space Telescope*, 4.3-meter Lowell Discovery Telescope, Keck Telescope, and Very Large Telescopes. We note that new optical observations of the GRB hosts reported in Chapter 4 were performed at the Lowell Discovery Telescope in campaigns 2018A, 2019A, 2019B, and 2020A (PI: Gatkine). Both the afterglow spectroscopy and host photometry datasets mark the culmination of two decades of observations. Third, we used the fully upgraded Karl G. Jansky Very Large array (JVLA) to obtain deep radio observations of a selected group of GRB hosts as a part of VLA 18B-312 program (PI: Gatkine). These data are used in Chapter 3.

Apart from observational facilities, we used the Nano Fabrication Lab at the Maryland Nanocenter to fabricate various photonic chips that are presented in this thesis (Chapters 5 and 6). We also used the Maryland Astrophotonics Laboratory (MAPL) for testing, characterization, and integration of the astrophotonic chips and devices.

## A summary of software/codes used in this work

1. CASA [Emonts et al., 2019]
2. astropy [Robitaille et al., 2013]
3. emcee [Foreman-Mackey et al., 2013]
4. esoreflex [Freudling et al., 2013]
5. galfit [Peng, 2003]
6. lifelines [Davidson-Pilon et al., 2020]
7. ASURV [Feigelson and Nelson, 1985, Isobe et al., 1986, Isobe and Feigelson, 1990]
8. FIMMWAVE[1]
9. Rsoft/BeamPROP[2]
10. DCAM-CL (Hamamatsu)[3]

[1] https://www.photond.com
[2] https://optics.synopsys.com
[3] https://dcam-api.com/

# Chapter 2: Uncovering The Circumgalactic Medium around GRB hosts at redshifts 2−6

*In this chapter, we will explore the kinematics of CGM around GRB hosts at high redshifts.*

## 2.1 Introduction

The circum-galactic medium (CGM) is loosely defined as the multiphase material surrounding galaxies out to the virial radius (typically spanning 10 to 300 kpc, depending on the mass and redshift of the galaxy [Tumlinson et al., 2017]). The CGM resides at the interface between the interstellar medium (ISM) of the galaxy and the intergalactic medium (IGM), and thus harbors galactic outflows, accretion flows, and recycling flows. The gas inflows fuel star formation while stellar winds and supernova explosions inject energy and metal-enriched matter at large distances into the ISM and CGM. Studying the CGM and its evolution in the early universe is key to understanding the feedback mechanisms in galaxies. The synergy between these processes is thought to shape galaxies and drive their evolution over cosmic timescales [Tumlinson et al., 2011, Schaye et al., 2014, Hopkins et al., 2014, Voit et al., 2015, Anglés-Alcázar et al., 2017, Nelson et al., 2019].

The history and mechanisms of metal enrichment of the universe remain poorly understood, primarily due to limited probes of galaxies, CGM, and IGM, at high redshifts ($z2$). The metal content of the universe as a function of cosmic time can be estimated, given the cosmic star formation history and the models of stellar nucleosynthesis. Even with liberal estimates, current observations have only accounted for ∼50-70% of the metals created in stellar processes [Campana et al., 2015, Bouché et al., 2006]. As an example, the recent COS-Halos studies have inferred that at $z \sim 0$, only ∼20-25% of the metals produced by the stars remain in the galaxy (ISM, stars, and dust), while ∼40% of the metals reside in the CGM [Peeples et al., 2014].

At higher redshifts, the distribution of metals among the galaxy (ISM, stars, and dust), CGM, and IGM is even more uncertain due to limited observations. Simulations and observations at $z > 2$ suggest that the CGM could account for $\sim 30\%$ of the cosmic metal budget at that epoch ([Schaye et al., 2014, Lehner et al., 2014]). The transport of metals from their formation sites (i.e. galaxies) to the CGM and IGM is driven by galactic-scale outflows. The distribution of metals and baryons in the galaxy ecosystem provides critical constraints for galaxy evolution models and mechanisms of gas and metal transport [Rahmati et al., 2016, Muratov et al., 2017]. Therefore, probing the CGM at high redshifts is essential to develop and test theories of galaxy evolution and metal enrichment.

### 2.1.1 Methods to Probe the CGM

Various methods have been employed in past and ongoing observations to extract the diagnostic features of the multi-phased CGM. The most popular technique involves using a bright background quasar (QSO) to trace the CGM around an intervening galaxy. Various local CGM surveys ($z < 0.5$) including COS-Halos [Tumlinson et al., 2013, Werk et al., 2016, Prochaska et al., 2017], COS-Dwarfs [Bordoloi et al., 2014b], COS-GASS [Borthakur et al., 2015], and others [Stocke et al., 2013, Zhu and Ménard, 2013] utilize UV/optical absorption spectra to study CGM kinematics and physical properties through high ionization potential species (high-ion) such as O VI, N V, C IV, Si IV and low ionization potential species (low-ion) such as Fe II, Si II, C II, Ca II in the CGM. These observations allow matching the absorbers to their respective impact parameters from the galaxy with a precision of tens of kpc. The higher redshift surveys of QSO-galaxy pairings (eg: [Fox et al., 2007, Lehner et al., 2014, Turner et al., 2014, Rudie et al., 2019]), QSO-QSO pairings (QPQ; [Hennawi et al., 2006, Prochaska et al., 2014, Lan and Mo, 2018]), and galaxy-galaxy pairings [Steidel et al., 2010, Lopez et al., 2018] use rest-frame UV spectra for similar analysis with limited information about the associated galaxies and/or impact parameters.

In “down-the-barrel" spectroscopy, a star-forming galaxy’s own starlight is used as a background illumination to detect absorption from the intervening ISM and CGM [Martin, 2005, Steidel et al., 2010, Bordoloi et al., 2011, Rubin et al., 2012, Kornei et al., 2012, Heckman et al., 2015, Rubin et al., 2014, Rigby et al.,

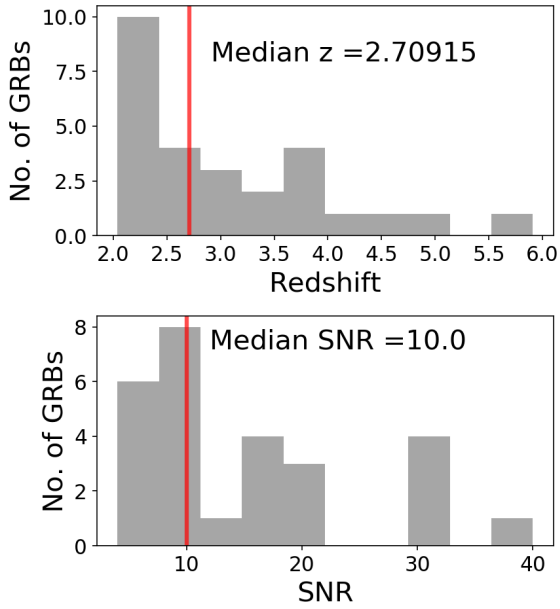


Figure 2.1: Upper panel: Distribution of redshifts in the GRB sample. The median redshift is 2.71. Lower panel: Distribution of the signal-to-noise ratios of the spectra used for this study. The median ratio is 10.

2018]. This technique has been successful in tracing the galactic inflows and outflows in the CGM of star-forming galaxies with a caveat that the radial coordinate of the absorbing component remains unconstrained.

### 2.1.2 The CGM-GRB Project

Our approach utilizes the spectra of bright afterglows of long Gamma-ray Bursts (GRBs) to derive the kinematic properties of the CGM around their host galaxies and use a simple toy model to further constrain the physical properties of the CGM gas. This technique will further enable the investigation of possible relations between the CGM and the galaxy properties that may govern feedback processes and their evolution with redshift. Thanks to the nature of GRBs and the extensive follow-up effort over the past ten years, we were able to collect enough

data to study the CGM of GRB hosts in the redshift range $2 \lesssim z \lesssim 6$.

Long-duration GRBs are the most powerful explosions in the universe, being several orders of magnitude more luminous than typical supernovae. The prompt emission is followed by a rapidly fading ($\sim$1$-$2 days) X-ray, UV, and optical afterglow. GRB afterglows have been detected from low redshift $\sim$0.01 out to a redshift of 8.2 [Tanvir et al., 2009, Salvaterra et al., 2009, Cucchiara et al., 2011], thus probing the first few billion years of the Universe, an era characterized by the formation and early evolution of galaxies that may have had a critical role in enriching the universe with metals.

Since GRB afterglows are bright background sources, their spectra harbor absorption features produced by the material along the line-of-sight including the host galaxy ISM as well as the CGM and intergalactic medium [Prochaska et al., 2007, Fox et al., 2008, Prochaska et al., 2008b, Cucchiara et al., 2015]. Thus it provides an excellent opportunity to probe the chemical composition and physical conditions of the entire galaxy ecosystem. The GRBs also fade rapidly, making it possible to study the host galaxy component separately, in the absence of the bright GRB.

Compared to QSO sightlines, GRB sightlines have key advantages: 1) GRBs happen within their host galaxy, thus probing the host galaxy ISM as well as the associated CGM, the main components of the galaxy ecosystem; 2) GRB discovery is based on gamma- and X-ray detection and hence, is largely independent with respect to host galaxy properties (further discussed in §2.2.2); 3) The optical afterglow fades in 1-2 days, clearing the path for future deep observations of the host galaxy to study

its global properties and surroundings.

However, at the same time, the number of GRBs suitable for CGM investigation is small, despite the detection rate of 100 $yr^{-1}$ by dedicated space-based mission like the Neil Gehrels Swift Observatory (*Swift*). Similarly, the fast-decaying nature of their afterglows requires opportune follow-up strategies in order to obtain high-SNR spectra. And finally, it requires separating the CGM and ISM contributions in the absorption spectra, which can be challenging. Our approach tackles this problem by using the kinematic information derived by absorption line spectroscopic data.

In this paper, we present the analysis of a dataset of 27 high-z ($z \gtrsim 2$) GRBs, out of which 6 are at $z \gtrsim 4$ (§2.2, §2.3). We use column density line profiles to study the kinematics and line ratios of the absorbing gas to distinguish between the CGM and ISM (§2.4). We designed a simple toy model (§2.5) to obtain an estimate of the outflow properties in the CGM. We estimate the CGM mass for a typical GRB host in this sample and summarize its possible evolution with redshift in §2.6. In §2.7, we discuss various implications our findings may have on our current understanding of the CGM kinematics, outflow rates, metal enrichment, and CGM-galaxy co-evolution. The key conclusions of this study are summarized in §8.

## 2.2 The GRB Sample

### 2.2.1 Sample Properties

Obtaining a good estimate of ionic column density as a function of velocity requires high signal-to-noise spectra (SNR $\gtrsim 5$) of medium resolution ($R \gtrsim 8000$, $\sim$

50 km $s^{-1}$). The cut-off in resolution is selected to clearly distinguish the absorption systems at different velocities and minimize the errors in column density estimation due to saturation effects and blending (see [Prochaska et al., 2006, Cucchiara et al., 2013]). Our CGM-GRB sample consists of 27 long GRBs that satisfy these stringent criteria. The sample properties are summarized in Fig. 2.1. The median redshift of the sample is 2.71 and median SNR is 10. Notably, six of the GRBs are at z > 4. Table 2.4 lists the GRBs in this sample along with the observational details.

As mentioned earlier, the transient nature of GRBs requires rapid-response facilities capable of observing their afterglow within a few minutes of their discovery. Our dataset comprises primarily of archival data acquired by the X-Shooter and UVES spectrographs on the Very Large Telescope (VLT). These spectra provide a wide wavelength coverage (from optical to NIR) and sufficiently high spectral resolution ($R \sim 8,000 - 55,000$). In addition, we retrieve spectra from the archival dataset of the Keck telescope's HIRES and ESI spectrographs.

The majority of these spectra were re-analyzed and normalized using the data analysis pipelines in [Cucchiara et al., 2013, Cucchiara et al., 2015]. More recent data (from 2014) were acquired from the PHASE 3 VLT archive[1,2], which provides fully reduced, research-ready one- and two-dimensional spectra. We utilized the flux-calibtrated one-dimensional spectra and normalized the GRB afterglow continuum using a spline function. Every spectrum is manually inspected and the overall continuum is determined using the python-based `linetool` package [3]. The error

[1] https://www.eso.org/sci/observing/phase3.html
[2] http://archive.eso.org/wdb/wdb/adp/phase3_main/form
[3] https://github.com/linetools/linetools

from the continuum fit is propagated into the flux error spectrum.

### 2.2.2 Selection Effects

Due to the high SNR and resolution requirement, this sample is biased towards the brighter end of GRB afterglows distribution. The afterglow magnitudes at the time of taking the spectra are listed in Table 2.4, clearly indicating a limit at $m_{AB}$ $\sim$ 21.0 (with an exception of GRB 100219). This selection effect is complex since the magnitude at the time of observation depends on the intrinsic brightness and distance of the afterglow as well as the time elapsed since the prompt gamma-ray emission. Regardless, it can be said that this sample selectively avoids intrinsically faint afterglows. However, considering that the apparent brightness of the afterglow also depends on the host galaxy dust extinction, it can be said that this sample selectively avoids heavily dust-obscured ($A_V > 0.5$) sightlines [Perley et al., 2009, Krühler et al., 2011, Zafar et al., 2018].

In general, long GRBs trace cosmic star formation [Greiner et al., 2015, Schady, 2017]. At z $\sim$ 2.5, the typical star formation rate of GRB hosts is $\sim$10 $M_\odot$ yr$^{-1}$ [Krühler et al., 2015], the typical GRB host stellar mass is $\sim 10^{9.3}$ $M_\odot$ [Perley et al., 2016b] and the typical gas phase metallicity is $\sim 0.05 - 0.5$ solar [Trenti et al., 2015, Arabsalmani et al., 2018]. Thus, from a CGM perspective, this sample traces star-forming, low-mass galaxies at $z > 2$.

## 2.3 Methods

### 2.3.1 Redshift Determination

In order to infer the kinematics of different chemical species, the redshifts of the GRB host galaxies in the sample need to be determined in a precise and uniform manner. Commonly, the galaxy redshifts are obtained using nebular emission lines (e.g. H$\alpha$) but this method is not viable for faint GRB hosts at high redshifts. Therefore, we use the local GRB environment (within few $\times$ 100 pc of the GRB) as a proxy for the systemic redshift of the GRB host galaxy.

The fine structure transitions of the species such as such as Ni II*, Fe II*, Si II*, and C II* in the rest-frame UV [Bahcall and Wolf, 1968] trace the ISM clouds in the vicinity of the GRB ($\sim$ few $\times$ 100 pc $-$ 1 kpc) due to UV pumping. This is further corroborated by temporal variations found in the strength of these lines in multi-epoch spectra of a few GRBs [Vreeswijk et al., 2007, Hartoog et al., 2015, D'Elia et al., 2014]. The strongest absorption components (i.e. velocity components) of these fine-structure transitions are therefore good proxies for the rest-frame velocity of the burst environment within a few hundred parsecs [Chen et al., 2005, Dessauges-Zavadsky et al., 2006, Prochaska et al., 2006]. Therefore, we choose the redshift by visual inspection such that the strongest absorption components in the fine-structure transitions occur at $\sim$ 0 km s$^{-1}$, i.e. rest frame. We primarily use Si II* and C II* transitions for estimating the redshift. In case of saturation or confusion between Si II* and C II*, we use Ni II* lines due to their lower oscillator strength.

In addition, we visually check for the presence of other low-ionization lines such as Fe II 1608, Si II 1526, and Al II 1670 (especially the weak transitions of Si II and Zn II) which are reliable tracers of the host galaxy ISM [Prochaska et al., 2006, Cucchiara et al., 2013], to visually confirm the redshift determination. With the use of the strongest components of fine-structure transitions to estimate the zero point, the GRB redshift is accurate to within 50 km $s^{-1}$.

### 2.3.2 Spectroscopic Analysis

GRB spectra show a plethora of signatures, ranging from the circumburst and interstellar media to the galactic winds and circumgalactic medium. Prior studies have extracted the intervening systems along the GRB sightlines (at $z < z_{GRB}$) to trace cosmic chemical evolution. These studies have used the doublets from Mg II, C IV, and Si IV, to determine the chemical enrichment of the universe similar to the analysis of quasars intervening systems [Prochaska et al., 2008b, Fox et al., 2008, Fynbo et al., 2009, Simcoe et al., 2011, Thöne et al., 2012, Sparre et al., 2014, Cucchiara et al., 2015, Vergani et al., 2017]. In this paper, we focus on the contrast between the high and low ion kinematics. The GRB spectra were normalized, binned, and fitted to extract the column density, Doppler parameter, and the line center (in velocity space) for each absorbing component within a velocity window of ±400 km $s^{-1}$ for key high- and low-ion species. The parameters of these species were then used to study the kinematics of the absorbing gas and estimate the likely origin of the absorbing component(s).

Filtering: Various intervening systems previously reported in the literature (references in Table 2.4) were identified and the regions where the absorption lines from the intervening system blend with rest-frame GRB absorption were flagged. In addition, the regions containing telluric absorption from the atmosphere were flagged. For lines with strong neighboring transitions (eg: Si II 1260 and S II 1259, etc), the velocity windows considered for fitting were carefully adjusted to minimize the confusion.

Voigt profile fitting: Thanks to the medium resolution spectra in this sample, it is possible to resolve the kinematics of absorbing systems residing in the ISM and CGM into individual components in the velocity space. The GRB spectra were analyzed by fitting individual components, where the optical depth of each component is modeled as a Voigt profile. Given the complex nature of GRB sightlines, typically more than 5 absorption components are observed in these spectra. While there are other $\chi^2$ grid-search-based codes (eg: VPFIT[4] and MPFIT [Markwardt, 2009]) for fitting the Voigt profiles, there are fundamental limitations of these methods for solving this particular problem. Obtaining useful results with a grid-search in such a large parameter space of a non-linear model is computationally expensive. Further, it is difficult to capture the degeneracy between various parameters in a quantitative manner, for instance, the degeneracy between Doppler parameter and column density for saturated components. The Bayesian approach provides a rigorous way to visualize the degeneracy and estimate the errors around the fit parameters in a systematic way for multi-component Voigt profiles.

[4]Available at https://www.ast.cam.ac.uk/~rfc/vpfit.html

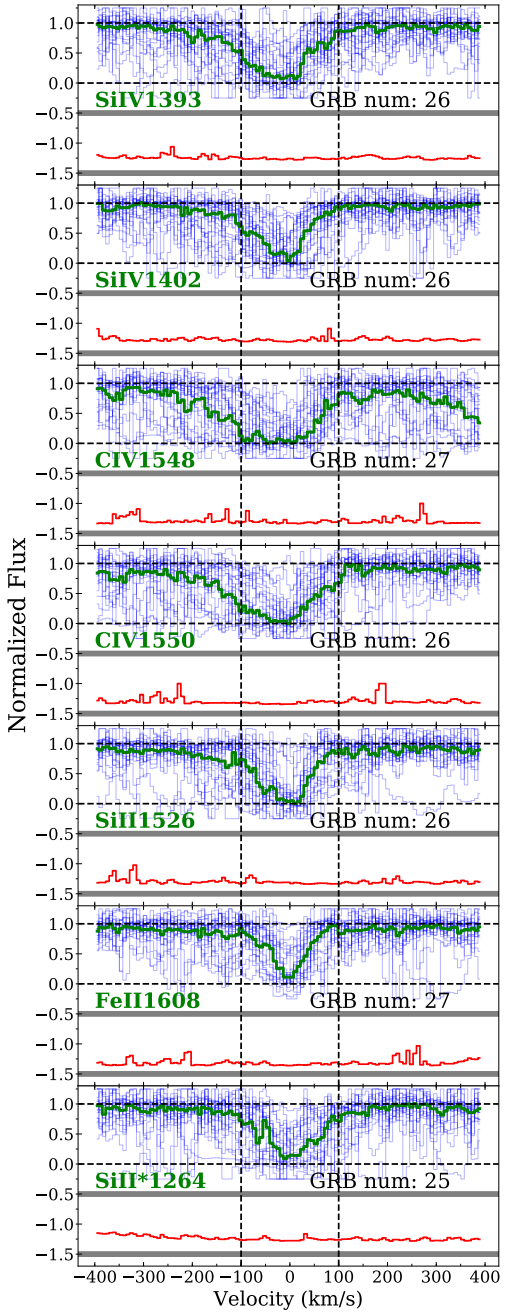


Figure 2.2: The median absorption line profiles (in green) of the individual spectra (in blue) in the CGM-GRB sample. The red line shows the rms noise (shifted vertically by $-1.5$).

For these reasons, we developed a Bayesian-inference-based, multi-component Voigt profile fitting code in Python to determine the best-fit values of the parameters for each component($i$), i.e. the column density ($N_i$), Doppler parameter ($b_i$), and

line center ($v_i$). To sample the posterior probability distributions, the Markov Chain Monte Carlo (MCMC) method was used. The MCMC sampling was implemented using `emcee` library in Python [Foreman-Mackey et al., 2013]. A detailed summary of the Bayesian Voigt-profile fitting method and error estimation is given in Appendix A.1. This code provides a robust and novel approach to fit the complex multi-component absorption systems such as GRB or QSO sightlines and obtain reliable estimates of the optimal parameters and the associated errors.

To fit multi-component Voigt profiles to a given transition, a velocity window spanning $\pm$400 km s$^{-1}$ around the GRB rest-frame is extracted. This velocity window enables fair comparisons with the simulations of CGM as well as previous observations of high- and low-redshift CGM. The spectra are binned by a factor of 2 to 4 depending on the noise level for easier visual inspection. The number of components to be fitted is determined through manual inspection of doublets (eg: C IV 1548 and 1550) and lines with similar ionization potential (eg: C IV, Si IV). The line spread function of the spectrometer is modelled as a Gaussian function and convolved with the synthesized multi-component Voigt profile to obtain the comparison spectrum for evaluating the residuals. The initial guesses of the parameters are manually provided to the MCMC routine (as priors) to find the optimal line-parameters and associated uncertainties corresponding to all the components ($N_i$, $b_i$, $v_i$). Also, doublets are fitted simultaneously. Our optimal parameters are consistent with the results from other references in Table 2.4 as shown in Fig. 2.3. The Voigt-profile fits are shown in figures A.4$-$A.30 and the line profile parameters are listed in Table 2.3.

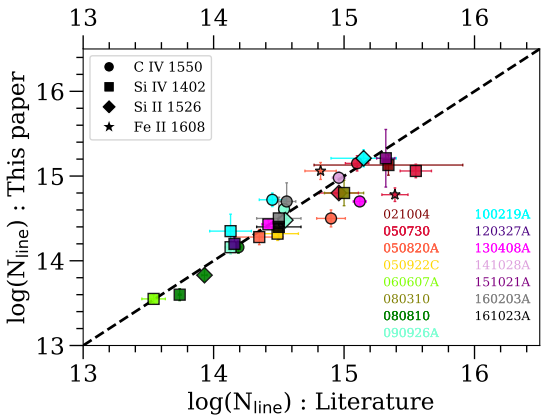


Figure 2.3: Comparison of total column densities partially compiled from the literature (references in Table 2.4) with the total column densities derived in this paper. The dotted line represents the line of equality.

Caveats: The kinematic resolution of the analysis is linked to the spectral resolution of each observation, leading to a variance in the precision of the parameter estimation throughout the sample due to different spectral resolutions. For warm CGM (T $\sim$ $10^{5-6}$ K), the thermal Doppler parameter is expected to be in the range $5 - 20$ km s$^{-1}$ for C and Si with further broadening expected due to turbulence [Lehner et al., 2014]. For spectra with R $\sim$ 10000, we can marginally resolve b $\sim$ 15 km s$^{-1}$. In saturated regions, the determination of optimal parameters has a higher uncertainty due to degeneracy between the Doppler parameter and column density. In such cases, lines with similar ionization potential and weaker oscillator strength help provide an estimate without breaking the degeneracy. While the Voigt profile fitting works well in case of mildly saturated lines, it does not fully alleviate the uncertainty for strongly saturated lines (such as saturation spanning $\sim$ 100 km s$^{-1}$). In Table 2.3, a quality flag of 0 indicates unsaturated or mildly saturated components while a quality flag of 1 indicates strongly saturated components. The tabulated profile parameters for strongly saturated components denote a likely but

non-unique solution.

## 2.4 Inferring Kinematics

### 2.4.1 Median Plots

In order to understand the overall kinematics of the sample, the normalized rest-frame spectra were plotted in velocity space. In Fig. 2.2, various high- and low-ion transitions of the individual GRBs are shown in blue, while the median kinematic profiles are shown in green. The key qualitative results from the median plots are:

a) There is a significant blueward absorption excess at velocities $v \lesssim -100$ km s$^{-1}$, which is a clear signature of outflowing gas.

b) This blueward asymmetry is stronger in the high-ion transitions than in the low-ion transitions. The median profile for the fine structure transition of Si II* is, not surprisingly, more symmetric.

c) The median absorption for the low-ion transitions is fairly limited to within $\pm$100 km s$^{-1}$ unlike the high-ion lines, which extend much further (especially blueward).

These qualitative observations may indicate outflowing gas predominantly traced by the high-ion transitions. Thus, we expect at least two different phases that are kinematically distinct. In order to test this hypothesis in greater details we use a toy model to reproduce the observed kinematic behavior (Section 2.5).

### 2.4.2 Integrated Line Profiles

The absorption lines in the afterglow spectra from various high- and low-ion species were fitted with multi-component Voigt profiles as described in Section 2.3.2. In order to quantitatively measure and compare the kinematics of high- and low-ion species as well as compare the observations with models (as described in Section 2.5), the fitted continuous line profiles were converted into integrated column density profiles. The fitted Voigt profiles profiles (with $N_i$, $b_i$, and $v_i$) were converted to apparent optical depth profiles as a function of velocity ($\tau_a(v)$) such that $\tau_a(v) = ln[F_c(v)/F(v)]$, where $F_c(v)$ is the normalized continuum flux level (i.e. 1) and $F(v)$ is the normalized flux from the fitted profile at velocity $v$ [Savage and Sembach, 1991]. The apparent column density is then evaluated as $N_a(v) = 3.768 \times 10^{14}\tau_a(v)/f\lambda$, where $f$ is the oscillator strength and $\lambda$ is the rest-frame wavelength of the line in Å. The integrated column density is the integral of $N_a(v)$ over bins of 100 km s$^{-1}$.

The integrated column density profiles are shown in blue in Figures 2.4, 2.10, and 2.11. The strongly saturated components are treated as lower limits evaluated by imposing a maximum cap on $\tau_a(v)$ of 4.5 (equivalent to a lower cap of $\sim$0.01 on the normalized flux) and they are marked as open circles. The saturation issue does not significantly affect the velocity bins beyond $\pm$ 100 km s$^{-1}$. The downward triangles show integrated column density for a bin with no detected absorption and is evaluated using $\tau(v) = 0.05$ which denotes the typical detection limit of the sample. The error bars on the integrated column density are evaluated by calculating the

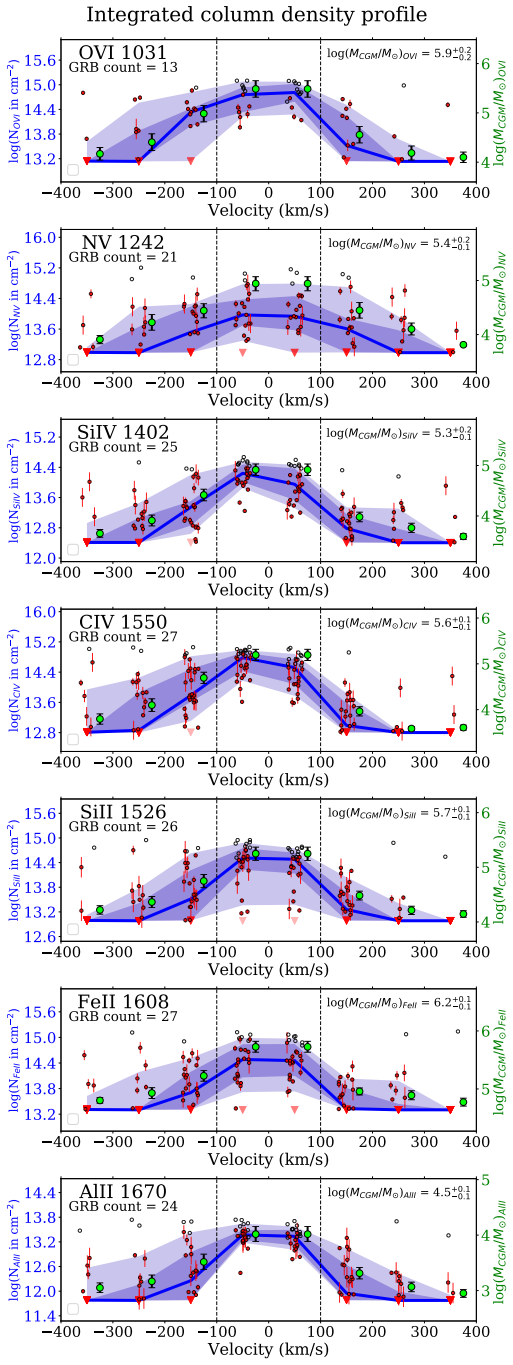


Figure 2.4: The integrated column density profiles for the high- and low-ion species of the CGM-GRB sample. The blue line and labels refer to the median values while the central 50 and 80 percentiles are shown in darker and lighter shades. The green line and labels indicate the estimated mass of the species in the CGM.

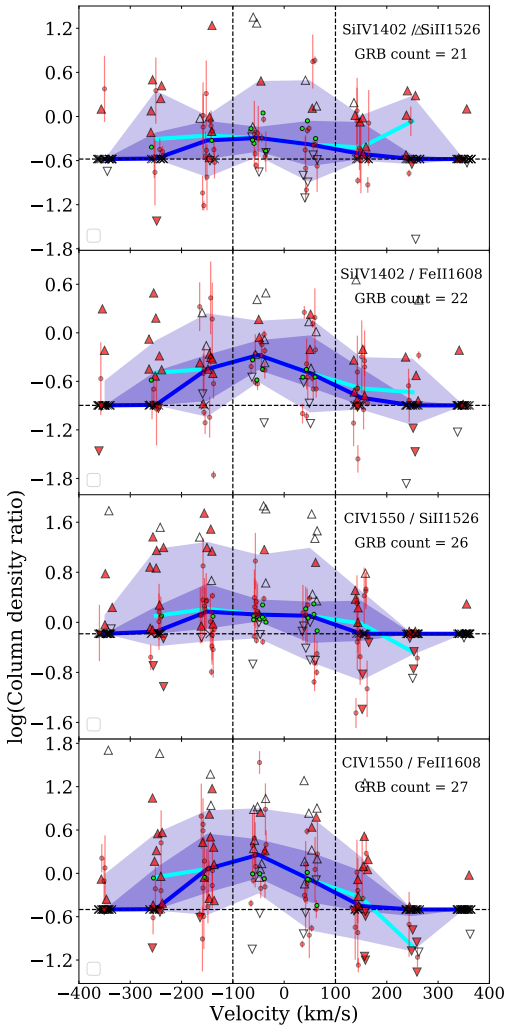


Figure 2.5: The high- to low-ion line ratios as a function of velocity. The line ratios are evaluated as the ratio of integrated column densities for the two lines as a function of velocity. The solid red symbols indicate that at least one of the two absorption lines is detected in that velocity bin. The empty symbols indicate that one of the two lines is saturated, while the green circles show the cases where both the lines are saturated in that velocity bin (double saturation points). A circle denotes detection of both lines, an upwards (downwards) triangle denotes lower (upper) limits. A cross symbol indicates points where both the lines have non-detections (double non-detection points). The blue line traces the median of the line ratios including double non-detection points at each velocity bin with the purple shades spanning the 50- and 75-percentile zones. The cyan line traces the median excluding the double non-detection points (i.e. requiring the detection of at least one of the two lines in the given velocity bin).

difference between the Voigt profiles generated using the optimal parameters and the profiles generated using the 1-$\sigma$ deviation parameters (as shown in Fig. A.1). This captures both the fitting uncertainty as well as the noise spectrum. The median integrated column density profile for each line is shown in blue. The inner and outer purple-shaded regions show the central 50 and 80 percentiles of the integrated column density distribution for each bin, respectively.

### 2.4.3 Detection Fractions

The integrated column density profiles help visualize the fraction of sightlines where various species are detected as a function of velocity. Broadly speaking, the detection fractions can be categorized in three kinematic regions: central ($|v| <$ 100 km s$^{-1}$), blue wing ($v < -100$ km s$^{-1}$), and red wing ($v > +100$ km s$^{-1}$). The detection fractions of various high- and low-ion species are calculated as the number of detected sightlines divided by the number of sightlines with the spectral coverage for that ion and are reported in Table 2.1. The O VI and N V absorption lines are redshifted to the low-sensitivity (blue) regions of the spectrographs for $z \sim 2$, which leads to a poor signal-to-noise ratio. In addition, the vicinity to the Lyman-alpha forest and possible doublets contamination can prevent reliable detection of these species. Therefore, we only consider the detections where both doublets show absorption lines that can be reasonably fitted. The uncertainty on the detection fractions for these ions reflects the small number of cases where these lines are within the spectral coverage and are not affected by low SNR, saturation,

Table 2.1: Detection fractions in various kinematic regions

| Species | Blue wing (v < -100 km s$^{-1}$) | Central ($\|v\|$ < 100 km s$^{-1}$) | Red wing (v > 100 km s$^{-1}$) |
|---|---|---|---|
| O VI | $0.65^{+0.2}_{-0.0}$ | $0.8^{+0.2}_{-0.0}$ | $0.6^{+0.2}_{-0.0}$ |
| N V | $0.52^{+0.16}_{-0.0}$ | $0.76^{+0.16}_{-0.0}$ | $0.56^{+0.16}_{-0.0}$ |
| Si IV | $0.92^{+0.04}_{-0.0}$ | $0.96^{+0.04}_{-0.0}$ | $0.69^{+0.04}_{-0.0}$ |
| C IV | 0.96 | 1.00 | 0.63 |
| Al III | 0.67 | 1.00 | 0.62 |
| Si II | 0.73 | 0.96 | 0.61 |
| Fe II | 0.67 | 0.92 | 0.55 |

or mismatch between the doublets.

The central region within ±100 km s$^{-1}$ shows the highest detection fraction for all the ions. The blue wings have a higher detection fraction compared to the red wings for all the ions except N V, as expected from the stacked spectra (Fig. 2.2). We compare the detection fractions in this sample with KODIAQ sample − a QSO-based survey of CGM absorbers at $z \sim 2 - 3.5$ [Lehner et al., 2014]. The overall detection fractions in the KODIAQ survey for O VI (75%), N V (55 ± 20%), Si IV (95%), C IV (90%), and Fe II (78%) are consistent with the detection fractions in blue wing region of the CGM-GRB sample within ∼ 10%.

### 2.4.4 Kinematic Asymmetry

It is evident from the stacked spectra in Fig. 2.2 that there is a clear excess of absorption in the blue wing ($v < -100$ km s$^{-1}$) relative to the red wing ($v >$ 100 km s$^{-1}$). The excess also appears to be stronger for the high-ionization species such as Si IV and C IV relative to the low-ionization species such as Si II and Fe II. We quantify this kinematic asymmetry using the median integrated column density

profiles shown in Fig. 2.4. The median of the total integrated column densities are tabulated in three distinct kinematic regions in Table 2.2: central ($|v| < 100$ km s$^{-1}$), blue wing ( $v < -100$ km s$^{-1}$), and red wing ($v > 100$ km s$^{-1}$). The reported uncertainties are evaluated as 2-$\sigma$ intervals of the distribution of medians of total integrated column densities derived via a simple resample-with-replacement bootstrap technique. The degree of asymmetry is calculated as the ratio of blue- to red-wing column densities. The median asymmetry in the high ions C IV and Si IV are 0.36 and 0.52 dex, respectively, in contrast to $\sim$ 0.17 and 0.19 dex for the low ions Si II and Fe II, respectively.

The blue absorption excess (or asymmetry) has been interpreted as a galactic outflow signature in previous GRB-afterglow sightline studies (eg: with 7 high-z GRBs in [Fox et al., 2008] and GRB 080810 in [Wiseman et al., 2017a]). From the kinematic distribution in the blue wing, the typical outflow velocity is $\sim 150 - 250$ km s$^{-1}$. Another important aspect is the higher degree of asymmetry in Si IV and C IV relative to Si II and Fe II. These high ionization species are more asymmetric by roughly a factor of $\sim 1.5 - 2$ than the low ionization species. This key observation implies that not only there is an excess of outflowing gas compared to infalling gas, but also the outflowing gas is more highly ionized than the infalling gas. Unlike all the other ions presented here, N V has no significant asymmetry and therefore, could be tracing a phase (or a combination of phases) that is kinematically distinct from the gas phase (or a combination of phases) traced by the other high- and low-ion lines. We return to this point in section 2.7.

Table 2.2: Kinematic asymmetry in high and low ions

| Species | Integrated col. density in $cm^{-2}$ Blue wing $log(N_B)$ | Central $log(N_C)$ | Red wing $log(N_R)$ | Asymmetry (dex) |
|---|---|---|---|---|
| O VI | $14.39^{+0.15}_{-0.22}$ | $14.98^{+0.08}_{-0.19}$ | $13.80^{+0.13}_{-0.17}$ | 0.59 |
| N V | $13.72^{+0.17}_{-0.25}$ | $14.36^{+0.18}_{-0.24}$ | $13.80^{+0.20}_{-0.31}$ | -0.08 |
| Si IV | $13.46^{+0.18}_{-0.22}$ | $14.49^{+0.15}_{-0.15}$ | $13.10^{+0.14}_{-0.16}$ | 0.36 |
| C IV | $13.87^{+0.09}_{-0.13}$ | $14.99^{+0.14}_{-0.11}$ | $13.35^{+0.07}_{-0.07}$ | 0.52 |
| Al III | $12.48^{+0.14}_{-0.22}$ | $13.70^{+0.09}_{-0.05}$ | $12.32^{+0.06}_{-0.06}$ | 0.16 |
| Si II | $13.75^{+0.19}_{-0.25}$ | $14.82^{+0.10}_{-0.19}$ | $13.58^{+0.09}_{-0.30}$ | 0.17 |
| Fe II | $13.97^{+0.15}_{-0.17}$ | $14.89^{+0.17}_{-0.23}$ | $13.78^{+0.05}_{-0.10}$ | 0.19 |

### 2.4.5 Line Ratios

The ratio of column densities of various high- and low-ion species provides another perspective to learn about the physical conditions of the intervening gas in different kinematic regions. We select Si IV, C IV, Si II, and Fe II for this analysis since they have excellent spectral coverage in the sample and are fit reasonably well due to high signal-to-noise ratio in the corresponding observed wavebands. Si II 1526 and Fe II 1608 are taken as representative low-ion lines since a) they have a moderate line strength, thus preventing saturation, and b) there are no adjacent strong lines in the rest frame that could potentially blend/contaminate the ± 400 km $s^{-1}$ region.

Figure 2.5 shows the high- to low-ion line ratios as a function of velocity. The line ratios are evaluated as the ratio of the integrated column densities for the two lines as a function of velocity. The solid red symbols indicate that at least one of the two absorption lines is detected in that velocity bin. The empty symbols indicate that one of the two lines is saturated, while the green circles show the cases

where both the lines are saturated in that velocity bin (double saturation points). The double saturation ratios are evaluated by taking the ratios of integrated column densities by putting a lower limit on the observed flux (as described in section 2.4.2). A circle denotes detection of both lines, an upwards (downwards) triangle denotes lower (upper) limits. A cross symbol indicates points where both the lines have non-detections (double non-detection points). In such cases, the ratio is taken as the ratio of their typical detection thresholds evaluated using $\tau(v) = 0.05$ (see section 2.4.2). The blue line traces the median of the line ratios including the double non-detection points with the purple shades spanning the 50- and 75-percentile zones. The cyan line traces the median excluding the double non-detection points (i.e. requiring the detection of at least one of the two lines in the given velocity bin).

To avoid large number of double non-detection points, we focus on velocity bins from $-250$ to 150 km s$^{-1}$, where the double non-detection cases are limited to less than 40%. In this region, the high- to low-ion ratio is higher in the blue wing relative to the red wing. This is more clearly noticeable in the Si IV / Fe II and C IV / Fe II ratios. The actual ratios in the blue wing are likely to be higher due to a large number of lower limits in the blue wings (i.e. detection of high ions and non-detection of low ions). This can also be seen by comparing the high- and low-ion lines in Table 2.2. The line ratios in the central region are more uncertain due to high occurrence of double saturation cases, but they appear to be commensurate with the blue wing ratios. Qualitatively, the line ratios highlight the distinct physical characteristics of the three kinematic zones and hint towards a general presence of high-ion rich outflowing gas at a projected speed of $\sim 150 -$

250 km $s^{-1}$.

## 2.5 Toy Model

In order to explain these observations, we simulate the sightlines through the ISM and CGM of the GRB hosts using the known characteristics of the GRB hosts at these redshifts. This modeling will help us disentangle the relative contributions of the host ISM and CGM to the observed column densities as a function of velocity.

Unlike the detailed models that are available for the local multi-phase CGM (eg: [Stern et al., 2016]), the CGM models for high-redshift galaxies are few and limited, especially for galaxies with $M_* < 10^{10} M_\odot$. Therefore, we constructed a simple toy model to extract typical estimates of the physical properties of the CGM and thus help us interpret the observed kinematics. We adopt simple assumptions to derive CGM kinematics in terms of a few model parameters and compare the resulting column densities with the observations. Ultimately, we aim to obtain a coarse estimate of typical kinematic properties of the CGM of GRB hosts at high redshifts. We will focus on the C IV kinematics since this feature is ubiquitously detected in all the sightlines, and the outflow component is prominent in the C IV kinematics.

### 2.5.1 Line-of-sight Simulations: Setup

To simulate how the GRB sightlines sample the kinemaics of the CGM-galaxy system, we constructed a simple geometrical model of the system as shown in Figure

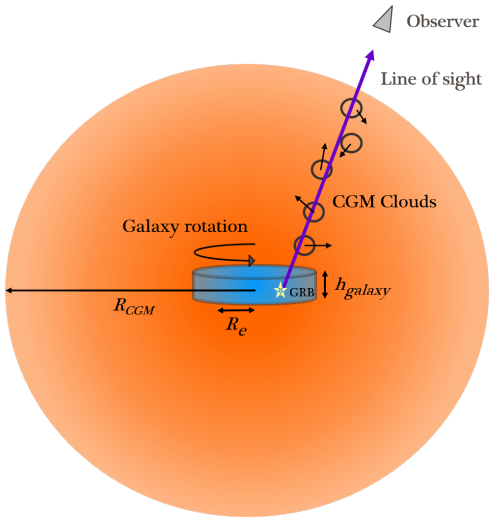


Figure 2.6: A schematic of the toy model used for simulating a sightline that probes the kinematics of the ISM and CGM in a GRB host.

2.6. The galaxy ISM is modeled as a disk with an exponential gas density distribution in the radial direction. The ISM parameters of the galaxy are chosen to reflect a typical, representative galaxy from the known population of GRB hosts in the redshift range $z \sim 2 - 3$ [Wainwright et al., 2007, Perley et al., 2016b, Blanchard et al., 2016, Arabsalmani et al., 2018]. The CGM is modeled as an isothermal sphere populated by clouds where the density of the cloud is inversely proportional to the square of the radial coordinate of the cloud (see Equation A.5). This distribution assumes the clouds have originated from a mass-conserving outflow [Chisholm et al., 2017, Steidel et al., 2010]. In addition to the isothermal velocity distribution, a certain fraction of clouds ($f_{out}$) are randomly selected to have an additional radial outward velocity component to simulate the outflows. The value of the additional radial velocity depends on the radial coordinate of the cloud and follows a ballistic velocity profile with radial launch velocity of $v_{out}$ at an outflow launching radius $R_{launch}$ of 2 kpc. The entire simulation setup is described in detail in Appendix A.2.

To create a complete sample of sightlines for each of these models, 200 GRB sightlines were synthesized by randomly sampling uniform distributions of a) GRB positions within the galactic disk and b) the 3D direction vectors of the sight line. The projected velocity of the intervening gas (from the ISM and CGM) along the GRB sightline was calculated with respect to the projected velocity of the gas in the immediate vicinity of the GRB. Setting this velocity reference is important to maintain consistency with the observations, where $v = 0$ is assigned to the strongest fine structure line absorption, a tracer of gas in the vicinity of the GRB as evident from the UV-pumping argument ([Prochaska et al., 2006] and [Vreeswijk et al., 2007]).

The most important model parameters affecting the observed CGM-ISM kinematics are listed in Table A.1. We approximate the typical stellar mass of GRB hosts at $z > 2$ as $\sim 2 \times 10^9$ $M_\odot$ [Perley et al., 2016b], thereby constraining the halo mass [Hopkins et al., 2014, Wechsler and Tinker, 2018] and thus the typical rotation and dispersion velocities. The volume filling fraction is approximated as 0.1 from prior CGM studies at lower redshifts [Werk et al., 2016, Stocke et al., 2013]. With these assumptions, the free parameters of the model are: the CGM mass (traced by C IV), $M_{CGM}$, the launching velocity of the outflow, $v_{out}$, and the outflow fraction, $f_{out}$. Hence, we synthesize a matrix of 27 models with three distinct values of each of these model parameters, as stated in Table A.1.

The C IV kinematics are evaluated by making certain assumptions about the CGM and ISM metallicities and the ionization fraction for C IV, $f_{CIV}$. The C IV

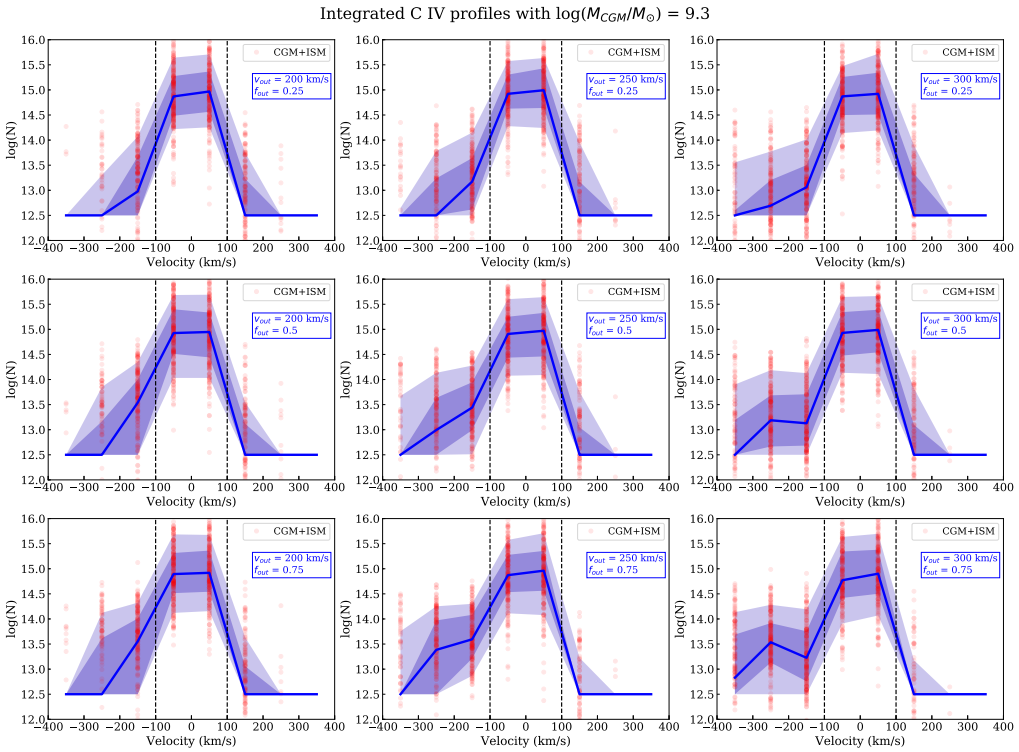


Figure 2.7: Integrated C IV column density from the toy model assuming $M_{CGM}$ = $10^{9.3} M_\odot$. The panels show the results using an outflow launch velocity of 150 km $s^{-1}$, 220 km $s^{-1}$, and 300 km $s^{-1}$ (at 2 kpc) and an outflow fraction of 0.25, 0.5, and 0.75.

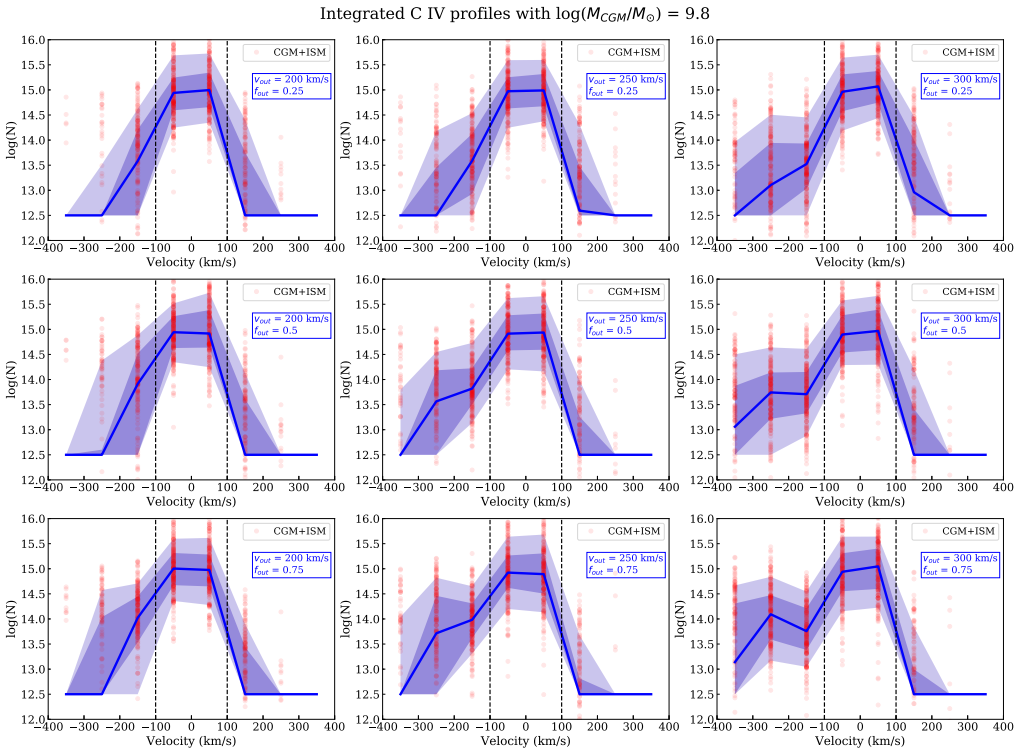


Figure 2.8: Integrated C IV column density from the toy model assuming $M_{CGM} = 10^{9.8} M_\odot$. The panels show the results using an outflow launch velocity of 200 km s$^{-1}$, 250 km s$^{-1}$, and 300 km s$^{-1}$ (at 2 kpc) and an outflow fraction of 0.25, 0.5, and 0.75.

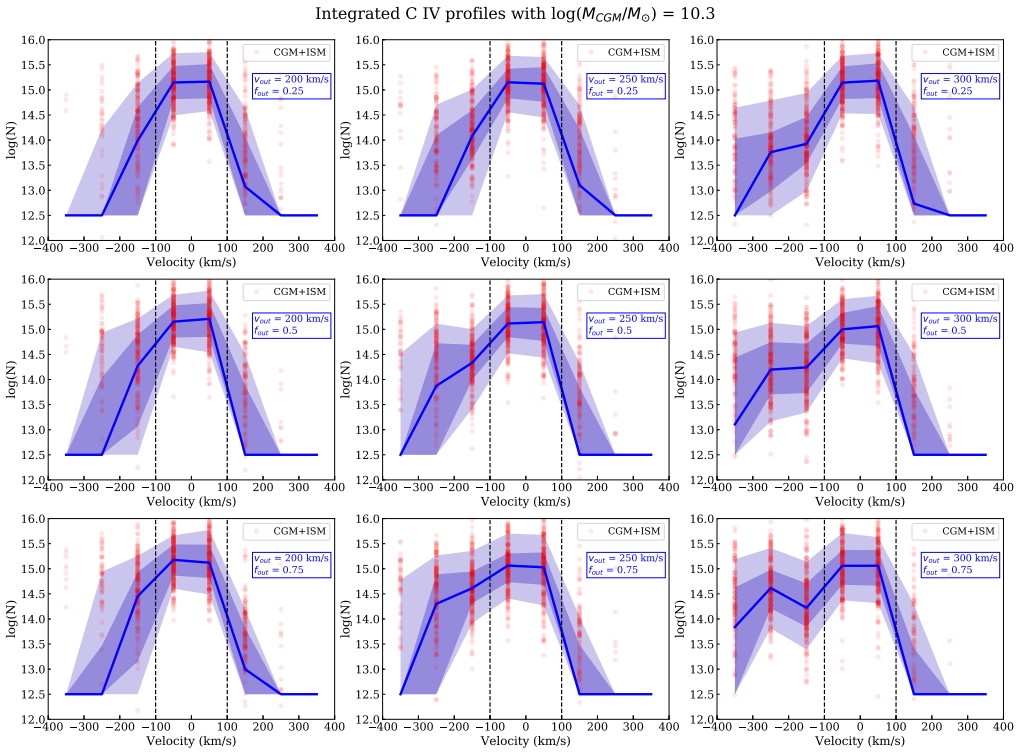


Figure 2.9: Integrated C IV column density from the toy model assuming $M_{CGM}$ = $10^{10.3} M_\odot$. The panels show the results using an outflow launch velocity of 200 km s$^{-1}$, 250 km s$^{-1}$, and 300 km s$^{-1}$ (at 2 kpc) and an outflow fraction of 0.25, 0.5, and 0.75.

column density is evaluated as:

$$N_{CIV} = N_{total} \times \frac{f_{CIV}}{0.3} \times \frac{Z}{Z_{\odot}} \times (n_C/n)_{\odot} \tag{2.1}$$

We conservatively assume $f_{CIV} = 0.3$ as a maximal ionization fraction similar to [Bordoloi et al., 2014b] and as derived in [Oppenheimer and Schaye, 2013] for $z > 2$. The CGM and ISM metallicities are assumed to be 0.25 and 0.15 solar, respectively [Trenti et al., 2015, Arabsalmani et al., 2018, Shen et al., 2013]. The solar ratio of carbon number density to total number density is $3.26 \times 10^{-4}$.

### 2.5.2 Line-of-sight Simulations: Results

The kinematic separation of the CGM and ISM has been used in various previous studies (eg: to study the CGM of Andromeda galaxy) to distinguish the CGM and ISM contributions in the velocity profiles [Fox et al., 2014, Fox et al., 2015, Lehner et al., 2015]. In this paper, we performed kinematic simulations to infer the relative contributions of the CGM and ISM as a function of velocity using the characteristic parameters of GRB host galaxies of our sample.

Figure 15 in Appendix A.2 shows the breakdown of the total column density into ISM and CGM components, with (left) and without an outflow (right). Two key inferences can be drawn from this illustration: a) an outflow component is necessary to explain the observed kinematic asymmetry, and b) the ISM component kinematically dominates the central region ($|v| < 100$ km s$^{-1}$), while the CGM component is the main contributor of column density in the red and blue wings

($v > 100$ km s$^{-1}$ and $v < -100$ km s$^{-1}$, respectively). With this insight, we use the kinematic separation to further estimate the physical properties of the CGM.

Figures 2.7−2.9 show the integrated CGM + ISM column density for C IV as a function of velocity bins of width 100 km s$^{-1}$ in a fashion similar to the observations. The results are shown for 27 synthesized models with different combinations of CGM mass (as traced by C IV), outflow launch velocity ($v_{out}$), and outflow fraction ($f_{out}$). The red dots indicate the integrated column density for each simulated GRB sightline. The blue line shows the median profile and the purple shades indicate the central 50 and 80 percentiles. The vertical dotted lines separate the central region dominated by the ISM from the blue and red wings dominated by the CGM.

We compare the blue and red wings with the observations since the central region is often saturated in the observations. As clearly seen in these figures, a higher outflow fraction increases the kinematic asymmetry while a higher outflow velocity shifts the asymmetry blueward, as expected. A higher CGM mass proportionally increases the median column densities in the red and blue wings, while the increment in the central region is slower since it is dominated by the ISM.

Despite its simplicity, this kinematic model does an excellent job at reproducing the median kinematics profile as well as typical detection fractions and column density distribution as a function of velocity. These simulations rule out an outflow fraction of $\gtrsim 0.5$ and a CGM mass of $\gtrsim 10^{10.3} M_{\odot}$ by simple comparisons of the median profiles and the percentile distributions. However, it should be noted that a lower metallicity for the CGM would favor a higher CGM mass to explain the observations while a higher ionization fraction would favor a lower CGM mass.

Nonetheless, the current assumptions are reasonable within a factor of 2. The model that best explains the observed kinematics is: $M_{CGM} = 10^{9.8} M_{\odot}$, $v_{out} = 300$ km s$^{-1}$, $f_{out} = 0.25$. Note that $v_{out}$ is the launch velocity at 2 kpc for a ballistic outflow. In section 2.6, we use these kinematic simulations to estimate the contribution of CGM in the central $\pm$ 100 km s$^{-1}$ velocity region, which is crucial in estimating the typical CGM mass in our sample.

No extra inflow component has been added in these kinematic simulations. Various feedback simulations suggest that at $z \sim 2.5$, cold inflows are hardly detectable in metal lines due their low metallicity and low covering factors [Fumagalli et al., 2011, Goerdt et al., 2012]. Given the observational challenges in detecting the inflows, we do not include an inflow component in our toy model. However, a plausible inflow scenario is explored in section 2.7.3.

## 2.6 CGM Mass Estimate

Estimating the mass of the CGM at high redshifts is a key step in determining the cosmic baryonic budget as well as the distribution of metals throughout the universe and the various mechanisms at play [Bouché et al., 2006, Bouché et al., 2007, Peeples et al., 2014, Muratov et al., 2017]. In this section, we will estimate the typical mass of the CGM for high-z GRB hosts, explore its evolution with redshift, and compare the carbon mass in the CGM and ISM. The length scales considered here are proper distances.

### 2.6.1 Converting Column Densities into Mass

Our kinematic toy models provide a reasonable handle on the CGM mass ($M_{CGM} \sim 10^{9.8} M_{\odot}$). In this section we provide further insights on the CGM mass from the observed column densities, adopting realistic geometrical assumptions, and compare the results with the toy models. For this, we assume the CGM-GRB sample as a set of random GRB sightlines probing the typical ISM and CGM of a GRB host at $z \sim 2 - 5$.

#### 2.6.1.1 Method

A key uncertainty in this formulation is the contribution of the CGM to the column density in the central region ($|v| < 100$ km s$^{-1}$). To resolve the CGM-ISM degeneracy in this region, we make certain assumptions based on the insights we gained from the toy models. Since the central region also suffers from saturation issue leading to the measurement of only the lower limit of the column density, we avoid making a direct use of the CGM to ISM ratio in this region. Instead, we use the column density in the $-150$ km s$^{-1}$ bin (i.e. $-200 < v < -100$ km s$^{-1}$) to extrapolate the central column density since the column density in the $-150$ km s$^{-1}$ velocity bin is measured more accurately. This ratio is in the range of 2 to 4 for the models that were found viable in the previous section. Hence, we use a factor of 3 to estimate the CGM-contributed column density in the observed spectra. To calculate the CGM mass, we will make use of C IV column density since it is ubiquitous and a good tracer of the outflow component.

To convert the integrated CGM column density of C IV, as approximated above, into the mass of C IV in the CGM, we assume that the CGM density profile is a power law given by:

$$n_{CGM}(r) = n_0 \left(\frac{r}{R_0}\right)^{-\alpha} \tag{2.2}$$

For convenience, we select the reference radius $R_0$ as the starting point of the CGM, equivalent to twice the half-light radius ($R_e$) of the galaxy. We assume a typical $R_e$ of 2 kpc for GRB hosts at $z > 2$, following previous observations of GRB hosts [Wainwright et al., 2007, Blanchard et al., 2016], and thus $R_0 = 4$ kpc. Both the detailed simulations and our toy model indicate that the gas which leads to the observed absorption in C IV is spread out to about 2 $\times R_{vir}$. Beyond that, the gas density is too low to give rise to a detectable absorption component (assuming $n(r) \propto r^{-2}$). Given a constant volume filling fraction of $f_{vol}$, the mass of the CGM (for $\alpha \neq 3$) can be stated as:

$$M_{CGM} = 4\pi m_H f_{vol} \int_{R_0}^{R_{CGM}} n(r) \times r^2 dr \tag{2.3}$$

$$= 4\pi m_H f_{vol} n_0 R_0^{\alpha} \left(\frac{1}{3-\alpha}\right) \left[R_{CGM}^{3-\alpha} - R_0^{3-\alpha}\right] \tag{2.4}$$

We further define the line covering fraction $f_{line}$ as the typical fraction of a sightline that passes through a CGM cloud. The typical line fraction does not strongly vary with radius if the volume filling fraction is constant. Given a constant

$f_{line}$, the typical column density (for $\alpha \neq 1$) can be expressed as:

$$N_{obs} = f_{line} \int_{R_0}^{R_{CGM}} n(r) dr \tag{2.5}$$

$$= f_{line} n_0 R_0^{\alpha} \left( \frac{1}{1-\alpha} \right) \left[ R_0^{1-\alpha} - R_{CGM}^{1-\alpha} \right] \tag{2.6}$$

Combining the two equations, we get:

$$M_{CGM} = 4\pi m_H N_{obs} \left( \frac{f_{vol}}{f_{line}} \right) \left( \frac{1-\alpha}{3-\alpha} \right) \left[ \frac{R_{CGM}^{3-\alpha} - R_0^{3-\alpha}}{R_0^{1-\alpha} - R_{CGM}^{1-\alpha}} \right]$$

In the following, we take $\alpha = 2$, i.e. we consider the case where a significant fraction of the metal-rich CGM takes part in a mass-conserving outflow [Chisholm et al., 2017, Pallottini et al., 2014, Steidel et al., 2010]. Since $R_0 \ll R_{CGM}$, the expressions can be simplified. Further, we evaluate the typical value of $f_{vol}/f_{line}$ by simulating various volume filling fractions in a spherical shell and measuring the distribution of line covering fraction for random sightlines. For small filling fractions ($\sim 0.05 - 0.25$, eg: as derived in [Werk et al., 2014]), the typical value of $f_{vol}/f_{line}$ ratio is found to be 1.2. Using this value, we estimate the mass of C IV in the CGM (in solar mass units) as:

$$M_{CGM,CIV} = 1.2 \times m_C N_{CIV} R_0 R_{CGM} \times 10^{-13} \tag{2.7}$$

where $m_C$ is the atomic mass number of carbon, $R_0$ and $R_{CGM}$ are in kpc, and $\mathrm{M}_{CGM}$ is in solar masses.

#### 2.6.1.2 Results

As stated earlier, we estimate $R_0$ as 4 kpc and $R_{CGM}$ as $2{\times}R_{vir} \sim 100$ kpc. We choose the geometric mean of all the sightlines in the sample as a representative value of $N_{CIV}$ since it best captures the large range in column density as a function of velocity whereas an arithmetic mean tends to be skewed to high values by the small number of large column densities. Similar mass estimates were performed for other species. The CGM mass estimates for various species as a function of velocity are shown in Fig. 2.4. For evaluating carbon mass in the CGM, the fraction of carbon in C IV phase ($f_{CIV}$) needs to be constrained which depends on the temperature, density, and ionization process. We assume a conservative maximal $f_{CIV}$ of 0.3 (see Fig. 7 in [Bordoloi et al., 2014b]), which gives:

$$\begin{aligned} \mathrm{M_{CGM,C}} \gtrsim\ & 4.8 \times 10^4 \mathrm{M_\odot} \left(\frac{N_{CIV}}{10^{14}\mathrm{cm^{-2}}}\right) \\ & \left(\frac{R_0 R_{CGM}}{100\,\mathrm{kpc^2}}\right) \left(\frac{0.3}{f_{CIV}}\right) \end{aligned} \tag{2.8}$$

Based on this formulation, the conservative lower limit on the carbon mass in the CGM of GRB hosts in our sample is $\sim 1.5 \times 10^6 M_\odot$. The carbon mass in the CGM can be further extrapolated to derive the total mass of the CGM in the phase traced by C IV ($\mathrm{T} \sim 4.5 - 5.5 \times 10^5$ K). For this, we assume that the metallicity in the CGM is roughly 0.25 solar. This assumption is informed by the detailed simulations of CGM at $z > 2$ [Shen et al., 2013] and the low-z CGM metallicity estimates (eg: [Prochaska et al., 2017]). This is further supported by the

observed gas-phase metallicity of $\sim 0.1 - 0.2$ solar for the ISM of the GRB hosts [Krühler et al., 2015, Arabsalmani et al., 2018]. Due to the metal-enriched outflows, the typical CGM metallicity tends to be $\sim 1.5$ times the ISM metallicity [Muratov et al., 2017]. Thus, the total mass of the CGM gas traced by C IV can be expressed as:

$$M_{CGM,total} \sim 10^9 M_\odot \times \left(\frac{M_{CGM,C}}{10^6 M_\odot}\right)\left(\frac{0.25}{Z_{CGM}}\right) \tag{2.9}$$

Thus, the typical mass of the CGM gas traced by C IV in this sample is $\sim 10^{9.2}$ $M_\odot$, which is comparable to the typical stellar mass of the GRB hosts at these redshifts ($z \sim 2-4$). This implies that the CGM is a very significant reservoir of baryons and metals in the galactic ecosystem at high redshifts. Thus, from a galaxy evolution standpoint, the CGM appears to be already in place at $z \sim 2-4$. Despite various uncertainties in the assumed parameters, we can say with high significance that the mass of the CGM in GRB hosts is at least as much as the mass that resides in the stars, and it can be higher by as much as $\sim$0.3 dex if the conservative assumptions are relaxed.

The CGM mass estimates from the toy models (§ 2.5.2) and column density profiles are complementary in nature, strengthening our CGM mass estimate of $\sim 10^{9.2-9.8} M_\odot$. It should be noted that the difference between the CGM mass of the optimal toy model ($10^{9.8} M_\odot$) and the CGM mass estimated here ($\sim 10^{9.2} M_\odot$) arises for two key reasons: a) the conservative estimate of the CGM contribution to the central $\pm$ 100 km s$^{-1}$ and b) the use of geometrical mean of column densities in the CGM mass measurement instead of arithmetic mean.

#### 2.6.1.3 Caveats

In this analysis, various simplifying assumptions have been made based on previous observations or simulation efforts. Here, we briefly discuss the sensitivity of the results to the assumed parameters. We assumed a CGM density profile of the CGM that follows $n(R) \propto R^{-2}$. A more compact profile, for instance $R^{-2.3}$, can reduce the CGM mass by 0.4 dex, whereas a more diffuse profile, eg. $R^{-1.7}$, increases the CGM mass estimate by 0.4 dex. The product $R_0 R_{CGM}$, which can be written as $4R_e R_{vir}$, marks the bounds we have defined for the CGM. We ascribe an uncertainty of $-0.3$ dex (reducing the $M_{CGM}$ estimate) to this product due to the gap in our knowledge associated with the faint nature and inherent variety of GRB hosts.

On the other hand, $f_{CIV} = 0.3$ is a conservative upper limit on the ionization fraction for the warm phase [Bordoloi et al., 2014b]. This factor can be lower by a factor of $\sim 2-4$ in the range of temperatures and densities traced by C IV absorption in the CGM. Despite the evolution in the extragalactic background UV (ionizing) flux between $z \sim 0$ (COS-Dwarfs, [Bordoloi et al., 2014b]) and $z \sim 2.7$ (this sample and [Gilmore et al., 2009]), the ionization fraction $f_{CIV}$ does not exceed 0.3 for both collisional and photoionization models for a range of temperature ($10^{4.5} - 10^{5.5}$), number density ($10^{-2} - 10^{-5}$ cm$^{-3}$), and metallicity ($0.1 - 1$ solar, [Oppenheimer and Schaye, 2013]). The typical value expected in the warm phase traced by C IV is $\sim 0.1 - 0.2$. Thus, we attribute an uncertainty of $+0.3$ dex to $f_{CIV}$ (raising the $M_{CGM}$ estimate).

We have also assumed a constant typical metallicity for the CGM. While constraining the radial gradient of metallicity is an observational challenge, it is unlikely that the average metallicity of the CGM is significantly larger than 0.25 solar at these redshifts (based on the observed metallicities of the DLAs asssociated with the GRB hosts at $z > 2$ [Cucchiara et al., 2015, Toy et al., 2016]). As a limiting case, if the typical metallicity of the CGM gas traced by C IV is assumed to be the same as the typical ISM metallicity of these GRB hosts ($\sim 0.1$ solar), then we can expect an increment of $\sim 0.4$ dex in the CGM mass (from equation 2.9).

Despite the simplifying assumptions and uncertainties stated here, it can be seen that the overall uncertainty in the CGM mass is small and would likely favor a higher warm CGM mass than calculated here. Thus, the robust mass estimates from our sample and the kinematic inferences drawn with the help of our toy model clearly indicate that the CGM is already a significant component of the GRB host galaxies at high redshifts, comparable to the mass of the host ISM. This has important implications on the evolution of the CGM and the distribution of metals and baryons throughout the galactic ecosystem as a function of time.

### 2.6.2 CGM Mass Evolution with Redshift

To study the evolution of the CGM mass with redshift, we divide the CGM-GRB sample into two roughly equal time bins of 1 Gyr − group 1 ($z1 \sim 2 - 2.7$, midpoint: $z = 2.3$) and group 2 ($z2 \sim 2.7 - 5$, midpoint: $z = 3.6$). The number of GRBs in these two bins are also nearly equal. The integrated column density as

a function of velocity for high- and low-ion species are plotted in Figures 2.10 and 2.11 in the same way as Figure 2.4.

It can be seen in these figures that the high-ion kinematics in both redshift groups are quite similar with respect to the blue asymmetry. In the case of Si II, the blue asymmetry is weaker in the lower redshift bin (Fig. 2.10). There are two possible reasons for this lack of asymmetry in Si II: a) The ionization level of the outflows is different in at low z leading to a higher [Si IV / Si II] ratio relative to the high-z bin, or b) there is more inflowing gas in the low-z bin compared to the high-z bin which produces a relatively stronger Si II red wing. From the high-z simulations in [Shen et al., 2013], it is clear that Si II is a much stronger tracer of the inflows compared to outflows by almost an order of magnitude. However, a more rigorous treatment using ionization modeling is required to distinguish between the two scenarios and constrain the physical state of the outflows and inflows.

We follow the same procedure as the one described in section 2.6.1 for estimating the mass of the CGM in these two redshift bins. The key changes in the assumed parameters are: a) the typical value of $R_{vir}$ and b) the typical value of $R_e$ in these two redshift bins. The other parameters are not expected to change significantly. The virial radius is calculated as the radius within which the normalized density, $\rho/\rho_{cosmic} > 200$, using the NFW profile for dark matter distribution and standard cosmological parameters ($\Omega_m = 0.3$, $\Omega_{rad} = 0$, $\Omega_\Lambda = 0.7$). Thus, the typical virial radii for the $z1$ and $z2$ redshift bins are 53 and 39 kpc, respectively. Therefore, $R_{CGM}$ for the two bins are 106 and 78 kpc. The typical half-light radius for the two bins are assumed to be 2 and 1.5 kpc, respectively, following the previous population

study of the GRB hosts at these redshifts [Wainwright et al., 2007, Blanchard et al., 2016]. Hence, the typical $R_0$ for the two bins are taken as 4 and 3 kpc, respectively. With this setup, the masses of various species were calculated in the two redshift bins and are shown in Figures 2.10 and 2.11. The C IV in the CGM was estimated to be $\log(M_{CIV,z1}/M_\odot) = 5.6^{+0.1}_{-0.2}$ and $\log(M_{CIV,z2}/M_\odot) = 5.1^{+0.2}_{-0.1}$. The total CGM masses in the two redshift bins (following the same procedure as described in section 2.6.1) are estimated as $M_{CGM,z1} = 10^{9.2} M_\odot$ and $M_{CGM,z2} = 10^{8.7} M_\odot$.

The C IV mass in the CGM, as shown in Figures 2.10 and 2.11, is higher in the lower redshift bin by almost 0.5 dex. However, it is quite likely due to the combined effect of redshift evolution and the difference in typical stellar mass and star formation rate between the two redshifts. This will be explored in more depth by associating the CGM properties with the host properties in an upcoming paper on this sample.

To convert the C IV mass to carbon mass, we make a conservative assumption for $f_{CIV}$. Despite the extragalactic ionizing UV background flux evolution (within a factor of 2) between the two redshift bins, $f_{CIV}$ does not exceed 0.3 for both photo- and collisional ionization models [Oppenheimer and Schaye, 2013]. Hence, we consider the maximal $f_{CIV}$ as 0.3 for both the redshift bins (same as in section 2.6.1). The $M_{CGM,C}$ is thus estimated using Eqn. 2.8 for both redshift bins and plotted in Fig. 2.12 to compare with the $M_{CGM,C}$ estimates from COS-dwarfs study (at $z \sim 0$). The typical GRB host stellar masses in the redshift bins shown in the figure are median values from the SHOALS (Swift GRB Host Galaxy Legacy Survey) sample which is the largest systematic survey of long GRB hosts [Perley

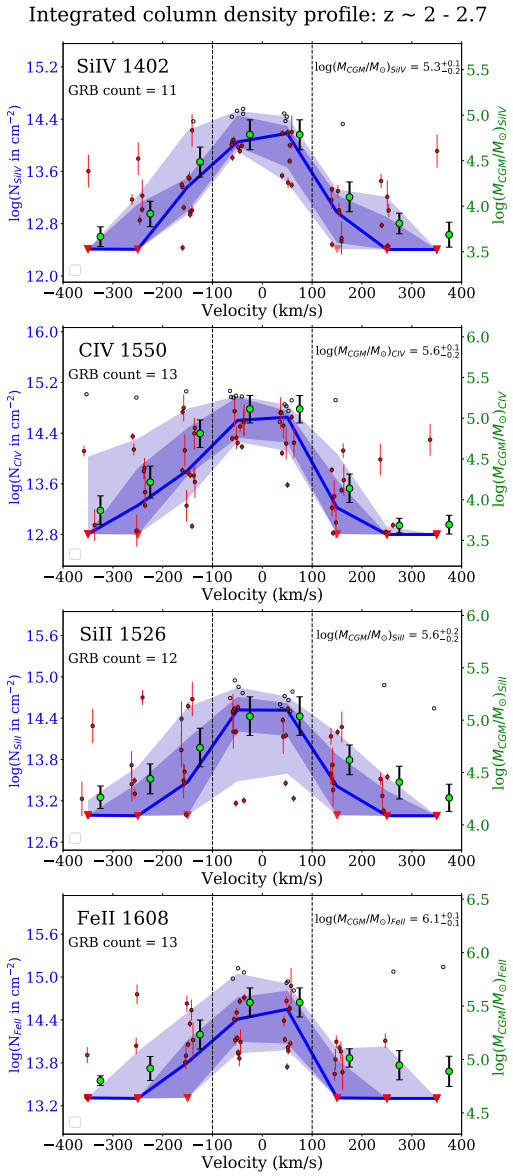


Figure 2.10: CGM column densities and mass estimates for high- and low-ion species in the redshift group #1 (z $\sim$ 2 $-$ 2.7).

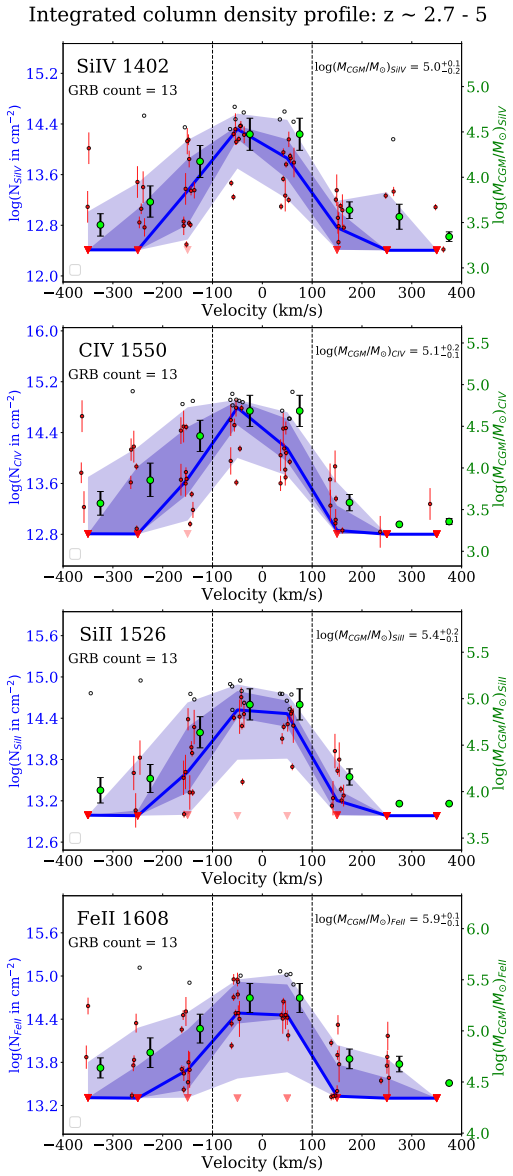


Figure 2.11: CGM column densities and mass estimates for high- and low-ion species in the redshift group #2 (z $\sim$ 2.7 $-$ 5.0).

et al., 2016b]. The stellar mass uncertainties are the bootstrapping $1\sigma$ intervals from the SHOALS survey. As described in 2.6.1, our estimates for $M_{CGM,C}$ are evaluated within 2 virial radii. Hence, for a better picture of redshift evolution, the COS-dwarfs estimates within $\sim 1$ virial radius are shown in green and the estimates within $\sim 2$ virial radii in light green.

From Fig. 2.12, it can be seen that the CGM carbon mass (or by extension, metal mass) increased by only a factor of $\sim 2$ (comparing with the $2R_{vir}$ estimates) from $z > 2$ to $z \sim 0$ for dwarf galaxies. Despite the fact that $f_{CIV}$ is assumed to be a conservative upper limit for all of these calculations, it can be clearly observed that most of the metal mass in the CGM of the low-mass galaxies represented by GRB hosts is already in place by $z \sim 2.5$. While the COS-dwarf galaxies are not the descendents of galaxies represented by GRB hosts at $z > 2$, this comparison has significant implications on the distribution of metals throughout the galaxy ecosystem as a function of redshift, as discussed in section 2.7.2.

### 2.6.3 Comparison with Carbon Mass in the ISM

By comparing the carbon mass in the ISM with that in the CGM, we can infer the level of CGM enrichment for GRB hosts at high redshifts. We estimate the gas phase carbon mass in the ISM of the GRB hosts by assuming a modest gas-phase metallicity of 0.15 solar [Arabsalmani et al., 2018, Davé et al., 2017] with solar-like relative abundance pattern. Here, we assume a metallicity slightly lower than the median value reported in [Arabsalmani et al., 2018] since the UV/optical

absorption- and emission-based metallicity estimates do not account for potentially lower metallicity gas in the ISM. The total ISM gas mass is estimated as $2 \times M_*$ based on various molecular and neutral hydrogen measurements and simulations of high redshift main-sequence galaxies, where $f_{gas} = M_{gas}/M_*$ is reported to be $\sim$ 2 for $10^9 < M_*/M_\odot < 10^{10}$ ([Daddi et al., 2010, Carilli and Walter, 2013, Lagos et al., 2014, Davé et al., 2017, Tacconi et al., 2018]). We estimate an uncertainty of roughly $\pm$0.3 dex in the product of metallicity and the gas fraction ($f_{gas}$) to account for the uncertainty associated with the mass-metallicity relation for GRB hosts at $z > 2$ and the variation of $f_{gas}$ with redshift. Note that here we are considering total gas mass of the ISM to estimate the carbon mass in the ISM (and not just the warm phase of the ISM). With these reasonable assumptions, we plot the ISM mass of carbon in Figure 2.12.

The carbon mass in the ISM is higher than the minimum carbon mass in the CGM by a factor of $\sim 3-5$. It should be noted again that the carbon mass in the CGM is a lower limit and considers only the warm phase traced C IV. In principle, the actual value of total carbon in the CGM can be higher by a factor of as much as $\sim 2-3$ (see section 2.6.1). This observation indicates that the carbon (metal) content of the CGM is $\sim 20-50\%$ of the carbon (metal) content of the ISM, indicating that a significant fraction of metals synthesized in the galaxy are able to escape into the CGM due to the galactic outflows. In [Bordoloi et al., 2014b], this fraction is $50-80\%$ for $z \sim 0$ galaxies of similar stellar mass. This finding hints towards a modest evolution in the carbon (metal) content, or in other words, a modest enrichment of the CGM over $\sim$ 11 Gyr span.

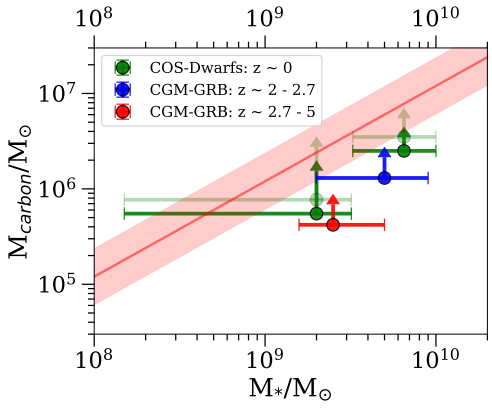


Figure 2.12: Estimates of the minimum carbon mass in the CGM of the GRB hosts in this sample. The typical minimum carbon mass in the CGM in the two redshift regions described in Figures 2.10 and 2.11 are compared with the z $\sim$ 0 dwarf-galaxy CGM from the COS-Dwarfs survey [Bordoloi et al., 2014b]. The COS-dwarfs estimates within one virial radius are shown in dark green, while the estimates within two virial radii are shown in light green for easier comparison with the high-z values also derived within two virial radii.

## 2.7 Implications

Using a sample of high SNR and medium resolution spectra of GRB afterglows at $z \sim 2-6$, we estimated various properties of the CGM for a typical GRB host at these redshifts. The observed blue asymmetry indicates a clear signature of an outflowing component predominantly traced by the high-ions (C IV, Si IV). Using the toy models and observed column density profiles, the typical mass of the host galaxy's CGM is estimated to be $\sim 10^{9.2-9.8} M_\odot$ (§ 5.2 and § 6.1). In this section, we discuss the implications of our analysis on various important aspects of the CGM.

### 2.7.1 Outflows and Metal Enrichment

In §2.6.2, the CGM-GRB sample is divided into two redshift bins each spanning 1 Gyr (bin 1: $z \sim 2-2.7$, bin 2: $z \sim 2.7-5$). Outflows are clearly detected in both

redshift bins as shown in figures 2.10 and 2.11. As described in §2.4.4, the outflows are inferred from the blue asymmetry that is observed in both the high- and low-ion lines, but they are primarily traced by the high-ions (C IV and Si IV). Using the kinematic information from the observations and further clarity from the toy models, we can estimate various aspects of the outflows. From the toy models, the optimal model for explaining the observed kinematics has a typical outflow launch speed of $\sim$ 300 km s$^{-1}$ (at 2 kpc), and $\sim$ 25% of the CGM clouds in the model contribute to outflows in excess of the virial motion in the CGM of a typical dark matter halo mass $M_h \sim 10^{11.2} M_\odot$. With this insight, we estimate the key properties of the outflowing material in this section. We assume an NFW profile for the dark matter distribution with a concentration parameter of 4.5 (derived by forcing $R_{200} = R_{vir}$ and defining the mass enclosed within a virial radius as the halo mass).

#### 2.7.1.1 Outflow Mass

The optimal toy model has $f_{out} = 0.25$, i.e. the outflow mass is 25% the CGM mass within $R_{CGM}$. Thus, the estimates for the outflow masses in the two redshift bins are $M_{out,z1} \sim 10^{8.6} M_\odot$ and $M_{out,z2} \sim 10^{8.1} M_\odot$, where (z1: $z \sim 2 - 2.7$ and z2: $z \sim 2.7 - 5$). Assuming a halo mass of $10^{11.2} M_\odot$, a radial launch velocity of 250 km s$^{-1}$ (at 2 kpc) is just high enough for the outflowing gas to escape the CGM (i.e. 2 $\times$ $R_{vir}$).

The fraction of outflowing gas with a radial velocity $v_{radial} > 250$ km s$^{-1}$ at launch can be estimated using the velocity distribution of outflowing clouds in the

toy model (see Appendix A.2). The velocity distribution is reasonably assumed to be an isotropic Gaussian with a standard deviation ($\sigma_{v,CGM}$) of 100 km s$^{-1}$ given by the virial velocity of the halo. The radially outward component of the isotropic standard deviation is $100/\sqrt{3}$ (= 57.7) km s$^{-1}$. For the outflows, an extra radiallly outward component of $v_{out}$ is added to this distribution at launch, thus centering the Gaussian at $v_{out}$ (= 300 km s$^{-1}$ at launch for the optimal toy model). From this distribution, the fraction of clouds with a launch velocity $v_{radial} > 250$ km s$^{-1}$ is 80% of the total outflowing gas (for the optimal toy model). Thus, the mass of outflowing gas in the CGM with sufficient initial kinetic energy to escape into the IGM is $M_{esc,z1} \sim 10^{8.5} M_{\odot}$ and $M_{out,z2} \sim 10^{8} M_{\odot}$. It should be noted that the time to traverse $2 \times R_{vir}$ in this dark matter halo is $\sim 0.5$ Gyr.

#### 2.7.1.2 Mass Outflow Rate

We can now evaluate the mass outflow rate in these two redhsift bins. The outflow rate out of a spherical shell is given as:

$$\dot{M}_{out} = \bar{m} n(R_{shell}) \times 4\pi R_{shell}^2 \times v_{out}(R_{shell}) \times f_{vol} \times f_{out} \tag{2.10}$$

where the average mass per atom or ion is $\bar{m} = 1.15\ m_H$. We consider $R_{shell}$ = 4 kpc (3 kpc) for the redshift bin $z1$ ($z2$) to estimate the outflows coming out of the galaxy disk. Note that we assume 4 kpc (3 kpc) as the boundary of the galaxy disk, $R_0$, in section 2.6.2. Considering $M_{CGM} = 10^{9.2} M_{\odot}$ ($10^{8.7} M_{\odot}$), we get $n(R_{shell})$ = 0.028 (0.02) cm$^{-3}$ (following equation 3.1). The outflow launch velocity in the

2-4 kpc range is approximated as $\sim$ 300 km s$^{-1}$ from the optimal toy model and the observed kinematics for both redshift bins. Following the optimal toy model, we assume a volume filling fraction $f_{vol} = 0.1$ and an outflow fraction $f_{out} = 0.25$. Within this framework, we estimate the mass outflow rates (in the gas phase traced by C IV) as:

$$\dot{M}_{out} = 0.27 M_{\odot} \mathrm{yr}^{-1} \left(\frac{n(R)}{10^{-2}\ \mathrm{cm}^{-3}}\right) \left(\frac{R^2}{10\ \mathrm{kpc}^2}\right) \left(\frac{v_{out}(R)}{300\ \mathrm{kms}^{-1}}\right), \tag{2.11}$$

where $R$ is the radius of the shell, $R_{shell}$. Inserting the appropriate values for the two redshift bins, we get $\dot{M}_{out,z1} = 1.2\ M_{\odot}$ yr$^{-1}$ and $\dot{M}_{out,z2} = 0.5\ M_{\odot}$ yr$^{-1}$. This warm-phase mass outflow rate is comparable to the latest TNG simulation for galaxies with $M_* \sim 10^{9-10} M_{\odot}$ at $z = 2$ (area under the curve for warm phase in Fig. 10 of [Nelson et al., 2019]) . Note that the gas outflow rate in [Nelson et al., 2019] is measured at 20 kpc, however. In our density profile assumption, $n(R) \times R^2$ is independent of $R$ and the cloud velocities at 20 kpc reduce to $\sim$70% of their launch velocities for $v_{launch} = 200 - 300$ km s$^{-1}$. Hence, for comparison, $\dot{M}_{out,20kpc} \sim 0.7 \dot{M}_{out,launch}$ in our framework.

As a corollary of the escaping mass ($M_{esc}$) calculation, we can now estimate the mass escape rate by modifying equation 2.10. For this, we consider the boundary of the CGM as $R_{CGM} = 2R_{vir}$. At this radius, a ballistic outflow launched at 2 kpc with a velocity of 250 km s$^{-1}$ decelerates to 50 km s$^{-1}$ (from the NFW dark matter profile). Due to our assumption of mass conserving outflow (i.e. $n(R) \propto R^{-2}$), the

product $n(R) \times R^2$ is invariant. The modified equation for the mass escape rate becomes:

$$\dot{M}_{esc} = \bar{m} n(R_{esc}) \times 4\pi R_{esc}^2 \times v_{out}(R_{esc}) \times f_{vol} f_{out} f_{esc} \tag{2.12}$$

Using 50 km s$^{-1}$ for $v_{out}(R_{esc})$ and 80% for $f_{esc}$ (the fraction of outflowing gas with a launch velocity $> 250$ km s$^{-1}$ from Sec. 7.1.1), we get $\dot{M}_{esc} \sim 0.14 \times \dot{M}_{out}$. Thus, the estimates for the mass escape rate into the IGM for the two redshift bins are: $\dot{M}_{esc,z1} = 0.17\ M_\odot$ yr$^{-1}$ and $\dot{M}_{esc,z2} = 0.07\ M_\odot$ yr$^{-1}$. These estimates are robust within a factor of 2 over $\pm 30$ km s$^{-1}$ variations in the launch velocity ($v_{out}$) in the optimal toy model.

The calculations described in this section suggest that $\sim 80\%$ ($f_{esc}$) of the mass ejected from a GRB host galaxy of median halo mass ($M_h \sim 10^{11.2} M_\odot$) escapes to enrich the IGM while only 20% ($f_{retain}$) stays within the CGM of a typical GRB host in this sample at $z > 2$. Combining this result with the 0.5 Gyr timescale to traverse $2 \times R_{vir}$, one can say that $\sim 20\%$ ($f_{out} \times 80\%$) of the total CGM mass of a typical GRB host at $z \sim 2-5$ escapes out to the IGM over 0.5 Gyr. Conversely, the CGM mass in warm phase grows by $\sim 5\%$ ($f_{out} \times 20\%$) every 0.5 Gyr if we assume that the non-escaping gas becomes a part of the virialized CGM. Such a growth rate, if steady, is sufficient to significantly grow the warm-phase CGM over a 5 Gyr period.

#### 2.7.1.3 Mass Loading Factor and Energetics

The mass loading factor is defined as $\eta = \dot{M}_{out}/SFR$ and serves as an important indicator of the mechanism driving the outflow. We consider a median SFR of 10 $M_{\odot}$ yr$^{-1}$ for GRB hosts from [Krühler et al., 2015] at $z > 2$ (typical range $5-50 M_{\odot}$ yr$^{-1}$). The mass loading factors at the launch radii can then be estimated as: $\eta_{z1} = 1.2/10 = 0.12$ and $\eta_{z2} = 0.5/10 = 0.05$. Several simulations calculate the mass loading factors at some intermediate radius such as 20 kpc. The mass loading factors at 20 kpc can be evaluated by using decelerated velocities as (see section 2.7.1.2): $\eta_{z1,20kpc} = 0.7 \times 0.12 = 0.084$ and $\eta_{z2,20kpc} = 0.7 \times 0.05 = 0.035$.

While the outflow velocities in comparable mass ranges to our sample are always in the range of $200 - 400$ km s$^{-1}$, there is at least an order of magnitude variation in the mass-loading factors reported in various observational studies at high redshifts due to the diversity in probes, underlying assumptions, and the phases traced in the outflow. Therefore only an order-of-magnitude comparison can be done.

[Crighton et al., 2014] use a QSO sightline probe at $z = 2.5$ for a $M_* \sim 10^{9.1} M_{\odot}$ galaxy and infer a mass-loading factor of order 1. [Weiner et al., 2009] also infer an $\eta$ of order unity at launch for cold phase outflow (tracer: Mg II) in star-forming galaxies at $z \sim 1.4$ using rest-frame UV spectra of the galaxies. Along similar lines, [Martin et al., 2012] report an $\eta$ of order 1 for Fe II-traced outflows in a redshift range $z \sim 0.4 - 1.4$ for star-forming galaxies over a wide range of stellar mass ($10^{9.5-11.5} M_{\odot}$). With a similar method, [Rubin et al., 2014] conservatively estimate

a cold gas mass loading factor $\eta_{5\ kpc} \gtrsim 0.02 - 0.6$ for galaxies with $M_* \gtrsim 10^{9.6} M_\odot$ and SFR $\gtrsim 2 M_\odot$ yr$^{-1}$ in the redshift range $z \sim 0.3 - 1.4$. [Davies et al., 2018] use IFU spectra of star-forming galaxies with $z \sim 2 - 2.6$ and $M_* \sim 10^{9.5-11.5} M_\odot$ to estimate the mass loading factor $\eta \sim 0.05 - 0.5$ at launch. This sampling of the literature shows that overall, for galaxies of comparable mass with our sample, the mass-loading factor estimates range from $0.05 - 5$. It is likely that the higher mass loading in the down-the-barrel observations is due to the line-of-sight effects (down-the-barrel versus random sightlines of GRBs). This highlights the need for a multi-probe approach to trace the outflow process in various phases and for various orientations of a galaxy to capture the full picture of the CGM outflows.

The mass loading factors estimated here are smaller than the estimates from various galaxy evolution and zoom-in simulations by 1-2 orders of magnitude. For example, cosmological zoom simulations such as [Anglés-Alcázar et al., 2014] and [Shen et al., 2012] suggest an $\eta \sim 1$ at $z > 2$ to reproduce the morphological and dynamical properties of galaxies with $M_h \sim 10^{11-12} M_\odot$ at $z \sim 2$. However, it should be noted that these mass-loading factors encompass all the phases, and not just the warm phase traced by C IV or Si IV. The latest TNG simulations appear to resolve this issue by separating the phases in the outflows [Nelson et al., 2019]. The total (all-phase) mass loading factor $\eta_{tot,20kpc} \sim 4$ (Fig. 5 in [Nelson et al., 2019]) for a main-sequence galaxy of $M_* \sim 10^{9.3} M_\odot$ at $z = 2$ whereas the loading factor for the warm phase is $\eta_{warm,20kpc} \sim 0.15$ (Fig. 10 in [Nelson et al., 2019]). This warm phase mass loading factor is within a factor of 2 of the mass loading factor evaluated here. This also implies that a significant fraction of the outflowing mass is in other phases.

It will be of further interest to carry out such comparisons at higher redshifts to synthesize a complete picture of the impact of outflows on galaxy evolution and vice versa.

It should be noted that here we have assumed a ballistic outflow driven by star formation and no halo drag or outflow acceleration (eg: by cosmic rays, ram pressure, or radiation pressure) is considered ([Murray et al., 2011, Hayward and Hopkins, 2016, Girichidis et al., 2016]). The comparative effects of the two can be non-trivial and need to be explored in the future. At the same time, the observational mass-loading factors have several uncertainties that need to be considered while comparing them to numerical simulations. The current analysis has been conducted for an ensemble, so only typical values are considered here. We will do this for individual hosts in an upcoming paper by connecting the CGM and galaxy properties. While comparing the outflow characteristics with simulations and other surveys, the ionization fraction, outflow fraction in various phases, and the dynamics of an outflow (various accelerations and drags) need to be treated more carefully. In addition, the relative fraction of the re-accretion of the enriched gas versus its virialization in the CGM needs to be explored in the simulations.

The modest mass outflow rates estimated here can be entirely supernova-driven. The kinetic energy of the outflow can be estimated as $\frac{1}{2}\dot{M_{out}}{v^2}_{out} \sim 5.7\times10^{40}$ ergs/s. Following the formalism described in [Murray et al., 2005] (see equations 34 and 35), we assume a Salpeter IMF and that $\xi \sim 10\%$ of the supernova energy ($E_{SN} \sim 10^{51}$ ergs) is efficiently thermalized in the ISM and thus, driving the displacement of the gas. With a supernova rate ($f_{SN}$) of $10^{-2}$ per $M_{\odot}$ of star formation,

the energy deposition from supernovae becomes:

$$\dot{E}_{SN} \sim \xi f_{SN} E_{SN} \times SFR \sim 3 \times 10^{40} \frac{\xi}{0.1} \frac{\mathrm{SFR}}{1 \mathrm{M}_{\odot} \mathrm{yr}^{-1}} \mathrm{ergs/s} \tag{2.13}$$

Thus, SFR $\sim 2$ M$_{\odot}$ yr$^{-1}$ is energetically sufficient to drive the observed warm outflows. While a comparable mass outflow rate may be hidden in other gas phases (not traced by C IV), given the typical SFR $\sim 10$ M$_{\odot}$ yr$^{-1}$ for $z > 2$ GRB hosts, it is very likely that the outflows are predominantly driven by supernova energy injection.

### 2.7.2 CGM-Galaxy Co-Evolution

From the standpoint of galaxy evolution, it is interesting to compare the evolution of the CGM with the evolution of the host galaxy. We have combined published data from the literature ([Steidel et al., 2010]; [Borthakur et al., 2013]; COS-Dwarfs: [Bordoloi et al., 2014b]; KODIAQ: [Lehner et al., 2015]; [Burchett et al., 2016]; COS-burst: [Heckman et al., 2017]; [Rudie et al., 2019]) with our new observations to investigate the evolution of C IV mass in the CGM relative to the stellar mass ($\frac{M_{\mathrm{CIV}}}{M_*}$), as a function of redshift. For uniformity, we have only considered C IV column density within respective $R_{vir}$ (estimated using $M_* - M_{halo}$ relation; [Wechsler and Tinker, 2018]) and converted that into a C IV mass estimate using equation 4 in [Bordoloi et al., 2014b]. The results are summarized in Figure 2.13.

It can be seen that $\log(M_{\mathrm{CIV}}/M_*) \sim -4.5$ throughout the evolution of current-day galaxies with $M_* > 10^{10} M_{\odot}$. This relatively uniform ratio within $\pm$ 0.5 dex

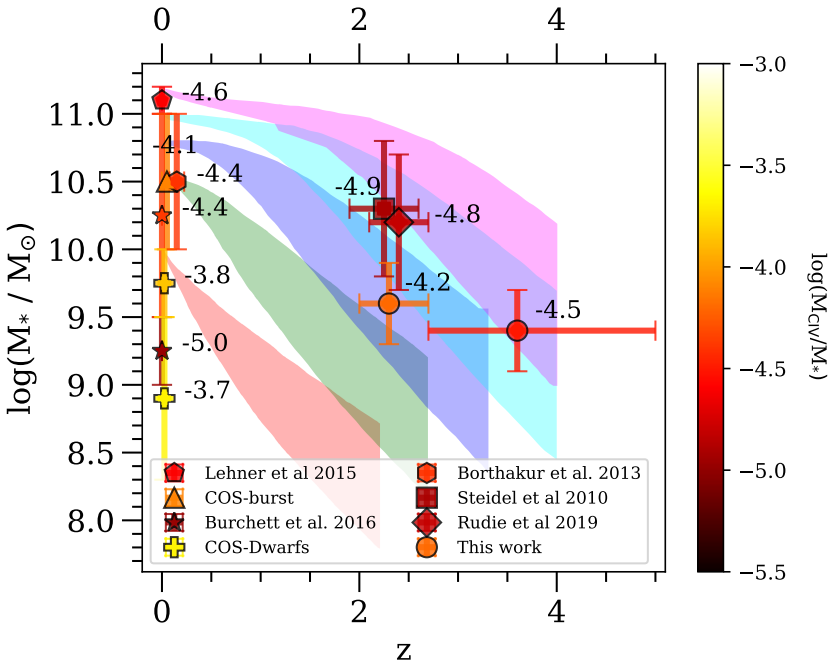


Figure 2.13: The evolution of $M_{\rm CIV}/M_*$ as a function of redshift. The background colored regions (from [Wiklind et al., 2019]) track the history of galaxies with current stellar mass $log(M_*/M_\odot)$ = 10.0, 10.5, 11.0 and 11.2 (red, green, blue, magenta and purple) using the MEAM (multi-epoch abundance matching) selection method ([Moster et al., 2012]; [Behroozi et al., 2013]). The spread of the selection slices represents the $1\sigma$ uncertainty as defined in [Behroozi et al., 2013]. The foreground points show the ratio of C IV mass within $R_{vir}$ to the stellar mass of the galaxy. The color of a point indicates the ratio, scaled according to the colorbar on the right. For convenience, the log of the ratio is also written next to the points. The ratios have typical error bars of ± 0.5 dex due to uncertainties in the hosts stellar masses (thereby, virial radii) and C IV column density.

indicates that typically the CGM co-evolves with the stellar mass of the galaxy all the way from $z \sim 4$ to $z \sim 0$. It is possible to explain this co-evolution with the cosmic star formation history. The star formation builds the stellar mass of the galaxy as well as the warm, ionized CGM traced by C IV. This important aspect of the CGM-galaxy co-evolution needs to be explored further in large-scale galaxy evolution simulations.

Another possible explanation for the co-evolution of warm ionized CGM and the galaxy stellar mass can be the scaling of the virial radius with redshift and galaxy mass. This is especially important since the virial radius is an arbitrary choice to define the CGM. [Chen, 2012] studied the radial distribution of $L_*$ galaxies from $z \sim 2$ to $z \sim 0$ with similar halo mass ($M_h \sim 10^{12} M_\odot$) in that redshift range. An alternative definition of the extent of the CGM was used in this case to reveal that the radial distribution of column density (normalized to the 'CGM radius') did not evolve substantially from $z \sim 2$ to $z \sim 0$. So it is very likely that the radial distribution of column density (normalized to the corresponding virial radius) remains fairly constant and the evolution of the CGM mass is observed due to the scaling of virial radius with redshift. From Figure 2.13, it could also be inferred that any major mergers leading to an increased halo and stellar mass grow the CGM metal mass in the same proportion as $M_*$. Further theoretical investigation of the CGM-galaxy co-evolution is necessary to corroborate these growth pathways.

For current-day low-mass galaxies ($M_* < 10^{10} M_\odot$), there is a seemingly larger scatter in the $\log(M_{CIV}/M_*)$ at $z = 0$, going from $-3.7$ to $-5.0$. The COS-Dwarfs sample ([Bordoloi et al., 2014b]; primarily made of star-forming dwarf galaxies) has

a systematically higher ratio suggesting that the CGM of low-mass galaxies could be relatively more enriched in terms of either the metallicity or baryons. On the other hand, the low-mass sample (predominantly star-forming dwarfs) in a blind survey for C IV absorbers in QSO spectra [Burchett et al., 2016] shows a systematically lower ratio. However, one should note that the C IV column densities reported in [Burchett et al., 2016] refer only to high impact parameters ($> 0.3R_{vir}$), which may substantially underestimate the total C IV mass. Therefore, further observations at a range of imapct parameters would be required to asses whether the $M_{\rm CIV}/M_*$ ratio is indeed higher for these low-mass galaxies.

### 2.7.3 Existence of Inflows?

The cold ($T < 10^4$ K) phase is almost exclusively traced by low-ions [Tumlinson et al., 2017]. If the relative proportions of warm (traced by C IV, Si IV) and cold (traced by Fe II, Si II) phases were the same for red and blue wings, we would expect to see a blue asymmetry in the low ions that resembles that of the high ions ($\sim 0.45$ dex, see Table 2.2), but instead the asymmetry is only $\sim 0.18$ dex. We interpreted this relatively stronger blue asymmetry in the high ions to be due to the outflows being more enriched in high ions. While this is our favorite explanation, another plausible explanation is the existence of cold inflows which make the red wings of low ions stronger compared to the red wings of high ions, thus leading to a lower 'blue asymmetry' in low ions. In this section, we briefly explore this possibility.

Under the aforementioned scenario, the inflow contribution of low ions can be

evaluated as the fraction of red-wing column density of low ions that is leading to their relatively stronger red wings compared to the high-ions. From Table 2.2, we can estimate that $N_{SiII} \sim 10^{13.2}$ cm$^{-2}$ and $N_{FeII} \sim 10^{13.4}$ cm$^{-2}$ are contributed by the inflows moving at $v \sim 150$ km s$^{-1}$. This column density is consistent with the feedback simulations in [Shen et al., 2013] at $z \sim 3$.

Since the characteristics of inflows at high-z are not well understood observationally, we rely on existing inflow models to infer a rough estimate of the inflow mass. Assuming a pristine inflow of 0.03 solar metallicity ([Fumagalli et al., 2011, Glidden et al., 2016]) and an ionization fraction for Si II of ∼50% for the cold phase (see Fig. 5 in [Shen et al., 2013]), we derive $N_{H,inflow} \sim 10^{19.8}$ cm$^{-2}$. We get a similar estimate with Fe II. However, we note a caveat that, although we have considered a pristine metallicity of 0.03 solar, it is not clear how the circulation of metals enrich the inflows by the time they reach the galactic disk. In addition, the metal-enriched recycling flows also manifest itself as inflowing gas and could dominate the observational signature due to their high metal content.

Assuming a constant average density in the accretion stream and a typical area covering fraction of the inflow of $\sim 5\%$ (mostly concentrated along the direction of rotation of the galaxy; [Fumagalli et al., 2011, Goerdt et al., 2012]), we can estimate the inflowing mass as:

$$\mathrm{M_{in}} = 10^9 \mathrm{M_\odot} \left(\frac{R_{vir}}{50\mathrm{kpc}}\right)^2 \left(\frac{N_{H,in}}{10^{19.8}\mathrm{cm^{-2}}}\right) \left(\frac{f_{area}}{0.05}\right) \left(\frac{0.03}{Z/Z_\odot}\right) \tag{2.14}$$

Note that we have considered $R_{vir}$ as the extent of the inflow instead of 2 ×

$R_{vir}$ since we are assuming a constant average density for the inflow stream. Thus, we get an inflowing mass of $\sim 10^9 M_\odot$ within $R_{vir}$, which amounts to $\sim 60\%$ of the diffuse warm CGM traced by C IV that we calculated in section 2.6.2. Note that this is a lower limit since we have only considered the high-velocity inflows ($v_{los} > 100$ km s$^{-1}$). This is an order-of-magnitude estimate owing to uncertainties in metallicity and covering fraction.

The mass accretion flow rate can be approximated by considering the inflow motion as a free fall in the halo. Various theoretical models predict large radial streams for inflows until the inner few percents of the virial radius (eg: [Fumagalli et al., 2011]). Thus, the inflow timescale can be well approximated as free-fall timescale of the halo. From the typical stellar masses of GRBs at $z > 2$ we estimated a halo mass of $10^{11.2}$ M$_\odot$ (section 2.7.1 and Appendix A.2). The free-fall timescale for such a halo is 500 Myr. This gives an overall inflow rate estimate of $\dot{M}_{in} = M_{in}/t_{ff} = 2$ M$_\odot$ yr$^{-1}$.

How can this modest gas inflow rate drive a typical high-z GRB host SFR of the order of 10 M$_\odot$ yr$^{-1}$ ? It should be noted that the rate evaluated above is over a 500 Myr (free-fall) timescale, while the UV-derived star formation rates are fairly instantaneous in comparison ($< 100$ Myr). GRBs typically take place in a transient (age $\sim 10 - 100$ Myr, see [Erb et al., 2006] and [Levesque et al., 2010]) high-SFR phase of its host. Therefore, a lower and steady cold gas accretion may be sufficient to support the typical long-term SFR history of a GRB host galaxy. In addition, large reservoirs of cold gas (from prior accretion) seem to be already present in these low-mass galaxies due to an order of magnitude lower star formation efficiency at

$z > 4$ compared to $z < 3$ owing to the low metallicity [Reddy et al., 2012].

While this is not a direct observational evidence of cold inflows, these calculations provide an order-of-magnitude insight into the inflow rates of the low-mass galaxies at $z > 2$. Constraining the weak inflows will require high-quality spectra over a much larger sample.

### 2.7.4 Origin of O VI and N V: CGM vs Circumburst?

The cases of O VI and N V in the CGM-GRB sample are interesting because of two key reasons: they trace similar regions in the temperature-density phase space ($T \sim 10^{5.5}$ K, $n \sim 10^{-4.5}$ cm$^{-3}$ from [Tumlinson et al., 2017]), but their kinematics appear to be distinct from each other. While O VI, like C IV and Si IV, shows a strong blue asymmetry of $\sim 0.6$ dex, there is no such asymmetry in N V. The overall N V kinematics more closely resemble the low-ion kinematics. Despite the small number of sightlines (13) with O VI in the bandpass and often lower SNR in O VI due to lower sensitivity and Lyman-alpha forest, the kinematic differences are significant. It is important to understand the origin of N V and its distinct nature compared to O VI, in order to study the warm-hot CGM phase (T $\sim 10^{5.5}$K), as well the nature of photo- or collisional-ionized gas harboring N V.

In various low-$z$ CGM surveys using QSO sightlines such as COS-Halos [Werk et al., 2016], N V is rare. In a similar survey at high $z$ (KODIAQ; [Lehner et al., 2014]), N V is more prevalent, but still with a detection rate of only $\sim 50\%$ and with a typical column density $\log(\mathrm{N(N\ V)/cm^{-2}}) \sim 13.6$ (it is $\sim 14.0$ in the CGM-

GRB sample). On the other hand, O VI is ubiquitous in both high- and low-z surveys. Several sightlines through the Milky Way galactic halo and disk show N V absorption ([Savage et al., 1997, Fox et al., 2015, Karim et al., 2018]), but only $\sim$ 10% show column densities N(N V) $\gtrsim 10^{14}$ cm$^{-2}$.

The nature of the excess N V absorption in the GRB spectra is not well understood. Possible explanations for the N V absorption in the GRB spectra include: 1. photoionization of the circumburst medium within r $\sim$ 10 pc ([Prochaska et al., 2008c, Fox et al., 2008]), 2. recombination of the promptly ionized nitrogen (all electrons stripped) to N V within 10 pc [Heintz et al., 2018], and 3. N V in the CGM ([Heintz et al., 2018, Fox et al., 2008]). The kinematic similarity of N V absorption with the UV-pumped fine-structure lines (such as C II*, Si II*), which are associated with absorbers within a few hundreds of parsecs from the GRB [Vreeswijk et al., 2013], is considered an indicator for the circumburst origin of N V.

For the GRB spectra presented here, the N V absorption within $\pm$400 km s$^{-1}$ typically comes from an ensemble of kinematically distinct absorbing components. Therefore, it is difficult to imagine that the absorption is produced solely by the circumburst medium. While most of the absorption components of N V (especially the strongest components) have a counterpart that is kinematically associated with fine-structure transitions (C II*, Si II*, as also seen in [Prochaska et al., 2008b]), there are also weaker components that are not associated with an excited transition within $\pm$ 30 km s$^{-1}$ (Fig. A.4$-$A.30). Therefore, we suggest that the low-$|v|$ N V absorption seen in the GRB spectra comes primarily from the highly ionized / recombining gas associated with the circumburst medium while the weaker absorption

at higher $|v|$ comes primarily from the warm gas associated with the CGM. This would explain the relatively higher N V detection rate and column density along GRB sightlines.

The typical O VI column densities derived in this survey are comparable to the typical O VI column densities in the high-z QSO sightline surveys [Lehner et al., 2014] and the CGM of local star-forming galaxies [Tumlinson et al., 2011]. While O VI absorption could also have a circumburst component since the recombination rates of N V and O VI are similar [Heintz et al., 2018], the kinematics of N V are distinct. In fact, the O VI kinematics resemble the kinematics of C IV and Si IV more than those of N V. This strongly suggests that the ISM and CGM are the dominant contributors to the O VI column density, although a minor contribution from the circumburst medium cannot be ruled out. Detailed photoionization models addressing the circumburst O VI absorption are required to quantitatively ascertain this.

As shown in [Prochaska et al., 2006] and [Chen et al., 2007], C IV and Si IV absorption have no association with the circumburst medium up to several tens of parsecs. The ionizing photon flux from the GRB strips electrons from these species (with ionization potentials of 64.5 and 45.1 eV, respectively) and their recombination timescales are of the order of 1 year for a typical H II region [Chen et al., 2007]. Therefore, the C IV and Si IV lines primarily trace the typical ISM and CGM of the GRB host and not the circumburst medium.

High-resolution rest-frame UV spectra of the afterglows at multiple epochs are required to probe their explosion sites and environments, constrain the ionization

models, and thus understand the origin of peculiar N V absorption in the GRB afterglow spectra.

## 2.8 Summary and Conclusions

In this paper, we collected a large sample of medium resolution ($\delta v < 50$ km s$^{-1}$) and high SNR (typical $\sim 10$) spectra of 27 GRB afterglows in the redshift range $z \sim 2-6$ to systematically probe the kinematics and physical properties of the CGM at high redshifts using the absorption features of high- and low-ion species in the spectra. A simple toy model was constructed to aid this analysis through geometric and kinematic modeling of the CGM and the outflows. We further estimated the CGM mass and mass outflow rates in two different redshift regimes ($z1 : 2 - 2.7$ and $z2 : 2.7 - 5$). Finally, combining the results of past studies and this work, we investigated the CGM-galaxy co-evolution as a function of redshift. The key conclusions of this study are summarized as follows:

1. Detection fractions: By inspecting the median plots of the rest-frame spectra for each species, three clear kinematic regions were identified: central region ($|v| < 100$ km s$^{-1}$), blue wing ($v < -100$ km s$^{-1}$), and red wing ($v > 100$ km s$^{-1}$). The high-ion species (C IV and Si IV) were found to have substantially higher detection fractions in the blue wings compared to the red wings (difference $\sim 30\%$). On the other hand, the low-ion species (Fe II, Si II, Al III) had a marginal excess in detection fraction in the blue wings (difference $\sim 10\%$). This shows that the blue wing component is substantially dominated by the high-ions compared to the red wings (Table 2.1).

We interpret this as an evidence for warm phase (T $\sim 10^{4.5-5.5}$K) outflows.

2. Kinematic asymmetry: By stacking the spectra of individual absorption lines (Fig. 2.2), a significant absorption excess was observed in the blue wings compared to the red wings, especially for the high-ions (C IV, Si IV). We further quantified this using multi-component Voigt-profile fitting and converting the Voigt profiles to integrated column densities in 100 km s$^{-1}$ windows (from $-400$ km s$^{-1}$ to $+400$ km s$^{-1}$). The blue-red kinematic asymmetry was stronger in high-ion species compared to the low-ion species by 0.2-0,3 dex in column density (Table 2.2). This key difference was further highlighted in the high- to low-ion line ratios (Fig. 2.5). This is a strong signature of warm outflows in the GRB hosts.

3. Kinematic simulations: To resolve the relative contributions of the CGM and ISM in terms of absorption line kinematics, we modeled a typical GRB host galaxy and the CGM around it using a simple toy model. The results from the toy model showed that the absorption produced by the host ISM is typically found within the central region ($\pm$100 km s$^{-1}$ in terms of line-of-sight velocity), while the CGM absorption dominates the absorption in the blue and red wings beyond $\pm$100 km s$^{-1}$. An outflow component was further added to the virialized CGM to simulate star-formation driven outflows. We made various simplifying assumptions for the halo mass ($M_h \sim 10^{11.2} M_\odot$), the CGM density profile ($r^{-2}$), the CGM/ISM metallicity, and the outflow itself (ballistic, no halo drag). By comparing the predictions of the toy models with the observed column density profiles, we estimated the physical properties of the CGM, including the outflow launch speed (300 km s$^{-1}$), the fraction of CGM clouds that are outflowing (25%), and the CGM mass ($\sim 10^{9.8} M_\odot$).

4. CGM mass estimates: In § 2.6.1, we used the geometric mean of the integrated column density and a conservative extrapolation to estimate the CGM contribution in the central ± 100 km s$^{-1}$. From this, we deduced the mass of the warm-phase CGM traced by C IV ($M_{CGM} \sim 10^{9.2} M_{\odot}$). The CGM mass estimates from the toy models (§ 2.5.2) and column density profiles (§ 2.6.1) are complementary in nature, strengthening a CGM mass estimate of $\sim 10^{9.2-9.8} M_{\odot}$. These estimates show that a) the mass contained in the CGM ($\sim 2 \times R_{vir}$) is comparable to the typical stellar mass of GRB hosts at $z > 2$ ($M_{*} \sim 10^{9-10} M_{\odot}$) and b) the CGM is already a significant component of the galaxy ecosystem for GRB host galaxies at $z > 2$.

5. Evolution of the CGM mass: The CGM-GRB sample was divided into two redshift bins each spanning $\sim 1$ Gyr ($z1 : 2-2.7$ and $z2 : 2.7-5$). Their CGM C IV masses were estimated to be $M_{CIV,z1} = 10^{5.6} M_{\odot}$ and $M_{CIV,z2} = 10^{5.1} M_{\odot}$ (Figs. 2.10 and 2.11). A comparison with the COS-Dwarfs survey for similar low-mass galaxies at low redshifts ($z < 0.3$) shows that the low-z galaxies are slightly more enriched by a factor of 2 relative to galaxies of similar masses at high z. This shows that the dwarf galaxies had metal-enriched environments as early as $z \sim 3-5$ and thus, most likely played a major role in the metal enrichment of the universe due to their shallow potential wells.

6. Outflow mass: The optimal toy model indicates that the fraction of outflowing clouds in outflow state is $f_{out} = 25\%$ and the outflow launch velocity at 2 kpc is $v_{launch} = 300$ km s$^{-1}$. The (warm) outflow mass in the two redshift ranges was estimated to be $M_{out,z1} \sim 10^{8.6} M_{\odot}$ and $M_{out,z2} \sim 10^{8.1} M_{\odot}$. Assuming no halo drag or outflow acceleration mechanisms, as much as 80% of this outflowing gas has

$v > v_{esc}$ at launch. Given a typical halo mass of $M_h \sim 10^{11.2} M_\odot$, the crossing time for $2 \times R_{CGM}$ is $\sim 0.5$ Gyr. This in turn implies that the CGM mass in the warm gas phase grows by $\sim 5\%$ ($f_{out} \times 20\%$) in 0.5 Gyr by retaining the slower outflows in the CGM.

7. Mass loading factor: We further estimated that the warm-phase mass outflow rates at a radius of 20 kpc radius is $\dot{M}_{out,z1} \sim 0.8\ M_\odot\ \mathrm{yr}^{-1}$ and $\dot{M}_{out,z2} \sim 0.35\ M_\odot\ \mathrm{yr}^{-1}$. The median SFR of GRB hosts at $z : 2-5$ is $\sim 10 M_\odot\ \mathrm{yr}^{-1}$. Therefore, the warm-phase mass loading factors in the two redshift bins are estimated to be $\eta_{z1,20kpc} = 0.084$ and $\eta_{z2,20kpc} = 0.035$. These mass-loading factors suggest that the outflows and thereby, the CGM metal enrichment, for these low-mass galaxies are exclusively driven by star formation. While these mass-loading factors are low, it is important to note that this only includes warm-phase outflows and thus highlights the need for a multi-probe approach to trace the outflows in various phases to produce a complete picture of the CGM outflows.

8. CGM-galaxy co-evolution: We compared the evolution of C IV mass in the CGM with the stellar mass evolution as a function of redshift (Fig. 2.13). We find that $\log(M_{\mathrm{CIV}}/M_*) \sim -4.5$ within $\pm 0.5$ dex throughout the evolution history of current-day galaxies with $M_* > 10^{10} M_\odot$. This relatively uniform ratio indicates that the CGM metal mass co-evolves with the stellar mass of the galaxy all the way from $z \sim 4$ to $z \sim 0$, for the progenitors of local galaxies with $M_* > 10^{10} M_\odot$. Therefore, the CGM-galaxy co-evolution is an important piece of the galaxy growth puzzle which needs to be explored further in large-scale galaxy simulations.

In this paper, we systematically probed the CGM of high-z, low-mass, star-

forming galaxies for the first time using a GRB host sample. We used typical stellar and dark matter halo masses to derive the CGM masses and outflow rates. However, the GRB host population is quite diverse and spans two order of magnitudes in stellar mass and SFR at $z > 2$. In a future paper, we plan to examine the properties of individual GRB hosts and compare them with the properties of their CGM to help refine the CGM-galaxy connection. Detailed ionization modelling will be a crucial next step to derive better constraints on the physical properties of the CGM.

## Acknowledgements

P.G. was supported by NASA Earth and Space Science Fellowship (ASTRO18F-0085) for this research. S.V. acknowledges support from a Raymond and Beverley Sackler Distinguished Visitor Fellowship and thanks the host institute, the Institute of Astronomy, where this work was concluded. S.V. also acknowledges additional support by the Science and Technology Facilities Council (STFC) and Kavli Institute for Cosmology, Cambridge. This work was partly based on data obtained from the ESO Science Archive Facility. This research has also made use of the Keck Observatory Archive (KOA), which is operated by the W. M. Keck Observatory and the NASA Exoplanet Science Institute (NExScI), under contract with the National Aeronautics and Space Administration (NASA). The authors are grateful to Drs. Andrew Fox and S. Bradley Cenko for their useful comments in the early stages.

Table 2.3: Fit parameters of the spectra

| GRB | $z_{GRB}$ | line | Component No. | log(N) | $\sigma_{\log(N)}$ | b (km s$^{-1}$) | $\sigma_b$ | center (km s$^{-1}$) | $\sigma_{center}$ | Flag[a] |
|---|---|---|---|---|---|---|---|---|---|---|
| 000926 | 2.0385 | C IV 1548 | 1 | 13.28 | 0.18 | 7 | 4 | -368 | 4 | 0 |
| 000926 | 2.0385 | C IV 1548 | 2 | 14.08 | 0.05 | 29 | 6 | -332 | 19 | 0 |
| 000926 | 2.0385 | C IV 1548 | 3 | 14.07 | 0.07 | 29 | 5 | -239 | 5 | 0 |
| 000926 | 2.0385 | C IV 1548 | 4 | 14.35 | 0.21 | 20 | 5 | -181 | 19 | 0 |
| 000926 | 2.0385 | C IV 1548 | 5 | 14.55 | 0.21 | 18 | 5 | -136 | 19 | 0 |

[a] A flag of 0 indicates convergent fit, flag of 1 indicates saturated/degenerate fit.
This table is published in its entirety in machine-readable format. Only a small portion is shown here.

Table 2.4: List of GRBs in the sample

| GRB | $z_{GRB}$ | Instrument | Resolution | Acq. Mag$_{AB}$ | SNR per pixel[a] | log N$_H$ in $cm^{-2}$ | References |
|---|---|---|---|---|---|---|---|
| 000926 | 2.0385 | Keck/ESI | 20,000 | 20.5 | 10 | 21.3 ± 0.25 | [Castro et al., 2003] |
| 021004 | 2.3281 | UVES | 40,000 | 18.8 | 6 | 19.0 ± 0.2 | [Fiore et al., 2005][b] |
| 050730 | 3.9672 | UVES | 40,000 | 18.0 | 10 | 22.1 ± 0.1 | [D'Elia et al., 2007][b] |
| 050820A | 2.6137 | UVES | 40,000 | 21.0 | 12 | 21.1 ± 0.1 | [Prochaska et al., 2007][b] |
| 050922C | 2.1996 | UVES | 45,000 | 19.5 | 10 | 21.55 ± 0.1 | [Prochaska et al., 2008c][b] |
| 060607A | 3.0738 | UVES | 55,000 | 16.5 | 30 | 16.95 ± 0.03 | [Prochaska et al., 2008c][b] |
| 071031 | 2.6912 | UVES | 55,000 | 18.5 | 10 | 22.15 ± 0.05 | [Fox et al., 2008] |
| 080310 | 2.4274 | UVES | 55,000 | 17.5 | 30 | 18.7 ± 0.1 | [Fox et al., 2008] |
| 080804 | 2.205 | UVES | 55,000 | 19.5 | 10 | 21.3 ± 0.1 | [Fynbo et al., 2009] |
| 080810 | 3.351 | Keck/HIRES | 50,000 | 17.0 | 30 | 17.5 ± 0.15 | [Page et al., 2009] |
| 090926A | 2.106 | X-shooter(UVB) | 6000 | 17.9 | 20 | 21.73 ± 0.07 | [D'Elia et al., 2010] |
| 100219A | 4.665 | X-shooter(VIS) | 10,000 | 22.2 | 4 | 21.13 ± 0.12 | [Thöne et al., 2012] |
| 111008A | 4.989[c] | X-shooter(UVB) | 6500 | 21.0 | 10 | 22.3 ± 0.06 | [Sparre et al., 2014] |
| 120327A | 2.813 | X-shooter(UVB)<br>X-shooter(VIS) | 6250<br>10000 | 18.8 | 30 | 22.01 ± 0.09 | [D'Elia et al., 2014] |
| 120815A | 2.358 | X-shooter(UVB)<br>X-shooter(VIS) | 6000<br>11000 | 18.9 | 12 | 21.95 ± 0.1 | [Krühler et al., 2013] |
| 120909A | 3.929 | X-shooter(VIS) | 10000 | 21.0 | 9 | 21.20 ± 0.10 | [Cucchiara et al., 2015] |
| 121024A | 2.298[c] | X-shooter(UVB)<br>X-shooter(VIS) | 6000<br>12000 | 20.0 | 15 | 21.50 ± 0.10 | [Friis et al., 2015] |
| 130408A | 3.757 | X-shooter(UVB)<br>X-shooter(VIS) | 6000<br>12000 | 20.0 | 20 | 21.70 ± 0.10 | [Cucchiara et al., 2015] |
| 130606A | 5.911 | X-shooter(VIS)<br>X-shooter(NIR) | 8000<br>6500 | 19.0 | 10 | 19.93 ± 0.2 | [Hartoog et al., 2015] |
| 130610A | 2.091 | UVES | 40000 | 20.9 | 6 | – | [Smette et al., 2013] |
| 141028A | 2.333 | X-shooter(UVB)<br>X-shooter(VIS) | 5600<br>9600 | 20.0 | 8 | 20.60 ± 0.15 | [Wiseman et al., 2017b] |
| 141109A | 2.993[c] | X-shooter(UVB)<br>X-shooter(VIS) | 6000<br>10000 | 19.2 | 5 | 22.10 ± 0.10 | [Heintz et al., 2018] |
| 151021A | 2.329 | X-shooter(UVB)<br>X-shooter(VIS) | 6000<br>10000 | 18.2 | 5 | 22.3 ± 0.2 | [Heintz et al., 2018] |
| 151027B | 4.0633 | X-shooter(VIS) | 9000 | 20.5 | 5 | 20.5 ± 0.2 | [Heintz et al., 2018] |
| 160203A | 3.518 | X-shooter(VIS) | 12000 | 18.0 | 5 | 21.75 ± 0.10 | [Heintz et al., 2018] |
| 161023A | 2.709 | X-shooter(UVB)<br>X-shooter(VIS) | 6000<br>10000 | 17.5 | 40 | 20.96 ± 0.05 | [Heintz et al., 2018] |
| 170202A | 3.645 | X-shooter(UVB)<br>X-shooter(VIS) | 6300<br>10500 | 20.8 | 8 | 21.55 ± 0.10 | [Selsing et al., 2018] |

[a] Typical SNR in the bandpass.

[b] Also previously analyzed in [Fox et al., 2008]

[c] Ni II* transition has been used in addition to Si II* and C II* for defining the redshift.

# Chapter 3: New radio constraints on the obscured star formation rates of massive GRB hosts at redshifts $2 - 3.5$

*In this chapter, we will explore whether GRB hosts in our sample are likely to be heavily obscured by dust.*

## 3.1 Introduction

Long gamma-ray bursts (GRBs) are bright bursts of gamma-rays followed by extremely luminous multi-wavelength afterglow, from the X-rays to the radio wavelengths. They have been shown to be associated with the collapse of massive stars [Hjorth et al., 2003, Stanek et al., 2003]. GRBs have been observed across the cosmic history, from $z \sim 0.01$ to $z \sim 8.2$ [Tanvir et al., 2009, Salvaterra et al., 2009, Fynbo et al., 2000]. These attributes make them a viable probe for tracing the star-formation history of the universe, especially at $z > 2$ where other probes are scarce.

However, the exact relation between GRB rates and cosmic star formation rate (SFR) is still an unsolved problem [Greiner et al., 2015, Schulze et al., 2015, Perley et al., 2016a, Perley et al., 2016b]. Various observations of $z < 1.5$ GRB hosts have raised questions on whether GRBs can be used as unbiased tracers of star formation

[Boissier et al., 2013, Perley et al., 2013, Vergani et al., 2015, Schulze et al., 2015, Perley et al., 2016b]. Particularly, GRB hosts at $z < 1$ show a strong bias towards faint, low-mass ($M_* < 10^{10}$ $M_\odot$), star-forming galaxies and lower metallicities (below solar metallicity) compared to other star-formation tracers, even after taking into account GRBs with high line-of-sight dust obscuration [Graham and Fruchter, 2013, Perley et al., 2013, Kelly et al., 2014, Vergani et al., 2015, Japelj et al., 2016, Perley et al., 2016b]. However, this bias appears to subside at $z > 2$ [Greiner et al., 2015] since the mean metallicity of typical star-forming galaxies is below solar. A significant amount of star formation at these redshifts is contributed by dusty massive starbursts (submm-bright; see [Casey et al., 2014] for a review). Thus, high-mass, (relatively) metal-rich, dusty galaxies with high star formation rates may form a significant fraction of the GRB host population at $z > 2$ [Perley et al., 2013, Greiner et al., 2016, Perley et al., 2016b]. On the other hand, some previous studies indicate that GRB explosions may have a bias against dusty host galaxies based on the relatively stronger Ly-$\alpha$ emission of the hosts [Fynbo et al., 2003] and the higher incidence of GRBs in the brightest regions in the galaxy compared to core-collapse supernovae [Fruchter et al., 2006]. To understand whether GRBs truly trace star formation at $z > 2$, it is important to measure the total SFR (i.e. dust-obscured + dust-unobscured).

Radio observations provide a probe of recent total star formation rate. In star-forming galaxies, the radio luminosity at frequencies below a few $\times$ 10 GHz is dominated by the synchrotron emission from relativistic electrons, previously accelerated by supernova remnants, propagating in the interstellar magnetic field

[Condon, 1992]. The relativistic electrons probably have lifetimes $\leq$ 100 Myr, thus this component traces recent ($<$ 100 Myr) star formation.

There are about 100 GRB host observations at radio frequencies down to limits between $3-500$ $\mu$Jy (see [Greiner et al., 2016] for details). So far, there have been 19 cm-wave observations of GRB hosts at $z > 2$, out of which two were detections: GRB 080207A and GRB 090404 [Greiner et al., 2016, Perley et al., 2013, Perley et al., 2015, Perley et al., 2016d]. However, none of these high-z GRBs have high-resolution, high-SNR optical afterglow spectra.

GRBs with high-resolution afterglow spectra can be excellent test cases for examining the biases in GRB host population at high-z since a measure of the host metallicity may be derived from these spectra to help characterize the galaxy population traced by GRBs at $z > 2$. The availability of a high-resolution rest-frame UV spectrum of the GRB afterglow implies that the rest-frame UV is largely unobscured ($A_{UV} \lesssim 2-3$ mag). The radio observations of these GRB hosts may be used to find out whether this lack of obscuration is simply due to a clear line-of-sight or due to an overall lack of dust obscuration in the host galaxy. Dusty sightlines do not necessarily imply dusty host galaxies. This needs to be tested, especially in light of past cm-wave observations of [Hatsukade et al., 2012] and [Perley et al., 2013], where the deep upper limits on the radio flux from the galaxy hosts of so-called 'dark GRBs' (i.e. UV-dark afterglow due to high line-of-sight extinction) imply that the dark GRBs do not always occur in galaxies enshrouded by dust or in galaxies exhibiting extreme star formation rates (few $\times$ 100 $-$ 1000 $M_{\odot}yr^{-1}$).

New radio-based SFR constraints are particularly needed for massive ($M_* \gtrsim 10^{10}M_{\odot}$)

GRB hosts at $z > 2$ since the massive star-forming galaxies at high-z are likely to be significantly dusty [Casey et al., 2014, Shapley, 2011]. One of our objectives is therefore to understand whether massive GRB hosts at $z > 2$ share this characteristic of typical massive star-forming galaxies at $z > 2$.

This pre-selection of $z > 2$ GRB hosts based on high-resolution afterglow spectra is also useful to inform the total SFR of the GRB hosts in the CGM-GRB sample [Gatkine et al., 2019a], particularly for the massive GRB hosts which are likely to have a substantial dust-obscured star formation component. The high-resolution spectra quantitatively trace the kinematics of the circumgalactic and interstellar media of the host. The total star formation (obscured + unobscured) is a major driver of galactic outflows that feed the circumgalactic medium (CGM). Therefore, constraining the total SFR is necessary for studying the CGM-galaxy connection.

In this paper, we report deep, late-time radio observations of four $z > 2$ GRB hosts with existing high-resolution afterglow spectra. The sample includes GRB 080810 which is the highest-redshift GRB host yet ($z = 3.35$) with deep radio observations. These results were obtained using Karl Jansky Very Large Array (VLA) in C-band ($4 - 8$ GHz). Section 3.2 describes the target selection, VLA observations, and analysis. In section 3.3, we derive the constraints on the radio-based SFRs and discuss the obscured fraction of the SFR in each GRB host individually. The implications of these results for dust obscuration in GRB hosts are discussed in Section 3.4 and the key conclusions are summarized in Section 3.5.

Table 3.1: Summary of the VLA observations

| GRB[a] | $z$ | R.A. | Dec. | Total $t_{int}$ (min) | $3\sigma$ Limit ($\mu$Jy) | Beam size ($''$) | Flux/ bandpass | Complex gain |
|---|---|---|---|---|---|---|---|---|
| 021004 | 2.323 | 00:26:54.68 | +18:55:41.6 | 270.5 | 3.0 | 3.7 × 4.5 | 3C48 | J0010+1724 |
| 080310 | 2.427 | 14:40:13.80 | −00:10:30.7 | 402 | 6 | 3.2 × 4.0 | 3C286 | J1445+0958 |
| 080810 | 3.35 | 23:47:10.49 | +00:19:11.5 | 343 | 3.8 | 3.7 × 4.9 | 3C48 | J2323-0317 |
| 121024A | 2.298 | 04:41:53.30 | −12:17:26.6 | 123 | 12 | 3.9 × 5.6 | 3C138 | J0437-1844 |

[a]All the observations were performed in the C-band ($4-8$ GHz) in C array configuration of the VLA.

## 3.2 Sample and observations

### 3.2.1 Sample Selection

The CGM-GRB sample is a sample of 27 $z > 2$ GRBs with high-resolution (resolving power $R > 6000$) and high signal-to-noise ratio (median SNR $\sim 10$) afterglow spectra [Gatkine et al., 2019a]. None of these GRBs have previously reported late-time radio observations. A subset of these objects is selected by imposing various criteria. Only GRBs that occurred at least six years ago are considered to ensure that the radio flux contribution from the afterglow is minimal [Perley et al., 2015]. From the remaining 17, only GRB hosts with existing $M_\star$ measurements and $M_\star > 10^{9.5}$ $M_\odot$ are selected since their UV-based SFR is expected to be most affected by dust obscuration. This resulted in a set of four GRB hosts: GRB 021004, GRB 080310, GRB 080810, and GRB 121024A. Further, the VLA observations of GRB 080810 reported here (at $z = 3.35$) make it the the highest-redshift GRB with a late-time radio observation of the host. Table 3.1 summarizes the sample and its key properties.

### 3.2.2 VLA Observations

We performed the radio observations using the fully upgraded Karl G. Jansky Very Large array (VLA) using C-band receivers spanning $4 - 8$ GHz and with a central frequency of 6 GHz. We used 3-bit samplers to utilize the entire 4096 MHz bandwidth of the C band to maximize the continuum sensitivity. The dual polarization setup was used. The observations were conducted in the C array configuration during the months of December 2018 to January 2019 (program VLA 18B-312, PI: Gatkine). The integration time for each GRB host is listed in Table 3.1 (typical $\sim$ 4.5 hours). A nearby complex gain (amplitude and phase) calibrator was observed every $30 - 40$ minutes during any scheduling block and a standard flux calibrator was observed every hour. The 3-$\sigma$ rms and the synthesized beam size for each source are listed in Table 3.1.

The data reduction was carried out using the Common Astronomy Software Applications package (CASA) version 5.5.0 [Emonts et al., 2019]. The standard `CASA` pipeline was used to flag and calibrate the observations. Imaging and deconvolution was performed using the `tclean` function in `CASA`. Natural weighting was employed while cleaning the measurement sets to maximize the continuum sensitivity. In the case of GRB 121024A, additional flagging was performed to clip the outlier visibilities and channels heavily affected with radio frequency interference. Further, self-calibration was performed to clean the image around a bright source at a separation of $6'$, a robust weighting was employed, and a multi-term multi-frequency synthesis (mtmfs, with 2 terms) deconvolver was used to account

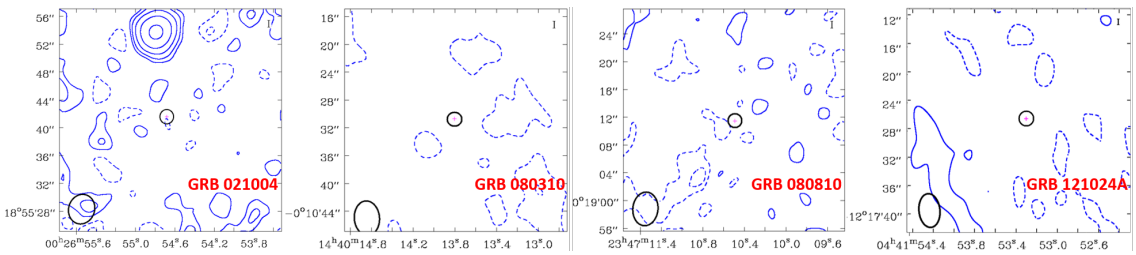


Figure 3.1: Contour maps of the radio flux density in 30″ × 30″ fields centered on the four GRBs of our sample. The location of the GRB and 2″ error circle are marked as red crosses and black circles, respectively. The synthesized beam is shown in the bottom left corner. The contours are marked as -12, -6, -3, -1.5, 1.5, 3, 6, 12 $\times\sigma$ with negative values marked as dotted contours. None of the GRB hosts are detected at the $3\sigma$ level.

for spectral index gradient in the much brighter contaminating source.

The synthesized beam size for C-configuration observations is significantly coarser (beam size $\sim 4''$) than the angular extent of the galaxy (1 kpc translates to $\sim 0.1''$ at $z \sim 2.5$). Therefore, the host galaxies are unresolved and can be treated as point sources here. The $1\sigma$ flux-density level was derived by sampling a blank region spanning $\sim$100 $\times$ synthesized beam area around the target.

The maps for GRB 021004 and GRB 080810 have rms sensitivities close to that predicted by the VLA noise calculator. However, GRB 121024A and GRB 080310 had particularly bright sources near the half-power response of the primary beam. At this location in the primary beam, the amplitude response is variable owing to antenna pointing errors, which result in amplitude gain errors in the visibilities that are a function of field position in addition to antenna, frequency, and time. Standard self-calibration does not work well if there are position-dependent errors; antenna pointing errors limited the dynamic range of the maps for GRB 080310 and especially GRB 121024A, and consequently our sensitivity for these objects.

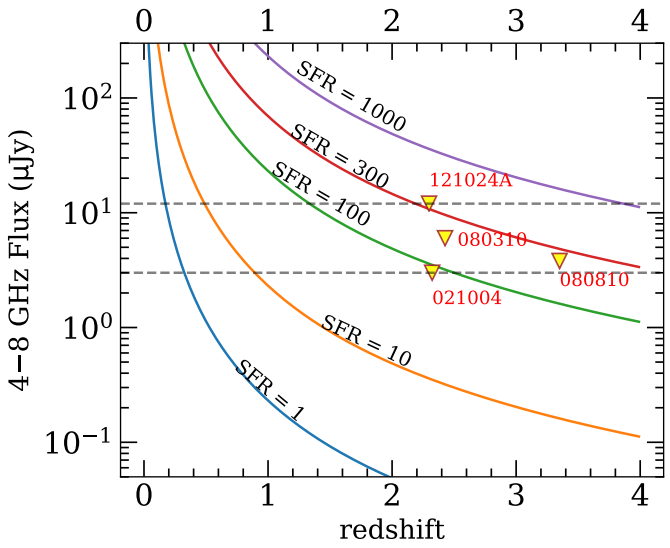


Figure 3.2: Curves showing the radio flux density averaged over $4-8$ GHz for various star formation rates ($M_\odot$/yr) over a redshift range $z \sim 0-4$ using a spectral index of $\alpha = 0.7$. The $3\sigma$ upper limits of various GRBs are shown with downward triangles. The horizontal dotted lines are drawn to guide the eye.

## 3.3 Radio- and UV-based SFR

### 3.3.1 Radio-based SFR

As described in Section 4.1, the radio continuum at frequencies below a few $\times$ 10 GHz traces the total (i.e. dust-obscured + dust-unobscured) star formation activity in the last 100 Myr [Condon, 1992]. The radio-far-IR relation for star-forming galaxies which quantifies the radio-SFR relation is shown to hold true at intermediate and high redshifts [Sargent et al., 2010]. On the other hand, the UV/optical light (including the emission lines) primarily probes the portion of the SFR that is not significantly obscured by dust (i.e. dust-unobscured SFR) even with dust attenuation included in the modeling (see the example of GRB 100621A in [Stanway et al., 2014]). Thus, a significant discrepancy between the UV-based and radio-based

SFR measures would imply the presence of substantial dust obscuration within the galaxy. In the discussion below, we use the following naming system:

$\mathrm{SFR_{total}}$: Radio-based total SFR

$\mathrm{SFR_{unobscured}}$: UV-based unobscured SFR (without dust correction),

$\mathrm{SFR_{obscured}}$: the portion of SFR that is obscured due to the dust ($= \mathrm{SFR_{total}} - \mathrm{SFR_{unobscured}}$).

Here, we observe the GRB hosts in C-band ($4-8$ GHz) at $z \sim 2-3.5$, thus we are sensitive to $\nu_{rest} = 25 \pm 10$ GHz. The rest-frame radio luminosity is produced by three mechanisms: non-thermal synchrotron emission ($\epsilon_1$), free-free emission ($\epsilon_2$), and thermal emission from dust ($\epsilon_3$), as shown in [Yun and Carilli, 2002]. The thermal dust component is insignificant ($< 1\%$) at the frequencies of interest. The radio-SFR relation for star-forming galaxies [Yun and Carilli, 2002] is thus given by:

$$S(\nu_{obs}) \quad = \quad \Big(\epsilon_1 + \epsilon_2 + \epsilon_3\Big) \times \frac{(1+z)SFR}{D_L^2} \tag{3.1}$$

where,

$\epsilon_1 = 25 f_{nth} \nu_0^{-\alpha}$

$\epsilon_2 = 0.71 \nu_0^{-0.1}$

$\epsilon_3 = 1.3 \times 10^{-6} \frac{\nu_0^3 [1 - e^{-(\nu_0/2000)^\beta}]}{e^{0.048\nu_0/T_d - 1}}$.

Here, the symbols $\epsilon_1$, $\epsilon_2$, and $\epsilon_3$ represent the contributions from non-thermal synchrotron, free-free, and dust thermal emission respectively. $D_L$ is luminosity

distance in Mpc, SFR is star formation rate in $M_{\odot}yr^{-1}$, $\nu_0$ is rest-frame frequency in GHz, $f_{nth}$ is the scaling factor, $\alpha$ is the synchrotron spectral index, $T_d$ is the dust temperature in K, and $\beta$ is the dust emissivity. For the typical values of $T_d$ ($\sim$ 60 K) and $\beta$ (1.35), the dust emission is insignificant for $\nu_{\rm rest} \sim 25$ GHz. hence, we neglect this term. The non-thermal synchrotron emission is the most dominant contributor in the given frequency range. Since we do not have a robust measurement of the actual spectral index for any of our objects, we assume a canonical average value of $\alpha = -0.7$. Past literature has used values ranging from $-0.6$ to $-0.75$ [Hatsukade et al., 2012, Perley et al., 2013, Perley et al., 2015, Stanway et al., 2014, Greiner et al., 2016]. This range of $\alpha$ affects the radio luminosity by 25%. This equation assumes a Salpeter initial mass function (IMF). Due to various assumptions in the calibration of radio-based SFRs, it is subject to a systematic uncertainty of about a factor of $\sim$2 [Yun and Carilli, 2002, Bell, 2003, Murphy et al., 2011].

Figure 3.2 shows the observed flux densities averaged over $4-8$ GHz for various star formation rates as a function of redshift and the respective $3\sigma$ upper limits of our targets. The UV- and radio-derived SFRs for our four targets are summarized in Table 3.2 along with the stellar masses and ratios of radio-based (total) and UV-based (dust-unobscured) SFRs.

### 3.3.2 Late-time afterglow emission

The GRBs have long-lived radio afterglows. Therefore, any estimates of SFR using the radio emission can only be made after the afterglow has faded considerably

to ensure minimal/no contamination due to the afterglow. We compiled the past early-time radio observations of the afterglows of our target GRBs available in the literature and extrapolated the afterglow decay using a canonical long GRB radio light curve model (forward shock model) with a $t^{-1}$ decay [Chandra and Frail, 2012] as follows:

$$f(t) = \begin{cases} F_m t_m^{-1/2} t^{1/2}, & \text{if } t < t_m. \\ F_m t_m t^{-1}, & \text{if } t > t_m \ . \end{cases} \tag{3.2}$$

Here, $F_m$ is the peak flux density at a given frequency and $t_m$ is the time of the peak in that frequency. For this extrapolation, we used a conservative approach. We use the latest flux density measurement in C-band (if available) as the peak flux density. If it is not available (eg: GRB 121024A), we extrapolate the flux density using the standard GRB radio afterglow model described in [Chandra and Frail, 2012]. The typical values of $t_m$ range between rest-frame 3 and 6 days at a rest-frame frequency of $\sim 25$ GHz (which we probe since our targets are at $z \sim 2-3.5$). We translate this $t_m$ to the observer frame for each GRB and plot the radio afterglow evolution in Figure 3.3. The three lines show the decay with $t_m = 3$, 4.5, and 6 days (in the rest frame). No early-time radio observations are available for GRB 080310. The conservative approach used here gives the upper limit of radio flux density due to the afterglow and further shows that the late-time radio fluxes for our observations are dominated by the host galaxy and are not likely to be contaminated by the afterglow.

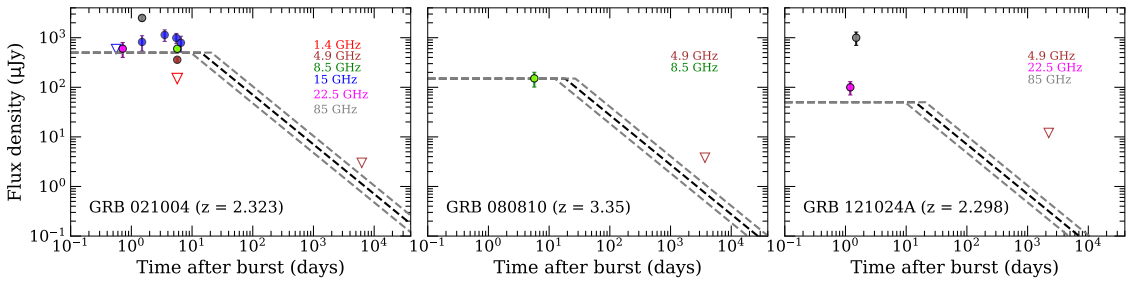


Figure 3.3: Radio evolution of the afterglows of GRB 021004, GRB 080810, and GRB 121024A, extrapolated using the canonical afterglow evolution model described in Section 3.3.1.

### 3.3.3 SFR in each GRB host

We summarize the UV-derived and radio-derived SFRs for the four GRBs in the following subsections. Note that the $SFR_{unobscured}$ signifies the uncorrected, UV-based SFR derived from the rest-frame UV luminosity. Using the VLA observations, we obtain an estimate of the total SFR ($SFR_{total}$), independent of assumptions on the dust extinction (in the line of sight or otherwise).

We also compare the observed ratio $SFR_{total}/SFR_{unobscured}$ for our GRB hosts with the same ratio for star-forming galaxies with a similar stellar mass at a redshift range $z \sim 2 - 2.5$, as derived from the CANDELS survey [Whitaker et al., 2017] and summarize this in Figure 3.4.

#### 3.3.3.1 GRB 021004

GRB 021004 is one of the best studied GRBs from the gamma-rays to radio wavelengths. The optical afterglow was detected 3.2 minutes after the prompt high-energy emission and was followed up extensively [Fynbo et al., 2005]. The extremely

blue host galaxy of GRB 021004 was identified and studied through late-time imaging in the rest-frame UV and optical bands. HST ACS imaging in the F606W band revealed that the host galaxy has a very compact core with a half-light radius of only 0.4 kpc (at $z = 2.323$). Based on HST ACS imaging in F606W filter (rest-frame UV), the impact parameter of the afterglow position is only 0.015″, corresponding to a distance of 119 pc, which is one of the smallest for long GRBs [Fynbo et al., 2005, Fruchter et al., 2006, Blanchard et al., 2016]. While this could be a chance projection, it is likely that the GRB progenitor could be associated with a circumnuclear starburst. We note a caveat here that given the typical irregular morphologies of low-mass high-z galaxies, we cannot rule out the small offset being due to the presence of a bright star-forming knot in the rest-frame UV. The line-of-sight extinction $A_V$ is 0.20 ± 0.02 mag (using the SMC extinction law) as derived after 1 week of afterglow decay [Fynbo et al., 2005]. The Ly$\alpha$-derived neutral hydrogen column density ($N_{HI}$) along the line of sight is modest ($\sim 10^{19}$ cm$^{-2}$; [Prochaska et al., 2008c]).

[Castro-Tirado et al., 2010] derived the host SFR of 40 $M_\odot yr^{-1}$ (without any dust correction) by attributing all of the H$\alpha$ emission to star formation. Given the small $A_V$, the dust correction was assumed to be minimal from the afterglow SED. On the other hand, [Jakobsson et al., 2005] have estimated a lower limit of SFR as 10.6 $M_\odot yr^{-1}$ by converting the Ly$\alpha$ flux to SFR [Kennicutt, 1998] and assuming a 100% Ly$\alpha$ escape fraction.

We derive a 3$\sigma$ upper limit on the C-band flux density of 3.0 $\mu$Jy, corresponding to a radio SFR limit of 85 $M_\odot yr^{-1}$ at $z \sim 2.323$. This result is consistent with the low

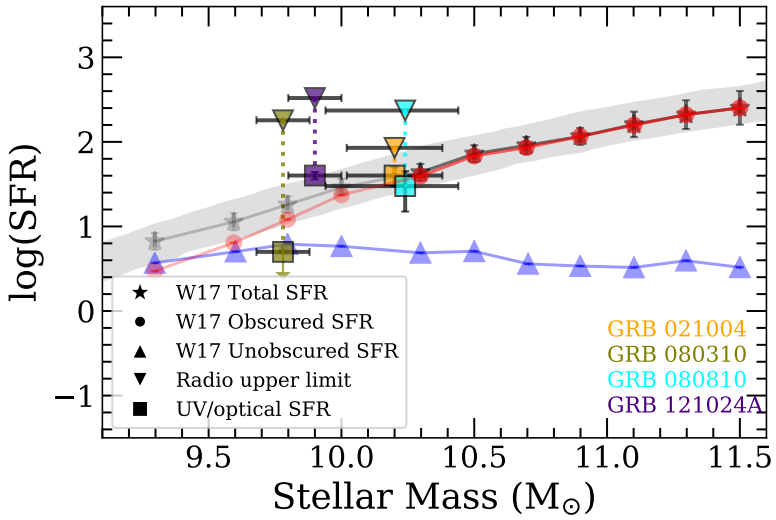


Figure 3.4: The SFR $- M_\star$ relation decomposed into total (black star), obscured (red circle), and unobscured components (blue triangle) of the star formation rate for the galaxies in the CANDELS survey at $z \sim 2 - 2.5$ [Whitaker et al., 2017]. The gray band corresponds to the typical 0.3 dex width of the observed relation. Individual GRBs in our sample are shown in various colors with their UV-derived SFR (tracing the dust-unobscured SFR) and the radio-derived SFR (tracing the total SFR).

$A_V$ derived from the optical-NIR SED and therefore suggests that the host galaxy as a whole is not significantly affected by dust. This observation identifies a galaxy that is able to sustain a SFR of $\sim 40$ $M_\odot yr^{-1}$ at $z \sim 2.3$ without significant dust obscuration. Using the non-extinction-corrected H$\alpha$ emission, we get $SFR_{unobscured} = 40$ $M_\odot yr^{-1}$, so the ratio $SFR_{total}/SFR_{unobscured}$ is $< 2.1$ for this $M_* > 10^{10} M_\odot$ galaxy. In contrast, the corresponding ratio derived for the main sequence of star-forming galaxies at $z \sim 2.5$ from [Whitaker et al., 2017] is $\sim 6$.

Given the small impact parameter of the afterglow (119 pc) from the centroid of the bright star-forming region, the apparent lack of significant dust extinction along the line of sight to the GRB, and in the host galaxy as a whole from the radio observations, is puzzling.

#### 3.3.3.2 GRB 080310

The afterglow of GRB 080310 was detected 1.5 minutes after the prompt high-energy emission and was followed up extensively (see [Littlejohns et al., 2012] for a full discussion). The redshift of this GRB is 2.427 [Prochaska et al., 2008a, Vreeswijk et al., 2008]. [Perley et al., 2008] estimated a low line-of-sight extinction $A_V$ of 0.10 $\pm$ 0.05 mag. using an SMC-like extinction law (at an average time of $t_0$ + 1750 s). The line-of-sight $N_{HI}$ is modest ($\sim 10^{18.8}$ cm$^{-2}$).

The late-time host galaxy imaging using the Low Resolution Imaging Spectrometer (LRIS) on the Keck-I telescope yielded a non-detection with a g-band limiting magnitude of 27.0 [Perley et al., 2009]. We estimate a SFR upper limit of 4.5 $M_\odot yr^{-1}$ using the UV luminosity-SFR relation for GRB host galaxies described in [Savaglio et al., 2009]. [Perley et al., 2016b] estimated $\log(M_*/M_\odot) = 9.8 \pm 0.1$ using *Spitzer* 3.6 $\mu m$ imaging. However, we caution the reader of the possibility that the *Spitzer* 3.6 $\mu m$ flux is contaminated by the diffraction spike from a nearby star despite careful modeling and subtraction of the spike [Perley et al., 2016b].

The VLA observations constrain the SFR to less than 180 $M_\odot yr^{-1}$ (3-$\sigma$ upper limit). However, this limit is not sufficiently deep to constrain the dust obscuration in the host galaxy of GRB 080310.

#### 3.3.3.3 GRB 080810

This is the highest-redshift GRB in our sample at $z = 3.35$. The afterglow of GRB 080810 was detected 80 seconds after the prompt emission by the X-ray

telescope (XRT; [Burrows et al., 2005]) and UV-optical telescope (UVOT; [Roming et al., 2005]) on board the Neil Gehrels Swift Observatory [Gehrels et al., 2004]. [Prochaska et al., 2008a] obtained the optical spectra of the afterglow using the Keck HIRES spectrograph starting 37 minutes after the trigger and derived a redshift of 3.35. The Ly$\alpha$-derived line-of-sight $N_{HI}$ is small ($\sim 10^{17.5}$ cm$^{-2}$). We refer the readers to [Page et al., 2009] for a discussion of the extensive multi-wavelength follow-up of this GRB.

Extensive late-time ground-based photometry and spectroscopy of the host galaxy of GRB 080810 revealed an extended structure with a bright compact region (see [Wiseman et al., 2017a] for more details). Further, a strong detection of redshifted Ly$\alpha$ emission at a redshift of 3.36 confirmed the association of the GRB and the detected host galaxy [Wiseman et al., 2017a]. They estimate a modest host extinction of $A_V \sim 0.4$ mag. from SED fitting. [Greiner et al., 2015] convert the extinction-corrected UV luminosity to SFR (using the $L_{UV} - SFR$ relation in [Duncan et al., 2014] and $A_{1600} \sim 1.3$ mag.) to obtain SFR $\sim 100$ M$_\odot$yr$^{-1}$, which is further corroborated by SED fitting [Wiseman et al., 2017a]. The uncorrected SFR is $\sim 30$ M$_\odot$yr$^{-1}$. The stellar mass, derived from the *Spitzer* 3.6 $\mu m$ photometry, is $\log(M_*/M_\odot) = 10.2 \pm 0.1$ [Perley et al., 2016c].

Here we report the first ever deep late-time radio observation of a GRB with a spectroscopic redshift $z > 3.1$. We derive a 3-$\sigma$ upper limit on the C-band flux density of 3.8 $\mu$Jy, corresponding to a radio-based SFR upper limit of 235 M$_\odot$ yr$^{-1}$ at $z \sim 3.35$. The dust-corrected SFR from the UV SED is therefore consistent with the total SFR limit derived from the radio observations. This further implies that

the modest $A_V$ estimated from the UV SED fitting reasonably takes into account the dust correction.

Using the uncorrected UV SFR, we derive a ratio $\mathrm{SFR_{total}/SFR_{unobscured}} < 7$ for this $\mathrm{M_*} > 10^{10}$ $\mathrm{M_\odot}$ galaxy. This is consistent with the corresponding ratio derived for the main sequence of star-forming galaxies at $z \sim 2-2.5$ from [Whitaker et al., 2017], which gives $\mathrm{SFR_{total}/SFR_{unobscured}} \sim 6$. Here, we extrapolate the non-evolution of this ratio from $z \sim 2.5$ to 3.3 for the star-forming galaxies on the main sequence at a given $\mathrm{M_*}$, as presented in [Whitaker et al., 2017].

#### 3.3.3.4 GRB 121024A

The afterglow of GRB 121024A was followed up 93 seconds after the prompt emission by the X-ray telescope (XRT; [Burrows et al., 2005]) on board the Neil Gehrels Swift Observatory [Gehrels et al., 2004]. [Tanvir et al., 2012] obtained the optical/NIR spectra of the afterglow using the X-shooter spectrograph on the Very Large Telescope (VLT) and determined a redshift of 2.298. The line-of-sight $\mathrm{N_{HI}}$ of $10^{21.5}$ $\mathrm{cm^{-2}}$ indicates that this is a damped Ly$\alpha$ system. We refer the readers to [Friis et al., 2015] for a detailed summary of the extensive multi-wavelength follow-up of this GRB.

Various emission lines including H$\alpha$, H$\beta$, [O II] $\lambda\lambda$3727, 3729 doublet, [N II] $\lambda$6583, and [O III] $\lambda\lambda$4959, 5007 were detected in the X-shooter NIR spectrum of the afterglow. Extensive optical and NIR photometry of the host galaxy was obtained using VLT/HAWK-I, NOT, and GTC (for details, see [Friis et al., 2015]). The

Table 3.2: Summary of GRB host properties

| GRB[a] | $z$ | $\log(N_{HI})$ [a] ($cm^2$) | $M_*$ ($M_\odot$) | $SFR_{UV}$ ($M_\odot$ $yr^{-1}$) | $SFR_{Radio}$ [b] ($M_\odot$ $yr^{-1}$) | $\frac{SFR_{total}}{SFR_{UV}}$ |
|---|---|---|---|---|---|---|
| 021004 | 2.323 | $19.00 \pm 0.2$ [c] | $10.2 \pm 0.18$ [g] | $40 \pm 10$ | $< 85$ | $< 2.1$ |
| 080310 | 2.427 | $18.80 \pm 0.1$ [d] | $9.78 \pm 0.2$ [h] | $< 5$ | $< 180$ | – |
| 080810 | 3.35 | $17.5 \pm 0.15$ [e] | $10.24 \pm 0.1$ [h] | $30 \pm 15$ | $< 235$ | $< 7.8$ |
| 121024A | 2.298 | $21.5 \pm 0.1$ [f] | $9.9^{+0.2}_{-0.3}$ [f] | $40 \pm 4$ | $< 330$ | $< 8.3$ |

[a]Ly$\alpha$-derived $N_{HI}$ [b]$3\sigma$ upper limit, [c][Prochaska et al., 2008c], [d][Fox et al., 2008], [e][Page et al., 2009], [f][Friis et al., 2015], [g][Savaglio et al., 2009], [h][Perley et al., 2016b]

stellar population synthesis modelling of the host yielded a modest extinction $A_V$ of $0.15 \pm 0.15$ mag. and $\log(M_*/M_\odot) = 9.9^{+0.2}_{-0.3}$.

[Friis et al., 2015] estimate the SFR from the extinction-corrected H$\alpha$ and [O II] fluxes as $42 \pm 11$ and $53 \pm 15$ $M_\odot$ $yr^{-1}$ using conversion factors from [Kennicutt, 1998]. However, note that the extinction correction to the SFR is small ($\sim 15\%$). They further corroborate this SFR by stellar population synthesis modelling.

The 3-$\sigma$ upper limit on the C-band flux density of GRB 121024A is 18 $\mu$Jy. The relatively higher background is due to a bright source at $6'$ angular separation. Using the VLA observations, we obtain a 3-$\sigma$ upper limit of the total SFR as 500 $M_\odot yr^{-1}$. However, this limit is not sufficiently deep to constrain the dust obscuration in the host galaxy of GRB 121024A. The limiting $SFR_{total}/SFR_{unobscured} < 12.5$ is consistent with the corresponding expected ratio ($\sim 5$) from [Whitaker et al., 2017] for a star-forming galaxy of this stellar mass on the main sequence at $z \sim 2 - 2.5$.

## 3.4 Discussion

Our observations have targeted massive ($M_* > 10^{9.5}$ $M_\odot$) high-z GRBs ($z \sim 2-3.5$) with high-resolution and high SNR rest-frame UV afterglow spectra (i.e. a rest-frame UV-bright afterglow). Previous studies have observed the host galaxies of so-called 'dark' GRBs (rest-frame UV/optically dark afterglows) in radio [Perley and Perley, 2013, Perley et al., 2015, Greiner et al., 2016]. These observations are summarized in Figure 3.5. However, we caution the readers that in Figure 3.5, the UV-based SFR from the literature are dust-corrected. In the future, a combined sample of the radio observations for the hosts of GRBs with UV-bright afterglows and UV-dark afterglows can help address the question as to whether GRB hosts are biased against the highly dust-obscured starburst population at high redshifts. This question has strong implications for the use of GRBs as SFR tracers at high redshift. Deeper radio limits (comparable to this paper) for the dark GRB hosts will be needed to address this question in the future.

The radio flux limits in our observations are a least 3 times deeper than the previous limits on the SFR at $z > 2$ [Perley et al., 2015], and thus provide tighter constraints on whether GRB hosts at these redshifts are more likely to be dusty starburst galaxies or not. Out of the four GRBs in this sample, we have well-defined upper limits of the $SFR_{Total}/SFR_{UV}$ for three of them (see Table 3.2). We compare these limits with the observed distribution of the dust-obscuration ratios at high redshifts from the CANDELS survey in [Whitaker et al., 2017] (hereafter W17; see Figure 2 therein; we compare against the inverse of $1 - f_{obscured}$).

The upper limits of $SFR_{Total}/SFR_{UV}$ for the host galaxies of GRB 080810 ($< 7.8$) and 121024A ($< 8.3$) are consistent with this distribution. We note here that the upper limits are derived using 3-$\sigma$ radio flux limits. On the other hand, for GRB 021004, the $SFR_{Total}/SFR_{UV} \lesssim 2$. Only 1% of the W17 sample with the corresponding stellar mass ( $\log(M_*/M_\odot) = 10.2 \pm 0.2$) falls in the $SFR_{Total}/SFR_{UV} \lesssim 2$ regime. Hence, GRB 021004 is inconsistent with being drawn from the W17 distribution. The ratio for GRB 080310 is unconstrained due to UV non-detection.

Given that 50% of our sample limits are consistent with the results of W17 (using 3-$\sigma$ limits), 25% of the sample is inconsistent with W17, and 25% is unconstrained, we can only draw a coarse conclusion. The deep radio limits suggest that the overall star formation activity in these GRB hosts is not heavily obscured by dust (i.e. $SFR_{Total}/SFR_{UV} < 10$, unlike LIRGs; [Bouwens et al., 2009, Howell et al., 2010, Casey et al., 2014]), and possibly slightly less obscured than the star-forming main sequence population at $z \sim 2.5$ [Speagle et al., 2014].

Particularly, GRB 021004 provides a striking example of lack of significant dust obscuration in the central region of a star-forming galaxy at $z > 2$, given that the separation of the GRB from the galaxy centroid is only 119 pc [Fynbo et al., 2005, Fruchter et al., 2006]. The sightline extinction, derived from the afterglow is also small ($A_V = 0.2 \pm 0.02$ mag.). Two possible scenarios can explain these results: a) the GRB occurred in a locally dusty cloud but globally, the host galaxy lacks significant amount of dust. The low sightline extinction would then imply that the burst occurred along a clear sightline within its star-forming cloud. b) the GRB occurred in a star-forming region which has cleared the dust from past star

formation and the overall galaxy also lacks significant amount of dust. The GRB sightline would then be a representative sightline.

The results from our limited sample suggest that the GRBs with UV-bright afterglows (i.e. optically thin sighltines in UV) at $z \sim 2 - 3.5$ are likely to be star-forming galaxies with SFRs moderately higher ($< 5\times$) than the star-forming main sequence [Speagle et al., 2014], but without significant dust obscuration in their star-forming regions.

However, it is likely that this result only applies to the GRBs with UV-bright afterglows due to our selection criteria. At the same time, the dust extinction along a sightline may not necessarily represent the dust obscuration on a galaxy scale, for optically thin as well as optically thick sightlines (in UV). More radio observations of GRB hosts at $z > 2$ with a depth at least $2 \times \mathrm{SFR_{UV}}$ are necessary to confirm this hypothesis. This is required for GRBs with UV-bright afterglows as well as with UV/optically dark afterglows to rule out any selection bias based on the line-of-sight extinction.

## 3.5 Summary

If the GRBs are unbiased tracers of star formation at high redshifts ($z > 2$), then we should expect that a large fraction of GRB hosts are highly dust-obscured starbursting galaxies, since these are well known to be major contributors to the cosmic star formation at high redshifts. The goal of our study was to investigate the galaxy-scale dust obscuration in the GRB hosts with optically thin sightlines in the

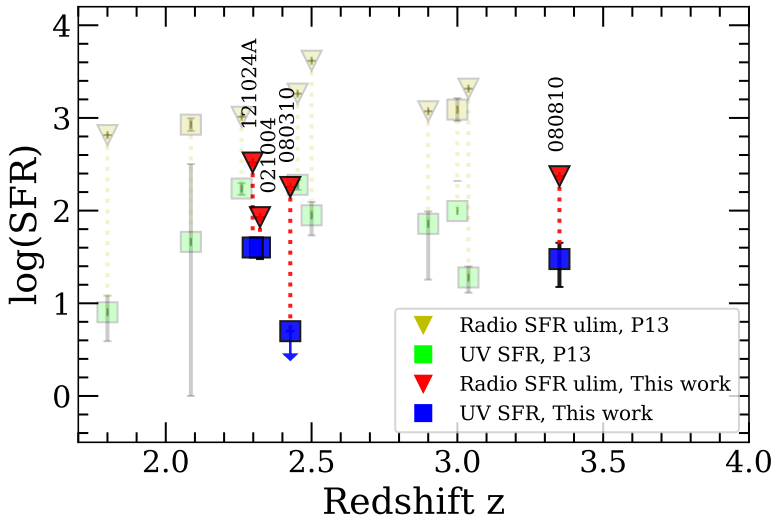


Figure 3.5: The comparison of the radio-derived SFR (tracing the total SFR) and UV-derived SFR (tracing the dust-unobscured SFR) as a function of redshift for the four GRBs presented here (in the foreground), and GRBs in the literature in the background. P13: [Perley et al., 2013] and one data point (GRB 060814) from [Greiner et al., 2016].

UV. We conducted deep radio observations of a subset of four massive ($M_* > 10^{9.5}$ $M_\odot$) GRB hosts at $z > 2$ for which high signal-to-noise (typical SNR $\sim 10$) and high-resolution ($\Delta v < 50$ km s$^{-1}$) rest-frame UV spectra of the afterglow are available. The selected targets are GRB 021004, GRB 080310, GRB 080810, and GRB 121024A. We measured the total SFR (= obscured + unobscured SFR) of the hosts using VLA C-band observations and compared them against the unobscured component of the SFR, measured from the rest-frame UV luminosity. The depth of the radio observations in this study has allowed us to put tight constraints on the ratio of the total-to-unobscured SFRs ($SFR_{total}/SFR_{unobscured}$).

We find that the radio-based star formation rates are in general not substantially higher than those obtained from the optical/UV measurements. Thus, the fraction of total star formation that is obscured by dust ($SFR_{obscured}/SFR_{total}$) in

most of the GRB hosts, even at $z > 2$, is less than 90%, unlike LIRGs or dusty starburst galaxies. Particularly, for the well-constrained case of GRB 021004 ($z = 2.323$), we find that the upper limit of the radio-based 'total SFR' is less than twice the UV-based 'unobscured SFR' of the GRB hosts (thus, $\mathrm{SFR_{obscured}/SFR_{total}} < 50\%$). Our results suggest that the dust obscuration in the star-forming regions of these galaxies is small, and sometimes (e.g. for GRB 021004) even smaller than the dust obscuration seen in typical main-sequence star-forming galaxies at these redshifts. We reiterate that the results obtained here may only apply to GRBs with UV-bright afterglows.

The present upper limits on the radio-based SFRs prevent us from determining where the GRB host population lies with respect to the main sequence of star-forming galaxies at $z > 2$. Deeper radio observations to a depth of $2 \times \mathrm{SFR_{UV}}$ are required to answer this question. Currently, we are limited by the sensitivity of the radio instrumentation (eg: JVLA) to reach these deep limits. They will be achievable with the higher sensitivity of upcoming radio telescope arrays such as ng-VLA and SKA1-MID.

# Chapter 4: Outflow-Galaxy Relations at $z \sim 2 - 6$

*In this chapter, we will explore how the outflows seen in the GRB hosts in Chapter 2 at high redshifts relate to the properties of those GRB hosts.*

## 4.1 Introduction

Galactic inflows and outflows shape the evolution of galaxies as well as enrich the circumgalactic medium (CGM) and intergalactic medium (IGM). The gas inflows fuel star formation while stellar winds, supernova (SN) explosions, and active galactic nuclei inject energy and metal-enriched matter (as well as entrained cold gas) at large distances into the interstellar medium (ISM) and CGM. The recycling flows from the CGM bring back the metal-enriched gas to refuel the star formation [Christensen et al., 2016]. At the same time, removal of cold gas from the ISM can quench the star formation activity. Thus, galactic outflows regulate stellar buildup and are an important piece of the galactic feedback puzzle. AGN-driven outflows are thought to be the dominant feedback in massive galaxies [Veilleux et al., 2005, Fabian, 2012, Heckman and Best, 2014, King and Pounds, 2015, Nelson et al., 2019] whereas SN-driven outflows are thought to be more important in low-mass, star-forming galaxies [Sharma and Nath, 2012].

Supernova-driven outflows at high-redshift are important for the early enrichment of the CGM and IGM [Tumlinson et al., 2017, Veilleux et al., 2020]. The low-mass star forming galaxies are of particular interest in this context since their outflows are most likely to escape their shallower potential wells. The relationship between the outflows and their host galaxies in the early universe holds the key to tune the models of galactic feedback and understand the history of galaxy growth and cosmic metal enrichment.

Observations at high redshift ($z > 2$) using various techniques have shown the presence of ubiquitous outflows in star-forming galaxies. The prominent techniques include down-the-barrel absorption-line studies [Frye et al., 2002, Shapley et al., 2003, Sugahara et al., 2017, Du et al., 2018, Rudie et al., 2019], outflows at larger radii using background quasar or galaxy sightlines [Steidel et al., 2010, Lehner et al., 2014, Turner et al., 2014, Rudie et al., 2019], quasar-quasar pairings [Hennawi et al., 2006, Prochaska et al., 2014], observing lensed galaxy spectra [Rigby et al., 2018], spatially-resolved spectroscopy in optical or radio [Harrison et al., 2012, Swinbank et al., 2015, Nielsen et al., 2020, Pizzati et al., 2020], and GRB afterglow sightlines [Fox et al., 2008, Gatkine et al., 2019a]. Galactic as well as cosmological zoom-in simulations provide the framework to understand the outflow mechanisms (for instance, [Hirschmann et al., 2013, Shen et al., 2013, Muratov et al., 2015, Nelson et al., 2019, Mitchell et al., 2020]). The high-$z$ outflow-galaxy relation and its evolution with redshift has recently been studied in [Sugahara et al., 2017, Sugahara et al., 2019].

However, the outflow-galaxy relation in low-mass galaxies in the early universe

remains poorly understood due to observational challenges. Two key challenges are: determining the redshift of the galaxy (in case of background QSO/galaxy sightlines) and obtaining high quality absorption spectra of these faint galaxies (for down-the-barrel technique). Apart from this, reliably removing the continuum spectrum of the background object can be a challenge.

Use of GRB sightlines to probe the outflows and CGM of its host galaxy offers a promising solution to these problems. In [Gatkine et al., 2019a], we described this method in detail. The main idea here is to use the bright GRB afterglow to probe the kinematics/outflows in the CGM of its host galaxy. GRB hosts at $z > 2$ are typically low-mass galaxies ($\log(M_*/M_\odot) < 10.5$), which makes them ideally suited for exploring the low-mass outflows which are difficult to probe using other techniques. The key advantages include: 1) clear identification of the host-galaxy redshift, 2) high signal-to-noise ratio (SNR) and high-resolution spectra due to the bright GRB afterglow, and 3) the featureless continuum of the GRB afterglow eliminates the problem of continuum subtraction.

In this paper, we use the CGM-GRB sample compiled in [Gatkine et al., 2019a] to explore the correlations between outflow and galaxy properties. The CGM-GRB sample consists of 27 GRBs at $z \sim 2-6$ with high SNR (median SNR $\sim 10$) and high-resolution ($\delta v < 50$ km s$^{-1}$) spectra. Multi-component Voigt-profiles were fit to the absorption spectra of various high- and low-ion species (including C IV, Si IV, Si II, Fe II, and O VI). The CGM kinematics of this sample were studied in [Gatkine et al., 2019a]. In this paper, we report the observations of their host galaxies in the optical and near-IR to estimate their star formation rate (SFR) and stellar mass

($M_*$). These observations and their analyses are described in Section 4.2. We then discuss the techniques used for visualizing and inferring correlations in Section 4.3. The key correlations between outflow properties and galaxy properties such as $M_*$, SFR, specific star formation rate (sSFR = SFR/$M_*$), and halo mass are detailed in Section 4.4. Finally, the implications of our results are discussed in Section 4.5.

Throughout this paper, we use the following model of cosmology: $H_0 = 70$ km s$^{-1}$Mpc$^{-1}$, $\Omega_M = 0.3$, $\Omega_\Lambda = 0.7$

## 4.2 Observations and Methods

As described earlier, we measure the galaxy properties in the CGM-GRB sample. The sample is selected strictly on the criterion of availability of a high-resolution ($\delta v < 50$ km s$^{-1}$) and high-SNR (SNR $> 5$) afterglow spectrum. No cuts are made to the sample based on galaxy properties. The redshift distribution of the sample is shown in the first panel of Fig. 4.2.

### 4.2.1 Optical Photometry

We performed optical photometry of previously unpublished or unobserved GRB hosts in the CGM-GRB sample. We observed GRB hosts using the 4.3-meter Lowell Discovery Telescope (LDT). We also obtained deep archival imaging of two GRB hosts using the FORS instrument on the Very Large Telescope (VLT) and one each using HST WFC3 (program ID 15644), the Kilo-Degree Survey (KiDS) [Kuijken et al., 2019], and PanSTARSS survey [Flewelling et al., 2016]. We consider

a GRB host as detected if the offset of the potential host and the GRB location is within 1″. At $z \sim 3$, 1″ roughly corresponds to 7.5 kpc. From previous HST observations of other GRB host samples at [Bloom et al., 2002, Lyman et al., 2017], more than 90% of the GRBs occur within this offset from their host galaxies. All the GRBs are localized with a $< 0.5$″ precision. The resulting magnitudes are further corrected for Milky Way Galactic extinction using the dust maps of [Schlafly and Finkbeiner, 2011] and the extinction law with $R_V = 3.1$ from [Cardelli et al., 1989]. The photometry results are presented in Table 4.1.

The LDT imaging was performed using the Large Monolithic Imager (LMI, [Massey et al., 2013]). The LMI data was detrended with a custom pythom-based pipeline[1]. Individual fields were astrometrically aligned and co-added using `SCAMP` and `SWARP` respectively. The aperture photometry of the co-added images was performed using `Sextractor`. The magnitudes were calibrated against the SDSS [Alam et al., 2015] and GAIA catalogs [Evans et al., 2018]. Conversion of GAIA magnitudes to Sloan magnitudes was performed using the conversion tables provided in GAIA data release 2 [Brown et al., 2018].

The FORS data was flat-fielded using the ESO pipeline `Esoreflex` [Freudling et al., 2013] and was further aligned, co-added, and calibrated as described above. PanSTARSS and KiDS surveys provide reduced, stacked, and zero-point calibrated images, which were used to determine the science magnitudes/upper limits. The HST photometry was performed using archived drizzled and calibrated images and the AB magnitude was derived using the provided zero point. A 1″ aperture was

[1]https://github.com/joedurbak/photometrypipeline

Table 4.1: Summary of new observations

| GRB[a] | $z^b$ | Tel./Instr. | Filter | AB Mag |
|---|---|---|---|---|
| 000926A | 2.0377 | *Spitzer*/IRAC | 3.6 $\mu m$ | 25.2 ± 0.15 |
| 021004 | 2.3281 | *Spitzer*/IRAC | 3.6 $\mu m$ | 24.22 ± 0.18 |
| 071031 | 2.6912 | *Spitzer*/IRAC | 3.6 $\mu m$ | > 25.3 |
| 080310 | 2.4274 | *Spitzer*/IRAC | 3.6 $\mu m$ | 23.74 ± 0.24 |
| 090926A | 2.106 | *Spitzer*/IRAC | 3.6 $\mu m$ | 22.96 ± 0.05 |
| | | VLT/FOR2 | $R_{Special}$ | 23.9 ± 0.1 |
| 111008A | 4.989 | *Spitzer*/IRAC | 3.6 $\mu m$ | 24.73 ± 0.3 |
| | | HST/WFC3 | F110W | 25.5 ± 0.07 |
| 120327A | 2.813 | DCT/LMI | SL-r | 24.9 ± 0.2 |
| 130606A | 5.911 | *Spitzer*/IRAC | 3.6 $\mu m$ | 24.91 ± 0.25 |
| 130610A | 2.091 | *Spitzer*/IRAC | 3.6 $\mu m$ | 23.46 ± 0.05 |
| | | DCT/LMI | SL-r | 23.7 ± 0.1 |
| 141028A | 2.333 | *Spitzer*/IRAC | 3.6 $\mu m$ | > 25.1 |
| | | DCT/LMI | SL-r | > 25.8 |
| 141109A | 2.993 | *Spitzer*/IRAC | 3.6 $\mu m$ | 23.4 ± 0.1 |
| | | DCT/LMI | SL-i | 24.1 |
| 151021A | 2.329 | *Spitzer*/IRAC | 3.6 $\mu m$ | > 25.7 |
| | | KiDS Survey | SL-r | 24.4 ± 0.2 |
| 151027B | 4.0633 | *Spitzer*/IRAC | 3.6 $\mu m$ | > 22.66 |
| | | DCT/LMI | SL-r | > 24.3 |
| | | | SL-i | 24.8 ± 0.4 |
| 160203A | 3.518 | *Spitzer*/IRAC | 3.6 $\mu m$ | 21.74 ± 0.02 |
| | | PanSTARRS | PS1-i | > 22.7 |
| 161023A | 2.709 | *Spitzer*/IRAC | 3.6 $\mu m$ | > 25.9 |
| | | VLT/FORS2 | $R_{Special}$ | > 25.7 |
| 170202A | 3.645 | DCT/LMI | SL-r | > 25.4 |
| | | | SL-i | > 23.4 |

[a] *Spitzer* Prog ID 40599, PI : R. Chary. All others are taken from *Spitzer* Prog ID 13104, PI: D. Perley.
[b] Taken from [Gatkine et al., 2019a]

used for HST images given the diffraction-limited imaging.

### 4.2.2 Spitzer IRAC Photometry

We obtained deep archival imaging of GRB hosts using *Spitzer* Infrared Array Camera (IRAC) channel 1 (3.6$\mu m$). Out of a total of 27 GRB hosts, we present new *Spitzer* IRAC photometry of 13 hosts in this paper and 12 were previously published as a part of the SHOALS survey [Perley et al., 2016b]. The remaining two GRBs

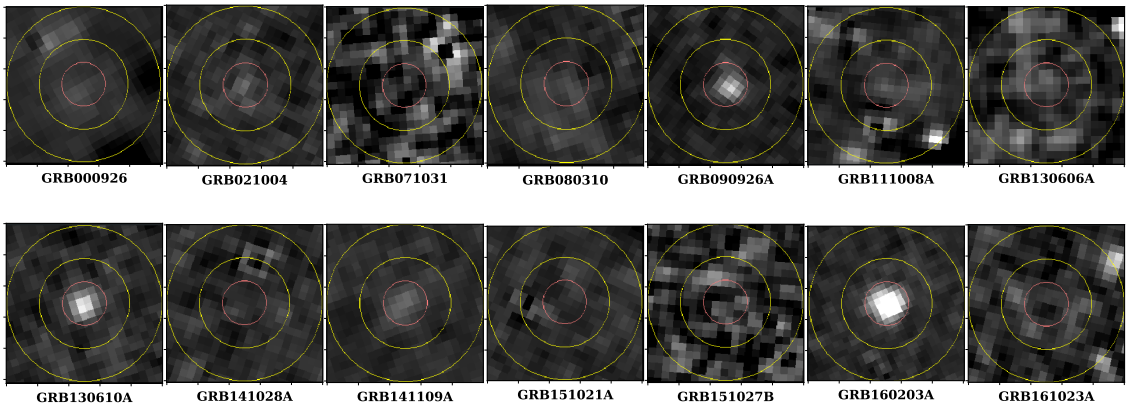


Figure 4.1: Contamination-subtracted images of GRB fields from *Spitzer*-IRAC in 3.6 $\mu m$ band. Each thumbnail is 8" × 8" in size. The central red circle is the 1.8″aperture used to define the source flux and the outer annulus is used to define the background flux. The circle is centered on the best-known position of the GRB or of the detected host galaxy. References for GRB positions: 000926 [Fynbo et al., 2001], 021004 [Henden and Levine, 2002], 071031 [Krühler et al., 2009], 080310 [Littlejohns et al., 2012], 111008A [Bolmer et al., 2018], 130606A [Castro-Tirado et al., 2013], 141109A [Xu et al., 2014], 151021A [McCauley and Melandri, 2015], 151027B [Greiner et al., 2018], 161023A [de Ugarte Postigo et al., 2018].

remained unobserved by the end of *Spitzer* mission. The newly presented data have been collected as a part of various previous programs which are summarized in Table 4.1.

By analyzing the new data the same way as [Perley et al., 2016b], we ensure procedural consistency with the previously published data. The reduction and photometry method is described in detail in [Perley et al., 2016b]. Here, we briefly summarize the key points. We acquired the Level-2 PBCD (Post-Basic Calibrated Data) from the *Spitzer* Legacy Archive. We use the default astrometry provided with the Level-2 products (with an accuracy of 0.3″). Due to the large PSF of *Spitzer* IRAC ($\sim$ 1.8″ at 3.6 $\mu m$), source confusion and flux contamination from neighboring sources is an important issue. We compare each IRAC image with deep ground-based optical images (as described in Section 4.2.1) to identify the primary

source and any neighboring contaminants. We used the `galfit` tool [Peng, 2003] over several iterations to model the sources (using the PSF and PRF files provided in *Spitzer* documentation[2]) and subtract the neighboring sources which may contaminate the host or sky background regions. The subtracted image is then used for performing aperture photometry.

We implemented the IRAC handbook recommendations for aperture photometry using a custom IDL wrapper around the `aper` procedure in the Astronomy User's Library[3] (see [Perley et al., 2016b] for details). For aperture photometry, we place a 1.8″ aperture on the host galaxy location (guided by deep optical imaging) and a sky annulus with an inner radius of 3.6″ and outer radius of 6″. The source aperture and sky annulus are marked in red and yellow respectively in Fig. 4.1. In the case of optical detection and IR non-detection, we specify a 2-$\sigma$ limit. However, in the case of optical as well as IR non-detection, we evaluate a 3-$\sigma$ upper limit to account for the uncertainty (typically $< 1''$) in the GRB host location.

### 4.2.3 Stellar Mass

We use the *Spitzer* IRAC 3.6$\mu m$ photometry to infer the stellar mass of galaxies in our sample. At $z \sim 2 - 6$, *Spitzer* IRAC measures the rest-frame optical light (beyond the Balmer break) from long-lived stars in the host galaxies. Here we follow the methodology used in [Perley et al., 2016b] to derive the stellar masses. SED fitting is a more accurate method to estimate $M_*$ (by breaking the degeneracy

[2]https://irsa.ipac.caltech.edu/data/*Spitzer*/docs/irac/calibrationfiles/psfprf/
[3]https://idlastro.gsfc.nasa.gov/

between age and extinction). However, this requires extensive, ultra-deep optical observations of faint GRB hosts in multiple filters, which is resource intensive. Instead, we use *Spitzer* single-band (3.6 $\mu m$) photometry, which can still provide a reasonable estimate of stellar mass, particularly for galaxies at $z > 2$.

We calculate the absolute magnitude at $\lambda_{rest} = 3.6\mu m/(1+z)$ as $M_{AB} = m_{AB,3.6\mu m} -$ DM $+ 2.5\log(1+z)$, where DM is distance modulus. In [Perley et al., 2016b], a grid of model galaxy SEDs is constructed for an array of redshifts ($z \sim 0-10$) and each decade in $M_*$ ($10^8$ to $10^{11} M_\odot$) by summing [Bruzual and Charlot, 2003] galaxy SED templates (using [Chabrier, 2003] initial mass function). The models also incorporate a modest dust attenuation to validate the single-band stellar mass conversion function against the more accurate SED-fit (optical + *Spitzer* multiband) stellar masses in the MODS [Kajisawa et al., 2009] and UltraVISTA samples [Caputi et al., 2015]. We then evaluate the stellar mass by interpolating on the $M_*$, redshift, and AB magnitude grid (see [Perley et al., 2016b] for more details). While the single-band method suffers from uncertainties associated with various model assumptions such as the IMF, dust extinction ($A_V$), and star formation history, this method is consistent with the masses obtained from SED fitting at the $\sim 0.3$ dex level. Further, by using the same method throughout our sample, we ensure that the correlations derived here are on an equal footing. The $M_*$ of our GRB hosts are summarized in Table 4.2.

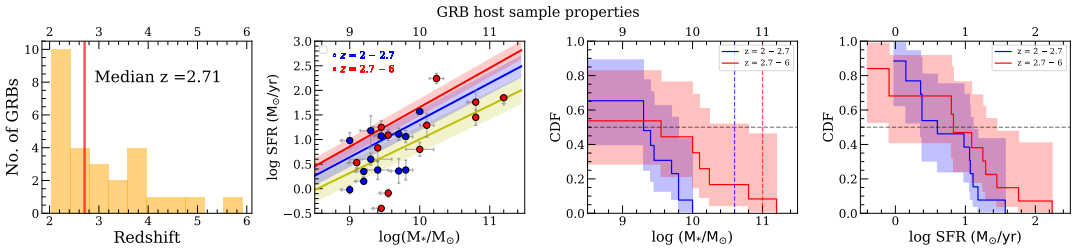


Figure 4.2: Properties of the CGM-GRB sample. Panel 1: The redshift distribution of the sample. Panel 2: The SFR *vs* $M_*$ of the GRB host galaxies in our sample. The lines show the main sequence curves (yellow: $z = 1$, blue: $z = 2$, red: $z = 4$) as described in [Speagle et al., 2014]. Panel 3: The cumulative distriution of the stellar mass in the CGM-GRB sample. The spread shows 95% confidence interval around the value by incorporating any upper limits. The dotted vertical lines show the value of characteristic mass, $M^*$ in the mass function (written as a Schechter function) at the respective redshifts. The horizontal line shows the median (i.e. CDF = 0.5). Panel 4: Same as panel 3, for SFR.

### 4.2.4 Dust Correction

UV dust extinction of the host galaxy needs to be estimated to convert the absolute magnitudes into intrinsic rest-frame UV luminosity. Following [Greiner et al., 2015], we perform the dust correction using empirical correlations of the spectral index of the UV continuum $\beta$ (where $f_\lambda = \lambda^\beta$), rest-frame absolute UV magnitude at $\lambda_{rest} = 1600$ Å ($M_{UV}$), and the dust extinction at rest-frame 1600Å ($A_{1600}$). Here we assume that GRB hosts at high redshift follow a power law SED ($f_\lambda = \lambda^\beta$) in the UV (redward of Ly$\alpha$) and the same correlations as the extensive high-$z$ (2.5 − 6) star forming galaxy sample of > 4000 galaxies from HST HUDF and CANDELS surveys studied in [Bouwens et al., 2009, **?**]. They derive the following empirical relation for star forming galaxies at $\langle z \rangle = 3.8$:

$$\beta = -1.85 - 0.11(M_{UV} + 19.5) \tag{4.1}$$

The uncertainties on the numerical coefficients here are small ($-1.85 \pm 0.06$ and $-0.11 \pm 0.01$). Then, we iteratively solve for $M_{UV}$ and $\beta$. The typical $\beta$ for the high-$z$ star forming sample in [Bouwens et al., 2009, **?**] is $\beta \sim -2$. In equation 4.2, this corresponds to $M_{UV} = -18.1$. Hence, we use $\beta = -2$ for our weaker upper limits (where $M_{UV} > -18.1$). For stronger upper limits (i.e. $M_{UV} < -18.1$, we use the $\beta$ corresponding to the limit. Finally, the $A_{1600}$ is evaluated using the following relation from [Meurer et al., 1999]:

$$A_{1600} = 4.43 \text{ mag} + 1.99\beta \tag{4.2}$$

This dust-correction method is described in detail in [Greiner et al., 2015].

### 4.2.5 Star formation rate

We use single-band photometry in the rest-frame UV to calculate UV-based SFR. To compute the SFR from dust-corrected UV luminosity ($L_{UV,corr}$), we follow the relations described in [Savaglio et al., 2009] where they simultaneously compare the emission-line and dust-corrected UV luminosities of GRB hosts to derive the conversion factor between dust-corrected UV luminosity and SFR. We use the $A_{1600}$ and $M_{UV}$ values calculated in Section 4.2.4 to compute $L_{UV,corr}$. The SFR is then calculated as follows:

$$\text{SFR}_{1500} = 1.62 \text{ M}_{\odot}\text{yr}^{-1} \times \frac{L_{1500,\text{corr}}}{10^{40} \text{ erg s}^{-1} \text{ Å}^{-1}} \tag{4.3}$$

As a validation step, we compare the $A_{1600}$ evaluated using the $\beta$ method

with that using the afterglow-derived $A_V$ (assuming an SMC extinction law). The resulting SFRs derived using the two methods are consistent with each other within a factor of two except for GRBs 130408A and 080810 where the afterglow $A_V$ is larger, leading to a higher SFR estimate (for the afterglow $A_V$ method) by a factor of 3. The star formation rates of our GRB hosts are summarized in Table 4.2.

For GRBs 071031, 080804, and 120815, photometric observations are either unavailable or too shallow. In the cases of GRBs 080804 and 120815, we have used H$\alpha$ emission-based SFRs from [Krühler et al., 2011] since they are more robust compared to UV-luminosity. For GRB 071031, we use the Ly$\alpha$-based SFR from [Milvang-Jensen et al., 2012]. While less robust, this measurement is consistent with the upper limit of 3 $M_\odot yr^{-1}$ from an archival HST WFC3 (F160W filter) observation.

Note however that our sample naturally has low line-of-sight dust extinction compared to the general GRB host population since we only select the afterglows that are bright enough for high-resolution rest-frame UV spectroscopy. While there may be a systematic bias in the dust correction, we have used the same SFR-tracer and analysis procedure for the entire sample (except GRBs 071031, 080804, and 120815), thus minimizing any relative bias. Our sample may contain a small number of heavily dust enshrouded galaxies, for which we may underestimate the SFR. However, we have minimized this possibility by ruling out heavy dust obscuration in 4 massive GRB hosts in our sample (where the probability of heavy dust obscuration is high) by using deep VLA observations [Gatkine et al., 2020] and hence, the typical dust corrections described here can be used for estimating their star formation rates.

These GRBs are marked with asterisk in Table 4.2.

## 4.3 Sample properties and analysis

### 4.3.1 Comparison with star formation main sequence

Figure 4.2 shows the distribution of $M_*$, SFR, and $z$ of the CGM-GRB sample. We compare the relative position of our sample with respect to the star forming main sequence at $z = 2$ and 4. The star forming main sequence and its scatter is computed using Equation (28) in [Speagle et al., 2014]. The key characteristics of our sample in terms of galaxy properties are summarized below.

1. We divide the sample in two groups – $z1$: 2-2.7 and $z2$: 2.7-5.9 – which have equal number of objects and roughly equal cosmological timescale (1 and 1.4 Gyrs). We highlight that there is no significant difference in the two groups in terms of SFR distribution. On the other hand, the mass distribution of the high-$z$ group is skewed towards higher masses. However, note that this is not an intrinsic bias in the sample selection since our sample is selected based only on the afterglow properties. Regardless, from Fig. 4.2, we conclude that our sample primarily traces the low-mass end of the galaxy mass function at the respective redshifts (by comparing against the characteristic stellar mass in the Schechter function).

2. While there is a significant spread, the majority of the GRB hosts in our sample are within 0.5 dex (i.e. 3x) of the star formation main sequence at their respective

Table 4.2: Summary of GRB host properties in the CGM-GRB sample

| GRB | $z$ | $\log(N_{HI})^a$ | $A_V$ [b] | $M_{3.6/(1+z)}$ | $\log(M_*/M_\odot)$ | $M_{UV}$ | SFR ($M_\odot yr^{-1}$) | References |
|---|---|---|---|---|---|---|---|---|
| 000926 | 2.0385 | 21.3 ± 0.25 | 0.15 | −19.6 | 9.3±0.3 | −19.5 | $4.0^{+1.3}_{-1.0}$ | [Castro et al., 2003] [Chen et al., 2009] |
| 021004* | 2.3281 | 19.0 ± 0.2 | 0.2 | −20.9 | 9.5±0.1 | −21.4 | $11.8^{+3.7}_{-2.8}$ | [Fiore et al., 2005] [Fynbo et al., 2005] |
| 050730 | 3.9672 | 2.1 ± 0.1 | 0.12 | > −20.5 | < 9.46[c] | −18.1 | $0.8^{+0.2}_{-0.1}$ | [D'Elia et al., 2007] [Toy et al., 2016] |
| 050820A | 2.6137 | 21.1 ± 0.1 | 0.08[d] | −20.42 | 9.4±0.15[d] | −19.1 | $2.4^{+1.3}_{-0.9}$ | [Prochaska et al., 2007] [Chen et al., 2009] |
| 050922C | 2.1996 | 21.55 ± 0.1 | 0.10 | −19.6 | < 9.0[d] | > −18.3 | < 1.0 | [Prochaska et al., 2008c] [Covino et al., 2013] |
| 060607A | 3.0738 | 16.95 ± 0.03 | 0.08 | > −20.52 | < 9.4[d] | > −17.5 | < 0.4 | [Prochaska et al., 2008c] [Schady et al., 2012] |
| 071031 | 2.6912 | 22.15 ± 0.05 | 0.14 | > −20.1 | < 9.2 | – | $1.4^{+0.3e}_{-0.3}$ | [Fox et al., 2008] [Li et al., 2018] |
| 080310* | 2.4274 | 18.7 ± 0.1 | 0.10 | −21.3 | 9.8±0.1[d] | −19.0 | $2.4^{+1.4}_{-0.9}$ | [Fox et al., 2008] [Perley et al., 2009] |
| 080804 | 2.205 | 21.3 ± 0.1 | 0.17 | −20.2 | 9.3±0.15[d] | – | $15.1^{+20e}_{-7}$ | [Fynbo et al., 2009] [Toy et al., 2016] |
| 080810* | 3.351 | 17.5 ± 0.15 | 0.40 | −22.15 | 10.24±0.1[d] | −22.9 | $173^{+45}_{-36}$ | [Page et al., 2009] [Wiseman et al., 2017b] |
| 090926A | 2.106 | 21.73 ± 0.07 | < 0.04 | −21.9 | 9.8±0.1 | −20.5 | $11.6^{+3.7}_{-2.8}$ | [D'Elia et al., 2010] [Zafar et al., 2018] |
| 100219A | 4.665 | 21.13 ± 0.12 | 0.13 | > −20.4 | < 9.4[d] | −20.0 | $6.7^{+5.5}_{-3.2}$ | [Thöne et al., 2012] [Toy et al., 2016] |
| 111008A | 4.989 | 22.3 ± 0.06 | 0.12 | −20.9 | 9.5±0.2 | −20.5 | $12.3^{+3.5}_{-2.7}$ | [Sparre et al., 2014] [Zafar et al., 2018] |
| 120327A | 2.813 | 22.01 ± 0.09 | < 0.03 | −23.2 | 10.8±0.1 | −21.2 | $28.1^{+12.5}_{-8.7}$ | [D'Elia et al., 2014] [Heintz et al., 2019] |
| 120815A | 2.358 | 21.95 ± 0.1 | 0.19 ± 0.04 | > −21.2 | < 9.7[d] | – | $2.3^{+2}_{-1}$ [e] | [Krühler et al., 2015] [Zafar et al., 2018] |
| 120909A | 3.929 | 21.20 ± 0.10 | 0.16 ± 0.04 | > −20.2 | < 9.5[d] | −20.8 | $17.9^{+6.2}_{-4.6}$ | [Cucchiara et al., 2015] [Heintz et al., 2019] |
| 121024A* | 2.298 | 21.50 ± 0.10 | 0.56[d] | −21.8 | 10.15±0.15 | −21.7 | $37^{+20}_{-15}$ | [Friis et al., 2015] [Toy et al., 2016] |
| 130408A | 3.757 | 21.70 ± 0.10 | 0.2 | – | – | > −21.1 | < 13.4 | [Zafar et al., 2018] |
| 130606A | 5.911 | 19.93 ± 0.2 | < 0.07 | −21.8 | 10.0±0.2 | −19.9 | $6.3^{+2.4}_{-1.7}$ | [Hartoog et al., 2015] [Zafar et al., 2018] |
| 130610A | 2.091 | – | 0.01 | −21.3 | 9.7±0.05 | −20.6 | $13^{+4.1}_{-3.1}$ | [Smette et al., 2013] [Littlejohns et al., 2015] |
| 141028A | 2.333 | 20.60 ± 0.15 | 0.13 | > −20.0 | < 9.2 | > −19.2 | < 2.3 | [Wiseman et al., 2017b] |
| 141109A | 2.993 | 22.10 ± 0.10 | 0.11 | −22.1 | 10.1±0.1 | −20.9 | $19.7^{+14}_{-8}$ | [Heintz et al., 2018] [Heintz et al., 2019] |
| 151021A | 2.329 | 22.3 ± 0.2 | 0.2 | > −19.4 | < 9.0 | −20.3 | $9.6^{+4.3}_{-3}$ | [Heintz et al., 2018] |
| 151027B | 4.0633 | 20.5 ± 0.2 | < 0.12 | −23.45 | < 10.8 | −21.9 | $58^{+40}_{-24}$ | [Heintz et al., 2018] [Zafar et al., 2018] |
| 160203A | 3.518 | 21.75 ± 0.10 | < 0.1 | −24.2 | 11.2±0.05 | > −22.9 | < 71 | [Heintz et al., 2018] |
| 161023A | 2.709 | 20.96 ± 0.05 | 0.09 | > −19.5 | < 9.1 | > −19.6 | < 3.4 | [Heintz et al., 2018] |
| 170202A | 3.645 | 21.55 ± 0.10 | <0.12 | – | – | > −21.0 | < 11.5 | [Selsing et al., 2018] [Zafar et al., 2018] |

$M_{3.6/(1+z)}$: AB mag in rest-frame optical/NIR from *Spitzer* data; $M_{UV}$: Absolute magnitude at $\lambda_{rest} = 1600$Å

[a] Neutral hydrogen column densities (in $cm^{-2}$) measured from the damped Ly-$\alpha$ absorption

[b] Extragalactic dust extinction in magnitude, derived assuming SMC extinction law [Gordon et al., 2003]

[c] Derived Using host galaxy SED

[d] From [Perley et al., 2016b]

[e] 071031: SFR using Ly$\alpha$ [Milvang-Jensen et al., 2012], 080804: SFR using H$\alpha$ [Krühler et al., 2015], 120815: SFR using H$\alpha$ [Krühler et al., 2015].

* GRBs with deep VLA observations from [Gatkine et al., 2020]

redshifts (within observational uncertainties). It should also be noted that their spread is skewed downwards of the main sequence function. Thus, our sample traces a moderately sub-main sequence galaxy population at $z \sim 2 - 6$.

### 4.3.2 Blue-wing column density and outflows

To quantify outflows, we use the multi-component Voigt-profile fits to the high-resolution GRB afterglow absorption spectra (in the rest-frame UV) and the resulting column densities from [Gatkine et al., 2019a]. We then integrate the apparent column density (derived from the fit) bluewards of $-100$ km s$^{-1}$. We define this quantity as blue wing column density ($N_{out}$), which is a measure of the galactic outflow. This velocity threshold is carefully chosen to minimize any contamination from the line-of-sight absorption in the interstellar medium. A detailed justification for this limit is provided in [Gatkine et al., 2019a] through kinematic and geometric modeling of the ISM + CGM of a representative galaxy in this sample. This is similar to down-the-barrel observations of outflows, albeit with random sightlines and using high-resolution and high signal-to-noise spectra.

We compare the blue wing column density as described above with host galaxy properties ($M_*$ and SFR). In particular, we focus on four species. These include two high ionization potential species (high-ion) − C IV and Si IV and two low ionization potential species (low-ion) − Si II and Fe II. These species are selected for three reasons. 1) Their absorption lines fall within the passbands over a large redshift range at $z > 2$. 2) These lines are not too weak (leading to underestimates) or not

too strong (saturated). In most cases, we do not have saturation in the blue wings. 3) They allow us to compare the differences between the relations of high-ion and low-ion species with host galaxy properties.

### 4.3.3 Inferring correlations and hypothesis testing

To investigate the presence of correlations between outflow and galaxy properties, we primarily focus on the parameter space of $M_*$, SFR, outflow column density, and maximum outflow velocity. First, we perform Kendall-$\tau$ test by using a null hypothesis that the data is consistent with no correlation. The $1-p$-value from Kendall-$\tau$ test gives us the confidence level at which the null hypothesis is rejected (i.e. a smaller p-value implies a stronger correlation). Second, we perform a linear regression to infer the best-fit line for each investigated correlation using Schmitt's binned regression [Schmitt, 1985]. Note that we include all the upper (and lower) limits in both of these analyses using the astronomy survival analysis code called ASURV [Feigelson and Nelson, 1985, Isobe et al., 1986, Isobe and Feigelson, 1990]. The resulting best-fit and Kendall-$\tau$ p-value are shown in the correlation figures.

Due to multiple upper limits in the stellar mass and/or star formation rates in the sample, simply using linear regression does not provide complete information on the underlying correlations and/or their spread. Therefore, we also divide the sample in two equal parts based on the galaxy property under consideration ($M_*$ or SFR) and investigate whether the sample distribution of the outflow property (eg: $N_{out}$) in the two bins is consistent with being drawn from the same population. Therefore,

for this hypothesis testing, our null hypothesis is that there is no correlation between the galaxy properties and outflow properties. If the null hypothesis is true, the two samples of outflow properties (eg: column density) split based on galaxy property (eg: $M_*$ or SFR) are consistent with being drawn from the same population, which would imply an absence of correlation between the given outflow property and the galaxy property.

We plot the cumulative densities of both the samples, which further visually shows the distinction or similarity between the two sample distributions. To accommodate the upper limits in our observations, we calculate the cumulative distribution function (CDF) and its spread are evaluated using a survival analysis method called Kaplan-Meier estimator[4] ([Isobe et al., 1986, Feigelson and Nelson, 1985]). The resulting $p$-values describe the probability of the two samples being drawn from the same distribution (and hence, no correlation). With a stronger correlation, the p-value would be smaller. In figures 4.3−4.8, the split in samples is shown with a vertical dotted line. The median of the sample on either side and its 68-percentile spread are shown in large square points for comparison (on X-axis, it is 68-percentile spread in the sample, on Y-axis, it is 68-percentile spread in the inferred median).

[4]We use a python package called `lifelines` to calculate the CDF and its 1-$\sigma$ spread using Kaplan-Meier method. For a two-sample hypothesis testing, we use the log-rank test in `lifelines`.

## 4.4 Outflow correlations

### 4.4.1 Outflow column density vs galaxy properties

In Figures 4.3 and 4.4, we plot the blue wing column densities of C IV, Si IV, Fe II, and Si II with SFR and $M_*$, respectively. The key findings are summarized in the following subsections.

#### 4.4.1.1 Blue-wing detection fraction

We define the detection fraction as the number of objects with detected blue-wing absorption ($N_{out}$) divided by the total number of objects in each sample. The detection fractions in the left and right samples in Fig. 4.3 ($N_{out}$ vs SFR) are: C IV (1 and 0.92), Si IV (0.92 and 1), Fe II (0.62 and 0.71), and Si II (0.66 and 0.77). The relative difference in the left and right samples is insignificant (i.e. contributed by an excess of one non-detection in one of the samples). We find the same result Fig. 4.4 ($N_{out}$ vs $M_*$). Thus, we conclude that the detection fractions in the outflow do not strongly depend on the galaxy's stellar mass or star formation rate. However, we note that the blue-wing detection fraction is significantly higher in high-ion species (C IV, Si IV) compared to the low-ion species, hinting at a prevalence of outflows primarily traced by the warm phase ($10^{4.5} - 10^{5.5}$ K, [Tumlinson et al., 2017, Gatkine et al., 2019a]).

#### 4.4.1.2 $N_{out}$ vs SFR

From visual inspection of $N_{out}$ vs SFR panels in Fig. 4.3, we note that there is a greater prevalence of high $N_{out}$ in the high-SFR sample compared to the low-SFR sample. The CDF plots provide a quantitative measure of any such relation. First, we focus on the high-ion species (C IV and Si IV). The low-SFR and high-SFR samples are most distinct (i.e. small $p$-value) in high-ion species. We can reject the hypothesis of absence of correlation (between $N_{out}$ vs SFR) for C IV and Si IV with 87% and 98% confidence $(1 - p)$ respectively. Thus, a higher star formation rate is correlated with a higher column density of C IV and Si IV in the outflows. In addition, we note that the spread of $N_{out}$ (as evident from the 68-percentile errorbars on the median points) is considerably higher in the high-SFR sample compared to the low-SFR sample (by $\sim$ 0.3-0.5 dex). This effect is discussed in more detail in section 4.5.3.

Unlike the case of high-ion species, the $p$-value is high, indicating a weak (for Si II) or no correlation (for Fe II) of low-ion $N_{out}$ with SFR. The fact that we see a stronger high-ion outflow with star formation but only a weak change in the low-ion species indicates that a higher SFR leads to a stronger warm-gas outflow (traced by C IV, Si IV) but does not significantly affect the cool gas outflow (traced by Si II, Fe II). In other words, a higher SFR selectively enriches the outflow with high-ions (i.e. warm ionized gas).

#### 4.4.1.3 $N_{out}$ vs $M_*$

From visual inspection of the $N_{out}$ vs $M_*$ panels in Fig. 4.4, there is a minor rise in $N_{out}$ of high-ions with stellar mass (better seen in C IV and Si IV), albeit with weak statistical significance (i.e. a high value of Kendall-$\tau$ p-value). More quantitatively, the correlation exists with a confidence level of 80% and 74% in C IV and Si IV respectively. Si IV plot also shows a significantly larger spread in column density at a higher stellar mass. On the other hand, the low-ions do not show any difference between the low-mass and high-mass samples (as evident from the CDF plots and high $p$-values). Thus, the overall column density of the low-ion outflow remains independent of the stellar mass and shows a weak correlation for the column density of high-ion outflow. This finding implies that the prevalence of low-ion traced outflows is largely independent of the stellar mass and for high-ion outflows (particularly Si IV), it is only moderately boosted at high $M_*$. Given the large spread ($\sim$ 2 dex) in the column densities at any mass (for both high- and low-ions), it is clear that the relation between outflow column density and stellar mass, if any, is complex with multiple contributing factors such as halo mass, SFR, and ionization state.

#### 4.4.1.4 $N_{out}$ vs sSFR

We explored the correlations, if any, between outflow column density and specific SFR (sSFR = SFR/$M_*$) in Fig. 4.5. We do not see any statistically significant correlation of sSFR with $N_{out}$. Previous studies at lower redshifts have shown only a

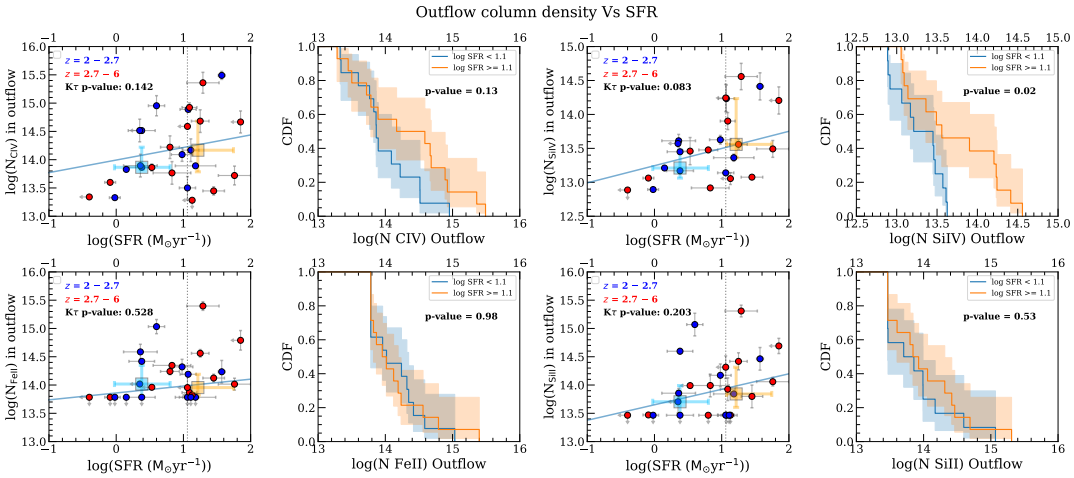


Figure 4.3: Column density in the outflows in GRB hosts traced by high-ion (C IV, Si IV) and low-ion (Fe II, Si II) species vs their SFR. The Kendall-$\tau$ $p$-value indicates the strength of correlation ($1 - p$ is the confidence level of the correlation). The vertical dotted line splits the sample into two equal groups around the median SFR. The CDF of each group is shown on the right to compare the distributions of low-SFR and high-SFR parts of the sample. The log-rank-test $p$-value shown in the CDF plot measures the extent to which the distributions are similar and hence consistent with no correlation. The median and 68-percentile spread of the median column density is shown using the blue and orange squares. The best-fit line (including limits in the data) is also shown here. Apart from a weak correlation, there is a significant increase in the spread of column density at high SFR (particularly for the high-ion lines).

weak or no correlation between outflow column density and sSFR for either low-ion or high-ion outflows. For instance, [Du et al., 2016] see only a weak correlation for C IV-traced outflows at $z \sim 1.25$ while [Bradshaw et al., 2013] see no correlation for Mg II-traced outflows at $z \sim 0.7 - 1.63$. Thus, the lack of $N_{out} - SFR$ relations for both high and low ions at $z \sim 2 - 6$ in our data, are consistent with previous results at lower redshifts.

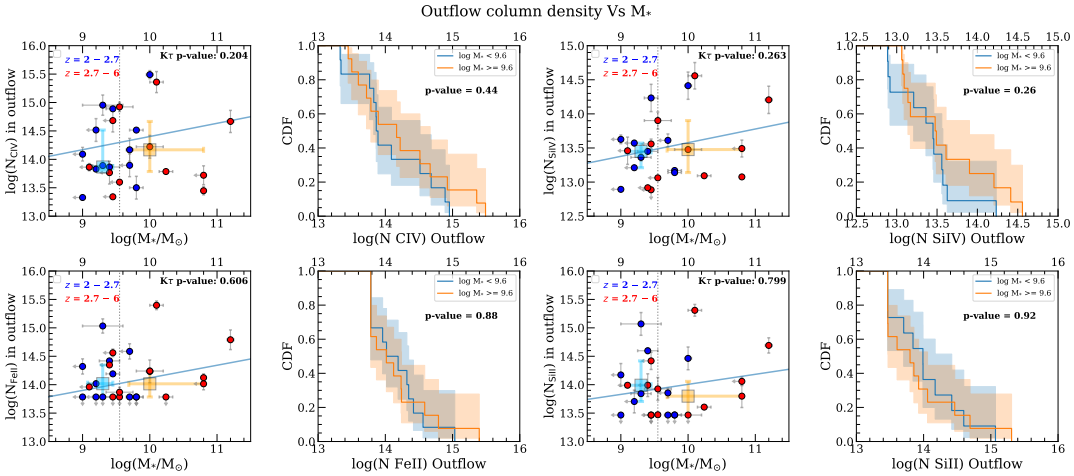


Figure 4.4: Same as Figure 4.3, for the outflow column density vs $M_*$

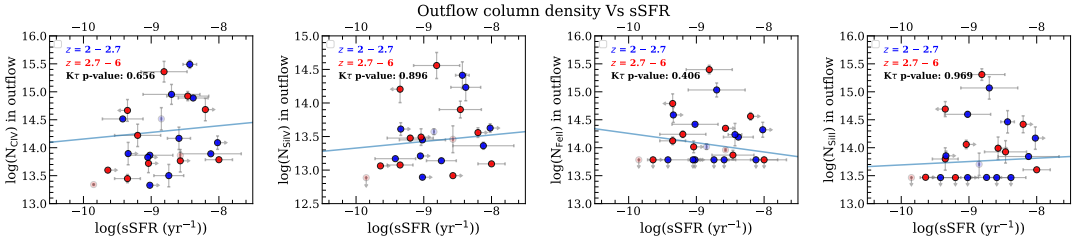


Figure 4.5: Same as Figure 4.3, for outflow column density vs specific SFR. The objects where both SFR and $M_*$ are not detected are shown in a lighter shade.

### 4.4.2 Outflow kinematics and galaxy properties

We study the relationship between outflow kinematics and galaxy properties using the maximum velocity of the outflow (i.e. maximum velocity in the blue wing), $V_{max}$. We define $V_{max}$ as the velocity of the most blue-shifted absorption component + the half-power width of that component. The maximal velocity is a key determinant of the outflow energy and mass outflow rate and hence, the enrichment of the CGM (and IGM). Therefore, in this paper, we use $V_{max}$ as a proxy for outflow kinematics to investigate the effect of galaxy properties.

#### 4.4.2.1 Outflow $V_{max}$ vs SFR

From Fig. 4.6, a strong correlation is observed between $V_{max}$ and SFR for high-ion species (2-$\sigma$ for C IV and 3-$\sigma$ for Si IV). The best-fit relations are given by $V_{max} \propto SFR^{0.12}$ and $SFR^{0.29}$ for C IV and Si IV, respectively. This correlation is much tighter than the SFR $-$ column density relation. The smaller variation would mean the velocity gain due to higher SFR is mostly independent of the sightline being probed. By combining this with previous results from Section 4.4.1.2, it can be said that star formation uniformly drives up the high-ion outflow velocity, but also imparts a large variance in the overall amount of outflowing material (column density) that is being driven. We discuss this aspect in more detail in Section 4.5.3.

On the other hand, for low-ion species, the correlation is weaker (39% and 93% confidence for Fe II and Si II respectively), primarily due to a larger spread in the $V_{max}$ compared to high-ion species (which can be easily seen by comparing their

CDF plots). This shows a larger variance in the kinematics of cool-phase outflows traced by low-ion species relative to the warm-phase outflows traced by high-ion species.

In addition, Fig. 4.6 also shows that the high-resdhift and the low-redshift populations (groups $z1$ and $z2$) follow the same trend for $V_{max} - SFR$ correlation. We do not observe any significant evolution in the relation of outflow kinematics and SFR. This further corroborates a previous result from [Gatkine et al., 2019a] which shows no evolution in the CGM kinematics in the same two redshift bins.

#### 4.4.2.2 Outflow $V_{max}$ vs $M_*$

This relation is summarized in Fig. 4.7. We observe a weak correlation in C IV (84% confidence or $\sim 1.5\sigma$) and a slightly stronger correlation in Si IV (98% confidence or $\sim 2.5\sigma$). We note a larger spread in the low-$M_*$ group, as evident from the errorbars around the low-$M_*$ in Fig. 4.7 (top panels). This spread can be directly explained by the larger spread of SFR in the low-$M_*$ group compared to the high-$M_*$ group in Fig. 4.2 (see panel 2). It is the variance in SFR that is directly causing the spread in the $V_{max} - M_*$ plot for high ions. By combining this with the result from Section 4.4.1.3, we can deduce that the stellar mass by itself does not significantly affect the kinematics or column density of the high-ion outflows, but is almost entirely driven by the SFR instead.

For low-ion species, we do not see any correlation between $V_{max}$ and $M_*$. We observe a large spread in both high-mass and low-mass groups. Overall, our high-$z$

results for cool low-ion outflows show a different picture compared to the results in low-$z$ studies. For instance, [Rubin et al., 2014] find a 3.5-$\sigma$ correlation between $V_{max}$ and $M_*$ and no correlation with current SFR. In contrast, for our sample at $z > 2$, we find a weak correlation ($\sim 2\sigma$ for Si II) with SFR and no correlation with the stellar mass.

#### 4.4.2.3 Outflow kinematics vs Halo mass

The halo mass is an important factor in determining whether the outflow will eventually escape and enrich the intergalactic medium or it will virialize and enrich the CGM. Therefore, it is important to understand how the outflow velocity compares with the characteristic velocity of the halo. To study how the outflow kinematics relate to the halo mass, we define a normalized velocity, $V_{norm} = V_{max}/V_{circ,halo}$, where $V_{circ,halo}$ is the halo circular velocity. The $V_{circ,halo}$ is calculated using the following equations from [Mo and White, 2002]:

$$V_{circ,halo} = \left(\frac{GM_{halo}}{r_{halo}}\right)^{1/2} \tag{4.4}$$

$$r_{halo} = \left(\frac{GM_{halo}}{100\Omega_m H_0^2}\right)^{1/3} (1+z)^{-1} \tag{4.5}$$

Here, $M_{halo}$ is calculated using the redshift-dependent stellar-to-halo mass ratio from [Wechsler and Tinker, 2018].

The $V_{norm} - M_{halo}$ relation is summarized in Fig. 4.8. We observe a clear inverse correlation in both high-ion and low-ion outflows. The inverse correlation is

slighlty stronger in high-ions (confidence: 99.7% in C IV, 99.9% in Si IV) compared to low-ions (confidence: 86.4% in Fe II, 99.2% in Si II). We note that most of the low-redshift points appear in the low-$M_{halo}$ group while the high-redshift points appear in the high-$M_{halo}$ group. This is because the stellar-to-halo mass ratio is larger at higher redshifts. Also, $V_{circ}$ scales as $M_{halo}^{1/3}$, thus lowering the value of $V_{norm}$ for the high-redshift objects.

The key takeaway from the $V_{norm} - M_{halo}$ relation is that the outflows in low-mass halos have a greater probability of reaching and/or escaping the outer CGM and enriching the intergalactic medium. Assuming that $V_{max}$ reflects the gas motion at the largest radii of the outflows, as interpreted in [Martin and Bouché, 2009] (with or without acceleration at larger radii), we can infer that outflows with $V_{max} > 2 \times V_{circ}$ (i.e. $\log(V_{norm}) > 0.3$ are most likely to escape the CGM and enrich the intergalactic medium at high redshifts.

#### 4.4.2.4 Outflow $V_{max}$ vs sSFR

We summarize the results of $V_{max}$ vs sSFR correlation in Fig. 4.9. We do not find any statistically significant correlation of sSFR with $V_{max}$. A weak, 1-$\sigma$ correlation appears to be present for $V_{max}$ *vs* sSFR for low-ion outflows, albeit with large scatter.

Correlations between outflow kinematics and sSFR have been seen in past observations. For instance, [Heckman et al., 2015, Heckman and Borthakur, 2016] report a strong ($> 2\ \sigma$) correlation between outflow velocity of warm ionized gas and

sSFR over 2.5 orders of magnitude in sSFR for starburst galaxies at $z < 0.2$. [Bradshaw et al., 2013] suggest a $V_{max} - sSFR$ correlation at $z \sim 0.7 - 1.63$, but shallower compared to $z \sim 0$ correlation. [Sugahara et al., 2017] also report $V_{max} - sSFR$ correlations at $z \sim 0 - 1$, albeit with a significant variation with redshift and over only one order of magnitude in sSFR. For comparison, we explore this correlation over almost 2 orders of magnitude in sSFR and do not find any statistically significant correlation.

This lack of correlation maybe due to a number of reasons: 1) an intrinsic weakening of the correlation at high redshifts, 2) presence of a large scatter in the correlation, thus requiring observations over a larger range in sSFR to see the correlation, and 3) the upper and lower limits in sSFR may mask the underlying correlation. In all the three cases, deeper observations of the host galaxy are needed to better constrain the sSFR and thereby, its relation with the outflow properties.

### 4.4.3 Outflow $V_{norm}$ vs specific SFR

Following the strong $V_{norm} - M_{halo}$ relation observed in Section 4.4.2.4, we set out to explore whether $V_{norm}$ (which is a gauge of whether the outflow can escape) is impacted by the sSFR. These results are summarized in Fig. 4.10. We clearly observe a strong correlation between $V_{norm}$ and sSFR for both high- and low-ions (except Fe II).

Our results are analogous to those found in [Heckman and Borthakur, 2016] for extreme starbursts at $z \sim 0 - 0.7$ using Si II line. They find that $V_{norm} \propto sSFR^{0.25}$

with a $> 3$-$\sigma$ confidence. Our scaling relations are consistent with this slope ($V_{norm}$ $\propto$ $sSFR^{0.26}$, $sSFR^{0.24}$, $sSFR^{0.26}$, and $sSFR^{0.39}$ for C IV, Si IV, and Si II, with 3-$\sigma$, 3.7-$\sigma$, and 2.6-$\sigma$ confidence, respectively).

We note that $V_{norm}$ is larger in [Heckman and Borthakur, 2016]. This is because they study extreme starburst galaxies with typical SFRs that are higher by at least an order of magnitude compared to our sample. This leads to a $2-3$x boost in outflow velocities. Regardless, the correlation is fairly robust in the sSFR range : $\log(sSFR) \sim -10$ to $-7.5$, similar to our range of interest. Given the strong agreement between the slopes obtained from the low-redshift results [Heckman and Borthakur, 2016] and our high-redshift results, we argue that the $V_{norm} - sSFR$ proportionality may be a redshift-independent fundamental property of star-forming galaxies. This should be investigated further using low- and intermediate-redshift analogs of high-$z$ star-forming galaxies.

This is the first such evidence of $V_{norm} - sSFR$ correlation at $z > 2$. The combined $V_{norm} - sSFR$ and $V_{norm} - M_{halo}$ relations (Section 4.4.2.4) imply that the outflows from the low-mass halos and high-sSFR galaxies have the highest probability of escaping the halo and transferring matter to the intergalactic medium, and thus enriching it with metals.

### 4.4.4 Relation of O VI absorption with galaxy properties

O VI traces the warm-hot medium ($10^5 - 10^6$ K). It is likely that O VI absorption traces a different phase compared to the gas traced by C IV and Si IV.

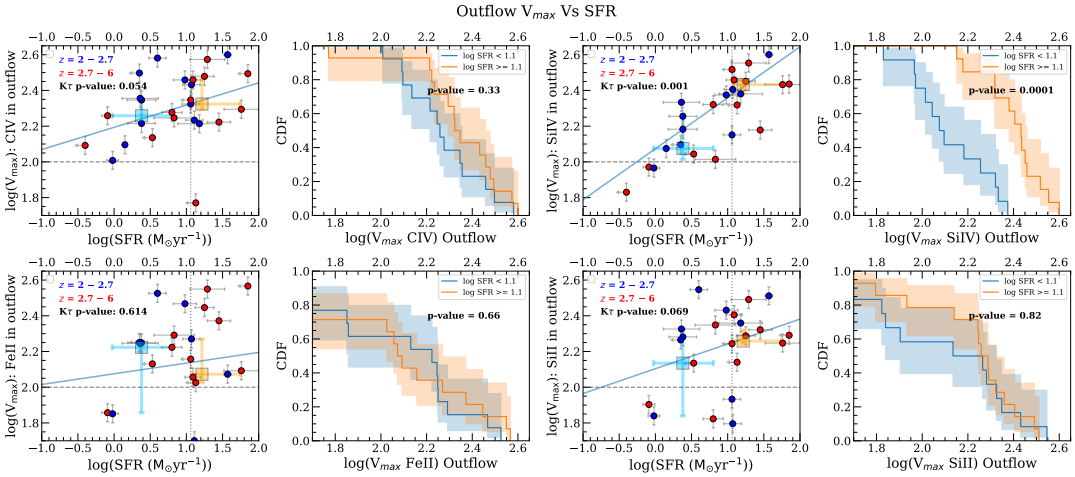


Figure 4.6: Same as Figure 4.3, for the maximum outflow velocity, $V_{max}$ vs SFR. The horizontal dashed line in the panels shows the 100 km $s^{-1}$ level, which we treat as the threshold for outflow.

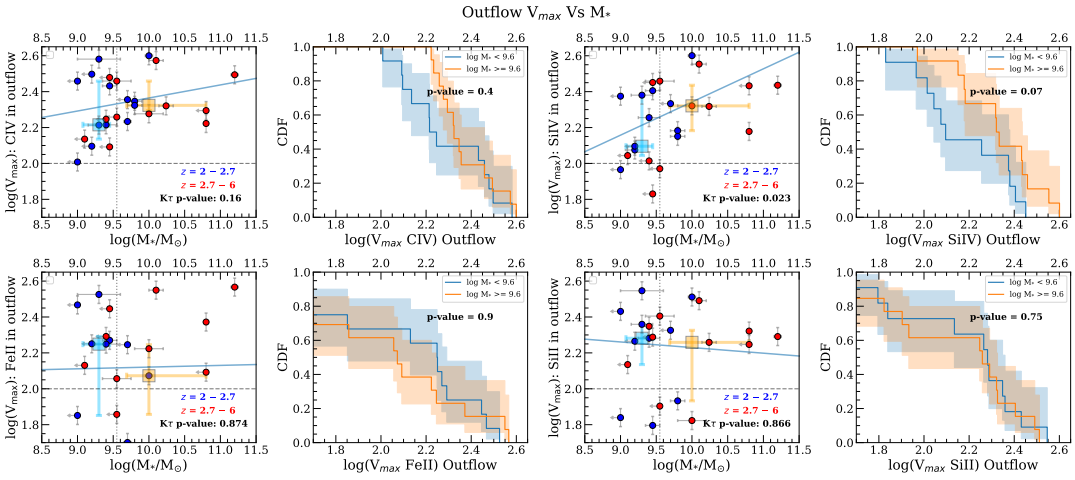


Figure 4.7: Same as Figure 4.3, for the maximum outflow velocity, $V_{max}$ vs $M_*$. The horizontal dashed line in the panels shows the 100 km $s^{-1}$ level, which we treat as the threshold for outflow.

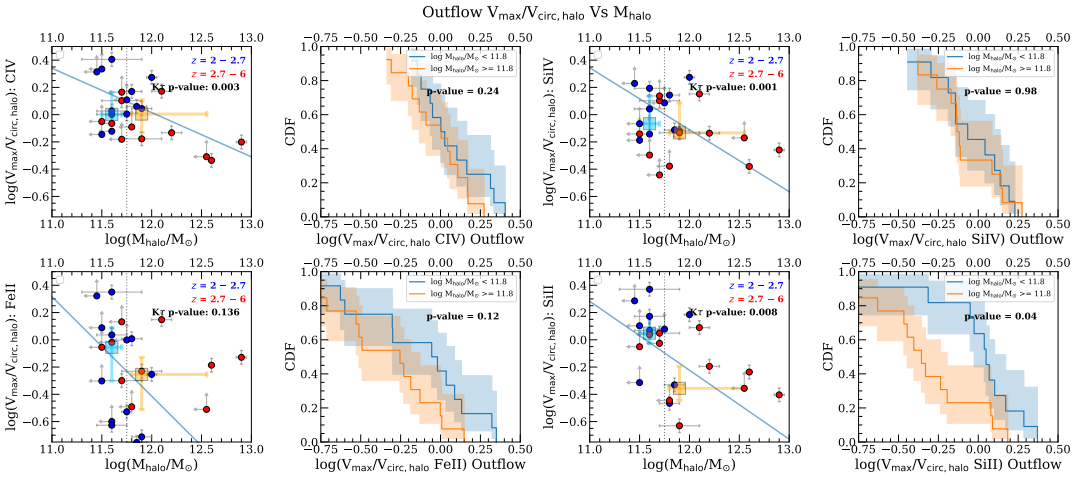


Figure 4.8: Same as Figure 4.3, for the normalized velocity, $V_{max}/V_{circ,halo}$ vs $M_{halo}$.

Here we look at the same relations studied above with O VI. Due to the location of O VI doublet ($\lambda_{rest}$ = 1031.9 and 1037.6 Å), fewer afterglow spectra in our sample cover the O VI band. Therefore, we caution that the relations observed for O VI are based on a smaller sample than other lines. Regardless, O VI correlations can provide useful insights into the warm-hot phase of the CGM.

From Fig. 4.11, it is clear that both the outflow column density and $V_{max}$ correlate with the stellar mass. The outflow column density is also correlated to the SFR, albeit less so than with the stellar mass. The O VI correlations appear to follow the correlations of high-ion species (C IV, Si IV) described earlier. With a caution of limited sample size, the data indicates that star formation activity also drives outflows in the OVI-traced phase (warm-hot phase) at $z \sim 2 - 6$.

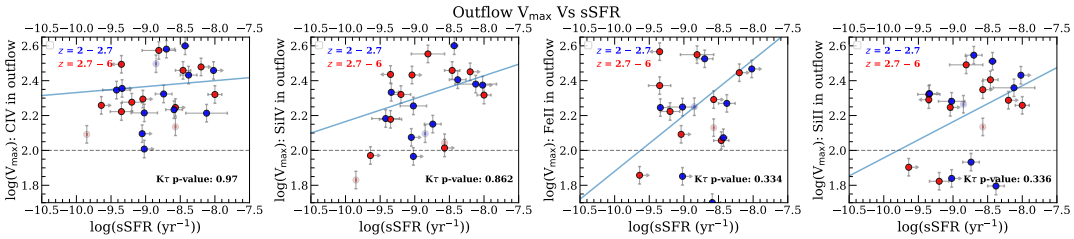


Figure 4.9: Same as Figure 4.5, for the the scaling relations of the maximum outflow velocity ($V_{max}$) with specific SFR (= SFR / $M_*$). The horizontal dashed line in the panels shows the 100 km s$^{-1}$ level, which we treat as the threshold for outflow.

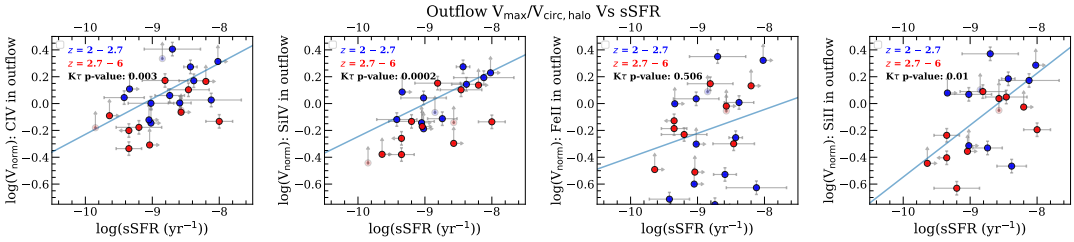


Figure 4.10: Same as Figure 4.5, for the the scaling relations of normalized maximum velocity ($V_{max}/V_{circ,halo}$) with specific SFR (= SFR / $M_*$).

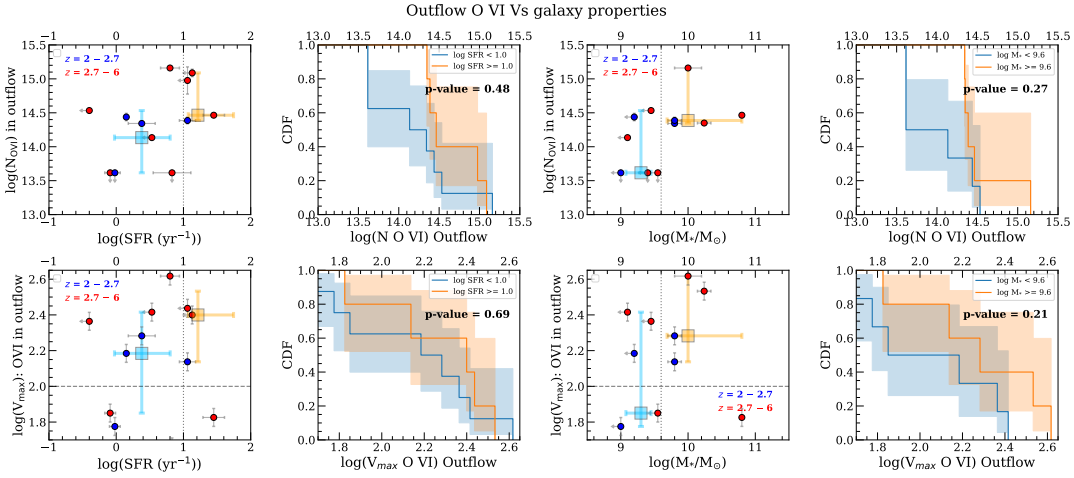


Figure 4.11: Same as Figure 4.3, for the correlations of the O VI-traced outflow with galaxy properties.

## 4.5 Discussion

### 4.5.1 SFR-driven outflow

The strong correlation of the blue-wing column density and maximum outflow velocity with SFR, as seen in Figs. 4.3 and 4.6 suggests that the outflow is driven by star formation activity. If we consider Si IV as the outflow tracer, the best-fit lines suggest $N_{SiIV} \propto SFR^{0.25}$ and $V_{max,SiIV} \propto SFR^{0.29}$. Our $V_{max}$ slope is in close agreement with the slope derived in [Sugahara et al., 2017] for $z \sim 2$ star-forming galaxies ($= 0.25$).

Similarly, the (weak) trends of high-ion column density and $V_{max}$ with $M_*$ are consistent with previous observations of C IV-traced outflows from [Du et al., 2018] at $z \sim 1 - 1.35$. However, our sample extends to 0.4 dex lower mass, where we start to see a systematic decline in $N_{out}$ as well as $V_{max}$ which is not seen in these previous observations. We argue that this decline is driven by the lower star formation rates. Similarly, the large spread (in $N_{out}$ and $V_{max}$ ) observed at $\log(M_*/M_\odot) > 9.4$ is due to the large spread in SFR at this mass range in our sample, as shown in Fig. 4.2. Hence, we conclude that the apparent trends between $V_{max}$ or $N_{out}$ and $M_*$ are almost entirely modulated by the SFR.

For low-ion outflows, the best-fit relation for Si II is $V_{max,SiII} \propto SFR^{0.14}$. Various surveys from low to high redshifts have reported correlation between some form of $V_{max}$ for low-ion species and SFR. Our results agree with the slopes observed in [Weiner et al., 2009, Bradshaw et al., 2013, Bordoloi et al., 2014a, Chisholm et al.,

2015] with redshifts ranging from $z \sim 0 - 1.6$. Our correlations also qualitatively agree with $z \sim 0.5$ sample of [Rubin et al., 2014] (only for galaxies without systemic absorption). From the $V_{max} - SFR$ slope derived here, we further corroborate the suggestion from [Sugahara et al., 2019] that the $V_{max} - SFR$ could be a more fundamental relation over a wide redshift range ($z \sim 0-6$) for star-forming main sequence. However, we caution that there is a significant spread in the relation depending on the species used for deriving them (for instance, we get a slope of 0.29 for Si IV and 0.14 for C IV).

Both [Erb et al., 2012] and [Rubin et al., 2012] find a strong correlation of $V_{max}$ with stellar mass and weak correlation with SFR for galaxies of similar mass and SFR range to our sample in the redshift ranges $z \sim 1-2$ and $z \sim 0.3-0.7$ for low-ion species. Similarly, [Bordoloi et al., 2014a] and [Chisholm et al., 2015] find a high-significance correlation with $M_*$ using Mg II and Si II species respectively. [Rubin et al., 2012] argue that this could be because star formation history and/or galaxy dynamics have a more direct physical link to maximum wind velocities than current star formation activity. However, we find that the trends flip – a stronger correlation with SFR compared to stellar mass (for instance, consider Si II in Figs. 4.6 and 4.7). This indicates that for low-mass galaxies at $z > 2$, the current star formation has a greater impact on the observed low-ion outflows than its star formation history. This is interesting from the perspective of causal connection. The timescale required for a 250 km $s^{-1}$ outflow to travel 50 kpc (roughly the virial radius of typical galaxies at $z \sim 3$) is about 200 Myr, while the UV-based SFR that we measure is from the past 100 Myr. This could indicate a long-lasting star formation activity. This is

in line with our typical depletion timescale of 500 Myr (using ($M_{gas} \sim M_*$)/SFR $\sim$ 1/sSFR).

We compare our scaling relations with the recently published results from the TNG50 simulations [Nelson et al., 2019]. We find that the slopes of our $V_{max} - SFR$ relation (for both high and low ions, slope $\sim 0.12-0.28$) are consistent with the slope of $0.15-0.2$ in [Nelson et al., 2019] (see Fig. 15 therein). However, our results do not fully agree with the predicted $V_{max} - M_*$ relation. While their slope of 0.2 at $z = 2$ is consistent with our high-ion results (slope = 0.19 for Si IV), [Nelson et al., 2019] show a slope that steepens with redshift (eg: slope = 0.3 at $z = 4$). We do not observe such steepening in our $V_{max} - M_*$ plots (Fig. 4.7). In fact, the slope appears to be shallower in the high-redshift group (group $z2 \sim 2.7 - 6$). This discrepancy may be explained by a combination of two factors: a) the increasing contribution of hotter phases in the outflow with increasing $M_*$ (see Fig. 10 in [Nelson et al., 2019]) and b) the outflow scaling relations shown in [Nelson et al., 2019] include all the phases while our observations only cover the warm phases (for high ions).

Given the strong $N_{out} - SFR$ and $V_{max} - SFR$ correlations, particularly for high-ion outflows, we argue that the mass outflow rate is strongly correlated with SFR. Using Si IV as the tracer, $N_{out} \propto SFR^{0.25}$ and $V_{max} \propto SFR^{0.28}$. The product $N_{out}V_{max}$ gives the maximum outflow volume flow rate. Assuming a constant density, this is a direct measure of the mass outflow rate. Thus, we can say that,

$$\dot{M}_{out} \propto N_{out}V_{max} \propto SFR^{0.58} \text{ for Si IV} \tag{4.6}$$

The slope obtained here is in good agreement with the slope observed in the FIRE simulations ($\sim 0.6$) at $4 > z > 2$ with the rate evaluated at $0.25R_{vir}$ (see Fig. B2 in [Muratov et al., 2015]). This slope is also in good agreement with EAGLE simulations at similar redshift range ($z \sim 2.4 - 4.7$) for gas particles ejected out of the ISM through galactic winds (see Fig. 3 in [Mitchell et al., 2020]). Both of these slopes have been obtained in the log(SFR) range of -0.5 to 1.5, similar to our SFR range.

### 4.5.2 Evidence for High-ion traced outflows

We observe three key differences between high-ion and low-ion outflows: 1) The detection fraction of low-ion outflows is lower than high-ion outflows ($\sim 65\%$ *vs* 95%), irrespective of the SFR. 2) The correlations of high-ion $N_{out}$ and $V_{max}$ with SFR are stronger compared to low-ions (see Figs. 4.3 and 4.6). Also, the spread in $V_{max}$ is higher in low-ions. 3) Low-ion outflows show a much steeper decline in $V_{norm}$ with higher halo masses compared to high-ion outflows (see Fig. 4.8). These difference point towards a systematic difference in the high-ion and low-ion outflows. In addition, we can infer that the outflows in our sample are primarily traced by high-ions.

It is well known that galactic outflows are multiphase in nature and the aforementioned differences can help understand the phase structure of the outflows. Cosmological simulations suggest a complex shift in the temperature distribution of the outflow with the dominant phase shifting towards higher temperatures as the stellar

mass increases at $z \sim 2$ (see Fig. 10 in [Nelson et al., 2019]). This trend is also seen in FIRE simulations with the contribution of $T > 10^{5.3}$ K phase increasing and that of $10^4 < T < 10^{4.7}$ K phase decreasing with an increasing halo mass at $z \sim 2$ (in the range $M_{halo} \sim 10^{11} - 10^{12}$ $M_\odot$ (see Fig. A1 in [**?**]). These effects can explain the sharp decline in low-ion $V_{norm}$ and their weaker and shallower correlations in terms of $N_{out}$. Photo-ionization modeling of the observations would help understand whether this explanation is correct. Regardless, we infer that the correlations seen in the star-forming galaxies using random, narrow sightlines (as offered by GRBs) imply high-ion dominated outflows in the star-forming galaxies at $z > 2$.

### 4.5.3 Outflow Geometry

The sharp increase in the spread of outflow column density at SFR $\gtrsim 10$ $M_\odot yr^{-1}$, particularly for high-ion lines is an indication of systematic variance in the outflow properties with SFR.

There are various possible causes that could lead to an elevated spread in the apparent outflow column density. Some of the scenarios include a variance in the metallicity of the outflowing clouds due to inefficient mixing of metals [Schaye et al., 2007], a variance in the entrainment efficiency of the ISM, or the onset of wind-stimulated condensation in the CGM (see [Heckman et al., 2017]) at high star formation rates. A more careful treatment of the physical processes in the outflows is warranted to explain this phenomenon.

Another possible explanation for such a variance is outflow geometry. Given

that GRBs sample a very narrow beam in a random direction offset from the galactic center, a spherical outflow is less likely to lead to the observed spread. In a structured outflow, with certain regions of high gas entrainment efficiency compared to others (eg: a biconical outflow), there will be preferred sightlines that exhibit high column density and others will exhibit a relatively lower column density. This is illustrated in Fig. 4.12. In addition, projection effects become more important in structured outflow as opposed to a spherical outflow. Therefore, the increased spread could indicate development of a structured outflow in the high-SFR systems, while the low-SFR galaxies having more uniform/spherical outflows.

Such development of outflow collimation naturally (hydrodynamically) emerges in the recent TNG simulation results along the minor axis of the galaxy despite isotropic injection of the stellar feedback [Nelson et al., 2019]. Thus, they come to the same conclusion in their simulations: the mass outflow rate of winds is not directionally isotropic, even for $M_* = 10^{10} M_\odot$ at $z = 1$. While they suggest that the effect is more pronounced as we go below $z \sim 2$, it will be interesting to probe how this effect evolves in the redshift-SFR space.

### 4.5.4 Evolution with redshift

While we see that $V_{max}$ for high-ion lines is correlated with SFR and $M_*$, we do not observe any systematic evolution in $V_{max}$ in our two redshift groups ($z1 : 2 - 2.7$ and $z2 : 2.7 - 6$). This is consistent with a weak or no evolution ($V_{max} \sim (1 + z)^{0.5}$) suggested in [Sugahara et al., 2017, Sugahara et al., 2019]. However,

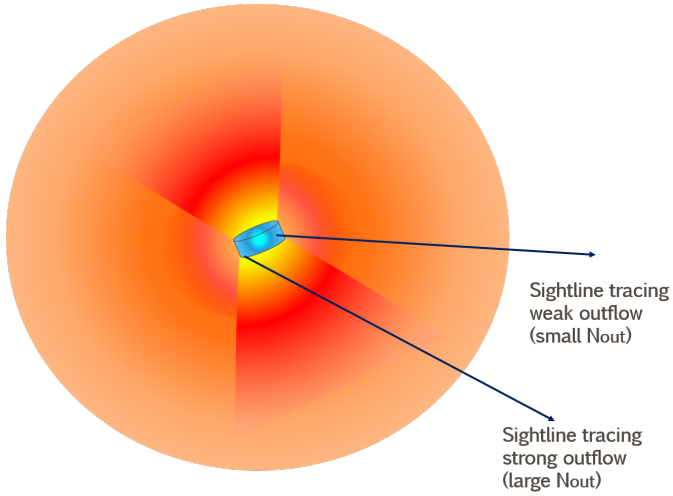


Figure 4.12: A schematic showing a stronger biconical outflow along the minor axis and weaker spherical outflow elsewhere. The narrow GRB sightlines are shown as arrows. Some of the narrow and randomly pointed GRB sightlines will trace the strong biconical outflow, giving a larger outflow column density, while others will trace the weaker outflow, giving a smaller outflow column density. This will produce a scatter in $N_{out} - SFR$ relation.

we do not observe as high $V_{max}$ values as seen in these studies. It is possible that this discrepancy is due to the small sample size (7 galaxies) in [Sugahara et al., 2019] or due to difference in the observational technique (down-the-barrel *vs* GRB sightlines).

## 4.6 Summary

We explored the outflow-galaxy correlations in low-mass ($M_* \sim 10^9 - 10^{11}$ $M_\odot$) star-forming galaxies at $z \sim 2-6$ using GRB sightline spectroscopy. This technique offers a narrow, off-centered, and randomly oriented sightline as opposed to a broad, down-the-barrel beam to probe the outflows in absorption. We summarize our results as follows:

1. SFR-driven outflows: We find strong correlations between outflow column density

($N_{out}$), outflow maximum velocity ($V_{max}$) and SFR. This correlation is stronger for high-ion outflows compared to low-ion outflows.

2. Correlation with $M_*$: We find a large spread, and therefore, weaker correlations of $N_{out}$ and $V_{max}$ in high-ion outflows with stellar mass. We find that this spread are almost entirely driven by the spread in SFR in a given stellar mass bin. On the other hand, we find that low-ion outflows are not correlated with stellar mass.

3. We observe a higher detection fraction in high-ions compared to low-ions (irrespective of the SFR or $M_*$) as well as typically higher $V_{max}$ and $N_{out}$ in high-ions, suggesting that the outflow is dominated by the warm phase traced by high-ionization lines.

4. We investigate how the normalized velocity ($V_{norm} = V_{max}/V_{circ,halo}$) depends on the halo mass ($M_{halo}$). We find that $V_{norm}$ declines with increasing halo mass, suggesting that the outflows from the low-mass halos are more likely to escape and enrich the outer CGM and/or IGM than those in the halos of higher masses. Also, we find a steeper decline in $V_{norm}$ for low-ions suggesting a systematic shift in the temperature distribution of the outflow as the halo mass increases.

5. sSFR and metal enrichment: While the sSFR is not correlated with either $N_{out}$ or $V_{max}$, we observe a strong correlation between $V_{norm}$ ($= V_{max}/V_{circ,halo}$) and sSFR at the 3-$\sigma$ and 3.7-$\sigma$ levels for C IV and Si IV, respectively, with $V_{norm} \propto sSFR^{0.25}$. This power law is consistent with the low-redshift results from [Heckman and Borthakur, 2016]. This result suggests that the outflows in galaxies with higher sSFR have higher velocities relative to the characteristic velocity of their halos. Thus, the outflows from high sSFR galaxies are more likely to escape and enrich the outer

CGM and IGM compared to low sSFR galaxies.

6. Redshift evolution: We do not observe any systematic difference in the $V_{max} - SFR$ and $N_{out} - SFR$ correlations (for high-ions) in our two redshift groups ($z1$: $2-2.7$ and $z2 : 2.7 - 6$) of similar size. This suggests that the correlations of the outflow with SFR do not significantly evolve with redshift and are more fundamental in nature.

7. Structure of the outflow: We observe a larger spread in the high-ion correlation with SFR beyond an SFR of $\sim$10 $M_{\odot}yr^{-1}$. We speculate that this spread could arise due to an emergence of structured outflow (eg: biconical) at high-SFR, leading to some sightlines cutting across a larger section of the outflow while others probing a weaker outflow. This characteristic can be uniquely probed using the GRB sightline technique due to the random orientation (i.e. not down the barrel) and narrow beam of the sightline (as shown in Fig. 4.12. However, a more detailed investigation of the physical processes in the outflows is needed to explain the observed spread in the outflow column densities at high SFR.

8. O VI-traced outflows: We observe tentative correlations of O VI-traced outflow with SFR and stellar mass. $N_{out}$ and $V_{max}$ appear to be better correlated with stellar mass than SFR, although the sample is small.

These results highlight the unique potential of GRB afterglow spectroscopy to explore the nature of stellar feedback at high redshifts.

## Acknowledgements

The authors are grateful to Drs. A. Cucchiara and V. Toy for their useful comments in the early stages of this paper. P.G. was supported by NASA Earth and Space Science Fellowship (ASTRO18F-0085) for this research. S.V. acknowledges partial support from the National Science Foundation under grant 1711377 and National Aeronautics and Space Administration under grant 16-APRA 16-0064.

These results made use of the Lowell Discovery Telescope (LDT) at Lowell Observatory. Lowell is a private, non-profit institution dedicated to astrophysical research and public appreciation of astronomy and operates the LDT in partnership with Boston University, the University of Maryland, the University of Toledo, Northern Arizona University and Yale University. The Large Monolithic Imager was built by Lowell Observatory using funds provided by the National Science Foundation (AST-1005313).

Based on observations made with ESO Telescopes at the La Silla Paranal Observatory under programme IDs 177.A-3016, 177.A-3017, 177.A-3018 and 179.A-2004, and on data products produced by the KiDS consortium. The KiDS production team acknowledges support from: Deutsche Forschungsgemeinschaft, ERC, NOVA and NWO-M grants; Target; the University of Padova, and the University Federico II (Naples).

# Chapter 5: Arrayed waveguide grating spectrometers for astronomical applications

*In this chapter, we will explore the design of AWGs, relevant issues, and a path towards an integrated photonic spectrograph.*

## 5.1 Introduction

The study of the first billion years of the universe, corresponding to cosmological redshifts $z \sim 6-12$ due to the expansion of the universe, is crucial to understand phenomena such as galaxy formation, the ionization of the intergalactic medium, and the formation and evolution of supermassive black holes. The rest-frame ultraviolet light coming from sources in this range of cosmological redshifts is shifted to the J and H bands ($1.15 - 1.4$ $\mu m$ and $1.45 - 1.7$ $\mu m$, respectively) in the near-infrared (NIR). Therefore, it is of astrophysical interest to study the NIR spectra of these distant and faint sources, for which large telescopes such as the Keck 10-meter telescopes are required. The next generation of ground-based extremely large telescopes (ELTs) in the optical and NIR will have diameters in the range of $20-40$ meters. This necessitates the development of suitable seeing-limited spectroscopic instrumentation for astrophysical studies [Bland-Hawthorn and Horton, 2006].

The application of photonic technologies [Pervez et al., 2010, Roelkens et al., 2013, Pathak et al., 2014] to astronomical spectroscopy is a promising approach to miniaturize the next-generation spectrometers for large telescopes [Harris and Allington-Smith, 2013]. This is attained mainly by leveraging the two-dimensional photonic structures on a chip [Chaganti et al., 2006, Bland-Hawthorn and Kern, 2009, Allington-Smith and Bland-Hawthorn, 2010, Subramanian et al., 2015], thus reducing the size of spectroscopic instrumentation to a few centimeters and the weight to a few hundreds of grams. Such integrated photonic spectrometers are also more amenable to complex light manipulation and massive multiplexing, cheaper to mass produce, easier to control, and much less susceptible to vibrations and flexures than conventional astronomical spectrographs with similar specifications (resolution, efficiency, and operating wavelength range) [Cvetojevic et al., 2010]. In this paper, we explore one such photonic technology, the arrayed waveguide gratings (AWGs), designed to be implemented as an astronomical spectrometer in the NIR H band.

## 5.2 Arrayed waveguide gratings

In many ways, arrayed waveguide gratings are analogous to conventional grating spectrographs (see Fig. 1 in [Gatkine et al., 2016]). In a conventional spectrograph, the light source illuminates the grating through an input lens, the grating creates a path difference between different light paths and the output lens focuses the emergent light on the focal plane. In an AWG, these actions take place on a chip, where the single-mode waveguides guiding the light serve as different light paths.

The light from the source is carried by a single-mode waveguide and launched into an input lens, called input free propagation region (FPR), where it illuminates an array of waveguides (similar to illuminating a grating). These waveguides are constructed to introduce a constant path difference between the adjacent waveguides, according to the spectral order. The light from the array of waveguides is focused in the output FPR, with different wavelengths interfering constructively at different spatial locations along the focal plane. The output waveguides carry this dispersed light for measurement. The various components of our AWG are shown in Fig. 5.2.

A detailed theory of AWG design is described in the pioneering work on AWG devices [Smit and Van Dam, 1996]. Traditionally, the AWG devices are used for wavelength division multiplexing (WDM) in telecommunication industry around a wavelength of 1550±50 nm. But in principle, the same theory can also be used for spectroscopic purposes. In particular, some of the recent work towards making low-loss AWG devices [Bauters et al., 2010, Dai et al., 2011, Akca et al., 2011] demonstrates the usability of these techniques for NIR spectroscopy. There have also been successful preliminary tests of using modified commercial AWGs for astronomical spectroscopy [Cvetojevic et al., 2012b, Cvetojevic et al., 2012a]. AWGs, along with other advances in the field of astrophotonics, such as photonic lanterns [Leon-Saval et al., 2010, Thomson et al., 2011, Birks et al., 2015] to convert multimode fibers to single mode fibers, Bragg gratings (in fibers [Othonos, 1997, Meltz et al., 1989, Trinh et al., 2013, Lindley et al., 2014] as well as on chips [Zhu et al., 2016a]) to suppress the unwanted atmospheric OH-emission background (in the NIR), and high-efficiency fiber bundles for directly carrying the light from the telescope focal

plane [Lawrence et al., 2012], offer a complete high-efficiency miniaturized solution for astronomical spectroscopy in the NIR. This solution has potential applications for future ground-, balloon- and space-based telescopes.

The technical requirements for our AWG spectrograph are driven by the science goals. Our main science goal here is the study of faint sources at high cosmological redshifts ($z \gtrsim 6$) to probe the first billion years of the universe. This requires a spectral resolving power ($\lambda/\delta\lambda$) of at least ~1500 in the H band to measure the redshifts of these sources and distinguish between different absorption lines produced by the intervening material between the observers and these sources [Vreeswijk et al., 2006, Salvaterra, 2015]. Also, a wide spectral range (preferably both J and H bands) is necessary to ensure that these absorption lines fall within the band-pass at cosmological redshifts larger than 6. The throughput of the spectrograph should at least be comparable to that of the conventional astronomical spectrographs (from slit to detector, typically ~20%, although this depends on the specific instrument and configuration [1] [2]).

In our previous paper [Gatkine et al., 2016], we demonstrated AWG spectrometers in the H band with a resolving power of 1250 and a peak overall throughput of 13% for transverse electric (TE) polarization. For practical implementation as a competitive astronomical spectrometer, this throughput needs to be improved. Also, the overlapping spectral orders of AWG (at the output focal plane) need to be cross-dispersed to extract the final spectrum, which requires the focal plane of the

[1] http://http://www.gemini.edu/sciops/instruments/gnirs/spectroscopy/slitsthroughputs
[2] https://www.subarutelescope.org/Observing/Instruments/MOIRCS/spec$_s$*ensitivity.html*

AWG to be exposed to the cross-dispersion optics [Cvetojevic et al., 2012b, Cvetojevic et al., 2012a]. This necessitates cleaving the AWG at its focal plane. The present paper addresses all of these issues. We first describe the procedures used to design, fabricate, and characterize the new AWGs. Two H-band AWG devices are fabricated to demonstrate the relevant techniques of coupling-taper optimization, annealing, and cleaving at the focal plane. A new way to design a polarization-insensitive AWG is discussed next. Future avenues of research to further improve the throughput of our devices and allow us to expand the wavelength range to the J band are discussed in the last section.

## 5.3 Methods

Two new AWGs are presented in this paper. Their characteristics are summarized in Table 5.1. The main difference between these two devices is the use of output waveguides in AWG #1, while AWG #2 has a cleaved, open-faced output. In this section, we discuss in detail the design, fabrication, and characterization methods of AWG #1. Most of this discussion also applies to AWG #2. The differences are discussed in detail in the next section.

### 5.3.1 Design

The selection of the waveguide material is crucial for building low-loss AWGs. In the recent past, $Si_3N_4$ has been proven to be one of the best suited materials for low-loss photonic devices [Dai et al., 2012]. Therefore, we use $Si_3N_4$ (refractive in-

Table 5.1: Summary of the characteristics of the two AWGs.

| | AWG #1 | AWG #2 |
|---|---|---|
| Waveguide cross-section | $2.0 \times 0.1\ \mu m$ | $2.0 \times 0.1\ \mu m$ |
| Number of waveguides | 34 | 34 |
| FPR length | $200\ \mu m$ | $200\ \mu m$ |
| $\Delta L$ | $172\ \mu m$ | $172\ \mu m$ |
| Separation between waveguides at array-FPR interface | $6\ \mu m$ | $6\ \mu m$ |
| Output waveguide spacing | $6\ \mu m$ | Cleaved, open faced |
| Inputs | Fiber-coupling tapers | Fiber-coupling tapers |
| Outputs | Fiber-coupling tapers | Cleaved, open faced |
| Footprint | 16 mm × 7 mm | 12 mm × 8 mm |

dex $\sim 2.0$) waveguides buried in $SiO_2$ (refractive index $\sim 1.45$) as shown in Fig. 5.1 for low on-chip transmission losses [Bauters et al., 2010, Gatkine et al., 2016]. The most important sources of losses in the AWGs are: a) the coupling loss (fiber to chip and vice versa), b) the sidewall scattering loss due to sidewall roughness and micro-cracks, c) the bending loss due to radiative loss (especially in weakly confined waveguide modes), and d) the absorption loss due to absorption features of the material and/or inadvertent impurities. In our previous work [Gatkine et al., 2016], we focused on sidewall scattering and bending losses by using a $2.8 \times 0.1\mu$m waveguide geometry and demonstrated a high on-chip throughput (peak $\sim 80\%$), but a relatively modest overall throughput ($\sim 13\%$). The present paper addresses this problem of low overall throughput.

The adopted geometry of the waveguides is shown in Fig. 1. A thickness of $0.1\ \mu m$ is selected for several reasons. Reproducibility of the fabrication process is

an important issue. It is easier to control the actual deposited thickness of the layer of nitride (within a tolerance of 5-10%) if it is $\sim 0.1\ \mu m$ or thicker. However, the sidewall scattering loss is proportional to the sidewall area and hence the height of the waveguide. So a $0.1\ \mu m$ thickness provides a balance between deposition non-uniformity and sidewall-roughness induced in the etching process [Bauters et al., 2010, Bauters et al., 2011b, Bauters et al., 2011a]. Moreover, with a thickness of $0.1\ \mu m$, we can use a relatively narrow waveguide and achieve a mode-confinement factor (13.3% for TE polarization) that is similar to that of a wider and thinner waveguide (eg. [Bauters et al., 2010]). This reduces the chip size and makes it easier to fabricate the devices with precise electron-beam lithography (e-beam writing time scales with the writing area). We select the waveguide width to be $2\ \mu m$, different from our previous $2.8\ \mu m$ design, because it helps in packing the same number of arrayed waveguides in a smaller area without degrading the confinement. With a relatively smaller footprint, it is easier to use a larger radius of curvature ($R_{min}$ = 2.5 mm) for the curved waveguides, thus preventing the curvature loss [Bauters et al., 2010]. In contrast to a waveguide with a square cross-section (such as $0.4 \times 0.4\ \mu m$), this high-aspect ratio waveguide is easier to fabricate; it has a greater tolerance for width errors and provides better etch-depth uniformity due to the thin structure. This waveguide geometry is also better matched to the taper geometry used to improve the fiber-AWG coupling efficiency [Zhu et al., 2016b], as described in section 4.1.

We calculated the mode profile for the $2\ \mu m \times 0.1\ \mu m$ waveguide using a full-

vectorial finite difference method simulation in FIMMWAVE software [3] and confirmed the single-mode nature of the waveguide over a wide range of wavelengths ($\lambda$ > 1000 nm). The simulated mode profiles for Transverse Electric (TE) and Transverse Magnetic (TM) polarizations at a wavelength of 1550 nm and the geometry of the waveguides are shown in Fig. 5.1. The index contrast of the waveguide is 23.7%. A moderate spectral order (m) of 165 (at $\lambda$ = 1600 nm) is used in this design to maximize the free spectral range and obtain the desired resolution, while keeping the required number of waveguides small (34 waveguides), thus reducing the electron-beam lithography time.

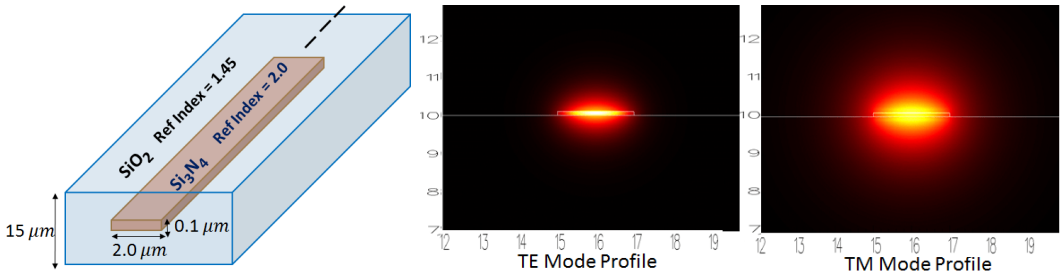


Figure 5.1: a) The $Si_3N_4/SiO_2$ waveguides used in AWG #1 and #2. b) Mode profile for TE ($n_{eff}$ = 1.4659) and TM polarizations ($n_{eff}$ = 1.4473). Note that the TM mode is weakly confined. The mode profiles are shown in the units of $\mu m$.

With these initial parameters, we designed an AWG for the H band (1450−1650 nm) using the design algorithm prescribed in [Smit and Van Dam, 1996]. To design the AWG, we used a central wavelength of 1550 nm and a desired spectral channel spacing of 1.6 nm. The H band is covered in 23 spectral orders, with a free spectral range (FSR) varying from 8 nm at a wavelength of 1450 nm to 10 nm at 1650 nm

[3] https://www.photond.com

($FSR \approx \lambda_0/m \times n_{eff}/n_{group}$, where $n_{eff}$ and $n_{group}$ are the effective and group indices of refraction, respectively). Five output waveguides are used to sufficiently sample the output FPR for AWG characterization. The AWG has a total of 34 waveguides in the array to ensure adequate sampling of the input free propagation region (FPR). The length difference ($\Delta L$) between adjacent waveguides of the array is 172 $\mu m$ ($\Delta L = m \times \lambda_0/n_{eff}$). The spatial channel spacing at the output FPR is 6 $\mu m$. The length of the FPR is 200 $\mu m$. The tapers at the input and output FPRs are linear, with a length of about 30 $\mu m$ and a width equal to the waveguide separation at the FPR (hence, the taper width at the FPR is 6 $\mu m$). This ensures optimal transmission of light from the FPR to the array of waveguides and vice versa. Such a geometry of touching tapers requires a precise fabrication which is made possible with electron beam lithography (within a tolerance of 10 nm). The minimum bending radius in the layout is 2.5 mm to reduce the curvature loss. Some straight and curved reference waveguides are also fabricated below the AWG to characterize the on-chip loss of the AWG. A coupling taper was added (on the chip) for all of the devices presented in this paper to optimize the coupling between the fiber (UHNA3) and the waveguide (further details are in section 4.1). The AWG layout is shown in Fig. 5.2

### 5.3.2 Fabrication

The fabrication sequence was the same as the one used in our earlier paper [Gatkine et al., 2016]. For completeness, it is summarized in Fig. 5.3 and briefly

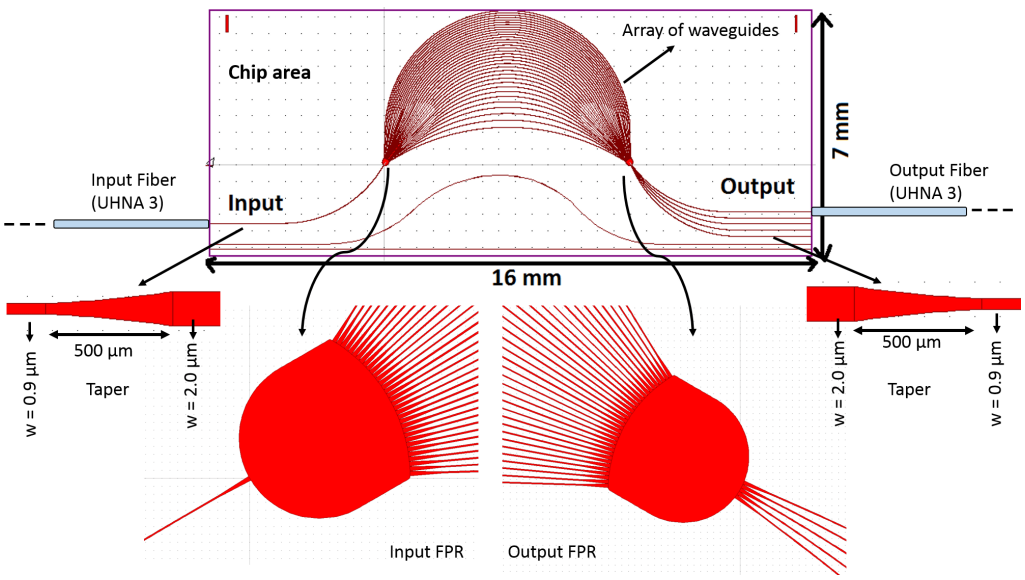


Figure 5.2: CAD of AWG #1. Note the vertical cleaving marks near the top corners of the chip to aid cleaving the edges to expose the optical quality cross-section of the waveguides for fiber coupling. The extra waveguides at the bottom are reference waveguides for calibration. The AWG has a small footprint of only 16mm × 7mm. The actual writing area is 11.5 $mm^2$, thus making it suitable for e-beam lithography. The AWG input, output and the reference waveguides have on-chip coupling tapers as a continuation of the waveguides, shown in left and right insets. UHNA3 fibers are used for characterization by butt-coupling one by one to the tapers. A zoomed-in version of the input and output FPRs are shown at the bottom for clarity.

described here again. A silicon wafer, pre-deposited with 10 $\mu m$ layer of thermal silica ($SiO_2$), was used for the fabrication of the AWG chip. A 0.1 $\mu m$ thick layer of silicon nitride ($Si_3N_4$) was deposited on top of that using LPCVD (Low Pressure Plasma Enhanced Deposition). A smaller sample of the wafer (30 × 15 mm) was obtained by dicing the wafer. The process sequence followed to fabricate the buried silicon nitride AWG device was: spin-coating the photoresist on the sample, electron-beam lithography (moving e-beam to write the pattern), electron-beam chromium metal deposition, chromium lift-off (leaving only the chromium mask for etching), reactive ion etching (RIE) to a depth of 0.1 $\mu m$, chromium etching to dissolve the

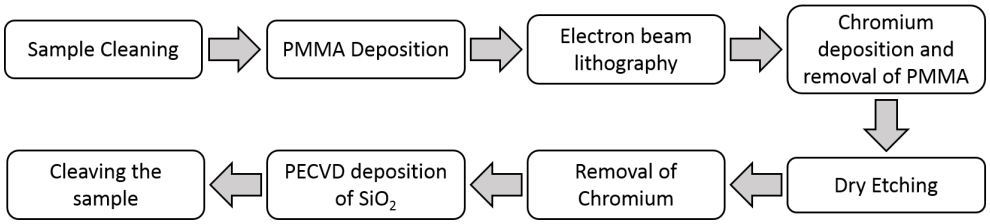


Figure 5.3: Fabrication sequence of AWGs [Gatkine et al., 2016].

mask and finally, PECVD (Plasma Enhanced Chemical Vapor Deposition) of 6 $\mu m$ of $SiO_2$ as the upper cladding layer of the device. After fabrication, the sample was cleaved at precise locations from left and right (along the crystal plane of the chip) to expose facets of the input and output waveguides for coupling the light. The facets were then examined for optical quality.

### 5.3.3 Characterization

To characterize the transmission response of the AWG, we used a polarization maintaining broadband superluminescent diode source by Thorlabs (S5FC1550P-A2, amplified spontaneous emission power of 2.5 mW) operating in a waveband of 1450 nm − 1650 nm (corresponding to 20 dB width). An Optical Spectrum Analyzer (OSA, YOKOGAWA AQ6370C) with a dynamic range of 72 dB across the H band was used to analyze the signal. Ultra-high numerical aperture (UHNA3) fibers with a typical mode-field diameter ($1/e^2$ diameter) of 4.1 $\mu m$ and a numerical aperture of 0.35 were used to carry the signal from the broadband source to the AWG and out to the OSA. These fibers are single mode over the entire range of H band. In the characterization setup, a UHNA3 fiber was connected to the broadband

source and butt-coupled to the AWG input waveguide through a fiber polarization controller (Thorlabs, FPC561) and a fiber rotator. The combination of polarization controller and fiber rotator were used to control the polarization since UHNA3 is not a polarization maintaining fiber. Another UHNA3 fiber was butt-coupled to one of the output waveguides and connected to the OSA. The optical butt-coupling of the fibers to the facet of the chip was done by carefully aligning the fibers and the AWG chip using a 9 degree-of-freedom alignment setup. An index matching solution (index = 1.45) was used to minimize any reflections at the fiber-waveguide interface. The characterization setup is shown in Fig. 5.4.

The broadband light source was measured to be steady as a function of time within 0.05 dB. The output fiber was coupled to each of the AWG output channels one-by-one and the transmission response (end-to-end) of each channel was recorded with the OSA. Similarly, the transmission response of the curved reference waveguide was obtained by butt-coupling the fibers to it. This transmission response (fiber-AWG-fiber) was normalized to the input power spectrum (fiber-fiber) to obtain the 'overall AWG response' (including the coupling efficiency). The overall AWG response was further normalized to that of the curved reference waveguide to isolate the 'on-chip response' of the AWG.

## 5.4 Results

In this section, we describe our results emphasizing three critical aspects of the new AWG devices: 1. fiber-coupling tapers, 2. annealing, and 3. cleaving at

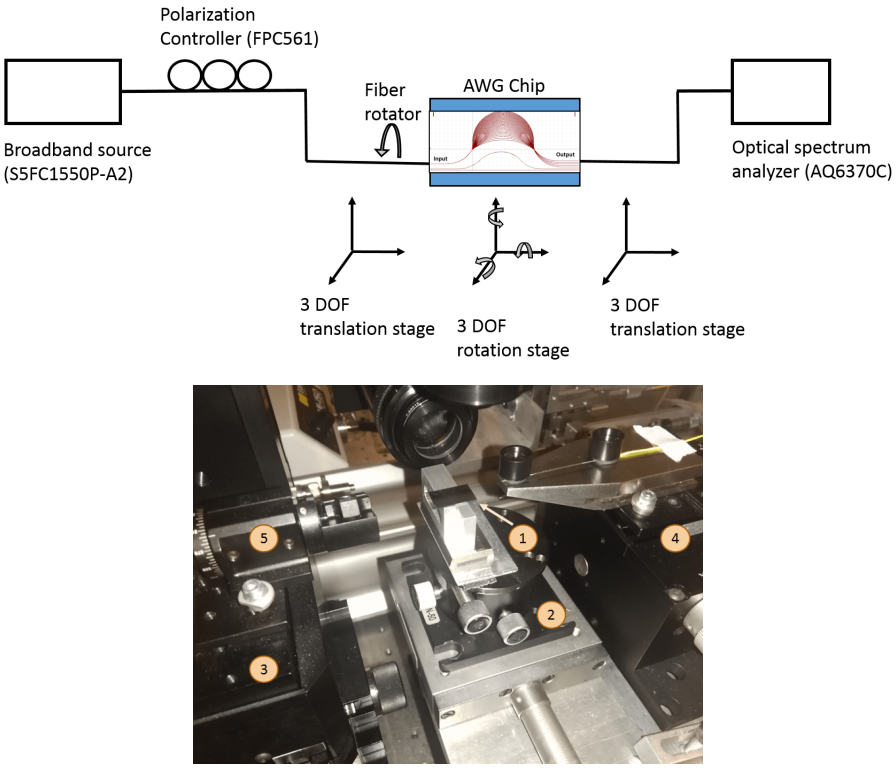


Figure 5.4: Top panel: A schematic of the setup used for AWG characterization. Bottom panel: The AWG sample (label 1) is mounted in the center on top of a tip-tilt-rotation mount (label 2). The input and output fibers are mounted on 3-axis stages with 10 nm precision (left:3 and right:4). The input fiber is mounted on a fiber rotator (label 5), which, along with the polarization controller, allows for polarization tuning.

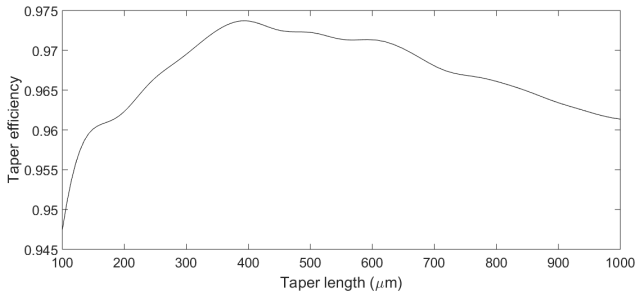


Figure 5.5: Simulation of taper conversion efficiency as a function of length for a linear taper. Here, we have also taken into account an estimated propagation loss for the taper of 1.5 dB/cm.

the output FPR. All of the results are measured for TE polarization.

### 5.4.1 AWG #1: fiber-coupling taper

Zhu et al. [Zhu et al., 2016b] demonstrated a coupling efficiency of >90% (1450 - 1650 nm) using UHNA3 fiber and 0.9 $\mu m$ × 0.1 $\mu m$ waveguide geometry for TE polarization. In this paper, we present a taper geometry to convert a weakly guided fiber-side waveguide cross-section (0.9 $\mu m$ × 0.1 $\mu m$) to a relatively strongly guided AWG-side waveguide cross-section (2.0 $\mu m$ × 0.1 $\mu m$) to improve the coupling efficiency and thus, the overall transmission of the AWG. In Fig. 5.5 we show the simulated conversion efficiency of a linear taper for this configuration as a function of the taper length for TE mode. Here, we have also added an estimated propagation loss for the taper ($\sim$ 1.5 dB/cm [Zhu et al., 2016b]) to find the optimal taper length. Thus, we selected a length of 500 $\mu m$ for the taper. This taper geometry is shown in Fig. 5.2 and is used on both the input and output sides of the AWG and reference waveguides.

AWG #1 was characterized according to the procedure discussed in section

5.3.3. Figure 5.6 shows the overall transmission (fiber-AWG-fiber) of the 2.0 $\mu m$ $\times$ 0.1 $\mu m$ AWG and that of the curved reference waveguide, both with coupling tapers on the input and output ends. The points indicate the transmission for the central wavelengths of each spectral order of the AWG. The second panel shows the on-chip throughput of the AWG (i.e. AWG transmission normalized to the curved reference waveguide). Note that the on-chip throughput is roughly uniformly high over the entire H band. The peak overall transmission is about 23% (−6.4 dB), which is twice that of our previous AWGs [Gatkine et al., 2016]. The fiber-taper coupling efficiency is $\sim$ 95% ($\sim$ 0.22 dB) per facet at 1550 nm [Zhu et al., 2016b] and the extra loss due to curvature of the waveguides is negligible compared to the propagation loss, since the minimum bending radius used is 2.5 mm [Bauters et al., 2010]. Thus, the propagation loss is about 1.5dB/cm after accounting for coupling and taper losses. The additional AWG loss is roughly 3 dB (50%) at 1.6 $\mu m$, which is due to additional propagation loss in the curved waveguides of the AWG of $\sim$ 0.3dB (from the length in excess of reference waveguide) and the loss at the waveguide-FPR interfaces of $\sim$0.7 dB per interface (i.e. 85% transmission per interface). This is a major contributor to the on-chip loss since there are four such interfaces.

Therefore, the waveguide-FPR interface taper needs to be further optimized for a better conversion efficiency between the slab mode of the FPR and the waveguide mode. The overall transmission degrades towards shorter wavelengths as a result of scattering from stress-induced microcracks [Irene, 1976] and broad absorption features due to hydrogen bonds to silicon, nitrogen, and oxygen in the PECVD

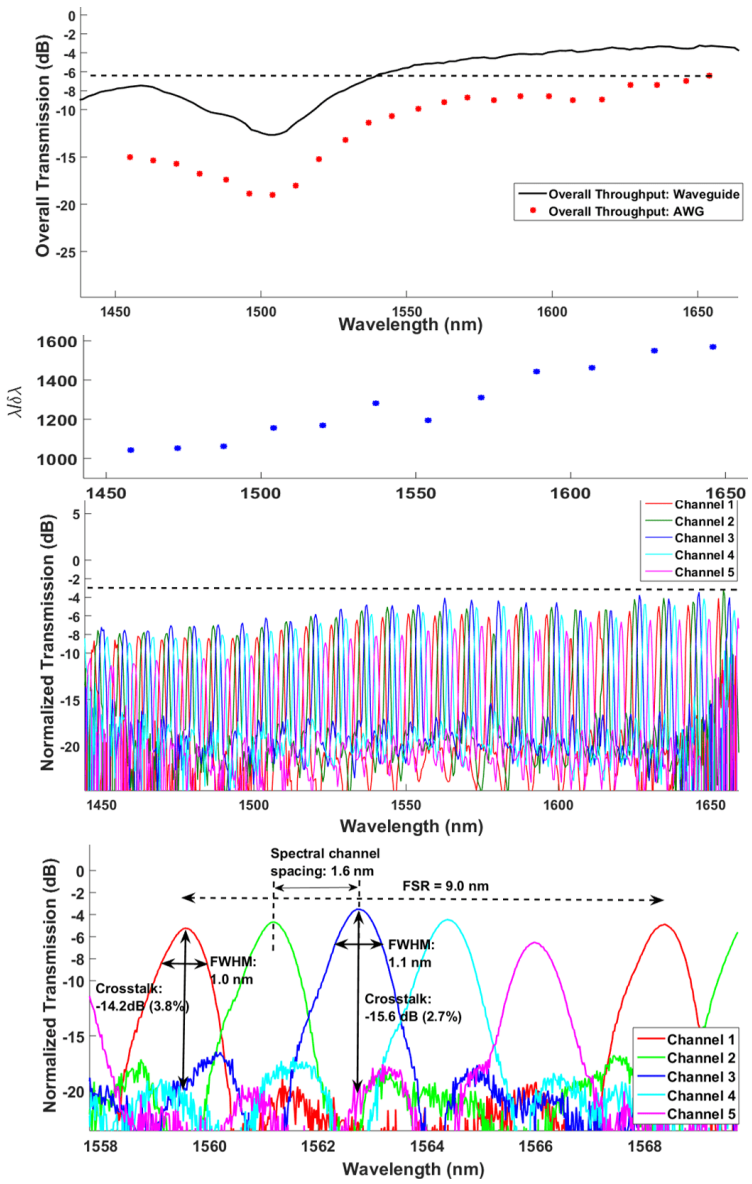


Figure 5.6: Panel 1: The overall throughputs of AWG #1 and the curved reference waveguide are shown. The dashed line indicates the peak overall throughput of the AWG (about $-6.4$ dB or $\sim 23\%$). The red dots represent the overall throughputs measured in the centers of the orders. Panel 2: The measured resolving power of the AWG as a function of wavelength. Panel 3: The transmission of the AWG normalized to the curved reference waveguide is shown for all 23 spectral orders. The five colors show the 'on-chip throughput' of the five output channels. The dashed line represents the peak on-chip (i.e. normalized to the reference waveguide) throughput of the AWG (about $-3$ dB or $\sim 50\%$). Panel 4: A more detailed view of one of the spectral orders is presented to show the FSR, spectral FWHM, spectral channel spacing, and crosstalk. The measurement errors are less than 0.1 dB, so no error bars are shown.

$SiO_2$ and LPCVD $Si_3N_4$. The broad absorption at 1505 nm due to Si-H bonds is particularly pronounced. We address the absorption problem in the next section.

The crosstalk of the AWG is in the range of −15 to −16 dB at wavelengths longer than 1540 nm. At shorter wavelengths, the crosstalk slowly increases to reach −10 dB at 1450 nm. This variation may not be real, since the source power drops by 20 dB at 1450 nm (compared to the power at 1550 nm). Therefore, the crosstalk degradation might simply be due to the Optical Spectrum Analyzer hitting the noise floor. It should be noted that, in an astronomical spectrograph, the spectral FWHM is the important parameter rather than the crosstalk. So a crosstalk of about −10 dB is acceptable. The spectral FWHM of the output channels is 1.2 ± 0.2 nm, which implies a spectral resolving power ($\lambda/\delta\lambda$) of roughly 1300. The measured resolving power as a function of wavelength is shown in the second panel of Fig. 5.6. The non-uniformity among the five channels within a spectral order, as seen in the bottom panel of Fig. 5.6, is due to the intensity envelope of the far-field pattern of the waveguides which illuminates the output FPR. These differences in intensity can be reduced by using suitable mode-field converters at the interface of arrayed waveguides and the output FPR [Sakamaki et al., 2009].

### 5.4.2 AWG #1: annealing

The hydrogen-bonds (especially Si-H) in the PECVD $SiO_2$ cladding cause a broad absorption feature seen in the overall transmission of the AWG [Henry et al., 1987]. We use high-temperature annealing of the sample to liberate the

trapped hydrogen and minimize the absorption. For this, we use a custom recipe of progressively heating the sample in the annealing chamber (in the presence of air) to 800°C and 1000°C for 30 minutes each, then heating up to 1200°C for 2 hours, followed by a progressive cool down. The overall transmission of the annealed sample and comparison with the original AWG (prior to annealing) is shown in Fig. 5.7. The main advantage of the annealed AWG is the improvement of the overall throughput in the 1475−1525 nm range. The overall throughput improved from 1.2% (−19.0 dB) at 1504 nm in the original AWG to 3.2% at 1508 nm in the annealed AWG for the same spectral order. However, at longer wavelengths, a degradation of the overall throughput is observed. The overall throughput dropped from 20% (−7.0 dB) at 1646 nm for the original AWG to 12% (−9.2 dB) at 1651 nm for the annealed AWG for the same spectral order. The propagation loss is estimated to be $\sim$ 2.6 dB/cm, from the comparison between the reference waveguide transmissions of the original and annealed reference waveguides. Thus, the annealing treatment removes the absorption peak, but it also reduces the overall transmission of the waveguides and the AWG. We believe this is due to the micro-cracks generated by stress along the $Si_3N_4/SiO_2$ interface at high temperatures. One way to alleviate this issue is to use LPCVD for the deposition of cladding $SiO_2$. We plan to explore this problem in the future. As shown in Fig. 5.7, the central wavelengths of the spectral orders also shift towards longer wavelengths by $\sim$ 4-5 nm due to densification, a thermally induced increase of $\sim$ 0.3% in the index of refraction of $SiO_2$ (this increment was calculated by comparing the central wavelength, $\lambda = n_{eff}\Delta L/m$ before and after annealing).

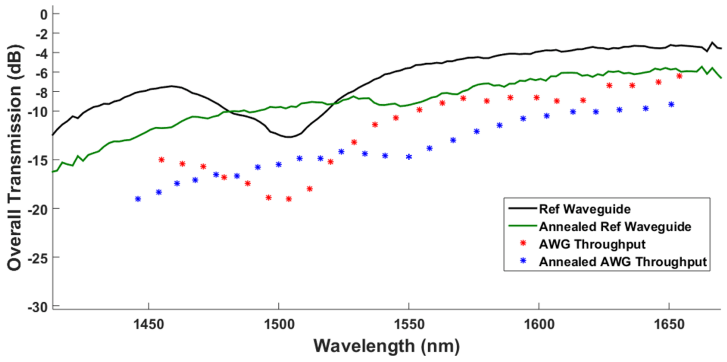


Figure 5.7: The overall transmission of AWG #1 and the curved reference waveguide before and after annealing. The absorption peak near 1500 nm is mitigated to a large extent by the annealing process, but the overall throughput has degraded. The wavelength shift between the order centers of the original and annealed AWGs is due to a change in the effective index of refraction of the waveguides as a result of annealing.

### 5.4.3 AWG #2: cleaving at the output FPR

For astronomical applications, the AWG needs to be connected to cross-dispersion optics to separate the spectral orders in the perpendicular direction and create a continuous 2D spectrum [Cvetojevic et al., 2012b] (unlike the discrete channels of an AWG). For this, the output FPR of the AWG needs to be exposed to illuminate the cross-dispersing optics. In this subsection, we present an AWG chip cleaved at the output FPR and the results of its characterization. The design of this AWG is the same as the first AWG, except that the output waveguides are not present. The fiber-coupling tapers are therefore used only on the input side. The CAD of this AWG is modified so as to have the focal plane of the output FPR along the crystal plane of the wafer for optical-quality cleaving. The length of the input waveguide is kept the same as that in AWG #1. The modified CAD is shown in Fig. 5.8. Since

the cutting edge has a tolerance of only about 10 $\mu m$, we added an extra rectangle of width 40 $\mu m$ at the end of the FPR to ensure that the light continues to propagate through the nitride region (i.e. FPR slab) even if there is an unintended offset in the cleaving position of a few tens of microns from the focal plane of the output FPR. In case of a cleaving offset, the effect of the extra rectangular section can be assessed by considering the extra length as an effective increment in the length of output FPR slab. This will alter the spectral channel spacing for a spectral order $m$, according to the following relation [Takahashi et al., 1995]:

$$\Delta\lambda = \frac{n_{slab}}{m} \times \frac{D_i D_o}{L_o}, \tag{5.1}$$

where $\Delta\lambda$ is the spectral channel spacing, $L_o$ (= 200 $\mu m$ + cleaving offset) is the length of the output FPR, and $D_i$ and $D_o$ are the waveguide separation at the FPR-output interface (6 $\mu m$) and arrayed waveguide-FPR interface (6 $\mu m$), respectively. Hence, for each spectral order, $\Delta\lambda$ is inversely proportional to $L_o$ and $d(L_o)/L_o = -d(\Delta\lambda)/\Delta\lambda$. Also, the focal plane of the AWG (i.e. the output FPR) is on the Rowland circle and therefore curved, but the cleaving happens along a line (i.e. crystal plane). This will cause a phase-mismatch of the interfering waves leading to a distortion of the spectral field pattern.

The sample was cleaved and had an unintended offset of nearly 20 $\mu m$ (10% of the length of FPR) from the focal plane of FPR (as shown in Fig. 5.8). The AWG was annealed and characterized with a UHNA3 fiber scanning across the output FPR line over a range of 12 $\mu m$ in steps of 2 $\mu m$, with a positional accuracy of 0.1

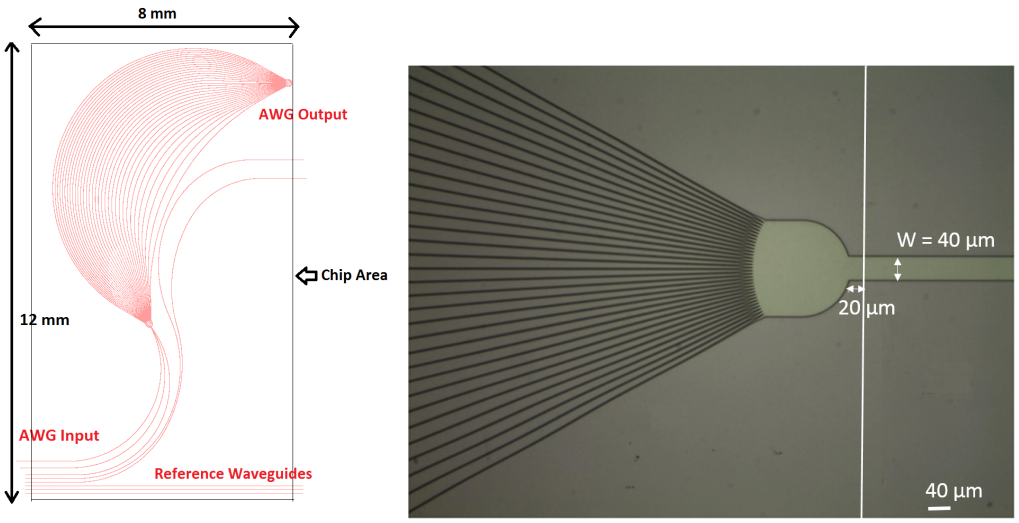


Figure 5.8: a) The modified CAD of AWG #2 to maintain the cleaving plane parallel to the crystal plane of the wafer. As a result, the device footprint is slightly smaller than Fig. 5.2. Out of the three inputs seen in the CAD, only the central input waveguide was used for characterization, the other two are redundant. b) A microscope image showing the extra rectangular region added to the output FPR to accommodate the cleaving tolerance of few tens of microns. The sample described in the text and Fig. 5.9 was actually cleaved with an unintended 20 $\mu m$ offset (indicated by the vertical white line).

$\mu m$. The same characterization setup as Fig. 5.4 was used.

The top panel of Fig. 5.9 shows a section of the spectral response (overall throughput) at six consecutive points (spaced by 2 $\mu m$) around the center of the FPR. For comparison with the transmission of the annealed AWG #1, the response needs to be integrated over 6 $\mu m$ (since the spatial output channel spacing of the AWG is 6 $\mu m$, as described in section 3.1). When the fiber samples a region of the FPR, the observed power is the convolution of the mode-profile of the fiber and the spatial distribution of power at the FPR. Therefore, ideally, the fiber response should be de-convolved from the observed power to obtain the spatial distribution of power across the FPR and then it should be integrated over 6 $\mu m$ for accurate comparison. However, such treatment would require a much finer scan with the

fiber with spatial steps of the order of 0.5 $\mu m$ across the FPR. This problem can be circumvented if we use a fiber with a narrow mode-size (FWHM) and arithmetically sum the outputs of the sampled sections of the FPR over 6 $\mu m$ to get the integrated power over 6 $\mu m$. The UHNA3 fiber has a narrow mode-FWHM of 1.6 $\mu m$ at 1550 nm. Therefore, it is safe to sum three consecutive steps of 2 $\mu m$ to obtain the integrated power over a 6 $\mu m$ region of the FPR. This integrated power is measured at the center of the scan range (in blue) and also at a point 6 $\mu m$ offset from the center (in red) in the bottom panel of Fig. 5.9.

As mentioned earlier, the added rectangle allows for cleaving offsets, albeit at the cost of introducing distortions of the spectral intensity distribution. The peak throughput at the output face of the FPR is 26% (−5.9 dB). For comparison, the overall throughputs of the annealed AWG #1 (shown in Fig. 5.7) and annealed-cleaved AWG #2 are 12% (−9.2 dB) and 19.4% (−7.1 dB), respectively, for the same spectral orders at $\sim$ 1650 nm. This improvement in throughput can be explained as a result of the absence of the output waveguides (avoiding $\sim$ 1.5 dB in propagation loss, estimated from section 4.2), the absence of coupling and taper losses ($\sim$ 0.4 dB), and the replacement of the output FPR-waveguide interface with an FPR-fiber interface. Note that the propagation loss in the annealed AWG was $\sim$ 2.6 dB/cm as estimated in section 4.2. The throughput for the 6 $\mu m$ offset channel is lower than the central channel by about 1-1.5 dB. A possible reason for the attenuation is the offset between the curved FPR focal plane and the actual cleaving plane, which results in increasingly out-of-focus images at locations far from the center.

In AWG #2, the 20 $\mu m$ offset is 10% of the length of the FPR and therefore

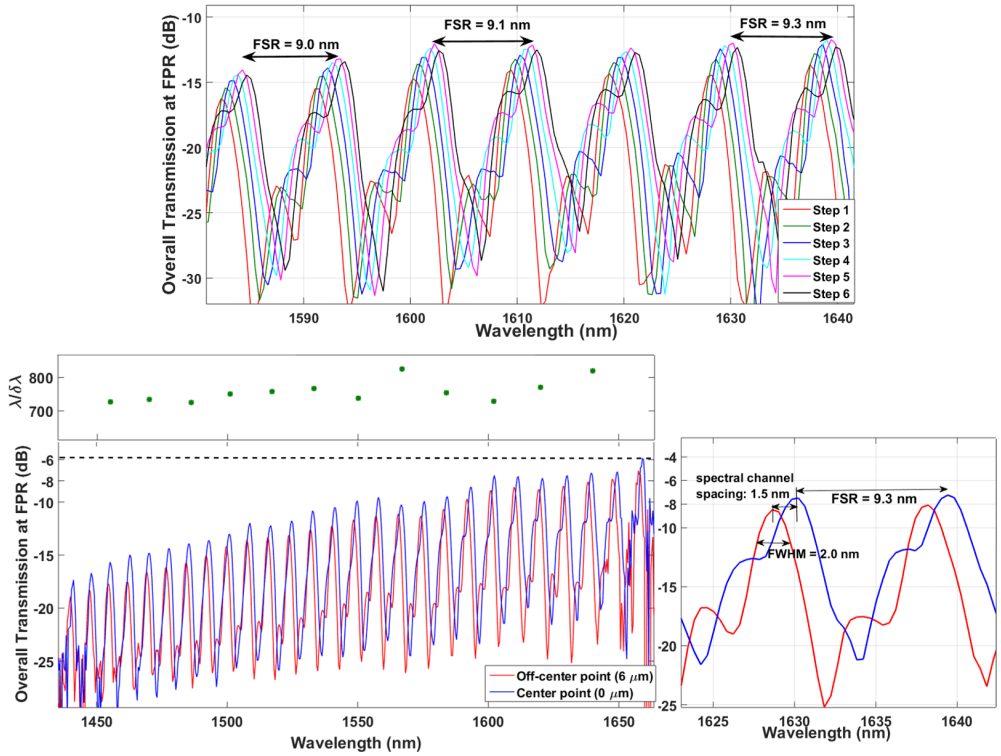


Figure 5.9: Top panel: A section of the spectral response (overall throughput) of AWG #2 at six consecutive points (spaced by 2 $\mu m$) around the center of the FPR. Bottom left panel: The overall throughput integrated over a length of 6 $\mu m$ along the FPR. The blue line shows the integrated throughput for the central point and the red line shows the same for a point 6 $\mu m$ offset from the center. The dashed line indicates the peak overall throughput. The window above shows the measured variation of resolving power as a function of wavelength. Bottom right panel: A zoomed-in view of a section of the 6 $\mu m$ integrated throughput response, showing the FSR, spectral channel spacing, and spectral FWHM.

results in the spectral channel spacing also being reduced by $\sim$ 10% (following eq. 5.1). As expected from this, the wavelength separation is 1.5 nm at 1630 nm between the center and the off-center response instead of 1.6 nm for the original AWG (note that 6 $\mu m$ is the spatial separation of the adjacent output channels of the designed AWG, as described in section 3.1). Further, the resolving power of the AWG has degraded as a result of de-focusing of the constructive interference peaks. The spectral FWHM measured in the central channel is 2 nm at a wavelength of 1630 nm, resulting in a resolving power ($\lambda/\delta\lambda$) of 815 instead of $\sim$ 1300 for the original AWG. Also, there are substantial sidelobes in the AWG response, as seen in the bottom right panel of Fig. 5.9. This is possibly due to a phase-mismatch of the interfering waves since the cleaving happens along a straight line instead of the curved focal plane on the Rowland circle. Resolving these problems will require tuning the path differences in the array of waveguides so that the focal plane is flat instead of a Rowland circle [Lu et al., 2003]. Despite these issues, the device is made robust to cleaving offsets due to the added rectangular patch, without which the throughput would have substantially dropped due to reflections at the silicon nitride − silion oxide interface in addition to de-focusing distortions. Therefore, the idea of adding the extended rectangle to the end of the FPR is pertinent to planning the next step of cross-dispersion and building an integrated photonic spectrograph.

## 5.5 Polarization insensitivity

The results presented in the previous section are for TE polarization. The TM mode is more lossy due to its weakly confined mode profile (with a confinement factor of $\sim 2\%$), leading to a substantial curvature loss in the AWG. For faint unpolarized astronomical sources, it is important to have a polarization-insensitive spectrograph to obtain maximum signal-to-noise ratios. The AWGs we presented here are based on rectangular ridge waveguides which make them intrinsically anisotropic and therefore birefringent. The TE and TM mode responses will be offset for any spectral order (by roughly $\Delta n_{eff}/n_{eff} \times \lambda$, where $\Delta n_{eff}$ is the difference between the effective indices of the TE and TM polarizations), unless special measures are taken to make the AWG polarization insensitive. One solution involves inserting a quarter-wave plate at the AWG axis of symmetry to equalize the path difference for the TE and TM modes [Takahashi et al., 1992]. But this method involves the added complexity of inserting material in the chip, which might incur substantial reflection losses. Another method is to have waveguides with a square cross-section. The fabrication of square waveguides with a high confinement factor (>10%) will require a thick (> 300 nm) deposition of $Si_3N_4$. This might lead to an additional sidewall scattering loss due to the non-uniformities associated with deep etching [Bauters et al., 2011a] and high stress in the deposited layers [Irene, 1976, Smith and Collins, 1990]. Also, a deeper etch would potentially make the thinnest structures in the AWG (eg. taper structures) more fragile, and thus the overall fabrication process more difficult. A better solution would be to achieve polarization independence

in waveguides with rectangular or square-like cross-sections that can be fabricated without inducing excessive stress associated with the thicker nitride deposition. One solution towards a polarization independent design is discussed next.

A polarization independent AWG may be designed by tuning the waveguide geometry to get different spectral orders of TE and TM modes to precisely overlap each other, thereby creating an apparent polarization independent response. Assume a birefringent waveguide with TE mode effective index ($n_{eff,TE}$) and TM mode effective index ($n_{eff,TM}$). Also, in our case, we know that ($n_{eff,TM} < n_{eff,TE}$). Say, at a particular wavelength $\lambda$, the TE mode is in spectral order $m$ and the TM mode is in spectral order $m'$. The AWG has a uniform incremental path difference between adjacent waveguides ($\Delta L$), which has to be the same for both polarizations since it is a fixed spatial length, and is given by [Okamoto, 2010]:

$$\Delta L = \frac{m\lambda}{n_{eff,TE}} = \frac{m'\lambda}{n_{eff,TM}} \tag{5.2}$$

For $m' = m - p$ where $p$ is an integer, we get the condition for order overlap polarization independence,

$$\frac{n_{eff,TM}}{n_{eff,TE}} = 1 - \frac{p}{m} \tag{5.3}$$

Thus, if we find a waveguide geometry with $n_{eff,TE}$ and $n_{eff,TM}$ such that it gives an integer solution to $p$, then we will essentially get the $m^{th}$ order of TE and the $(m-p)^{th}$ order of TM overlapping to give an apparent polarization independence. As an example, consider waveguides with a thickness of 100 nm and a width close

Table 5.2: Search for appropriate waveguide geometry (integer solution to $p$) for a polarization insensitive AWG for TE order = 165

| Width (nm) | Height (nm) | TE ($n_{eff,TE}$) | TM ($n_{eff,TM}$) | $p$ |
|---|---|---|---|---|
| 1000 | 100 | 1.4445 | 1.4436 | 0.59 |
| 1200 | 100 | 1.4494 | 1.4442 | 0.95 |
| 1400 | 100 | 1.4567 | 1.4452 | 1.30 |
| 1900 | 100 | 1.4647 | 1.4469 | 2.00 ** |
| 2600 | 100 | 1.4718 | 1.4492 | 2.54 |
| 3000 | 100 | 1.4744 | 1.4502 | 2.70 |

to 2 $\mu m$ to for a geometry that can give an integer solution to $p$ around our spectral order of 165 at a wavelength of 1600 nm. The search is summarized in Table 5.2. The solution was found to be $p = 2$ at width = 1.9 $\mu m$. Therefore, an AWG, constructed with a waveguide geometry of 1.9 $\times$ 0.1 $\mu m$ and designed to have a spectral order ($m$) of 165 at 1600 nm wavelength, will have an apparent polarization independence around 1600 nm due to the overlap of $165^{th}$ TE spectral order and $163^{th}$ TM order. This technique can also be used to attain apparent polarization independence by fixing the waveguide geometry and tuning the spectral order for the overlap. In the future, we will explore this property as a factor in selecting the waveguide geometry for the AWG. One important aspect of this approach is the impact of the refractive index dispersion coefficients for TE and TM modes on the free spectral range (FSR) as a function of wavelength. The FSR is given by:

$$FSR = \frac{\lambda}{m} \times \frac{n_{eff}}{n_{group}}, \tag{5.4}$$

where $n_{group}$ is the group index ($n_{group} = n_{eff} - \lambda \frac{dn}{d\lambda}$). Comparing the TE (order $m$)

and TM (order $m-p$) FSRs, we get:

$$\frac{(FSR)_{TE}}{(FSR)_{TM}} = \frac{m-p}{m} \times \frac{n_{eff,TE}}{n_{eff,TM}} \times \frac{n_{group,TM}}{n_{group,TE}} = \frac{m-p}{m} \times \frac{n_{eff,TE}}{n_{eff,TM}} \times \frac{(n_{eff} - \lambda\frac{dn}{d\lambda})_{TM}}{(n_{eff} - \lambda\frac{dn}{d\lambda})_{TE}} \tag{5.5}$$

Achieving the polarization insensitivity across several orders would require this ratio to be close to unity within 1-2% to avoid any significant offset between TE and TM spectral responses. For materials or geometries yielding small dispersion coefficients, a ratio of FSRs close to unity can be attained for a large m. For large spectral orders (say, $m > 100$) and small $p$ ($\sim 1$), the ratio of FSRs will be determined by $\frac{n_{eff,TE}}{n_{eff,TM}} \times \frac{n_{group,TM}}{n_{group,TE}}$, which needs to be as close to unity as possible. To investigate this ratio, we simulated several single-mode waveguide geometries for a silicon nitride waveguide buried in silica cladding. The simulations were performed using the full-vectorial FDM solver in the FIMMWAVE software[4]. It was found that for a fixed height, the wider waveguides yielded higher values for this ratio. In Fig. 5.10, the calculated ratios for the widest single-mode waveguide geometries are shown for the heights of 50 nm, 100 nm, 200 nm, and 300 nm. It was found that 5000 × 50 nm and 2000 × 300 nm are better-suited geometries for this method of polarization independence over a broad band. This technique can also be used for rectangular waveguide geometries and in materials with smaller dispersion coefficients such as $SiO_2$.

For non-square waveguides, the mode sizes for TE and TM modes will be different. Consequently, the resolving powers will also be different for the two polar-

[4]https://www.photond.com

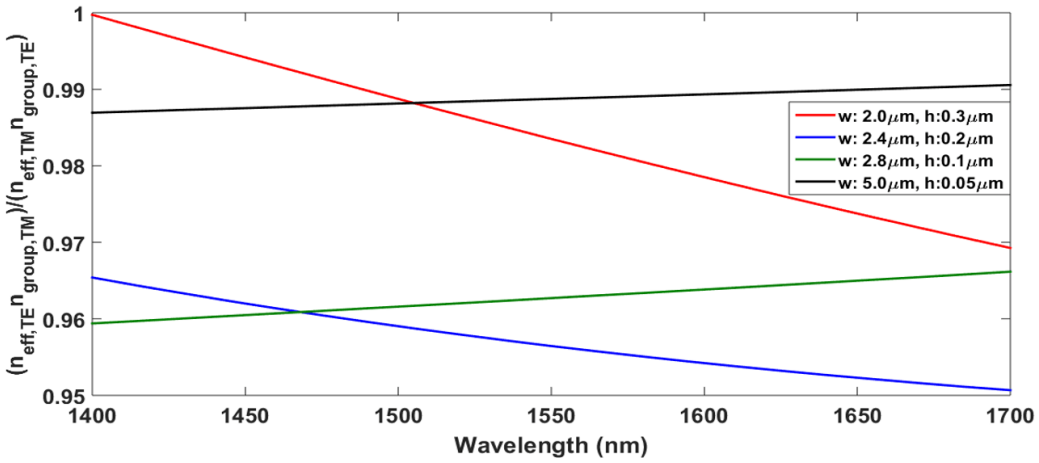


Figure 5.10: The ratio $\frac{n_{eff,TE}}{n_{eff,TM}} \times \frac{(n_{eff} - \lambda \frac{dn}{d\lambda})_{TM}}{(n_{eff} - \lambda \frac{dn}{d\lambda})_{TE}}$ (see eqn. 5) as a function of wavelength for a set of different single-mode waveguide geometries. A ratio close to unity is desirable to achieve broadband polarization insensitivity over a broad band using the TE-TM order overlap method.

izations, with the larger mode-size polarization leading to a lower resolving power [Janz et al., 2006]. Therefore, for a device where polarization insensitivity is attained by using this method, the resulting spectral resolving power will be driven by the polarization with the larger mode size. This simple method to achieve the polarization insensitivity by order overlap can in principle be applied to many other fields of photonic instrumentation with different materials and different geometries.

## 5.6 Conclusions

Various techniques of photonics are being widely applied to the field of astronomical instrumentation. This paper describes the fabrication process of new AWGs designed specifically for astronomical applications. These AWGs have peak throughput of $\sim$ 23%, resolving power of $\sim$ 1300, and cover 1450 nm to 1650 nm for TE polarization. The throughput is twice of that obtained in our previous work

[Gatkine et al., 2016]. These results were obtained using a combination of UHNA3 fiber and an optimized fiber-coupling taper, providing a high coupling efficiency. We further described key practical issues and their possible solutions, such as removing the broad absorption feature around 1500 nm using annealing, cleaving at the focal plane (output FPR) of the AWG to prepare for the cross-dispersion step, and a way to tackle the cleaving tolerances. Finally, a novel way of designing a polarization insensitive AWG without the need for quarter-wave plates was introduced. It is based on the basic idea of tuning the AWG geometry to get different spectral orders of TE and TM modes to precisely overlap each other. The techniques described and demonstrated here will pave the way for future integrated photonic spectrographs.

# Chapter 6: Towards an Integrated Photonic Spectrograph

*In this chapter, we will discuss the ongoing efforts towards the integration of multiple components of the spectrograph to build a complete system and make it ready for an on-sky test.*

## 6.1 An Integrated Photonic Spectrograph

The AWG chip described here is the principal component of the integrated astrophotonic spectrograph in the near-IR for ground-based telescopes (see Fig. 6.1). The other vital components include waveguide Bragg gratings (WBGs), photonic lanterns, and the cross-dispersion system. We briefly summarize WBGs and photonic lanterns here and describe the multi-input AWGs (needed to disperse the light from a photonic lantern) and the cross-dispersion system in more detail.

Ground-based near-IR spectroscopy, especially at moderate resolutions is challenging since the near-IR sky has a bright background due to the narrow ($\delta\lambda \sim 1$Å) and temporally fluctuating (over timescales of minutes) atmospheric OH-emission lines [Rousselot et al., 2000, Ellis and Bland-Hawthorn, 2008, Trinh et al., 2013, Zhu et al., 2016a]. For a low/moderate resolution spectrograph, it is important to selectively eliminate these OH-lines prior to dispersion to minimize the noise. Recently

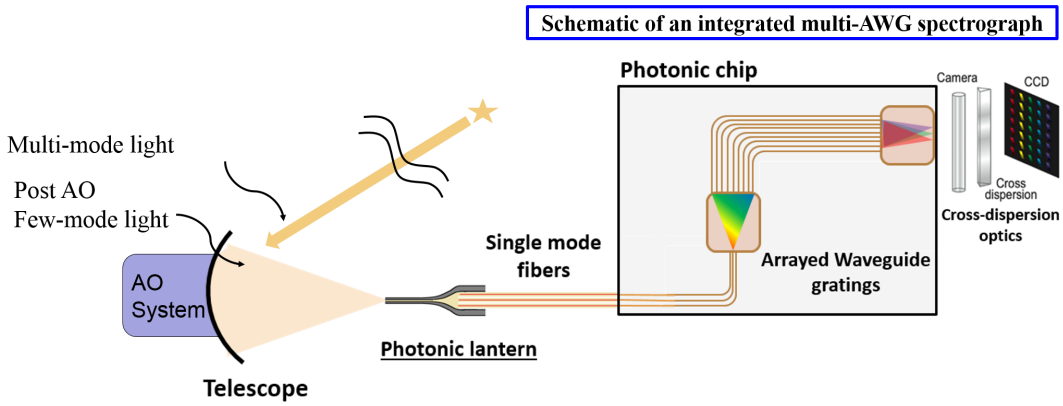


Figure 6.1: Full setup of an integrated photonic spectrograph with photonic lanterns, multi-input AWG, and cross-dispersion system. The waveguide Bragg Grating filters can be introduced in the input waveguides of the AWG before they illuminate the free propagation region.

demonstrated waveguide Bragg gratings (WBGs) construct notch filters in waveguides by carefully introducing subtle refractive index variations along their length to selectively eliminate the OH-emission lines prior to dispersion step in the AWGs [Zhu et al., 2016a, Hu et al., 2020].

These on-chip devices operate in single-mode waveguides, while the telescope illumination is multimode in nature due to atmospheric turbulence. A photonic lantern can be used to efficiently capture and guide the light into several single mode fibers/waveguides [Leon-Saval et al., 2010, Spaleniak et al., 2014]. The multimode light from the telescope is efficiently coupled into multimode fibers. A photonic lantern adiabatically tapers the multimode fiber into several single-mode fibers (the number depends on the point spread function [Horton and Bland-Hawthorn, 2007]). These single-mode fibers can then feed the integrated chip with WBGs and AWG on it. Various spectral orders of the dispersed AWG light are then separated in the orthogonal direction using a compact low-resolution cross dispersion setup and

thus the 2D spectrum will be imaged onto the detector. The schematic of such an integrated spectrograph is shown in Fig. 6.1. This design also provides the modularity to stack several of these integrated photonic chips fed by separate lanterns for multi-object spectroscopy or taking spectra of multiple wavebands simultaneously using dedicated photonic chips for each distinct waveband.

## 6.2 A Few-input AWG

In [Gatkine et al., 2017], we demonstrated a single-input, moderate resolution (R $\sim$ 1000), high-throughput (peak overall throughput $\sim$ 25%), broad-band AWG designed for H-band (1450$-$1550 nm). However, capturing the telescope light in a single mode fiber is not highly efficient since the beam is not diffraction limited due to atmospheric turbulence [Shaklan and Roddier, 1988]. Thanks to the recent developments in adaptive optics (eg. SCExAO), it is possible to achieve near-diffraction limited performance, thus allowing efficient coupling of light into a few-mode fiber in near-IR [Jovanovic et al., 2016]. In this paper, we are exploring the case of a three-input spectrograph as a test-bench to understand the challenges of a multi-input AWG from an astronomical perspective and propose solutions to effectively combine the light from multiple inputs to achieve a high signal-to-noise ratio spectrum. The combination also significantly reduces the number of detector pixels that would otherwise be required to image the spectrum from each single-mode fiber output of the photonic lantern.

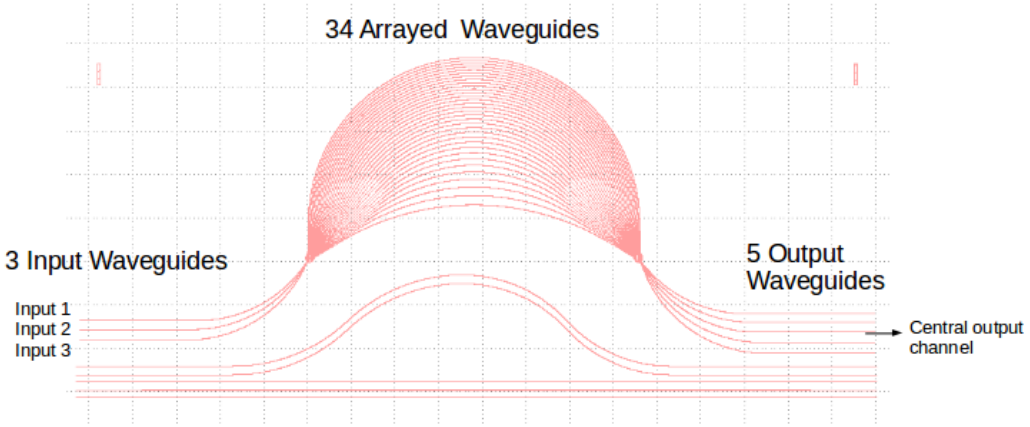


Figure 6.2: The CAD of the designed multi-input AWG. The input waveguides are on the left and the output is sampled by 5 waveguides. There are 34 waveguides in the array. The footprint of the chip is 16 mm $\times$ 7 mm

### 6.2.1 Design

The AWG design is similar to the AWG in [Gatkine et al., 2017], but with three input waveguides (instead of one) at the same spatial separation as designed for the output waveguides. This spatial separation is chosen since it is the standard in wavelength division multiplexing application in telecommunication industry where the AWG approach originated [Smit and Van Dam, 1996]. The detailed design, throughput and wavelegnth response of the single-input AWG are described in [Gatkine et al., 2017]. The physical parameters of the current multi-input AWG are described in Table 6.1. The design free spectral range of the AWG is 9.5 nm, thus covering the entire H-band in roughly 23 spectral orders. The size of the AWG chip is 16 mm $\times$ 7 mm.

Table 6.1: Summary of the AWG design

| **Parameters** | **Design value** |
|---|---|
| 1. Spectral resolution for each input ($\lambda/\delta\lambda$) | $\sim$ 1500 |
| 2. Free spectral range for each input | $\sim$ 9.5 nm |
| 1. Waveguide cross-section | 2.0 $\times$ 0.1 $\mu m$ |
| 2. Number of waveguides | 34 |
| 3. FPR length | 200 $\mu m$ |
| 4. $\Delta L$ | 172 $\mu m$ |
| 5. Separation between waveguides at array-FPR interface | 6 $\mu m$ |
| 7. Footprint | 16 mm $\times$ 7 mm |

### 6.2.2 Simulation

The AWG was simulated using `Rsoft` software [1] to study the characteristics of a representative spectral order centered around 1600 nm. There are 3 input waveguides for this AWG and the output FPR is sampled by 5 output waveguides. In the spectral domain, each of the 'discrete' output waveguides are separated by $\Delta\lambda \sim 1.6$ nm (by design) in all the spectral orders. This is also called 'channel spacing'. The AWG is simulated by illuminating each input waveguide one by one and calculating the response at each of the output waveguides. Here, we will focus on the central output channel of the AWG (as shown in Fig. 6.2) and explore how the wavelength response changes with various modifications in the input waveguides. For simplicity, we vary the input waveguide separation progressively as shown in Fig. 6.3.

[1] https://optics.synopsys.com

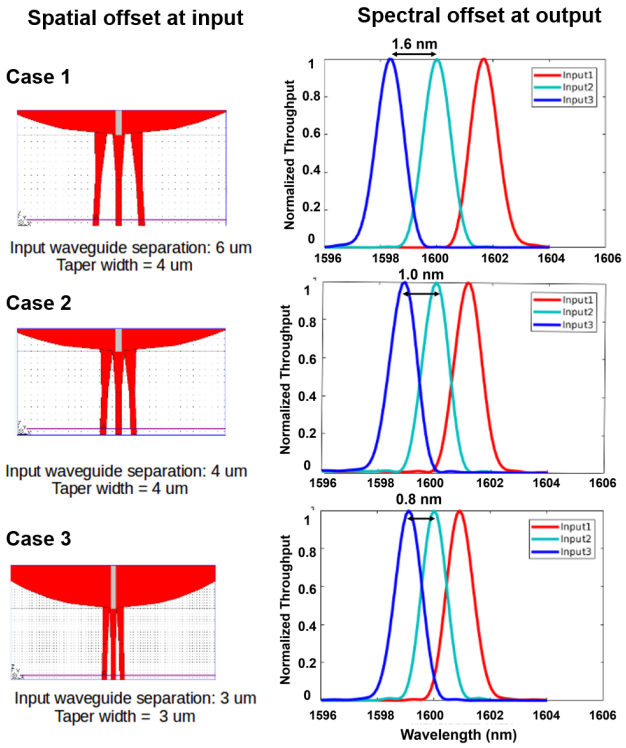


Figure 6.3: Simulation results: Each plot shows the normalized throughput of the central output channel in red, green and blue when input 1, 2, and 3 are illuminated respectively. The three cases show the effect of bringing the input waveguides progressively closer by changing the waveguide separation from 3 times the waveguide width (i.e. 6 $\mu m$) to 2 times (4 $\mu m$) and further to 1.5 times (3 $\mu m$).

### 6.2.3 Simulation Results

Each off-center input gives an output spectrum that is shifted in wavelength by an amount (say, $d\lambda$) proportional to the offset from the central input waveguide. This $d\lambda$ shift leads to degradation of the resolving power roughly by a factor of number of input waveguides $\times$ $d\lambda/\Delta\lambda$, where $\Delta\lambda$ is the channel spacing as described in the above paragraph (in this case, $\sim 1.6$ nm). The goal is to keep this shift minimal to reduce the degradation from the design resolving power. This way, the desired resolution can be achieved without increasing the intrinsic resolution of the AWG by a large factor (to compensate for the degradation).

Towards that objective, we employ the idea of minimizing the separation between the input waveguides to the maximum possible extent. We demonstrate this idea from the simulation described in Fig. 6.3. The waveguide separation and the effect on the resolving power degradation is summarized in Fig. 6.3 and Table 6.2. It is clear from these simulations that feeding the input light to the AWGs using a compact assembly of waveguides is a very effective approach for minimizing the central wavelength shift and thereby obtaining the desired resolution with minimal need of compensation.

Table 6.2: Summary of the AWG simulations

| **AWG case** | **Resolving power degradation factor** |
|---|---|
| 1. Input waveguide separation: $6\mu m$, taper width: $4\mu m$ | 1/3 |
| 2. Input waveguide separation: $4\mu m$, taper width: $4\mu m$ | 1/2.5 |
| 3. Input waveguide separation: $3\mu m$, taper width: $3\mu m$ | 1/2 |

### 6.2.4 Experimental Verification

We fabricated the multi-AWG shown in Fig. 6.2 corresponding to case 1 (input waveguide separation = 6 $\mu m$, taper width = 4 $\mu m$) using the fabrication methods described in Section 5.3.2. This AWG was characterized using the characterization setup described in Section 5.3.3. Each input waveguide of the AWG was illuminated individually and the spectrum at the central output waveguide was measured. The result of this measurement is shown in Fig. 6.4. As estimated from the simulations, the wavelength offset between the peaks corresponding to the neighboring inputs is $\sim$ 1.6 nm. This verifies and demonstrates the concept of multi-input AWG and its corresponding degradation of resolving power described in Section 6.2.3.

The other cases will be simulated in the future and a suitable multi-input AWG will be used in conjunction with a few-mode photonic lantern for the on-sky test. This demonstration will work as a stepping stone for fabrication and physically implementation of a higher resolution AWG (by increasing the spectral order) whose final resolution (including the resolution degradation) will be $\sim$ 1500.

## 6.3 Cross-dispersion setup

The cross-dispersion setup is to be used to separate the overlapping spectral orders at the output waveguides of the AWG or its exposed focal plane (as discussed in Section 5.4.3). In this section, we summarize the cross-dispersion system that we constructed, which will then be coupled with the multi-input AWG described above. This work was done in close collaboration with Meghna Sitaram.

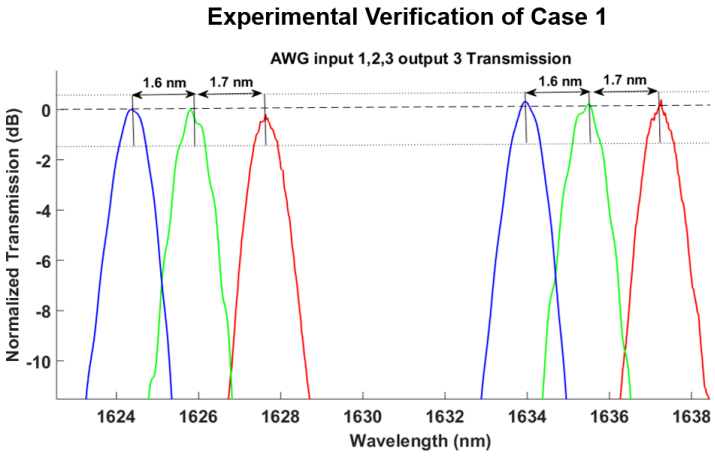


Figure 6.4: Experimental verification of case 1 in Fig. 6.3 and Table 6.2 with input waveguide separation = 6 $\mu m$ and taper width = 4 $\mu m$.

### 6.3.1 Detector Characterization

Considering the separation of 20-23 overlapping spectral orders (each order with a free spectral range, $\Delta\lambda \sim 10$ nm) as previously described in Chapter 5 and Table 6.1, we assumed roughly 5- to 6-pixel separation between the orders, thus requiring a 2D detector array with more than 128 $\times$ 128 pixels. Our choice of the 2D detector array for the preliminary demonstration of cross-dispersed AWG was mostly driven by the cost. Thus, we chose Hamamatsu G12242-0707W image sensor, an Indium Gallium-Arsenide (InGaAs) 2D detector array with dimensions of 128 x 128 pixels and a pixel pitch of 20 $\mu m$ [2]. The quantum efficiency of the detector in the H-band is 60%. We use the detector in conjunction with a C11512-02 detector head from Hamamatsu which includes the circuitry for driver, controller, thermo-

[2]The complete datasheet can be found here:
https://www.hamamatsu.com/resources/pdf/ssd/g12242-0707w_kmir1022e.pdf

electric cooler, and readout[3]. The data and control instructions are transferred using a high-speed CameraLink interface. The image readout and control is performed using a software called DCAM-CL. Before any image acquisition, we perform a dark calibration by capturing an image with the detector covered.

We measure the saturation characteristics of the detector to determine the range of linear operation. This test was performed at $\lambda = 1450$ nm. For this test, a laser source fed a single-mode fiber. The fiber was coupled to a fiber collimator, which illuminated the detector. The maximum counts (i.e. the peak) were plotted as a function of input power and are shown in Fig. 6.5. From the saturation characteristics, we estimate that the detector starts to deviate from a linear rise at 42000 ADU. We estimated the flux in the brightest pixel by fitting a 2D Gaussian to the beam profile. Thus, the flux where the detector starts to deviate from a linear rise is 1.3 $\mu$W pixel$^{-2}$.

### 6.3.2 Cross-dispersion optics

Next, we designed and tested a cross-dispersion setup using a collimated fiber as a source and a blazed grating as a cross-disperser. As described earlier, the AWG disperses the light in the vertical direction and the cross-disperser separate the order in horizontal direction. The setup of the cross-dispersion system in shown in Fig. 6.6. We use an off-the-shelf NIR grating from Thorlabs [4]. The blaze angle and the groove density are 28°41' and 600/mm, respectively. The angle of the diffracted

[3]The complete datasheet can be found here:
https://www.hamamatsu.com/resources/pdf/ssd/c11512_series_kacc1194e.pdf

[4]Datasheet here: https://www.thorlabs.com/thorproduct.cfm?partnumber=GR25-0616

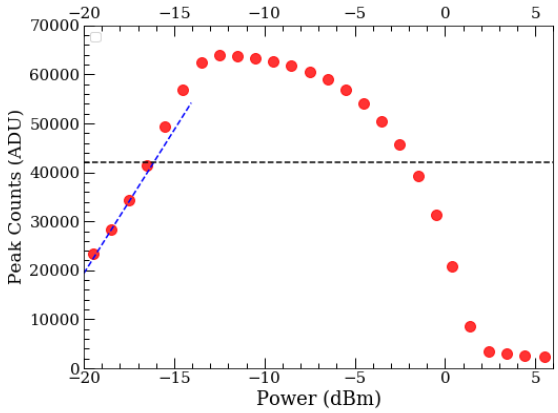


Figure 6.5: Saturation characteristics of the detector. The detector is in the linear regime upto 42000 ADU (as shown by the dashed lines). The saturation level is 65535 ADU.

light of spectral order $m$ for a blazed grating is given by the grating equation:

$$a[sin(\theta_m) + sin(\theta_i)] = m\lambda \tag{6.1}$$

Here, $a$ is the groove spacing (= 1666 nm), $m$ is the spectral order (= 1), $\theta_i$ is the incidence angle and $\theta_m$ is the angle of the diffraction ray. Note that $\theta_i$ and $\theta_m$ are both positive if they are on the same side of the normal. A blazed grating schematic is shown in Fig. 6.7. For cross-dispersion, the differential angle ($\Delta\theta_m$) for $\Delta\lambda = 10$ nm (which is the span or FSR of one spectral order of the AWG). $R\Delta\theta$ (for $\Delta\theta$ in radians) gives the distance between the two separated orders of the AWG on the detector plane. Here $R$ is the distance between the grating and the detector. Figure 6.7 shows the differential angle ($\Delta\theta_m$ in degrees) as a function of wavelength and incidence angle.

To ensure appropriate mounting and to accommodate maximum number of

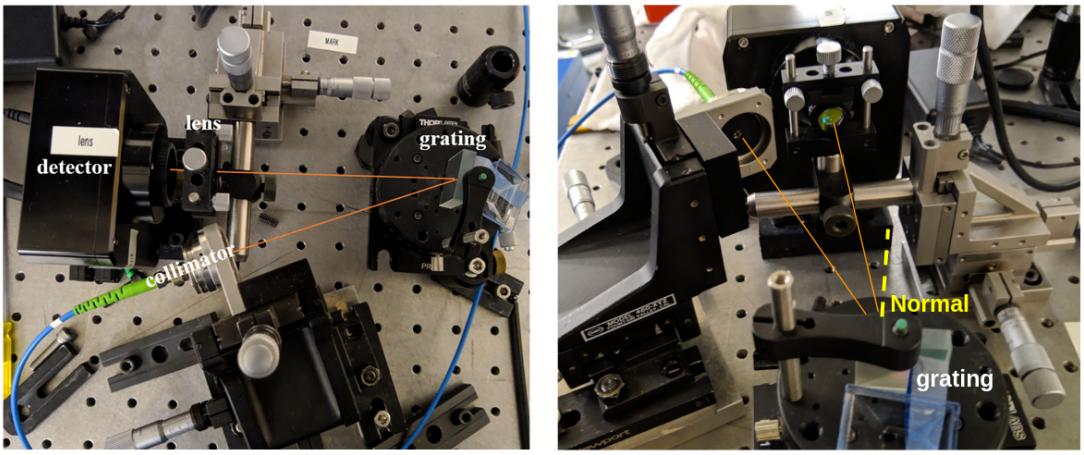


Figure 6.6: The cross-dispersion setup using the grating, including the collimator, grating, lens, and detector. The orange line show the path of the light, starting at the collimator and ending at the detector.

spectral orders, we select $\theta_i = 30°$. Using a converging lens of magnification 0.14, we achieve a dispersion of approximately 120 $\mu m$ or 6 pixels and a beam diameter of approximately 4.5 pixels, as shown in Fig. 6.8 for $\lambda_1 = 1355$ nm and $\lambda_2 = 1365$ nm. This will allow us to accommodate about 20 spectral orders from the AWG.

With a compact 3D-printed mounting setup in the future, the distance between the grating and detector will be smaller, making it possible to accommodate more than 20 spectral orders. The current size of the setup is $\sim$ 30 cm $\times$ 30 cm, but most of the space is taken up by the alignment stages on the optical bench. This can be condensed to a 15 cm $\times$ 15 cm form factor (including the AWG) using a custom 3D-printed mount with precise alignment. Thus, the eventual volume of the instrument will be just 15 $\times$ 15 $\times$ 15 cm$^3$, ideal for deployment at any telescope.

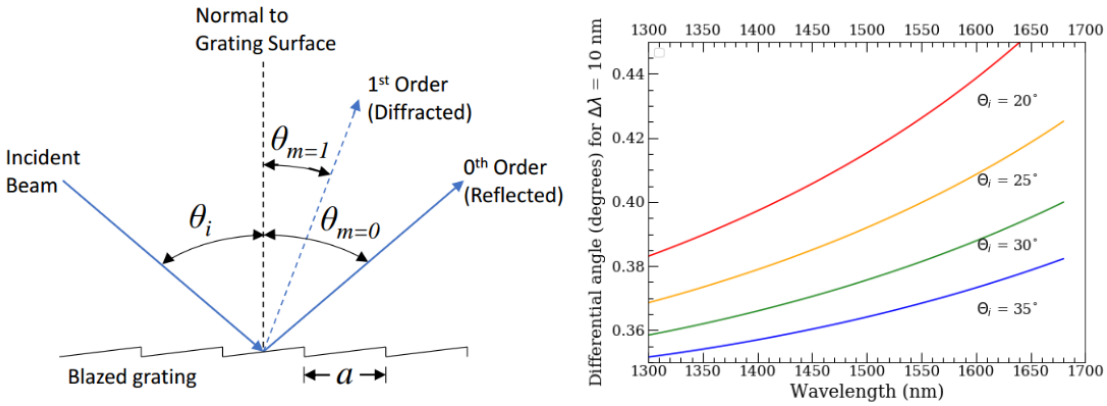


Figure 6.7: Left: A schematic of a blazed grating showing the angles of the incident beam, zeroth order beam, and first order beam (Reference: Thorlabs.com). Right: The computed variation of differential angle in degrees ($\Delta\theta_m$) for $\Delta\lambda = 10$ nm as a function of wavelength and incidence angle.

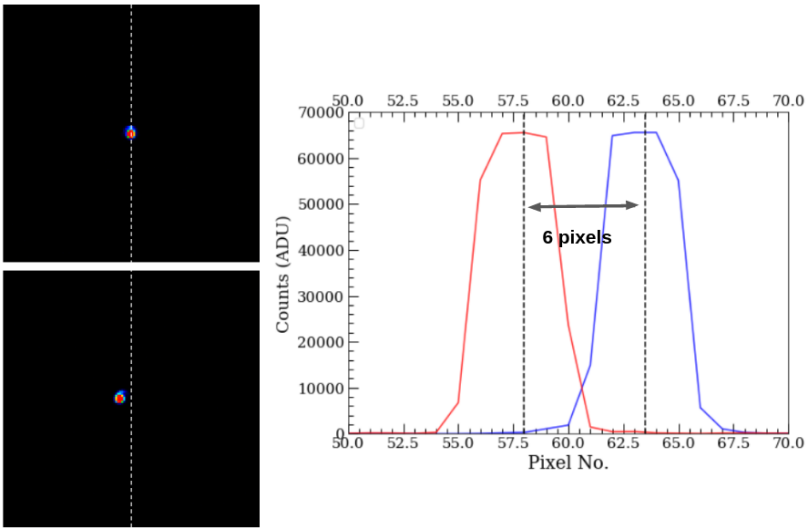


Figure 6.8: Left: Two images showing the light output from the grating setup at 1355 nm and 1365 nm. The beam has a diameter of about 5 pixels and has a dispersion of about 6 pixels between the 1355 nm beam and the 1365 nm beam. Right: The same result with the cross-sections of the beams of 1355 nm (blue) and 1365 nm (red) wavelengths.

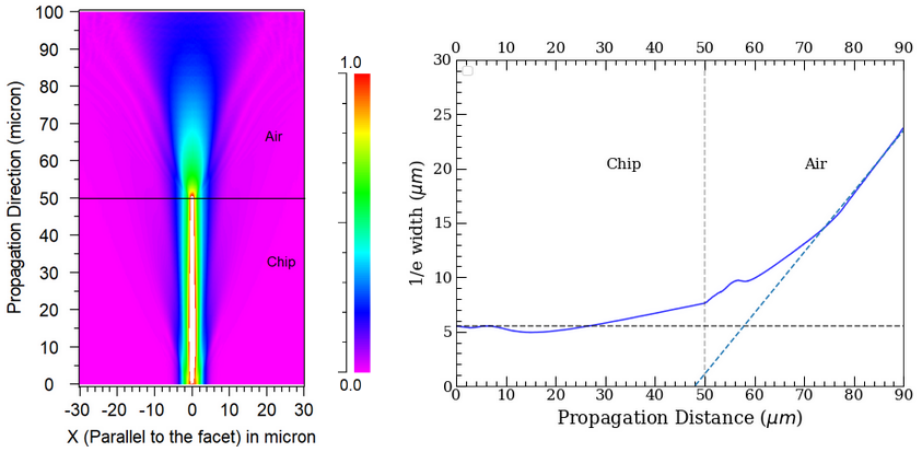


Figure 6.9: Left: Simulated electric field. The transition from chip to air is shown. The waveguide used here is a weakly confined SiN waveguide for the taper end (width = 600 nm , height = 100 nm), similar to the one described in Section 5.4.1. Right: The same result with $1/e$ width of the field as a function of propagation distance. The half-angle of the emergent beam is computed to be 29.5 °.

### 6.3.3 Future work: Integration with the AWG

The next step is to incorporate the AWG as in the input source instead of the fiber. The collimated light from the AWG will then be dispersed by the blazed grating in orthogonal direction (thus, separating the spectral orders of the AWG) and imaged on the detector. To collimate the AWG output, the opening angle of the emergent beam from the waveguide has to be determined. We simulated the chip-to-air propagation for an output waveguide using `Rsoft` software and estimated the opening angle to be 59 degrees (i.e. 2 × half-angle) as shown in Fig. 6.9. A schematic of the final assembly of the spectrograph with the AWG and cross-dispersion system is shown in Fig. 6.10. Once the AWG chip is packaged and mounted as per the schematic, the system will be ready for its first on-sky test.

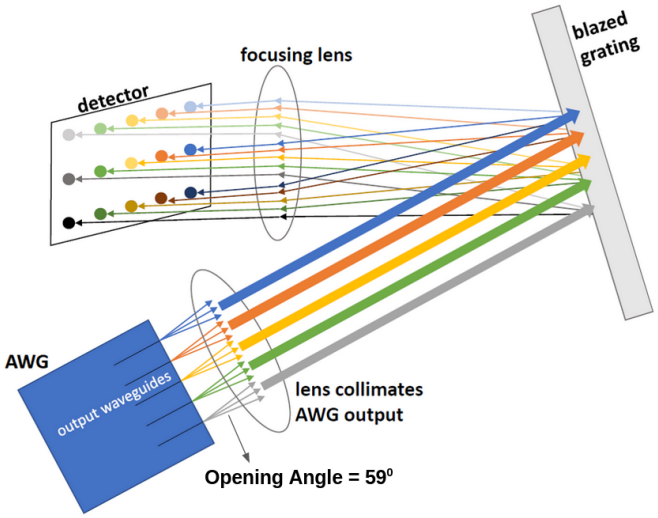


Figure 6.10: A schematic showing the AWG + cross-dispersion assembly. The AWG output facet will be mounted at the focal plane of the collimating lens. Each bright color indicates the finer dispersion by the AWG (with $\delta\lambda \sim 1$ nm), albeit with overlapping spectral orders. The blazed grating performs coarse dispersion ($\Delta\lambda \sim 10$ nm) and thus, separates the spectral orders in orthogonal direction (as shown by the shades of the colors). [Adopted from Meghna Sitaram's honors thesis].

## Acknowledgments

The authors thank the University of Maryland NanoCenter for the fabrication expertise and the astrophotonics group at University of Sydney and Maquarie University for providing valuable advice. I thank Meghna Sitaram, who worked in collaboration with me on the cross-dispersion project. The authors acknowledge the financial support for this project from the W. M. Keck Foundation, National Science Foundation, and NASA.

# Chapter 7: Summary and Future Work

*In this chapter, we highlight important takeaways from this thesis and lay down a path forward.*

## 7.1 GRB afterglows as probes of the CGM

### 7.1.1 Summary

In this part of the thesis, we set out to investigate the properties of the CGM at high redshifts using the bright afterglows of gamma-ray bursts (GRBs) as background sources probing the CGM of their own host galaxies. Our CGM-GRB sample consisted of 27 high-resolution (R > 6000) rest-frame UV spectra of GRB afterglows in a redshift range ($2 \lesssim z \lesssim 6$). We also measured the $M_*$ and SFR of their host galaxies to explore the CGM/outflow-galaxy correlations. For these correlations, we focused on three outflow properties − outflow column density ($N_{out}$), maximum outflow velocity ($V_{max}$), and normalized maximum velocity ($V_{norm} = V_{max}/V_{circ,halo}$, where $V_{circ,halo}$ is the halo circular velocity). The following are our key findings:

**1.** High-ion-traced outflows: We find stronger blue wings in high-ion species (Si IV, C IV) compared to the low-ion species (Si II, Fe II), indicative of the presence of

ubiquitous warm outflows in the GRB hosts at high redshifts. [Chapter 2]

**2.** CGM kinematics: Using kinematic models, we estimated typical values of CGM properties (for the sample) such as CGM mass ($10^{9.8}$ $M_\odot$) and outflow launch velocity (300 km $s^{-1}$). The mass of the CGM inferred from this model is comparable to the typical stellar mass of the host galaxies, thus suggesting a significant reservoir of baryons already existing in the CGM at $z \gtrsim 2$. [Chapter 2]

**3.** CGM-galaxy co-evolution: By comparing our results with previous C IV absorption studies, we find a possible CGM-galaxy co-evolution. Over the course of evolution of present-day galaxies with $M_* > 10^{10}$ $M_\odot$, the ratio of C IV mass in the CGM to the stellar mass remains fairly uniform, such that $\log(M_{CIV}/M_*) \sim -4.5$ within $\pm 0.5$ dex from $z \sim 4$ to $z \sim 0$, suggesting a CGM-galaxy co-evolution over 10 billion years. [Chapter 2]

**4.** Dust-obscuration: From the radio observations of four massive GRB hosts in our sample, we inferred that the GRB hosts in our sample are not heavily dust obscured, and hence, their SFRs can be estimated reliably using the established dust-correction methods for main-sequence galaxies. [Chapter 3]

**5.** Star-formation-driven outflows: We observe clear trends of $N_{out}$ and $V_{max}$ with increasing SFR in high-ion-traced outflows. These correlations indicate that these high-ion outflows are driven by star formation at these redshifts (in the mass range $\log(M_*/M_\odot) \sim 9 - 11$). [Chapter 4]

**6.** Outflows and metal enrichment: We find, for the first time at high redshifts, a strong ($> 3\sigma$) trend of normalized velocity ($V_{norm}$) decreasing with halo mass and increasing with specific SFR (sSFR), suggesting that outflows from low-mass halos

and high sSFR galaxies are most likely to escape and enrich the outer CGM and IGM with metals. [Chapter 4]

### 7.1.2 Future Work

The relevant future steps have been described in each chapter individually. Here we summarize a path forward for specific investigations.

**1.** Adding structured outflows to our toy models: Our kinematic toy models of the CGM-galaxy system have proved very useful in simulating various CGM/galaxy properties/scenarios and their implications on the observed spectra, in a simplified manner and without requiring a full-scale cosmological zoom-in simulation. In the current version, we have assumed spherically symmetric outflows. However, with the observed scatter in the $N_{out} - SFR$ correlations, there is a possibility that it may arise from a structured outflow. Therefore, we will add a structured outflow functionality to our toy models and investigate the implication of the structured (eg: biconical) outflows on the observed GRB afterglow spectra.

**2.** Photo-ionization modelling: We will use the industry standard code called `Cloudy` [Ferland et al., 2017] for ionization modeling of the multi-phase CGM. The main idea here is to build a Bayesian toolkit for photo-ionization modeling to constrain the ionization fraction and thus, the metal mass in the warm-phase CGM. A grid of models will be built using a parameter space of inputs including the extragalactic ionizing background, density profile in the CGM, temperature of the gas and its metallicity. A posterior probability distribution of the input parame-

ters will then be calculated using the Markov Chain Monte Carlo (MCMC) method. Using this analysis, we will constrain the ionization fraction of various species in the multi-phase CGM with robust uncertainties. This tool builds on the Bayesian Voigt-profile fitting tool presented in this thesis (Section A.1).

**3.** Measuring the molecular gas in the high-z GRB hosts: It is important to measure the gas mass in the host galaxies to estimate the mass of metals stored in the galaxy and compare it against the mass of metals in the CGM. At high redshifts, the majority of the gas is in the form of molecular clouds [Daddi et al., 2010, Tacconi et al., 2018]. We were recently awarded 26 hours of VLA time (PI: Gatkine, VLA 2020A) to probe CO 1-0 emission in two GRB hosts with high sensitivity. We have acquired the data and we see a tentative detection of redshifted CO 1-0 emission in one of the two GRB hosts in the preliminary data reduction. In the future, we plan to deepen our limits using ALMA observations.

Through our CO observations, we seek to address several important questions: **1)** Where do GRB hosts reside in the SFR vs $M_{gas}$ parameter space at $z > 2$ and what are its implications on their gas depletion timescales? **2)** Can metal enrichment be sustained for 1 Gyr timescales? What fraction of metals are distributed in the CGM vs ISM? **3)** How do the line-of-sight column densities compare with the bulk molecular gas content?

## 7.2 Development of photonic spectrographs

### 7.2.1 Summary

In this part of the thesis, we set out to develop a new tool − a spectrograph on a chip − which will eventually expand the galaxy evolution investigation to the first galaxies in the universe ($z > 6$). Astrophotonics is the new frontier technology to channel, manipulate, and disperse guided light to efficiently achieve various scientific objectives in astronomy in a miniaturized form factor. Our instrumentation efforts are summarized as follows:

**1.** A compact, high-throughput AWG: We used the concept of arrayed waveguide gratings (AWG) to develop an on-chip photonic spectrograph in the H band ($1.45 - 1.65\ \mu m$) with a moderate resolving power of ∼1500, a peak throughput of ∼23%, and a size of only 1.5 cm × 1.5 cm. [Chapter 5]

**2.** Adaptations for AWGs: We explored the following adaptations to enable practical implementation of an AWG for astronomical spectroscopy: a) high-coupling efficiency ($\sim$ 95%) tapers to couple the light between the fibers and AWGs, b) cleaving at the output focal plane of the AWG to provide continuous wavelength coverage, [Chapter 5] and c) a multi-input AWG design to simultaneously receive light from multiple single-mode fibers emanating from a photonic lantern and thus, produce a combined spectrum. While, combination reduced the total number of detector pixels required (and hence the readout noise), it also proportionally degrades the resolving power. [Chapter 6]

**3.** The cross-dispersion setup: We built a cross-dispersion setup which will orthogonally separate the overlapping spectral orders in the AWG and thus image the full spectrum on the detector. We achieved a spot diameter of 5 pixels and a spatial dispersion of 6 pixels for $\Delta\lambda = 10$ nm (i.e. the wavelength spacing between the consecutive spectral orders of our AWG).

### 7.2.2 Future Work

The work presented in this thesis is a crucial stepping stone towards building a high-throughput, miniaturized spectrograph for the next generation of ground-, balloon-, and space-based telescopes. Building on this work, the next step is to conduct an on-sky test and improve the AWG performance to match or exceed that of the conventional spectrographs while keeping a compact form factor. We summarize the future work in that direction with the following points:

**1.** Photonic Integration and on-sky test: In order to incorporate the AWG with the cross-dispersion setup, the input facet of the AWG will be permanently bonded with the input fibers. The fiber-waveguide alignment will be done using the 10-nm precision alignment stages described in Section 5.3.3 and a UV-curing epoxy will be used to permanently join the fiber with the chip. This step will be done with all the inputs of the multi-input AWG. The packaged AWG will then be integrated with the cross-dispersion setup as shown in Fig. 6.10. The AWG and the elements of the cross-dispersion system will be mounted in a custom 3D-printed enclosure to make it a fully-packaged portable instrument.

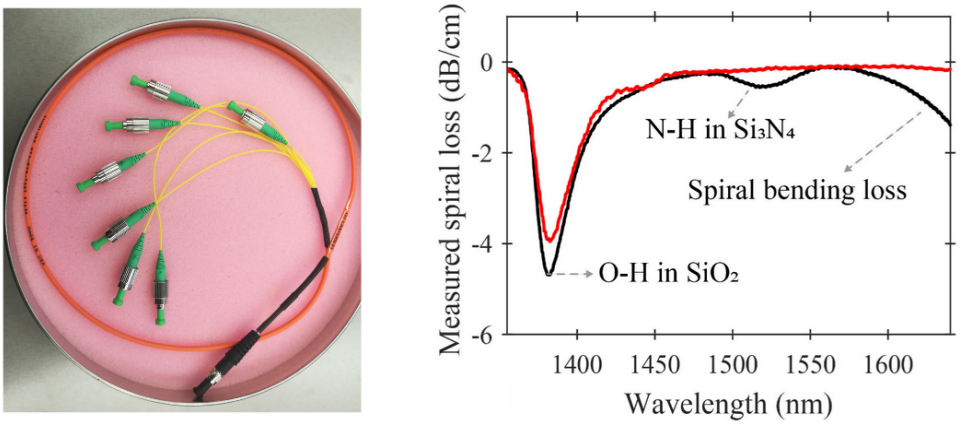


Figure 7.1: Left: A 1-to-7 photonic lantern that we fabricated at the Sydney Astrophotonic Instrumentation Laboratory (SAIL). The orange-black end is the multi-mode fiber end and the yellow-green ends are the single-mode fiber ends. Right: The improved propagation loss of $\sim$ 0.2 dB/cm across the H band (1450 - 1650 nm) using the TEOS recipe for top cladding deposition [Hu et al., 2020]. The black line shows the propagation loss without annealing (for a spiral of inner radius = 500 $\mu m$) and the red line shows the same with annealing at 1150 °C (for a spiral of inner radius 750 $\mu m$).

The fibers that feed the multi-input AWG will be connected to the single-mode ends of the photonic lantern. I fabricated 1-to-3 and 1-to-7 photonic lanterns with the help of Drs. Chris Betters and Sergio Leon-Saval at the Sydney Astrophotonic Instrumentation Laboratory (University of Sydney) in Australia. A 1-to-7 photonic lantern in shown in Fig. 7.1. We measured the throughput of the multi-mode to single-mode transition in these photonic lanterns to be 75 $\pm$ 5%.

The on-sky test will be conducted using a commercial 12-inch telescope. The multi-mode end of the photonic lantern will collect the light from the focal point of the telescope and the single-mode ends will feed the multi-input AWG and the 2D spectrum will be read out at the detector. The on-sky test will help characterize the overall throughput and the performance of the complete instrument pipeline.

**2.** Improving the AWG throughput: The AWG throughput can be significantly

enhanced using the new modifications in the fabrication recipe. As recently demonstrated in [Hu et al., 2020], the propagation loss and broadband absorption in our SiN waveguides can be substantially reduced over the H band by using the TEOS recipe ($Si(OC_2H_5)_4$ and $O_2$) instead of silane recipe ($SiH_4$, $NH_3$ and $N_2$) for the deposition of the $SiO_2$ top cladding (see Fig. 7.1). This recipe, in conjunction with high-temperature annealing can reduce the propagation loss in the waveguides to $\sim$ 0.2 dB/cm (versus the previous 1.5 dB/cm) over the H band. This will improve the total throughput of the AWG to more than 40% (versus the previous 25%).

**3.** Incorporating the waveguide Bragg gratings on the AWG chip: The waveguides can be used as an ensemble of sharp notch filters (width $\sim$ 1 Å, rejection ratio $\sim$ 1000) by carefully introducing subtle refractive index variations along their length in a complex pattern [Bland-Hawthorn et al., 2011, Zhu et al., 2016a]. The fiber-based version of these devices have been demonstrated for atmospheric OH-emission suppression in the near-IR to minimize the sky background [Trinh et al., 2013].

Our next step will be to integrate waveguide Bragg gratings on the AWG chip such that the incoming light passes through the Bragg gratings before being fed to the AWG. With this, the signal-to-noise ratio of the resulting spectrum will be significantly improved due to the pre-dispersion suppression of the OH background. Recently demonstrated spiral waveguide Bragg gratings on SiN platform [Hu et al., 2020] are ultra-compact (1 mm diameter), and hence are perfectly suited for integration on the AWG chip itself. This innovation will give rise to an ultra-compact, integrated filter-disperser with high throughput and low sky background, which can be easily deployed on both small as well as large telescopes.

**4.** Flat focal plane AWG: We discussed the characteristics of an AWG chip cleaved along its focal plane in Section 5.4.3. The exposed focal plane provides an access to a continuous spectrum as opposed to a discretized spectrum sampled by the output waveguides. However, the focal plane of a conventional AWG is a circle (called the Rowland circle). Hence, cleaving it along a flat plane leads to defocusing and distortion of the spectrum. One solution to this problem is using a three-point-stigmation design for an AWG, which can be used to create a flat focal plane [Lu et al., 2005]. Our collaborator, Yiwen Hu, is currently exploring this. We plan to integrate this design to create a continuous-spectrum AWG spectrograph in the near future. Eventually, this design will help us directly couple the AWG with a 1D detector array and eliminate all the free-space optical elements.

# Chapter A: Methods for CGM-GRB Paper I

## A.1 Voigt profile fitting using MCMC

As described in section 2.3.2, we developed an MCMC-based code for multi-component Voigt profile fitting. There are four key components in this Bayesian approach to Voigt-profile fitting: definition of Voigt function, prior distribution, log-likelihood of a set of parameters, and posterior function.

**Definition of Voigt function**: In this analysis, we convert the spectrum in rest frame for each transition under consideration. The line properties are taken from [Morton, 2003], [D'Elia et al., 2014], and the NIST database [1]. For given properties of a transition (wavelength $\lambda_0$, oscillator strength $f_{osc}$, and damping constant $\gamma$), the normalized flux at a wavelength $\lambda$ is given by:

$$F(v)_{N,b,\lambda_0} = exp[-\tau(\lambda)] \tag{A.1}$$

where $\tau(\lambda)$ is the optical depth as a function of wavelength in rest frame and

[1] https://physics.nist.gov/PhysRefData/ASD/lines_form.html

$\lambda_0$ is the line center. The optical depth is further parametrized as:

$$\tau(\lambda)_{N,b,\lambda_0} = \frac{N f_{osc} \sigma_0 \lambda}{b} \; V(\lambda)_{b,\lambda_0} \;\; , with \;\; \sigma_0 = \frac{\sqrt{\pi} e^2}{m_e c} \tag{A.2}$$

where $V(\lambda)$ is the Voigt function defined by a convolution of the Doppler-broadened Gaussian profile (depends on $N, b, f_{osc}$) and pressure-broadened Lorentzian profile (depends on the damping coefficient, $\gamma$). For the functional form of the Voigt profile, see eq. 6 in [Petitjean, 1995]. The Voigt function in our code is evaluated using the `Voigt1D` routine in `astropy` implemented using a high accuracy analytical approximation described in [McLean et al., 1994]). Since the continuum is separately fitted and normalized (see 2.3.2), we do not add a continuum model in this treatment. The modeled $F(v)$ is further filtered using a Gaussian kernel of width equal to the line spread function of the instrument used to obtain the spectrum.

**Posterior distribution function:** The posterior distribution function represents the probability distribution of a set of model parameters given the observed data. In this case, the model of the optical depth as a function of velocity ($\tau(v)$) is defined as a sum of Voigt profiles of multiple absorbing components for a given transition. The model parameters are denoted by $\Theta = [N_i, b_i, v_{0,i}]_{i=1,2,..,n}$ where $n$ is the number of absorbing components to be fitted to the line transition. According to Bayes' theorem,

$$p(\Theta|D) = \frac{p(D|\Theta)p(\Theta)}{p(D)} \tag{A.3}$$

where $D$ is the observed data. The distributions $p(\Theta|D)$, $p((D|\Theta)$, $p(\Theta)$ are

the posterior distribution, likelihood distribution, and prior distribution. The normalization $p(D)$ is independent of model parameters here and therefore, the parameter estimation can be achieved by maximizing the product of likelihood and prior distributions. We use a python package called `emcee` which implements the ensemble sampling algorithm as described in [Foreman-Mackey et al., 2013] to efficiently sample the posterior distribution in a high-dimensionality and often correlated parameter space in this particular problem.

**Definition of likelihood function:** To evaluate the likelihood of a particular set of parameters, a noise model is required. We use a Gaussian noise model assuming large photon number limit. This model is suitable for fitting the non-saturated absorption components. Although it may not serve as the best approximation for saturated parts of the spectrum, it is well suited for fitting the wings (due to large number of photons) of such saturated components. The likelihood function is defined as follows:

$$p(D|\Theta) = \frac{1}{\sqrt{2\pi\epsilon_i^2}} exp\left[-\frac{(D_i - F_i)^2}{2\epsilon_i^2}\right] \tag{A.4}$$

where $D_i$, $\epsilon_i$, $F_i$ are the observed flux, error in the flux, and model flux at a certain wavelength $i$.

**Prior distribution:** A uniform prior distribution is defined over the range of possible values for each parameter to ensure its non-informative nature over this range (eg: $\log(N_{SiIV})$ from 9 to 18 and b-parameter from 5 to 70 km $s^{-1}$). The number of absorbing components to be fitted to a line transition are manually selected by validating their presence and strength in another transition of the same species or

a doublet/triplet system and/or another transition of similar ionization state. This approach is particularly helpful for saturated lines where the number of absorbing components can be constrained by identifying the components in weaker transitions of the same species or the same class (high-/low-ion). The priors for line centers are manually provided as 50-90 % of the extent of the particular component in velocity.

The region very close to sky lines is not considered while defining components. In addition, we mark all the lower-z intervening systems identified in the literature for each GRB. This way, any undesirable contamination is avoided. The initial guesses provided to the algorithm are randomly sampled from the range defined in the prior distribution. In case of doublets or multiplets, the spectra are fit simultaneously. The likelihood distribution for these systems is defined as the product of likelihood distributions of individual transitions. This ensures that the resulting posterior distribution represents the complete doublet/multiplet system.

**Parameter estimation:** The number of steps required to establish a reasonable convergence of the Markov chains is estimated using the autocorrelation time method as described in the emcee package [Goodman and Weare, 2010, Foreman-Mackey et al., 2013]. We increase the number of steps (i.e. length of a Markov chain) in powers of 4 (capped at $10^5$ $\times$ no. of parameters due to computational limit) until the autocorrelation time converges within 10% of the previous step. The optimal parameters are obtained by maximizing the marginalized posterior distribution function for each parameter. The 1-$\sigma$ confidence interval is estimated as the range of parameter value that covers the central 68% of the marginalized posterior

distribution function.

## A.2 Line-of-sight simulation with toy model

The GRB sightline through the galaxy ISM and CGM is simulated using a simple toy model to understand the kinematic distinction between the ISM and CGM in a statistical sample and use it to better estimate the physical properties from the observed data. A large number of GRB explosions are simulated in a representative galaxy with randomly chosen burst locations in the galactic disk and pointing directions. We assume a typical stellar mass of the GRB host galaxy of $\sim 10^{9.3}$ $M_{\odot}$ at z $>$ 2 for these simulations ([Perley et al., 2016b]). The halo mass ($M_h$) is taken as $10^{11.2}$ $M_{\odot}$ as described in previous simulations in the literature [Hopkins et al., 2014, Wechsler and Tinker, 2018]. The virial radius is calculated using a NFW profile for the dark matter distribution and standard cosmological parameters ($\Omega_m$ = 0.3, $\Omega_{rad} = 0$, $\Omega_{\Lambda} = 0.7$). The virial radius for the simulated galaxy at z $\sim$ 2.5 is 50 kpc. The corresponding virial velocity is $\sim$ 100 km s$^{-1}$. The assumed setup for the simulation is summarized in Table A.1.

**Geometrical Setup:** The galaxy is modeled as a cylinder with radius $r_{galaxy}$ and height $h_{galaxy}$. This volume is treated as the extent of the ISM with an exponential density distribution such that the total enclosed mass equals $M_{ISM}$ and half of the mass is enclosed within the half-light radius ($R_e$). For simplicity, we assume that the mass of the ISM traced by high-ion species ($M_{ISM}$) is equal to the stellar mass of the galaxy ($M_{\star}$). $R_e$ is assumed to be 2 kpc following previous observations of

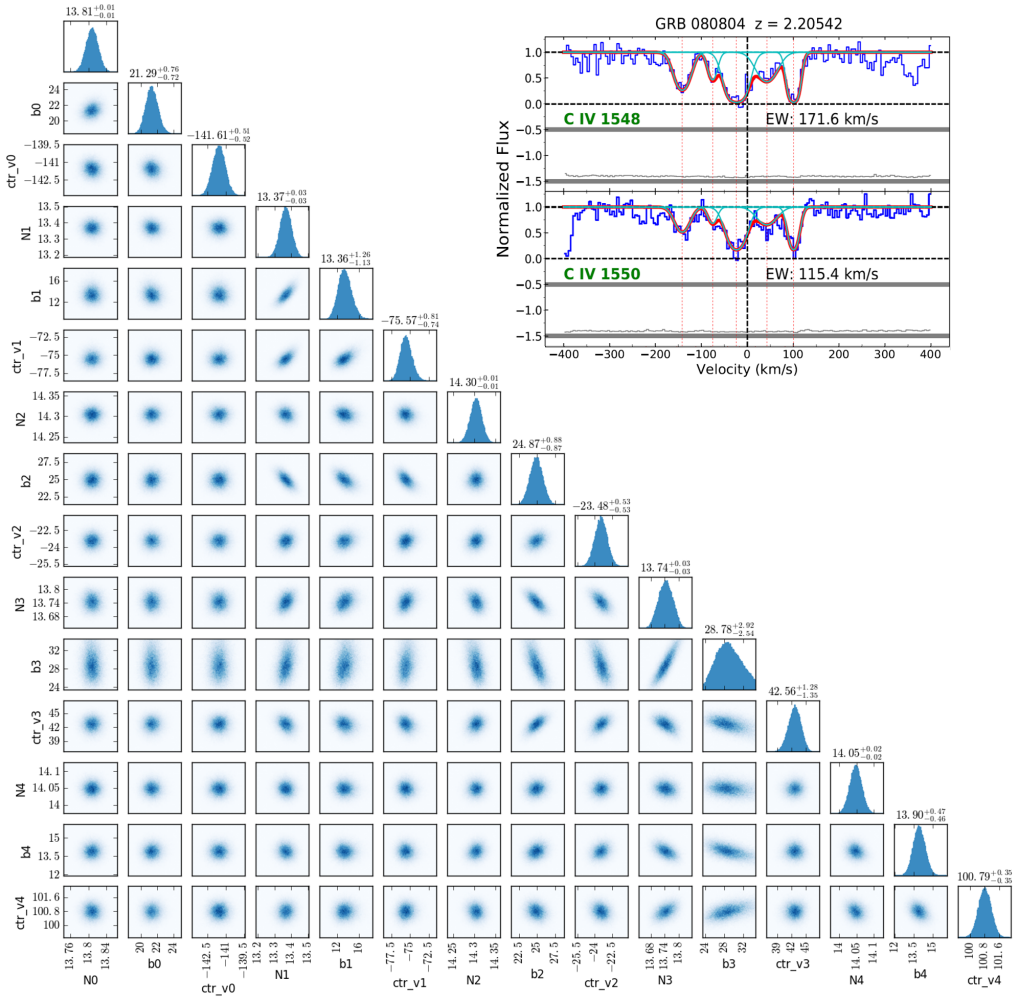


Figure A.1: A sample plot to show the parameter estimation using the MCMC-based method. N, b, and ctr_v indicate the column density, Doppler parameter and central velocity of the respective component. In this example, the C IV doublet is fitted together. The corner plot shows the marginalized posterior distribution function. The 1-$\sigma$ parameter uncertainty is estimated as the range of parameter value that covers the central 68% of the marginalized posterior distribution function.

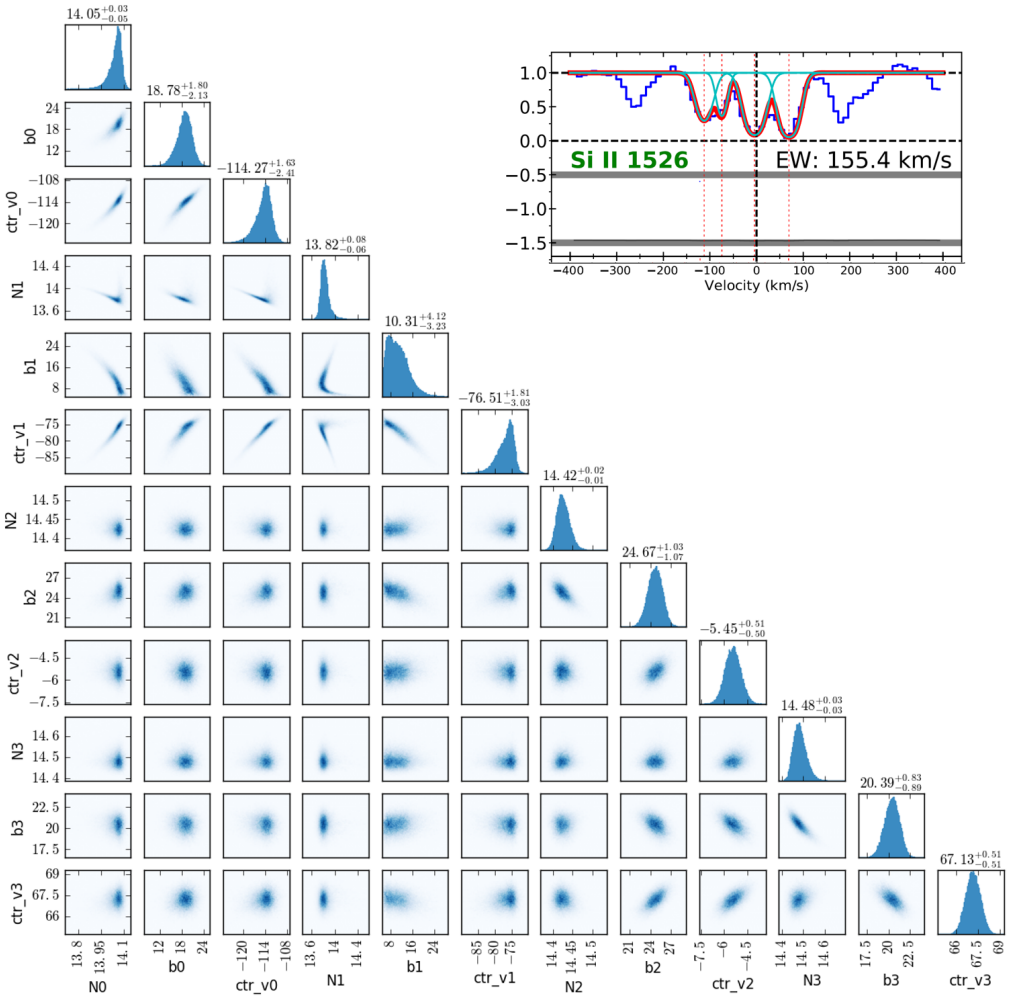


Figure A.2: Same as Fig. A.1 for GRB 161023A with an R $\sim$ 8000 spectrum (X-shooter). The corner plot shows the marginalized posterior distribution function for Si II 1526. The 1-$\sigma$ parameter uncertainty is estimated as the range of parameter value that covers the central 68% of the marginalized posterior distribution function.

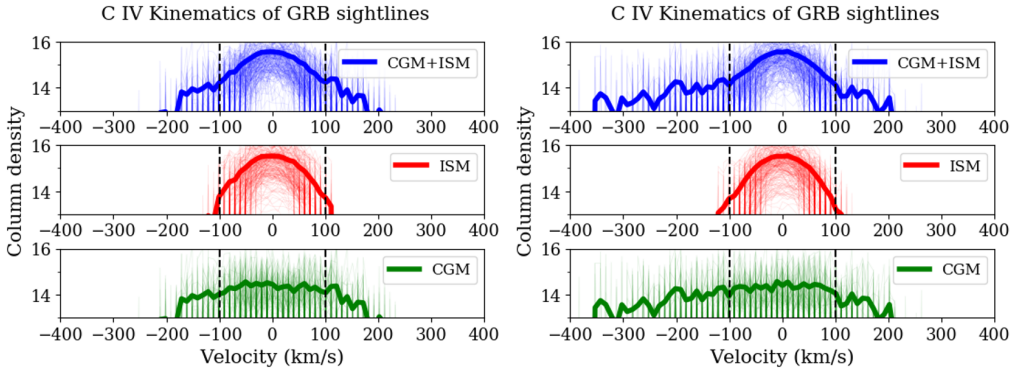


Figure A.3: Overall simulation CIV kinematics with $\log(M_{CGM}/M_{\odot}) = 9.8$ are decomposed into ISM and CGM components and shown with (right) and without (left) an outflow component. The simulations are run for 200 GRB sightlines, which are shown in faint traces and the average column density profiles are shown in dark traces. The figure on the right has $v_{out} = 250$ km s$^{-1}$ and $f_{out} = 0.25$.

Table A.1: Typical values of the toy model parameters, z $\sim$ 2.5

| Parameter | Symbol | Value | References (as applicable) |
|---|---|---|---|
| Galaxy stellar mass | $log(M_*)$ | 9.3 | [Perley et al., 2016b] |
| Galaxy halo mass | $log(M_h)$ | 11.2 | [Hopkins et al., 2014], [Wechsler and Tinker, 2018] |
| Mass in the ISM[a] | $log(M_{ISM})$ | 9.3 | |
| Mass in the CGM[a,b] | $log(M_{CGM})$ | 9.3, **9.8**, 10.3 | |
| Galaxy half-mass radius | $R_e$ | 2 kpc | [Wainwright et al., 2007], [Blanchard et al., 2016] |
| Galaxy radius | $r_{galaxy}$ | 4 kpc | |
| Galaxy height | $h_{galaxy}$ | 3 kpc | |
| Radial range of GRB location | $R_{GRB}$ | 0.4 – 4 kpc | [Blanchard et al., 2016] |
| Max. height of GRB location | $h_{max}$ | $\pm$ 1 kpc | |
| Virial radius | $R_{vir}$ | 50 kpc | |
| CGM cloud radius | $R_{cloud}$ | 0.4 kpc | |
| Volume filling fraction | $f_{vol}$ | 0.1 | [Stocke et al., 2013], [Werk et al., 2016] |
| Simulation region | – | 2×$R_{vir}$ | [Shen et al., 2013] |
| Flat rotation velocity | $v_{flat}$ | 100 km s$^{-1}$ | [Arabsalmani et al., 2018] |
| ISM dispersion velocity | $\sigma_{v,ISM}$ | 50 km s$^{-1}$ | [Lan and Mo, 2018] |
| CGM dispersion velocity | $\sigma_{v,CGM}$ | 100 km s$^{-1}$ | [Lan and Mo, 2018] |
| Outflow launch velocity[b] | $v_{out}$ | 200, 250, **300** km s$^{-1}$ | |
| Outflow launching radius | $R_{launch}$ | 2 kpc | |
| Outflow fraction[b] | $f_{out}$ | **0.25**, 0.5, 0.75 | [Ford et al., 2014], [Muratov et al., 2015] |
| Number of sightlines | – | 200 | |

The boldfaced values are for the optimal toy model which best explains the observed C IV column density profile

[a]The mass of warm ionized CGM traced by the C IV ion (T $\sim 10^{4.5-5.5}$K)

[b] These parameters are modified to obtain a model that closely matches the observations

GRB hosts [Wainwright et al., 2007, Blanchard et al., 2016]. The CGM is defined as a sphere of radius $R_{CGM}$ surrounding the galaxy. This sphere is populated with a uniform probability distribution by clouds of radius $R_{cloud}$ and each cloud has a gas number density that is given as:

$$n_{cloud} = n_0 \left(\frac{r}{r_0}\right)^{-2} \tag{A.5}$$

where $r$ is the radial coordinate of the cloud and $r_0$ is a reference radius. In this simulation, $r_0$ is taken to be the same as $r_{galaxy}$. The gas number density in the CGM clouds at $r_0$ is $n_0$. The radial density variation is modeled as inverse square law assuming the clouds originate from a mass conserving galactic outflow ([Chisholm et al., 2017]), consistent with other CGM modeling efforts at z $\sim$ 2.5 (eg: equation 22 in [Steidel et al., 2010]).

A constant volume filling fraction (i.e. the fraction of CGM volume filled by the clouds) of 0.1 is assumed, in line with the volume filling fraction estimates in local CGM studies [Werk et al., 2016, Stocke et al., 2013]. The value of $n_0$ is selected such that the integrated mass in the CGM (within 2 $\times R_{vir}$) equals $M_{CGM}$ for a given model. $M_{CGM}$ is the mass of CGM phase traced by C IV ion and is considered a variable quantity among different models. $M_{CGM}$ is selected to be roughly within an order of magnitude of the stellar mass. This assumption is in line with the observations and models presented in the literature (see Fig. 8 in [Tumlinson et al., 2017] and [Shen et al., 2013, Peeples et al., 2018]).

**GRB location:** The location of the GRB is randomly selected with a uniform

spatial probability distribution in the region within $r_{inner}$ and $r_{galaxy}$, where $r_{inner}$ is chosen to be 0.4 kpc since the GRB host imaging surveys indicate that ∼80% of the long GRBs to have an offset greater than 0.4 kpc [Blanchard et al., 2016]. The vertical location of the GRB is constrained within ± $h_{max}$, where $h_{max}$ is chosen to be 1 kpc to constrain the occurrence of GRBs in the region of active star formation. The GRB sightline is randomly chosen with a uniform probability distribution.

**Kinematics:** For the ISM kinematics, a flat rotation curve is assumed with $v_{circ}$ = 100 km s$^{-1}$, in accordance with the stellar mass of the GRB host galaxy [Arabsalmani et al., 2018]. A 3-dimensional velocity dispersion ($\sigma_{v,ISM}$) of 50 km s$^{-1}$ is added to this. The individual CGM clouds move at random velocities with an isothermal distribution described by a Gaussian centered at 0 km s$^{-1}$ with a standard deviation ($\sigma_{v,CGM}$) of 100 km s$^{-1}$, given by the virial velocity of the halo. The dispersion speed is informed by the assumption of the galaxy mass and prior estimates from local and high-z CGM observations ([Steidel et al., 2010, Lan and Mo, 2018]). In this construct, although the column density depends on the value of $M_{CGM}$, the kinematic extent of the CGM is fairly insensitive.

**Outflows:** In order to simulate galactic outflows, a radially outward component is added to a fraction $f_{out}$ of the CGM clouds. The outflow velocity varies with the radial coordinate of the cloud to model the ballistic motion under the gravity of the dark matter halo. The outflow launch velocity at a radial distance ($R_{launch}$) of 2 kpc is defined as $v_{out}$. The fraction $f_{out}$ is assumed to be $25 - 75\%$, in line with circumgalactic outflow simulations ([Muratov et al., 2015, Ford et al., 2014]). The

outflow launch velocity is varied between $200 - 300$ km s$^{-1}$ with a step of 50 km s$^{-1}$ ([Muratov et al., 2015, Lan and Mo, 2018]). The outflow component is only added up to the radius where it decelerates to zero, i.e., no inflow component is added. The kinematics obtained from the observed data can be used to constrain $f_{out}$ and $v_{out}$.

**Simulation scheme:** A GRB location and line of sight (LOS) is selected. Within the ISM portion of the LOS, the length is divided into 100 sections. For each section, the component of velocity along the LOS and the column density is evaluated. In the CGM portion, the column density contributed by intersecting clouds and the LOS velocity is evaluated. The zero velocity for kinematics is defined as the LOS velocity of the material in the immediate vicinity of the GRB location (similar to the use of strongest fine structure transitions to define the zero velocity for the observed spectra). The results are compiled to synthesize the column density as a function of velocity for the entire LOS, as well as for the separate portions from the ISM and CGM . This helps in visualizing the kinematic distinction between the ISM and CGM. The column density is further binned in 100 km s$^{-1}$ velocity bins in the same fashion as the observed data. The simulation is repeated 200 times with new GRB locations and LOS to infer the variation in kinematics. The velocity-binned column density profiles are further stacked to plot the kinematics for the sample which can then be compared with the observations.

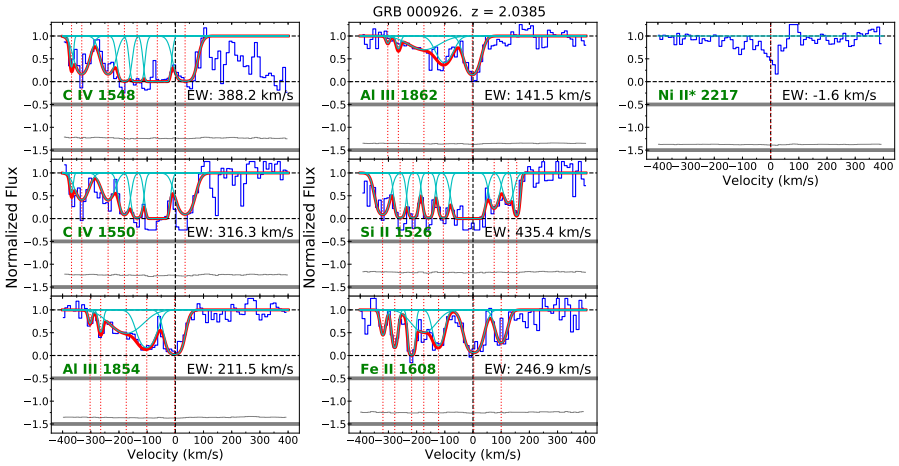


Figure A.4: Voigt profile fit for GRB 000926

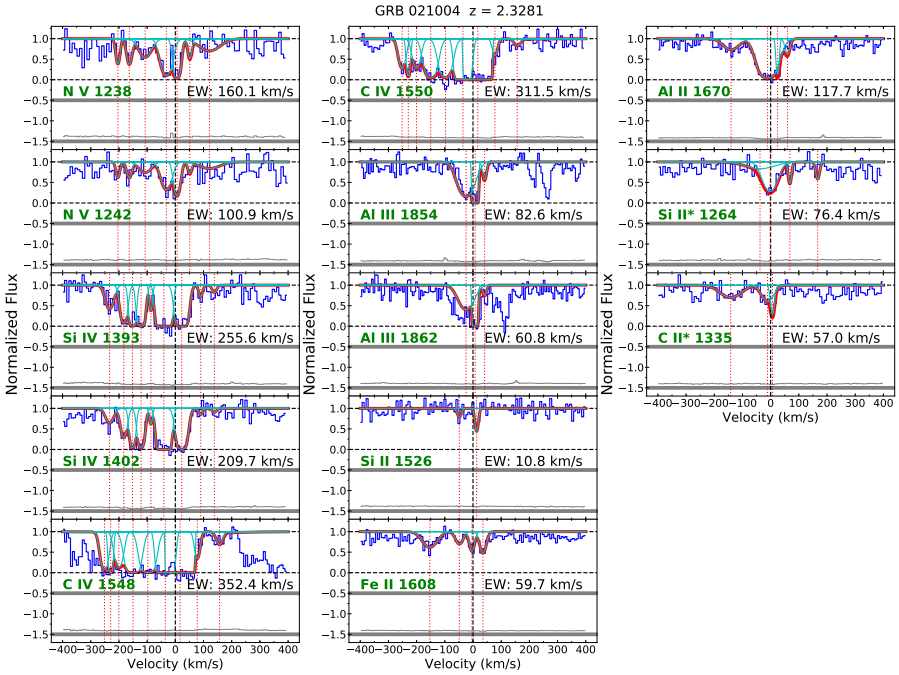


Figure A.5: Voigt profile fit for GRB 021004

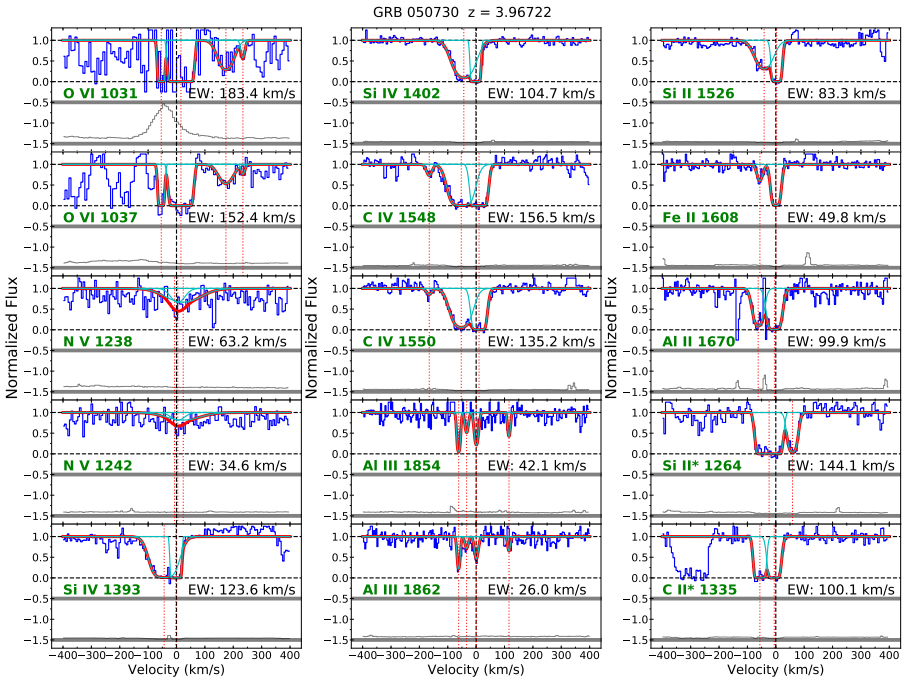


Figure A.6: Voigt profile fit for GRB 050730

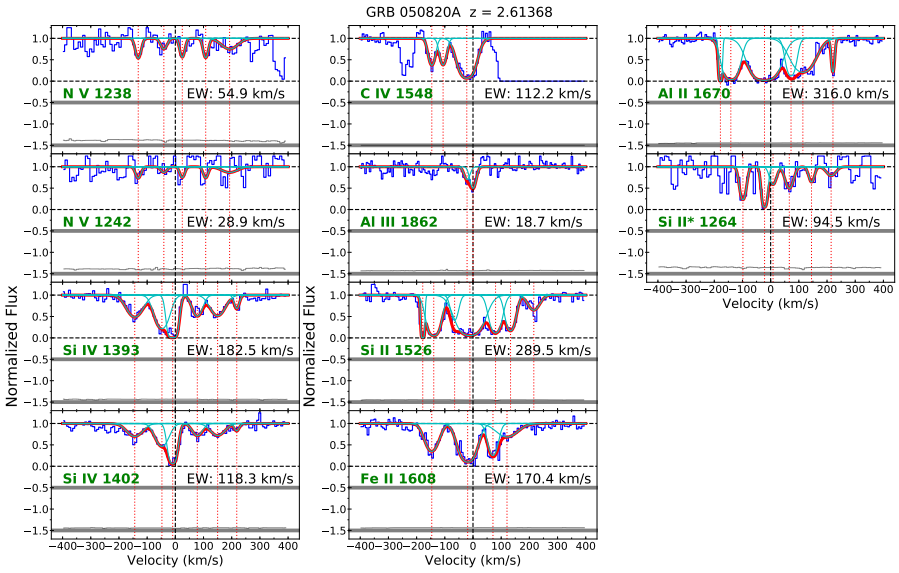


Figure A.7: Voigt profile fit for GRB 050820A

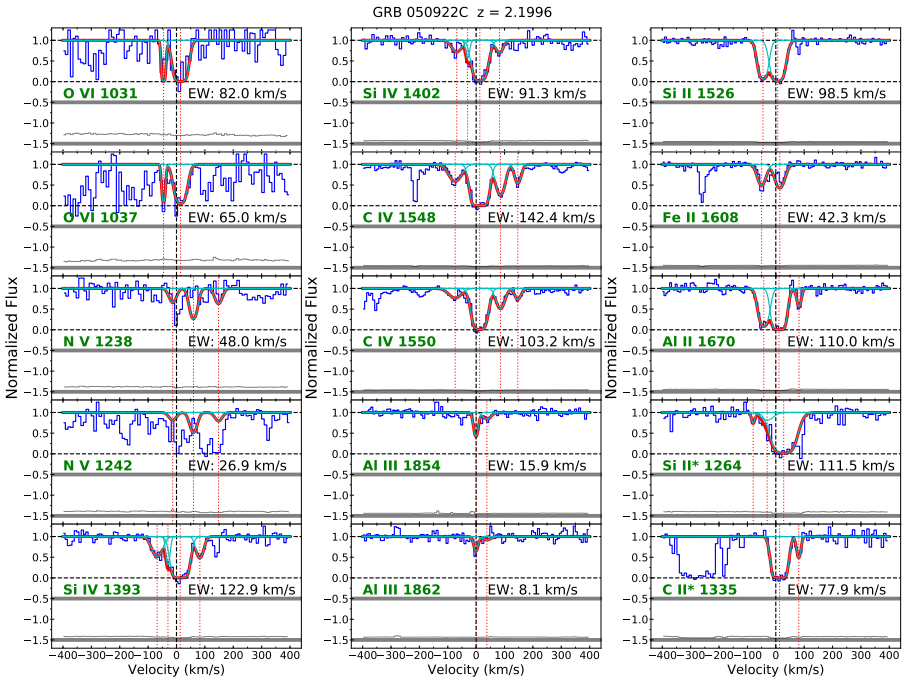


Figure A.8: Voigt profile fit for GRB 050922C

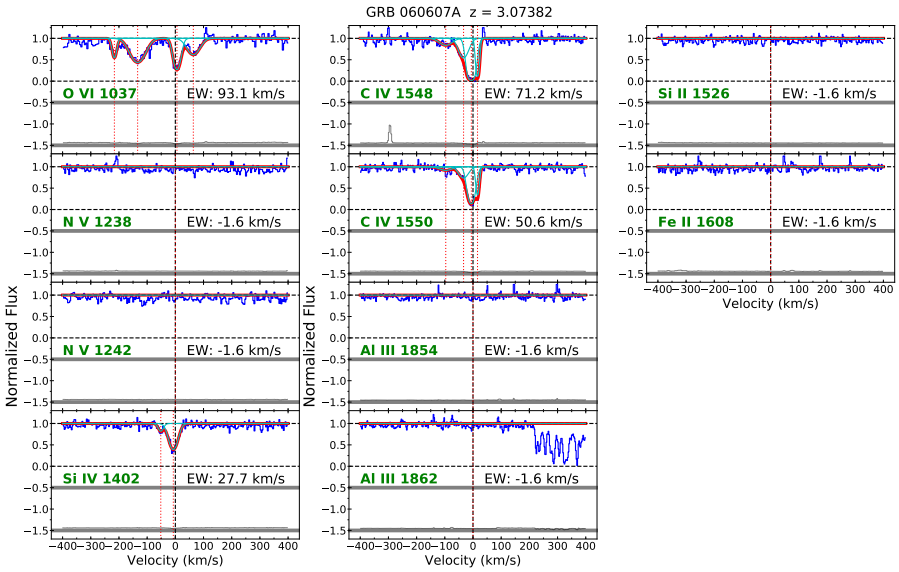


Figure A.9: Voigt profile fit for GRB 060607A


Figure A.10: Voigt profile fit for GRB 071031

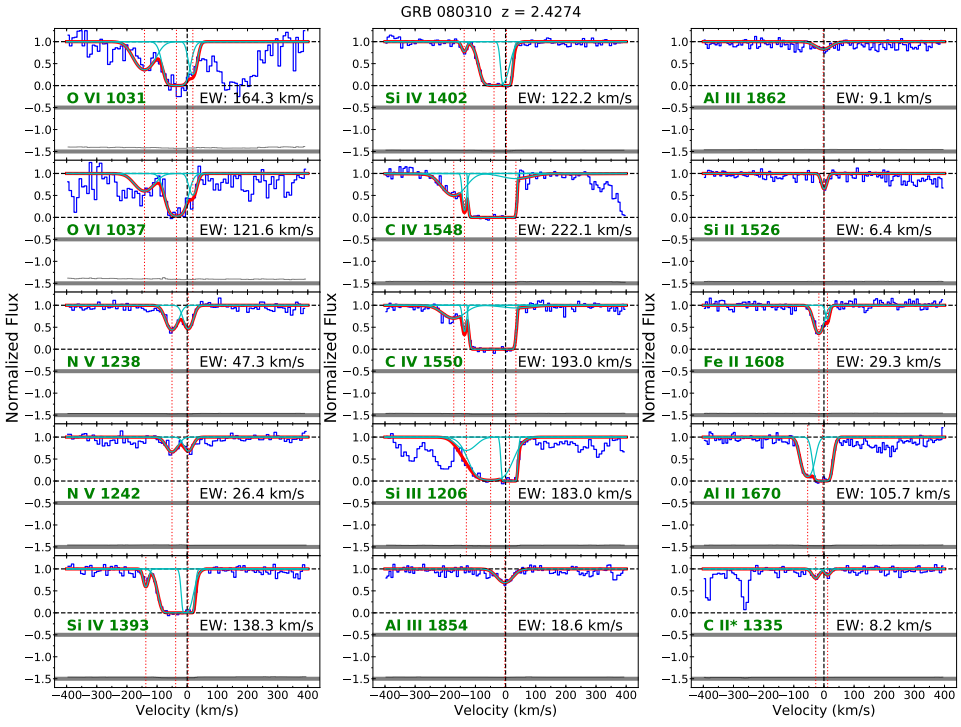


Figure A.11: Voigt profile fit for GRB 080310

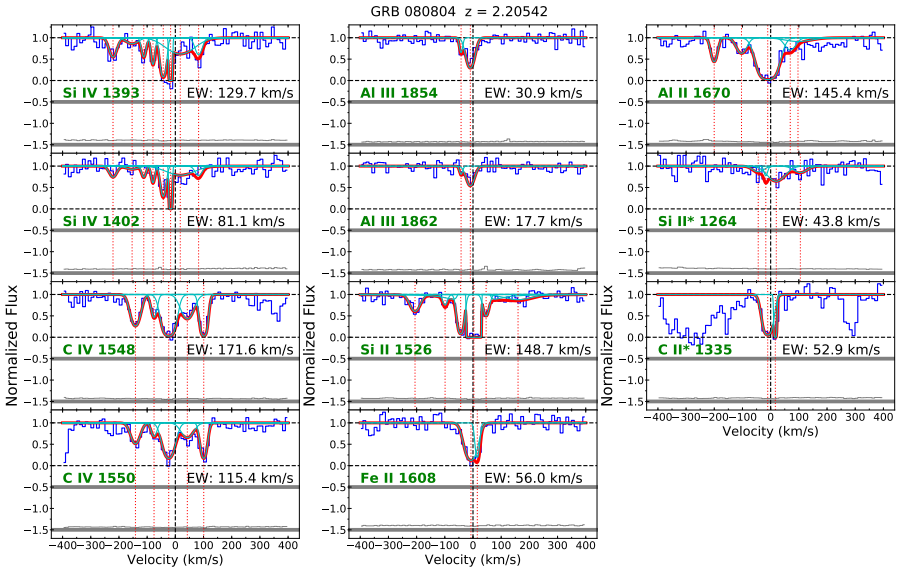


Figure A.12: Voigt profile fit for GRB 080804

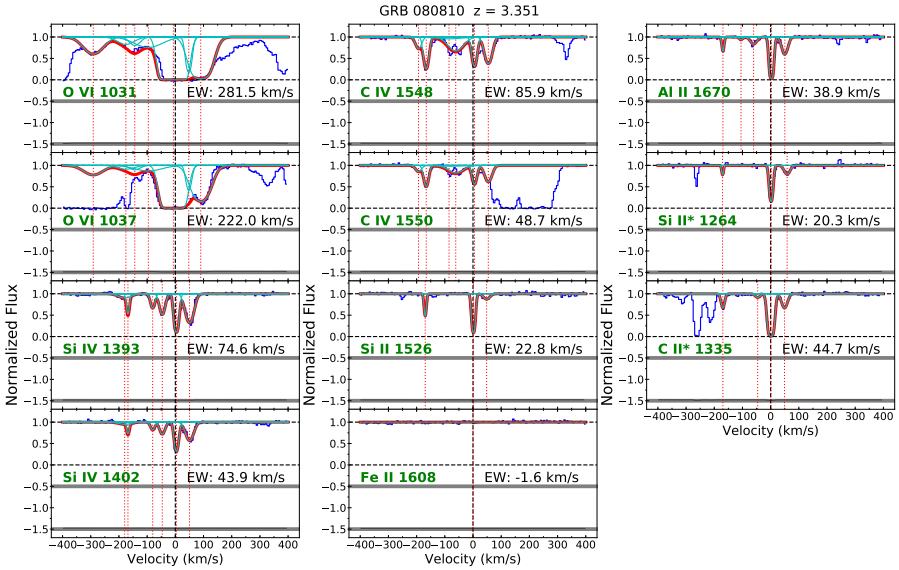


Figure A.13: Voigt profile fit for GRB 080810

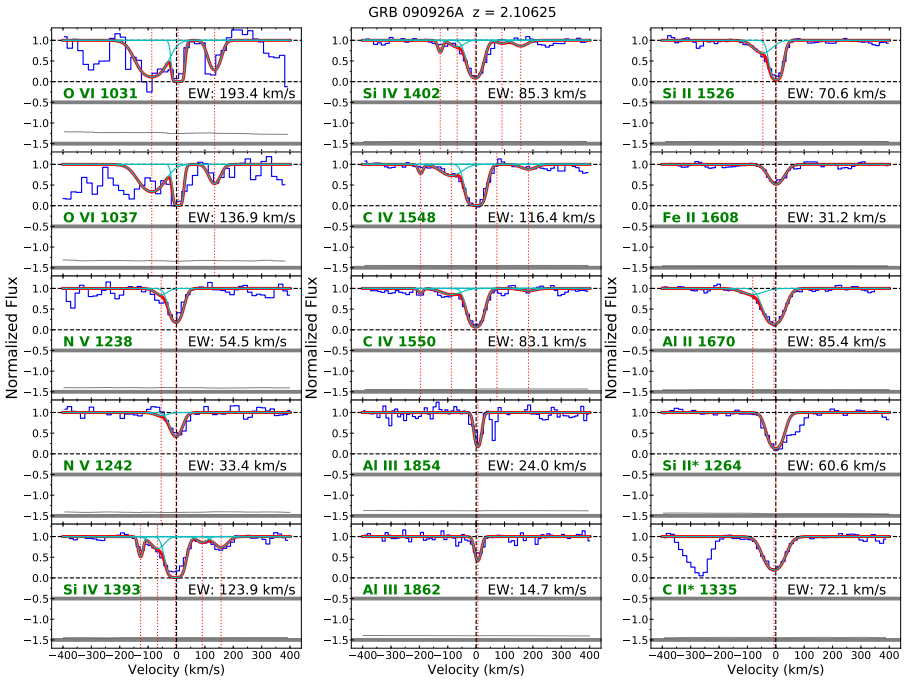


Figure A.14: Voigt profile fit for GRB 090926A

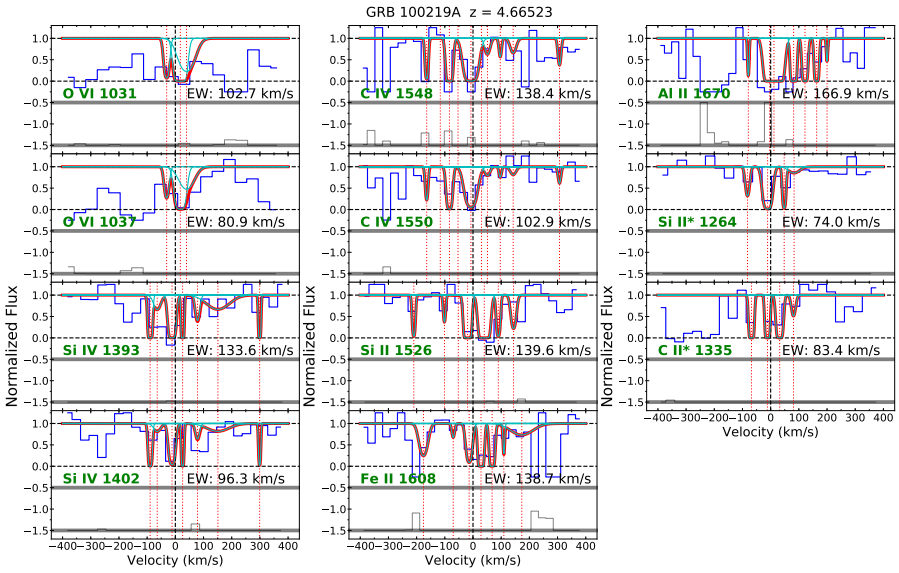


Figure A.15: Voigt profile fit for GRB 100219A

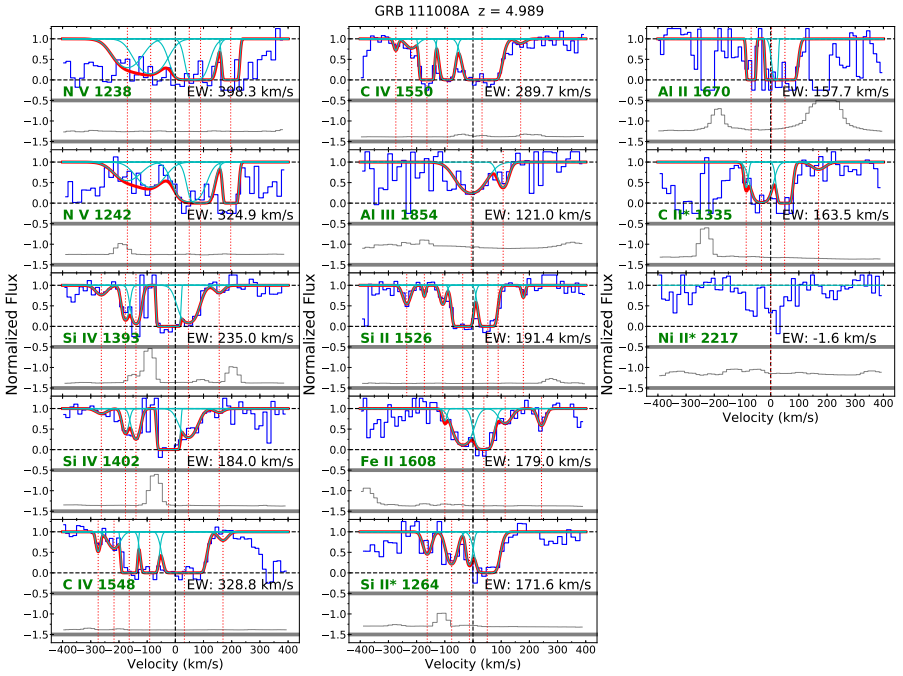


Figure A.16: Voigt profile fit for GRB 111008A

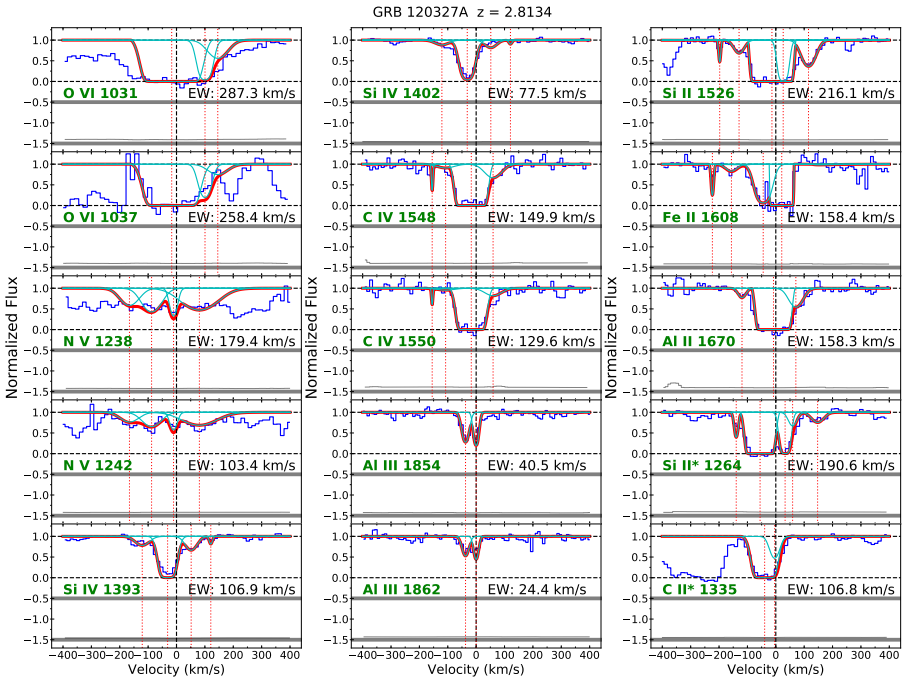


Figure A.17: Voigt profile fit for GRB 120327A

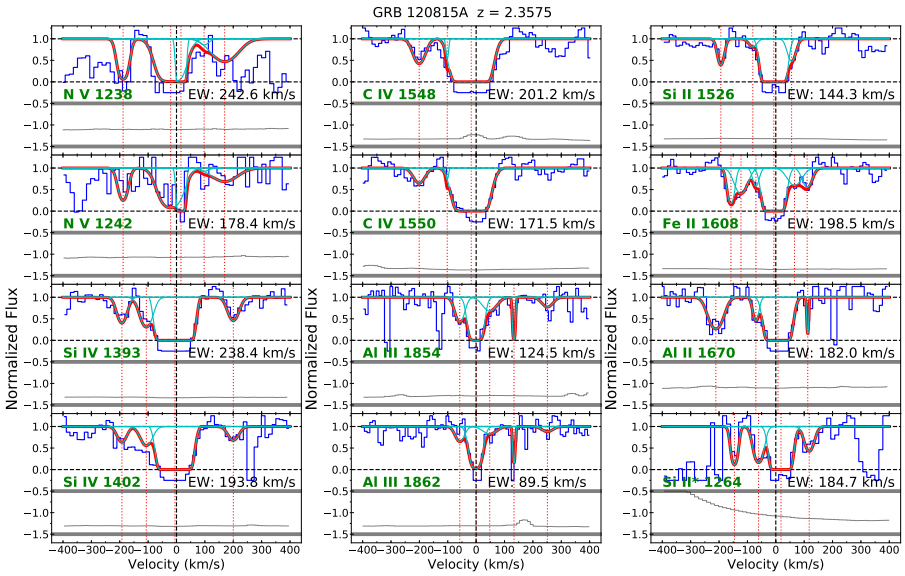


Figure A.18: Voigt profile fit for GRB 120815A

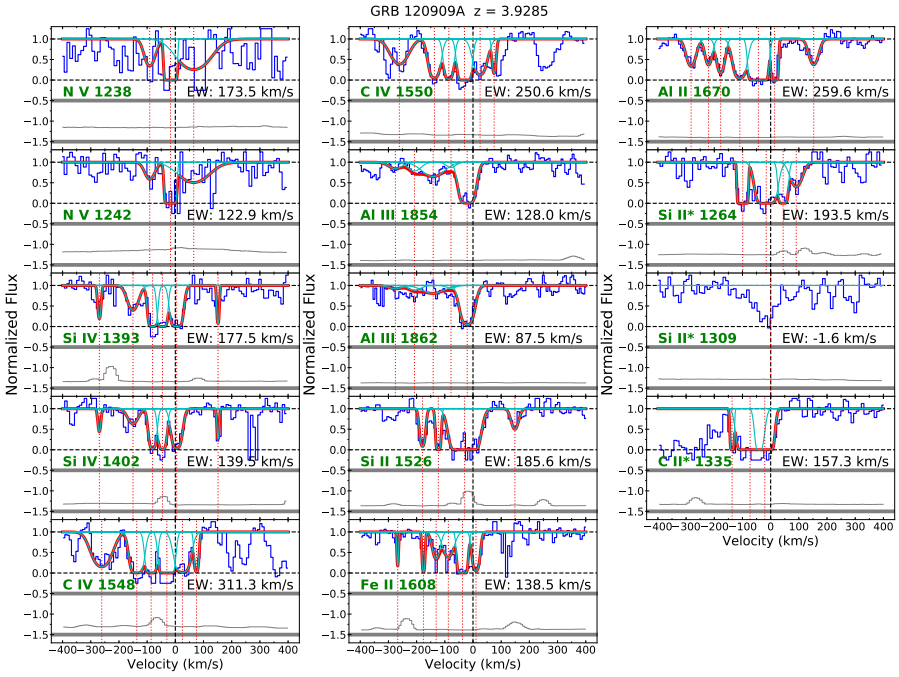


Figure A.19: Voigt profile fit for GRB 120909A

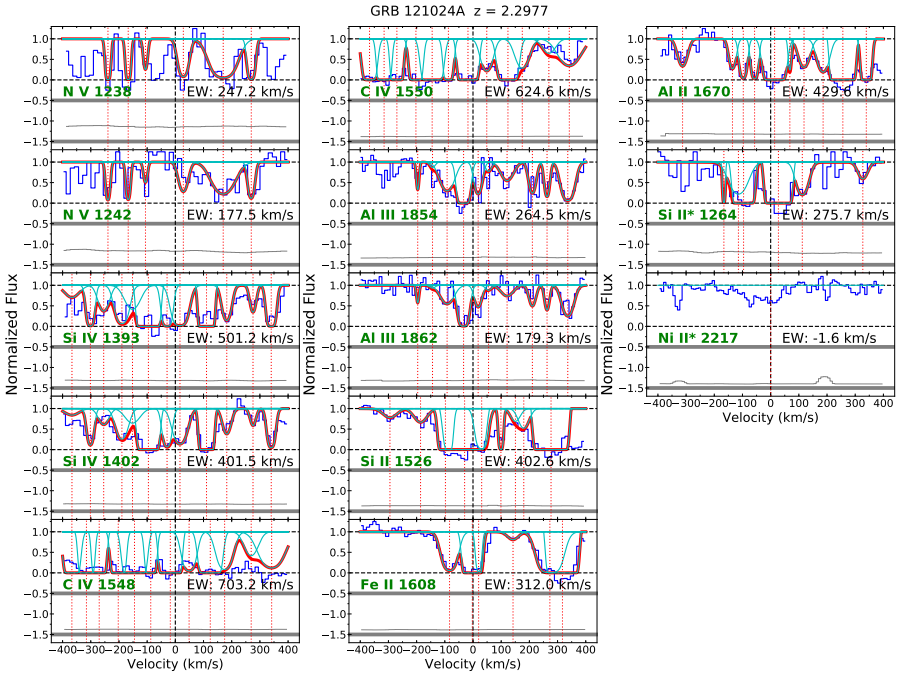


Figure A.20: Voigt profile fit for GRB 121024A

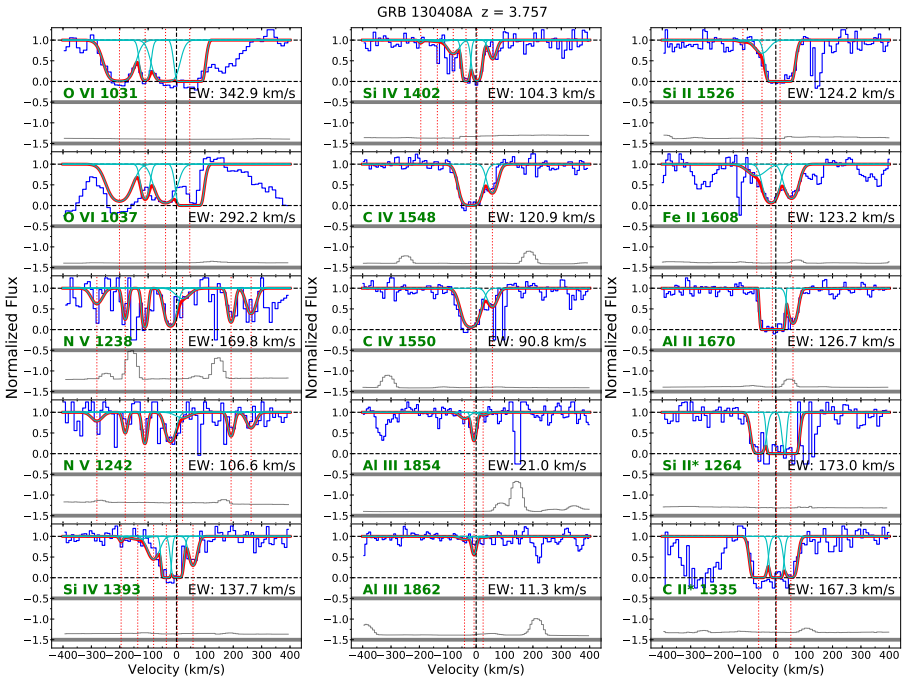


Figure A.21: Voigt profile fit for GRB 130408A

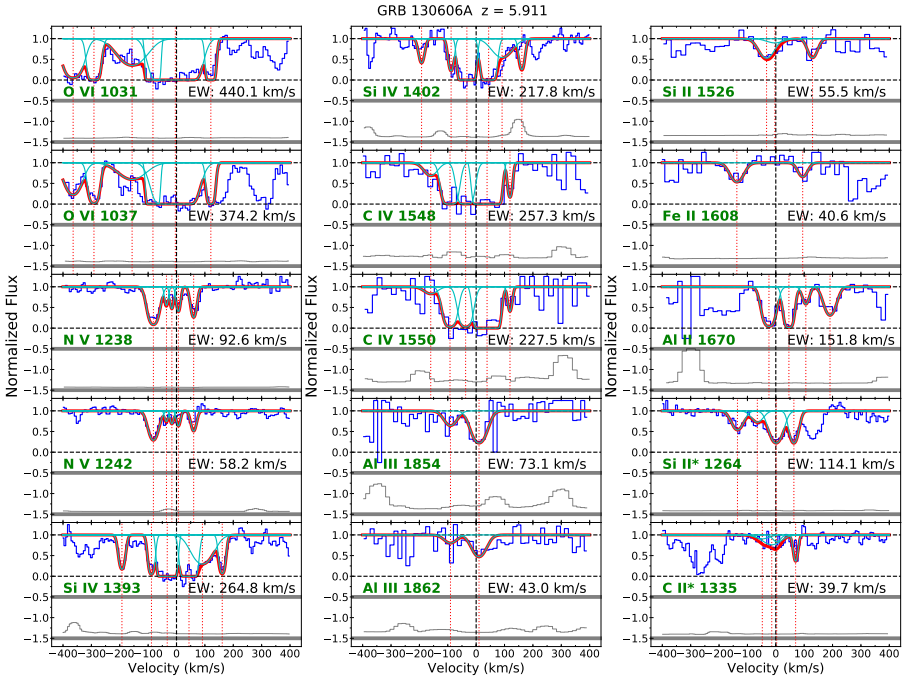


Figure A.22: Voigt profile fit for GRB 130606A

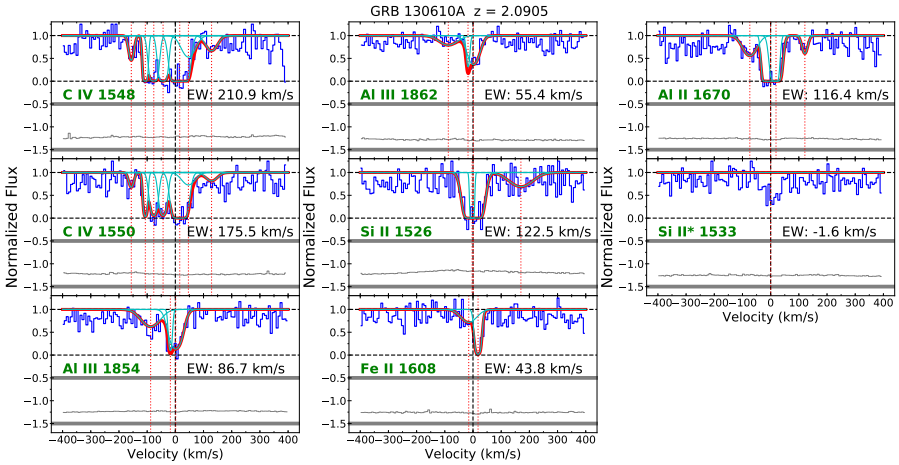


Figure A.23: Voigt profile fit for GRB 130610A

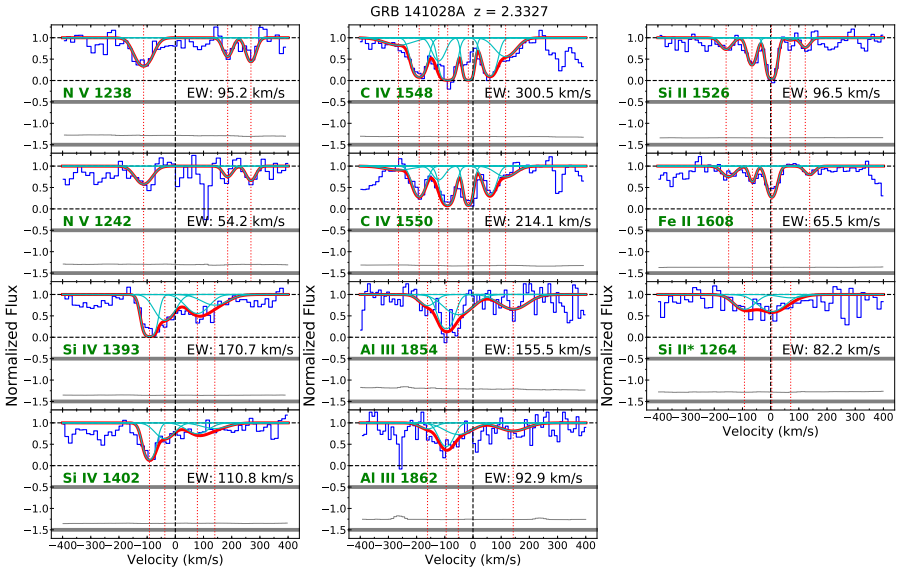


Figure A.24: Voigt profile fit for GRB 141028A

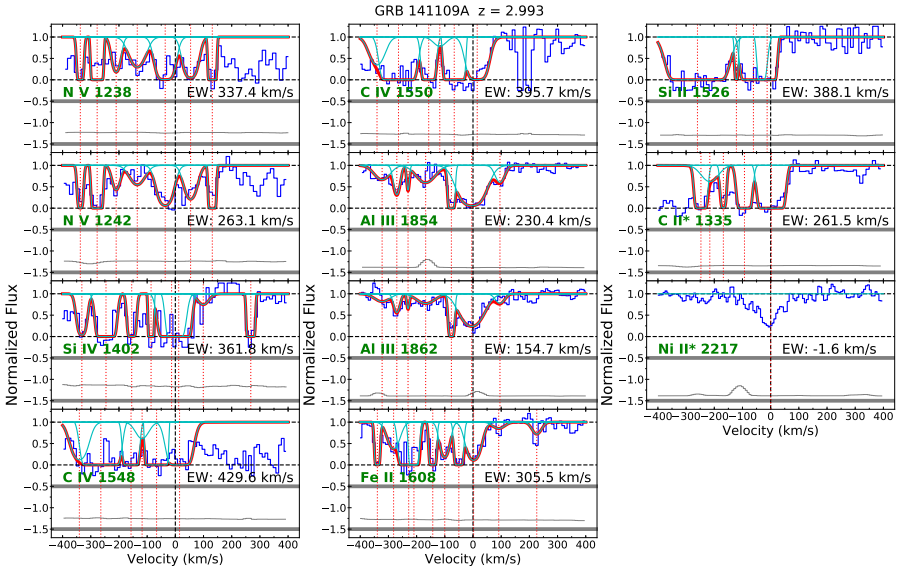


Figure A.25: Voigt profile fit for GRB 141109A

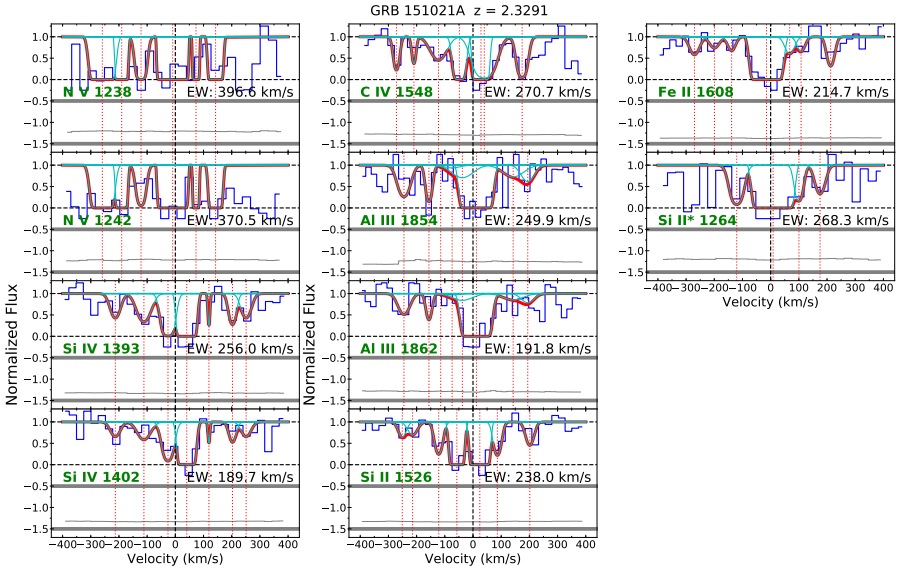


Figure A.26: Voigt profile fit for GRB 151021A

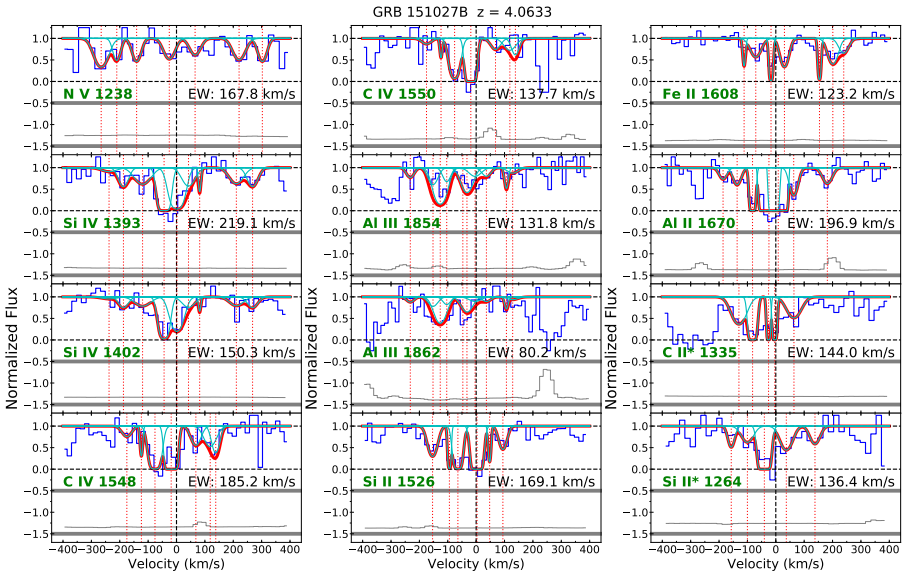


Figure A.27: Voigt profile fit for GRB 151027B

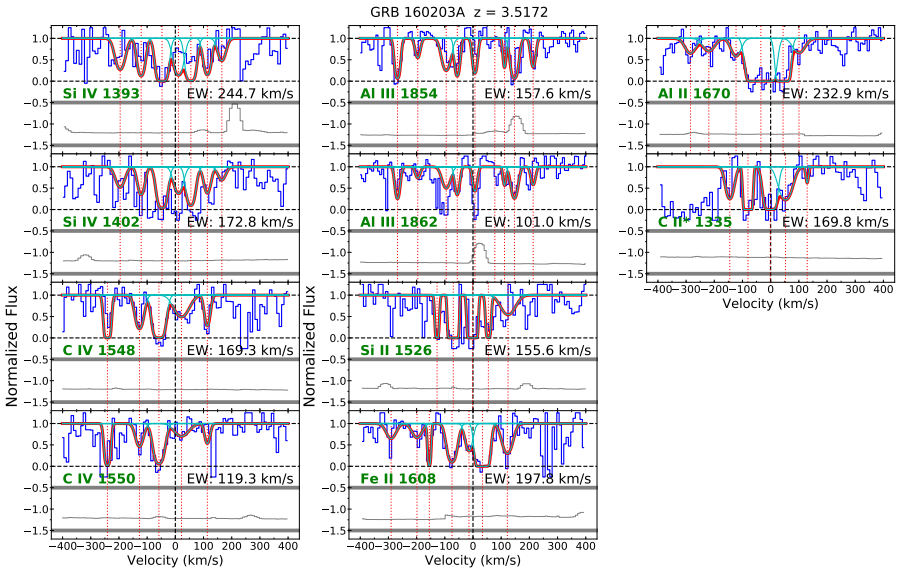


Figure A.28: Voigt profile fit for GRB 160203A

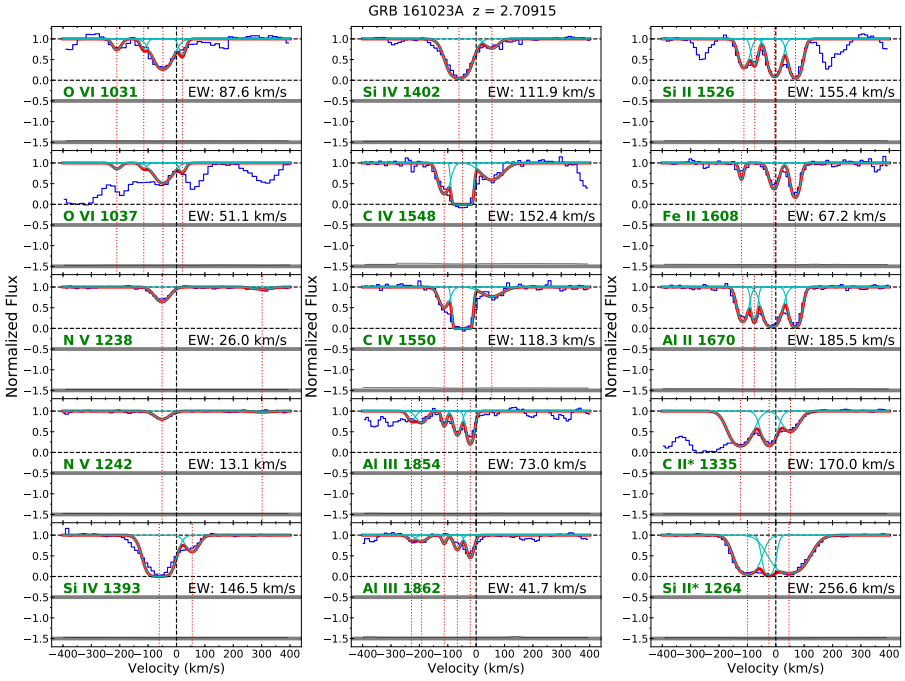


Figure A.29: Voigt profile fit for GRB 161023A

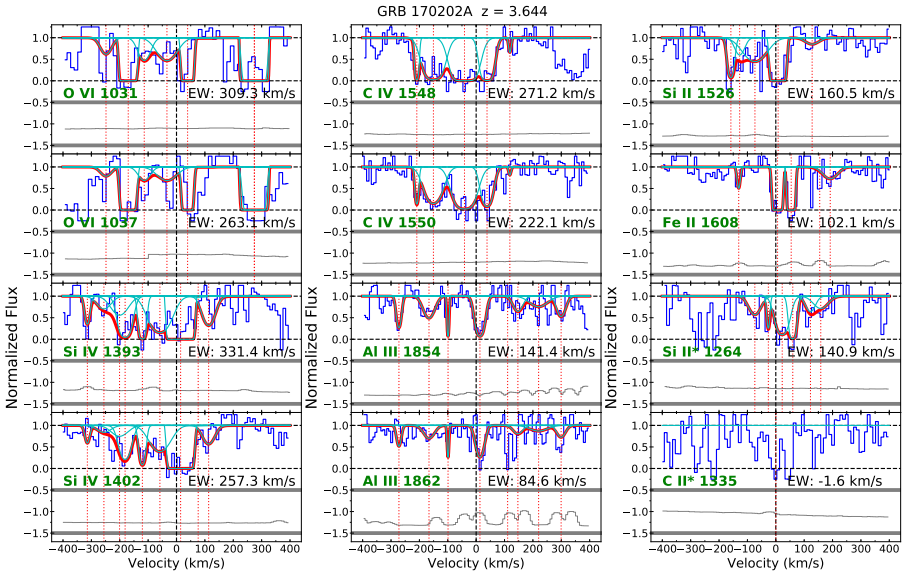


Figure A.30: Voigt profile fit for GRB 170202A

# Bibliography

[Akca et al., 2011] Akca, I. B., Ismail, N., Sun, F., Driessen, A., Worhoff, K., Pollnau, M., and de Ridder, R. M. (2011). High-resolution integrated spectrometers in silicon-oxynitride. In *CLEO: Applications and Technology*, page JWA65. Optical Society of America.

[Alam et al., 2015] Alam, S., Albareti, F. D., Prieto, C. A., Anders, F., Anderson, S. F., Anderton, T., Andrews, B. H., Armengaud, E., Aubourg, É., Bailey, S., et al. (2015). The eleventh and twelfth data releases of the sloan digital sky survey: final data from sdss-iii. *The Astrophysical Journal Supplement Series*, 219(1):12.

[Allington-Smith and Bland-Hawthorn, 2010] Allington-Smith, J. and Bland-Hawthorn, J. (2010). Astrophotonic spectroscopy: defining the potential advantage. *Monthly Notices of the Royal Astronomical Society*, 404(1):232–238.

[Anglés-Alcázar et al., 2014] Anglés-Alcázar, D., Davé, R., Özel, F., and Oppenheimer, B. D. (2014). Cosmological zoom simulations of z= 2 galaxies: the impact of galactic outflows. *The Astrophysical Journal*, 782(2):84.

[Anglés-Alcázar et al., 2017] Anglés-Alcázar, D., Faucher-Giguère, C.-A., Kereš, D., Hopkins, P. F., Quataert, E., and Murray, N. (2017). The cosmic baryon cycle and galaxy mass assembly in the fire simulations. *Monthly Notices of the Royal Astronomical Society*, 470(4):4698–4719.

[Arabsalmani et al., 2018] Arabsalmani, M., Møller, P., Perley, D., Freudling, W., Fynbo, J., Le Floc'h, E., Zwaan, M., Schulze, S., Tanvir, N., Christensen, L., et al. (2018). Mass and metallicity scaling relations of high-redshift star-forming galaxies selected by grbs. *Monthly Notices of the Royal Astronomical Society*, 473(3):3312–3324.

[Bahcall and Wolf, 1968] Bahcall, J. N. and Wolf, R. A. (1968). Fine-structure transitions. *The Astrophysical Journal*, 152:701.

[Bauters et al., 2011a] Bauters, J. F., Heck, M. J., John, D., Dai, D., Tien, M.-C., Barton, J. S., Leinse, A., Heideman, R. G., Blumenthal, D. J., and Bowers, J. E. (2011a). Ultra-low-loss high-aspect-ratio si 3 n 4 waveguides. *Optics express*, 19(4):3163–3174.

[Bauters et al., 2010] Bauters, J. F., Heck, M. J., John, D., Tien, M.-C., Leinse, A., Heideman, R. G., Blumenthal, D. J., and Bowers, J. E. (2010). Ultra-low loss silica-based waveguides with millimeter bend radius. In *Proceedings of the 36th European Conference on Optical Communication*.

[Bauters et al., 2011b] Bauters, J. F., Heck, M. J., John, D. D., Barton, J. S., Bruinink, C. M., Leinse, A., Heideman, R. G., Blumenthal, D. J., and Bowers, J. E. (2011b). Planar waveguides with less than 0.1 dB/m propagation loss fabricated with wafer bonding. *Optics express*, 19(24):24090–24101.

[Behroozi et al., 2013] Behroozi, P. S., Marchesini, D., Wechsler, R. H., Muzzin, A., Papovich, C., and Stefanon, M. (2013). Using cumulative number densities to compare galaxies across cosmic time. *The Astrophysical Journal Letters*, 777(1):L10.

[Bell, 2003] Bell, E. F. (2003). Estimating star formation rates from infrared and radio luminosities: the origin of the radio-infrared correlation. *The Astrophysical Journal*, 586(2):794.

[Birks et al., 2015] Birks, T. A., Gris-Sánchez, I., Yerolatsitis, S., Leon-Saval, S., and Thomson, R. R. (2015). The photonic lantern. *Advances in Optics and Photonics*, 7(2):107–167.

[Blanchard et al., 2016] Blanchard, P. K., Berger, E., and Fong, W.-f. (2016). The offset and host light distributions of long gamma-ray bursts: a new view from hst observations of swift bursts. *The Astrophysical Journal*, 817(2):144.

[Bland-Hawthorn et al., 2011] Bland-Hawthorn, J., Ellis, S., Leon-Saval, S., Haynes, R., Roth, M., Löhmannsröben, H.-G., Horton, A., Cuby, J.-G., Birks, T. A., Lawrence, J., et al. (2011). A complex multi-notch astronomical filter to suppress the bright infrared sky. *Nature communications*, 2:581.

[Bland-Hawthorn and Horton, 2006] Bland-Hawthorn, J. and Horton, A. (2006). Instruments without optics: an integrated photonic spectrograph. In *SPIE Astronomical Telescopes+ Instrumentation*, pages 62690N–62690N. International Society for Optics and Photonics.

[Bland-Hawthorn and Kern, 2009] Bland-Hawthorn, J. and Kern, P. (2009). Astrophotonics: a new era for astronomical instruments. *Optics Express*, 17(3):1880–1884.

[Bloom et al., 2002] Bloom, J. S., Kulkarni, S. R., and Djorgovski, S. G. (2002). The observed offset distribution of gamma-ray bursts from their host galaxies: a robust clue to the nature of the progenitors. *The Astronomical Journal*, 123(3):1111.

[Blumenthal et al., 2018] Blumenthal, D. J., Heideman, R., Geuzebroek, D., Leinse, A., and Roeloffzen, C. (2018). Silicon nitride in silicon photonics. *Proceedings of the IEEE*, 106(12):2209–2231.

[Boissier et al., 2013] Boissier, S., Salvaterra, R., Le Floc'h, E., Basa, S., Buat, V., Prantzos, N., Vergani, S., and Savaglio, S. (2013). A method for quantifying the gamma-ray burst bias. application in the redshift range of 0–1.1. *Astronomy & Astrophysics*, 557:A34.

[Bolmer et al., 2018] Bolmer, J., Greiner, J., Krühler, T., Schady, P., Ledoux, C., Tanvir, N. R., and Levan, A. J. (2018). Dust reddening and extinction curves toward gamma-ray bursts at z $>$ 4. *Astronomy & Astrophysics*, 609:A62.

[Bordoloi et al., 2014a] Bordoloi, R., Lilly, S. J., Hardmeier, E., Contini, T., Kneib, J.-P., Le Fevre, O., Mainieri, V., Renzini, A., Scodeggio, M., Zamorani, G., et al. (2014a). The dependence of galactic outflows on the properties and orientation of zcosmos galaxies at z $\sim$ 1. *The Astrophysical Journal*, 794(2):130.

[Bordoloi et al., 2011] Bordoloi, R., Lilly, S. J., Knobel, C., Bolzonella, M., Kampczyk, P., Carollo, C. M., Iovino, A., Zucca, E., Contini, T., Kneib, J.-P., et al. (2011). The radial and azimuthal profiles of mg ii absorption around $0.5 < z < 0.9$ zcosmos galaxies of different colors, masses, and environments. *The Astrophysical Journal*, 743(1):10.

[Bordoloi et al., 2014b] Bordoloi, R., Tumlinson, J., Werk, J. K., Oppenheimer, B. D., Peeples, M. S., Prochaska, J. X., Tripp, T. M., Katz, N., Davé, R., Fox, A. J., et al. (2014b). the cos-dwarfs survey: the carbon reservoir around sub-l* galaxies. *The Astrophysical Journal*, 796(2):136.

[Borthakur et al., 2013] Borthakur, S., Heckman, T., Strickland, D., Wild, V., and Schiminovich, D. (2013). The impact of starbursts on the circumgalactic medium. *The Astrophysical Journal*, 768(1):18.

[Borthakur et al., 2015] Borthakur, S., Heckman, T., Tumlinson, J., Bordoloi, R., Thom, C., Catinella, B., Schiminovich, D., Davé, R., Kauffmann, G., Moran, S. M., et al. (2015). Connection between the circumgalactic medium and the interstellar medium of galaxies: Results from the cos-gass survey. *The Astrophysical Journal*, 813(1):46.

[Bouché et al., 2007] Bouché, N., Lehnert, M. D., Aguirre, A., Péroux, C., and Bergeron, J. (2007). The missing metals problem–iii. how many metals are expelled from galaxies? *Monthly Notices of the Royal Astronomical Society*, 378(2):525–540.

[Bouché et al., 2006] Bouché, N., Lehnert, M. D., and Péroux, C. (2006). The missing metals problem–ii. how many metals are in z $\sim$ 2.2 galaxies? *Monthly Notices of the Royal Astronomical Society: Letters*, 367(1):L16–L19.

[Bouwens et al., 2009] Bouwens, R., Illingworth, G., Franx, M., Chary, R.-R., Meurer, G., Conselice, C., Ford, H., Giavalisco, M., and Van Dokkum, P. (2009). Uv continuum slope and dust obscuration from z $\sim$ 6 to z $\sim$ 2: the star formation rate density at high redshift. *The Astrophysical Journal*, 705(1):936.

[Bradshaw et al., 2013] Bradshaw, E., Almaini, O., Hartley, W., Smith, K., Conselice, C., Dunlop, J., Simpson, C., Chuter, R., Cirasuolo, M., Foucaud, S., et al. (2013). High-velocity outflows from young star-forming galaxies in the ukidss ultra-deep survey. *Monthly Notices of the Royal Astronomical Society*, 433(1):194–208.

[Brown et al., 2018] Brown, A., Vallenari, A., Prusti, T., De Bruijne, J., Babusiaux, C., Bailer-Jones, C., Biermann, M., Evans, D. W., Eyer, L., Jansen, F., et al. (2018). Gaia data release 2-summary of the contents and survey properties. *Astronomy & astrophysics*, 616:A1.

[Bruzual and Charlot, 2003] Bruzual, G. and Charlot, S. (2003). Stellar population synthesis at the resolution of 2003. *Monthly Notices of the Royal Astronomical Society*, 344(4):1000–1028.

[Burchett et al., 2016] Burchett, J. N., Tripp, T. M., Bordoloi, R., Werk, J. K., Prochaska, J. X., Tumlinson, J., Willmer, C., O'Meara, J., and Katz, N. (2016). A deep search for faint galaxies associated with very low redshift c iv absorbers. iii. the mass-and environment-dependent circumgalactic medium. *The Astrophysical Journal*, 832(2):124.

[Burrows et al., 2005] Burrows, D. N., Hill, J., Nousek, J. A., Kennea, J. A., Wells, A., Osborne, J., Abbey, A., Beardmore, A., Mukerjee, K., Short, A., et al. (2005). The swift x-ray telescope. *Space science reviews*, 120(3-4):165–195.

[Campana et al., 2015] Campana, S., Salvaterra, R., Ferrara, A., and Pallottini, A. (2015). Missing cosmic metals revealed by x-ray absorption towards distant sources. *Astronomy & Astrophysics*, 575:A43.

[Caputi et al., 2015] Caputi, K., Ilbert, O., Laigle, C., McCracken, H., Le Fevre, O., Fynbo, J., Milvang-Jensen, B., Capak, P., Salvato, M., and Taniguchi, Y. (2015). Spitzer bright, ultravista faint sources in cosmos: the contribution to the overall population of massive galaxies at z= 3–7. *The Astrophysical Journal*, 810(1):73.

[Cardelli et al., 1989] Cardelli, J. A., Clayton, G. C., and Mathis, J. S. (1989). The relationship between infrared, optical, and ultraviolet extinction. *The Astrophysical Journal*, 345:245–256.

[Carilli and Walter, 2013] Carilli, C. and Walter, F. (2013). Cool gas in high-redshift galaxies. *Annual Review of Astronomy and Astrophysics*, 51.

[Casey et al., 2014] Casey, C. M., Narayanan, D., and Cooray, A. (2014). Dusty star-forming galaxies at high redshift. *Physics Reports*, 541(2):45–161.

[Castro et al., 2003] Castro, S., Galama, T., Harrison, F., Holtzman, J., Bloom, J., Djorgovski, S., and Kulkarni, S. (2003). Keck spectroscopy and hubble space telescope imaging of grb 000926: Probing a host galaxy at z= 2.038. *The Astrophysical Journal*, 586(1):128.

[Castro-Tirado et al., 2013] Castro-Tirado, A., Sánchez-Ramírez, R., Ellison, S., Jelínek, M., Martín-Carrillo, A., Bromm, V., Gorosabel, J., Bremer, M., Winters, J., Hanlon, L., et al. (2013). Grb 130606a within a sub-dla at redshift 5.91. *arXiv preprint arXiv:1312.5631*.

[Castro-Tirado et al., 2010] Castro-Tirado, A. J., Møller, P., García-Segura, G., Gorosabel, J., Pérez, E., de Ugarte Postigo, A., Solano, E., Barrado, D., Klose, S., Kann, D. A., et al. (2010). Grb 021004: Tomography of a gamma-ray burst progenitor and its host galaxy. *Astronomy & Astrophysics*, 517:A61.

[Chabrier, 2003] Chabrier, G. (2003). Galactic stellar and substellar initial mass function. *Publications of the Astronomical Society of the Pacific*, 115(809):763.

[Chaganti et al., 2006] Chaganti, K., Salakhutdinov, I., Avrutsky, I., and Auner, G. W. (2006). A simple miniature optical spectrometer with a planar waveguide grating coupler in combination with a plano-convex lens. *Optics Express*, 14(9):4064–4072.

[Chandra and Frail, 2012] Chandra, P. and Frail, D. A. (2012). A radio-selected sample of gamma-ray burst afterglows. *The Astrophysical Journal*, 746(2):156.

[Chen, 2012] Chen, H.-W. (2012). The unchanging circumgalactic medium over the past 11 billion years. *Monthly Notices of the Royal Astronomical Society*, 427(2):1238–1244.

[Chen et al., 2009] Chen, H.-W., Perley, D. A., Pollack, L. K., Prochaska, J. X., Bloom, J. S., Dessauges-Zavadsky, M., Pettini, M., Lopez, S., Dall'aglio, A., and Becker, G. D. (2009). High-redshift starbursting dwarf galaxies revealed by $\gamma$-ray burst afterglows. *The Astrophysical Journal*, 691(1):152.

[Chen et al., 2005] Chen, H.-W., Prochaska, J. X., Bloom, J. S., and Thompson, I. B. (2005). Echelle spectroscopy of a gamma-ray burst afterglow at z= 3.969: a new probe of the interstellar and intergalactic media in the young universe. *The Astrophysical Journal Letters*, 634(1):L25.

[Chen et al., 2007] Chen, H.-W., Prochaska, J. X., Ramirez-Ruiz, E., Bloom, J. S., Dessauges-Zavadsky, M., and Foley, R. J. (2007). On the absence of wind signatures in grb afterglow spectra: constraints on the wolf-rayet winds of grb progenitors. *The Astrophysical Journal*, 663(1):420.

[Chisholm et al., 2017] Chisholm, J., Tremonti, C. A., Leitherer, C., and Chen, Y. (2017). The mass and momentum outflow rates of photoionized galactic outflows. *Monthly Notices of the Royal Astronomical Society*, 469(4):4831–4849.

[Chisholm et al., 2015] Chisholm, J., Tremonti, C. A., Leitherer, C., Chen, Y., Wofford, A., and Lundgren, B. (2015). Scaling relations between warm galactic outflows and their host galaxies. *The Astrophysical Journal*, 811(2):149.

[Chornock et al., 2013] Chornock, R., Berger, E., Fox, D. B., Lunnan, R., Drout, M. R., Fong, W.-f., Laskar, T., and Roth, K. C. (2013). Grb 130606a as a probe of the intergalactic medium and the interstellar medium in a star-forming galaxy in the first gyr after the big bang. *The Astrophysical Journal*, 774(1):26.

[Christensen et al., 2016] Christensen, C. R., Davé, R., Governato, F., Pontzen, A., Brooks, A., Munshi, F., Quinn, T., and Wadsley, J. (2016). In-n-out: the gas cycle from dwarfs to spiral galaxies. *The Astrophysical Journal*, 824(1):57.

[Condon, 1992] Condon, J. (1992). Radio emission from normal galaxies. *Annual review of astronomy and astrophysics*, 30(1):575–611.

[Covino et al., 2013] Covino, S., Melandri, A., Salvaterra, R., Campana, S., Vergani, S., Bernardini, M., D'avanzo, P., D'elia, V., Fugazza, D., Ghirlanda, G., et al. (2013). Dust extinctions for an unbiased sample of gamma-ray burst afterglows. *Monthly Notices of the Royal Astronomical Society*, 432(2):1231–1244.

[Crighton et al., 2014] Crighton, N. H., Hennawi, J. F., Simcoe, R. A., Cooksey, K. L., Murphy, M. T., Fumagalli, M., Prochaska, J. X., and Shanks, T. (2014). Metal-enriched, subkiloparsec gas clumps in the circumgalactic medium of a faint z= 2.5 galaxy. *Monthly Notices of the Royal Astronomical Society*, 446(1):18–37.

[Cucchiara et al., 2015] Cucchiara, A., Fumagalli, M., Rafelski, M., Kocevski, D., Prochaska, J., Cooke, R., and Becker, G. (2015). Unveiling the secrets of metallicity and massive star formation using dlas along gamma-ray bursts. *The Astrophysical Journal*, 804(1):51.

[Cucchiara et al., 2011] Cucchiara, A., Levan, A., Fox, D. B., Tanvir, N. R., Ukwatta, T., Berger, E., Krühler, T., Yoldaş, A. K., Wu, X., Toma, K., et al. (2011). A photometric redshift of z $\sim$ 9.4 for grb 090429b. *The Astrophysical Journal*, 736(1):7.

[Cucchiara et al., 2013] Cucchiara, A., Prochaska, J., Zhu, G., Ménard, B., Fynbo, J. P. U., Fox, D. B., Chen, H.-W., Cooksey, K., Cenko, S. B., Perley, D., et al. (2013). An independent measurement of the incidence of mg ii absorbers along gamma-ray burst sight lines: The end of the mystery? *The Astrophysical Journal*, 773(2):82.

[Cvetojevic et al., 2012a] Cvetojevic, N., Jovanovic, N., Betters, C., Lawrence, J., Ellis, S., Robertson, G., and Bland-Hawthorn, J. (2012a). First starlight spectrum captured using an integrated photonic micro-spectrograph. *Astronomy & Astrophysics*, 544:L1.

[Cvetojevic et al., 2010] Cvetojevic, N., Jovanovic, N., Bland-Hawthorn, J., Haynes, R., and Lawrence, J. (2010). Miniature spectrographs: characterization of arrayed waveguide gratings for astronomy. In *SPIE Astronomical Telescopes+ Instrumentation*, pages 77394H–77394H. International Society for Optics and Photonics.

[Cvetojevic et al., 2012b] Cvetojevic, N., Jovanovic, N., Lawrence, J., Withford, M., and Bland-Hawthorn, J. (2012b). Developing arrayed waveguide grating spectrographs for multi-object astronomical spectroscopy. *Optics express*, 20(3):2062–2072.

[Daddi et al., 2010] Daddi, E., Bournaud, F., Walter, F., Dannerbauer, H., Carilli, C., Dickinson, M., Elbaz, D., Morrison, G., Riechers, D., Onodera, M., et al. (2010). Very high gas fractions and extended gas reservoirs in z= 1.5 disk galaxies. *The Astrophysical Journal*, 713(1):686.

[Dai et al., 2012] Dai, D., Bauters, J., and Bowers, J. E. (2012). Passive technologies for future large-scale photonic integrated circuits on silicon: polarization handling, light non-reciprocity and loss reduction. *Light: Science & Applications*, 1(3):e1.

[Dai et al., 2011] Dai, D., Wang, Z., Bauters, J. F., Tien, M.-C., Heck, M. J., Blumenthal, D. J., and Bowers, J. E. (2011). Low-loss silicon nitride arrayed-waveguide grating (de) multiplexer using nano-core optical waveguides. *Optics express*, 19(15):14130–14136.

[Davé et al., 2017] Davé, R., Rafieferantsoa, M. H., Thompson, R. J., and Hopkins, P. F. (2017). Mufasa: galaxy star formation, gas and metal properties across cosmic time. *Monthly Notices of the Royal Astronomical Society*, 467(1):115–132.

[Davidson-Pilon et al., 2020] Davidson-Pilon, C., Kalderstam, J., Jacobson, N., sean reed, Kuhn, B., Zivich, P., Williamson, M., AbdealiJK, Datta, D., Fiore-Gartland, A., Parij, A., WIlson, D., Gabriel, Moneda, L., Stark, K., Moncada-Torres, A., Gadgil, H., Jona, Singaravelan, K., Besson, L., Peña, M. S., Anton, S., Klintberg, A., Noorbakhsh, J., Begun, M., Kumar, R., Hussey, S., Golland, D., jlim13, and Flaxman, A. (2020). Camdavidsonpilon/lifelines: v0.25.0.

[Davies et al., 2018] Davies, R. L., Schreiber, N. M. F., Übler, H., Genzel, R., Lutz, D., Renzini, A., Tacchella, S., Tacconi, L. J., Belli, S., Burkert, A., et al. (2018). Kiloparsec scale properties of star-formation driven outflows at z $\sim$ 2.3 in the sins/zc-sinf ao survey. *arXiv preprint arXiv:1808.10700*.

[de Ugarte Postigo et al., 2018] de Ugarte Postigo, A., Thöne, C. C., Bolmer, J., Schulze, S., Martín, S., Kann, D., D'Elia, V., Selsing, J., Martin-Carrillo, A., Perley, D., et al. (2018). X-shooter and alma spectroscopy of grb 161023a-a study of metals and molecules in the line of sight towards a luminous grb. *Astronomy & Astrophysics*, 620:A119.

[D'Elia et al., 2007] D'Elia, V., Fiore, F., Meurs, E., Chincarini, G., Melandri, A., Norci, L., Pellizza, L., Perna, R., Piranomonte, S., Sbordone, L., et al. (2007). Uves/vlt high resolution spectroscopy of grb 050730 afterglow: probing the features of the grb environment. *Astronomy & Astrophysics*, 467(2):629–639.

[D′Elia et al., 2014] D′Elia, V., Fynbo, J. P. U., Goldoni, P., Covino, S., de Ugarte Postigo, A., Ledoux, C., Calura, F., Gorosabel, J., Malesani, D., Matteucci, F., et al. (2014). Vlt/x-shooter spectroscopy of the grb 120327a afterglow. *Astronomy & Astrophysics*, 564:A38.

[Dessauges-Zavadsky et al., 2006] Dessauges-Zavadsky, M., Chen, H.-W., Prochaska, J. X., Bloom, J. S., and Barth, A. J. (2006). Temporal variation in the abundance of excited fe+ near a gamma-ray burst afterglow. *The Astrophysical Journal Letters*, 648(2):L89.

[Du et al., 2016] Du, X., Shapley, A. E., Martin, C. L., and Coil, A. L. (2016). The kinematics of c iv in star-forming galaxies at z $\sim$ 1.2. *The Astrophysical Journal*, 829(2):64.

[Du et al., 2018] Du, X., Shapley, A. E., Reddy, N. A., Jones, T., Stark, D. P., Steidel, C. C., Strom, A. L., Rudie, G. C., Erb, D. K., Ellis, R. S., et al. (2018). The redshift evolution of rest-uv spectroscopic properties in lyman-break galaxies at z $\sim$ 2–4. *The Astrophysical Journal*, 860(1):75.

[Duncan et al., 2014] Duncan, K., Conselice, C. J., Mortlock, A., Hartley, W. G., Guo, Y., Ferguson, H. C., Davé, R., Lu, Y., Ownsworth, J., Ashby, M. L., et al. (2014). The mass evolution of the first galaxies: stellar mass functions and star formation rates at $4 < z < 7$ in the candels goods-south field. *Monthly Notices of the Royal Astronomical Society*, 444(3):2960–2984.

[D'Elia et al., 2010] D'Elia, V., Fynbo, J. P. U., Covino, S., Goldoni, P., Jakobsson, P., Matteucci, F., Piranomonte, S., Sollerman, J., Thöne, C., Vergani, S., et al. (2010). Vlt/x-shooter spectroscopy of the grb 090926a afterglow. *Astronomy & Astrophysics*, 523:A36.

[Ellis and Bland-Hawthorn, 2008] Ellis, S. and Bland-Hawthorn, J. (2008). The case for oh suppression at near-infrared wavelengths. *Monthly Notices of the Royal Astronomical Society*, 386(1):47–64.

[Emonts et al., 2019] Emonts, B., Raba, R., Moellenbrock, G., Castro, S., Garcia-Dabo, C., Meyer, J. D., Ford, P., Garwood, R., Golap, K., Gonzalez, J., et al. (2019). The casa software for radio astronomy: status update from adass 2019. *arXiv preprint arXiv:1912.09437*.

[Erb et al., 2012] Erb, D. K., Quider, A. M., Henry, A. L., and Martin, C. L. (2012). Galactic outflows in absorption and emission: Near-ultraviolet spectroscopy of galaxies at $1 < z < 2$. *The Astrophysical Journal*, 759(1):26.

[Erb et al., 2006] Erb, D. K., Steidel, C. C., Shapley, A. E., Pettini, M., Reddy, N. A., and Adelberger, K. L. (2006). The stellar, gas, and dynamical masses of star-forming galaxies at z $\sim$ 2. *The Astrophysical Journal*, 646(1):107.

[Evans et al., 2018] Evans, D., Riello, M., De Angeli, F., Carrasco, J., Montegriffo, P., Fabricius, C., Jordi, C., Palaversa, L., Diener, C., Busso, G., et al. (2018). Gaia data release 2-photometric content and validation. *Astronomy & Astrophysics*, 616:A4.

[Fabian, 2012] Fabian, A. (2012). Observational evidence of active galactic nuclei feedback. *Annual Review of Astronomy and Astrophysics*, 50:455–489.

[Feigelson and Nelson, 1985] Feigelson, E. and Nelson, P. (1985). Statistical methods for astronomical data with upper limits. i-univariate distributions. *The Astrophysical Journal*, 293:192–206.

[Ferland et al., 2017] Ferland, G., Chatzikos, M., Guzmán, F., Lykins, M., Van Hoof, P., Williams, R., Abel, N., Badnell, N., Keenan, F., Porter, R., et al. (2017). The 2017 release of cloudy. *Revista mexicana de astronomía y astrofísica*, 53(2).

[Fiore et al., 2005] Fiore, F., d'Elia, V., Lazzati, D., Perna, R., Sbordone, L., Stratta, G., Meurs, E., Ward, P., Antonelli, L., Chincarini, G., et al. (2005). A flash in the dark: Uves very large telescope high-resolution spectroscopy of gamma-ray burst afterglows. *The Astrophysical Journal*, 624(2):853.

[Flewelling et al., 2016] Flewelling, H., Magnier, E., Chambers, K., Heasley, J., Holmberg, C., Huber, M., Sweeney, W., Waters, C., Calamida, A., Casertano, S., et al. (2016). The pan-starrs1 database and data products. *arXiv preprint arXiv:1612.05243*.

[Ford et al., 2014] Ford, A. B., Davé, R., Oppenheimer, B. D., Katz, N., Kollmeier, J. A., Thompson, R., and Weinberg, D. H. (2014). Tracing inflows and outflows with absorption lines in circumgalactic gas. *Monthly Notices of the Royal Astronomical Society*, 444(2):1260–1281.

[Foreman-Mackey et al., 2013] Foreman-Mackey, D., Hogg, D. W., Lang, D., and Goodman, J. (2013). emcee: the mcmc hammer. *Publications of the Astronomical Society of the Pacific*, 125(925):306.

[Fox et al., 2015] Fox, A. J., Bordoloi, R., Savage, B. D., Lockman, F. J., Jenkins, E. B., Wakker, B. P., Bland-Hawthorn, J., Hernandez, S., Kim, T.-S., Benjamin, R. A., et al. (2015). Probing the fermi bubbles in ultraviolet absorption: A spectroscopic signature of the milky way's biconical nuclear outflow. *The Astrophysical Journal Letters*, 799(1):L7.

[Fox et al., 2008] Fox, A. J., Ledoux, C., Vreeswijk, P. M., Smette, A., and Jaunsen, A. O. (2008). High-ion absorption in seven grb host galaxies at z= 2–4-evidence

for both circumburst plasma and outflowing interstellar gas. *Astronomy & Astrophysics*, 491(1):189–207.

[Fox et al., 2007] Fox, A. J., Petitjean, P., Ledoux, C., and Srianand, R. (2007). Hot halos around high redshift protogalaxies-observations of ovi and nv absorption in damped lyman-alpha systems. *Astronomy & Astrophysics*, 465(1):171–184.

[Fox et al., 2014] Fox, A. J., Wakker, B. P., Barger, K. A., Hernandez, A. K., Richter, P., Lehner, N., Bland-Hawthorn, J., Charlton, J. C., Westmeier, T., Thom, C., et al. (2014). The cos/uves absorption survey of the magellanic stream. iii. ionization, total mass, and inflow rate onto the milky way. *The Astrophysical Journal*, 787(2):147.

[Freudling et al., 2013] Freudling, W., Romaniello, M., Bramich, D., Ballester, P., Forchi, V., García-Dabló, C., Moehler, S., and Neeser, M. (2013). Automated data reduction workflows for astronomy-the eso reflex environment. *Astronomy & Astrophysics*, 559:A96.

[Friis et al., 2015] Friis, M., De Cia, A., Krühler, T., Fynbo, J., Ledoux, C., Vreeswijk, P., Watson, D., Malesani, D., Gorosabel, J., Starling, R., et al. (2015). The warm, the excited, and the molecular gas: Grb 121024a shining through its star-forming galaxy. *Monthly Notices of the Royal Astronomical Society*, 451(1):167–183.

[Fruchter et al., 2006] Fruchter, A., Levan, A., Strolger, L., Vreeswijk, P., Thorsett, S., Bersier, D., Burud, I., Cerón, J. C., Castro-Tirado, A., Conselice, C., et al. (2006). Long $\gamma$-ray bursts and core-collapse supernovae have different environments. *Nature*, 441(7092):463–468.

[Frye et al., 2002] Frye, B., Broadhurst, T., and Benítez, N. (2002). Spectral evidence for widespread galaxy outflows at z $>$ 4. *The Astrophysical Journal*, 568(2):558.

[Fumagalli et al., 2011] Fumagalli, M., Prochaska, J. X., Kasen, D., Dekel, A., Ceverino, D., and Primack, J. R. (2011). Absorption-line systems in simulated galaxies fed by cold streams. *Monthly Notices of the Royal Astronomical Society*, 418(3):1796–1821.

[Fynbo et al., 2001] Fynbo, J., Gorosabel, J., Dall, T., Hjorth, J., Pedersen, H., Andersen, M., Møller, P., Holland, S., Smail, I., Kobayashi, N., et al. (2001). The optical afterglow and host galaxy of grb 000926. *Astronomy & Astrophysics*, 373(3):796–804.

[Fynbo et al., 2000] Fynbo, J., Holland, S., Andersen, M., Thomsen, B., Hjorth, J., Björnsson, G., Jaunsen, A., Natarajan, P., and Tanvir, N. (2000). Hubble space telescope space telescope imaging spectrograph imaging of the host galaxy of grb 980425/sn 1998bw. *The Astrophysical Journal Letters*, 542(2):L89.

[Fynbo et al., 2003] Fynbo, J., Jakobsson, P., Möller, P., Hjorth, J., Thomsen, B., Andersen, M., Fruchter, A., Gorosabel, J., Holland, S., Ledoux, C., et al. (2003). On the ly$\alpha$ emission from gamma-ray burst host galaxies: Evidence for low metallicities. *Astronomy & Astrophysics*, 406(3):L63–L66.

[Fynbo et al., 2005] Fynbo, J. P. U., Gorosabel, J., Smette, A., Fruchter, A., Hjorth, J., Pedersen, K., Levan, A., Burud, I., Sahu, K., Vreeswijk, P., et al. (2005). On the afterglow and host galaxy of grb 021004: a comprehensive study with the hubble space telescope. *The Astrophysical Journal*, 633(1):317.

[Fynbo et al., 2009] Fynbo, J. P. U., Jakobsson, P., Prochaska, J., Malesani, D., Ledoux, C., de Ugarte Postigo, A., Nardini, M., Vreeswijk, P., Wiersema, K., Hjorth, J., et al. (2009). Low-resolution spectroscopy of gamma-ray burst optical afterglows: biases in the swift sample and characterization of the absorbers. *The Astrophysical Journal Supplement Series*, 185(2):526.

[Gatkine et al., 2019a] Gatkine, P., Veilleux, S., and Cucchiara, A. (2019a). The cgm–grb study. i. uncovering the circumgalactic medium around grb hosts at redshifts 2–6. *The Astrophysical Journal*, 884(1):66.

[Gatkine et al., 2019b] Gatkine, P., Veilleux, S., and Dagenais, M. (2019b). Astrophotonic spectrographs. *Applied Sciences*, 9(2):290.

[Gatkine et al., 2017] Gatkine, P., Veilleux, S., Hu, Y., Bland-Hawthorn, J., and Dagenais, M. (2017). Arrayed waveguide grating spectrometers for astronomical applications: new results. *Optics Express*, 25(15):17918–17935.

[Gatkine et al., 2016] Gatkine, P., Veilleux, S., Hu, Y., Zhu, T., Meng, Y., Bland-Hawthorn, J., and Dagenais, M. (2016). Development of high-resolution arrayed waveguide grating spectrometers for astronomical applications: first results. In *Advances in Optical and Mechanical Technologies for Telescopes and Instrumentation II*, volume 9912, page 991271. International Society for Optics and Photonics.

[Gatkine et al., 2020] Gatkine, P., Vogel, S., and Veilleux, S. (2020). New radio constraints on the obscured star formation rates of massive grb hosts at redshifts 2–3.5. *The Astrophysical Journal*, 897(1):9.

[Gehrels et al., 2004] Gehrels, N., Chincarini, G., Giommi, P., Mason, K., Nousek, J. A., Wells, A., White, N., Barthelmy, S., Burrows, D. N., Cominsky, L., et al. (2004). The swift gamma-ray burst mission. *The Astrophysical Journal*, 611(2):1005.

[Gilmore et al., 2009] Gilmore, R. C., Madau, P., Primack, J. R., Somerville, R. S., and Haardt, F. (2009). Gev gamma-ray attenuation and the high-redshift uv background. *Monthly Notices of the Royal Astronomical Society*, 399(4):1694–1708.

[Girichidis et al., 2016] Girichidis, P., Naab, T., Walch, S., Hanasz, M., Mac Low, M.-M., Ostriker, J. P., Gatto, A., Peters, T., Wünsch, R., Glover, S. C., et al. (2016). Launching cosmic-ray-driven outflows from the magnetized interstellar medium. *The Astrophysical Journal Letters*, 816(2):L19.

[Glidden et al., 2016] Glidden, A., Cooper, T. J., Cooksey, K. L., Simcoe, R. A., and O'Meara, J. M. (2016). Predominantly low metallicities measured in a stratified sample of lyman limit systems at z= 3.7. *The Astrophysical Journal*, 833(2):270.

[Goerdt et al., 2012] Goerdt, T., Dekel, A., Sternberg, A., Gnat, O., and Ceverino, D. (2012). Detectability of cold streams into high-redshift galaxies by absorption lines. *Monthly Notices of the Royal Astronomical Society*, 424(3):2292–2315.

[Goodman and Weare, 2010] Goodman, J. and Weare, J. (2010). Ensemble samplers with affine invariance. *Communications in applied mathematics and computational science*, 5(1):65–80.

[Gordon et al., 2003] Gordon, K. D., Clayton, G. C., Misselt, K., Landolt, A. U., and Wolff, M. J. (2003). A quantitative comparison of the small magellanic cloud, large magellanic cloud, and milky way ultraviolet to near-infrared extinction curves. *The Astrophysical Journal*, 594(1):279.

[Graham and Fruchter, 2013] Graham, J. and Fruchter, A. (2013). The metal aversion of long-duration gamma-ray bursts. *The Astrophysical Journal*, 774(2):119.

[Greiner et al., 2018] Greiner, J., Bolmer, J., Wieringa, M., van der Horst, A., Petry, D., Schulze, S., Knust, F., de Bruyn, G., Krühler, T., Wiseman, P., et al. (2018). Grb 151027b-large-amplitude late-time radio variability. *arXiv preprint arXiv:1802.01882*.

[Greiner et al., 2015] Greiner, J., Fox, D. B., Schady, P., Krühler, T., Trenti, M., Cikota, A., Bolmer, J., Elliott, J., Delvaux, C., Perna, R., et al. (2015). Gamma-ray bursts trace uv metrics of star formation over $3 < z < 5$. *The Astrophysical Journal*, 809(1):76.

[Greiner et al., 2016] Greiner, J., Michałowski, M. J., Klose, S., Hunt, L. K., Gentile, G., Kamphuis, P., Herrero-Illana, R., Wieringa, M., Krühler, T., Schady, P., et al. (2016). Probing dust-obscured star formation in the most massive gamma-ray burst host galaxies. *Astronomy & Astrophysics*, 593:A17.

[Harris and Allington-Smith, 2012] Harris, R. J. and Allington-Smith, J. (2012). Applications of integrated photonic spectrographs in astronomy. *Mon. Not. R. Astron. Soc.*, 428(4):3139–3150.

[Harris and Allington-Smith, 2013] Harris, R. J. and Allington-Smith, J. (2013). Applications of integrated photonic spectrographs in astronomy. *Monthly Notices of the Royal Astronomical Society*, 428(4):3139–3150.

[Harrison et al., 2012] Harrison, C., Alexander, D., Swinbank, A., Smail, I., Alaghband-Zadeh, S., Bauer, F., Chapman, S., Del Moro, A., Hickox, R., Ivison, R., et al. (2012). Energetic galaxy-wide outflows in high-redshift ultraluminous infrared galaxies hosting agn activity. *Monthly Notices of the Royal Astronomical Society*, 426(2):1073–1096.

[Hartoog et al., 2015] Hartoog, O., Malesani, D., Fynbo, J., Goto, T., Krühler, T., Vreeswijk, P., De Cia, A., Xu, D., Møller, P., Covino, S., et al. (2015). Vlt/x-shooter spectroscopy of the afterglow of the swift grb 130606a-chemical abundances and reionisation at z $\sim$ 6. *Astronomy & Astrophysics*, 580:A139.

[Hatsukade et al., 2012] Hatsukade, B., Hashimoto, T., Ohta, K., Nakanishi, K., Tamura, Y., and Kohno, K. (2012). Constraints on obscured star formation in host galaxies of gamma-ray bursts. *The Astrophysical Journal*, 748(2):108.

[Hayward and Hopkins, 2016] Hayward, C. C. and Hopkins, P. F. (2016). How stellar feedback simultaneously regulates star formation and drives outflows. *Monthly Notices of the Royal Astronomical Society*, page stw2888.

[Heckman et al., 2017] Heckman, T., Borthakur, S., Wild, V., Schiminovich, D., and Bordoloi, R. (2017). Cos-burst: Observations of the impact of starburst-driven winds on the properties of the circum-galactic medium. *The Astrophysical Journal*, 846(2):151.

[Heckman et al., 2015] Heckman, T. M., Alexandroff, R. M., Borthakur, S., Overzier, R., and Leitherer, C. (2015). The systematic properties of the warm phase of starburst-driven galactic winds. *The Astrophysical Journal*, 809(2):147.

[Heckman and Best, 2014] Heckman, T. M. and Best, P. N. (2014). The coevolution of galaxies and supermassive black holes: insights from surveys of the contemporary universe. *Annual Review of Astronomy and Astrophysics*, 52:589–660.

[Heckman and Borthakur, 2016] Heckman, T. M. and Borthakur, S. (2016). The implications of extreme outflows from extreme starbursts. *The Astrophysical Journal*, 822(1):9.

[Heintz et al., 2019] Heintz, K., Bolmer, J., Ledoux, C., Noterdaeme, P., Krogager, J.-K., Fynbo, J., Jakobsson, P., Covino, S., D'Elia, V., De Pasquale, M., et al. (2019). New constraints on the physical conditions in h2-bearing grb-host damped lyman-$\alpha$ absorbers. *Astronomy & Astrophysics*, 629:A131.

[Heintz et al., 2018] Heintz, K., Watson, D., Jakobsson, P., Fynbo, J., Bolmer, J., Arabsalmani, M., Cano, Z., Covino, S., D'Elia, V., Gomboc, A., et al. (2018). Highly-ionized metals as probes of the circumburst gas in the natal regions of gamma-ray bursts. *Monthly Notices of the Royal Astronomical Society*.

[Henden and Levine, 2002] Henden, A. and Levine, S. (2002). Grb021004, astrometric position. *GCN*, 1592:1.

[Hennawi et al., 2006] Hennawi, J. F., Prochaska, J. X., Burles, S., Strauss, M. A., Richards, G. T., Schlegel, D. J., Fan, X., Schneider, D. P., Zakamska, N. L., Oguri, M., et al. (2006). Quasars probing quasars. i. optically thick absorbers near luminous quasars. *The Astrophysical Journal*, 651(1):61.

[Henry et al., 1987] Henry, C. H., Kazarinov, R., Lee, H., Orlowsky, K., and Katz, L. (1987). Low loss silicon nitride – silica optical waveguides on silicon. *Applied optics*, 26(13):2621–2624.

[Hirschmann et al., 2013] Hirschmann, M., Naab, T., Davé, R., Oppenheimer, B. D., Ostriker, J. P., Somerville, R. S., Oser, L., Genzel, R., Tacconi, L. J., Förster-Schreiber, N. M., et al. (2013). The effect of metal enrichment and galactic winds on galaxy formation in cosmological zoom simulations. *Monthly Notices of the Royal Astronomical Society*, 436(4):2929–2949.

[Hjorth et al., 2003] Hjorth, J., Sollerman, J., Møller, P., Fynbo, J. P., Woosley, S. E., Kouveliotou, C., Tanvir, N. R., Greiner, J., Andersen, M. I., Castro-Tirado, A. J., et al. (2003). A very energetic supernova associated with the $\gamma$-ray burst of 29 march 2003. *Nature*, 423(6942):847.

[Hopkins et al., 2014] Hopkins, P. F., Kereš, D., Oñorbe, J., Faucher-Giguère, C.-A., Quataert, E., Murray, N., and Bullock, J. S. (2014). Galaxies on fire (feedback in realistic environments): stellar feedback explains cosmologically inefficient star formation. *Monthly Notices of the Royal Astronomical Society*, 445(1):581–603.

[Horton and Bland-Hawthorn, 2007] Horton, A. J. and Bland-Hawthorn, J. (2007). Coupling light into few-mode optical fibres i: The diffraction limit. *Optics Express*, 15(4):1443–1453.

[Howell et al., 2010] Howell, J. H., Armus, L., Mazzarella, J. M., Evans, A. S., Surace, J. A., Sanders, D. B., Petric, A., Appleton, P., Bothun, G., Bridge, C., et al. (2010). The great observatories all-sky lirg survey: Comparison of ultraviolet and far-infrared properties. *The Astrophysical Journal*, 715(1):572.

[Hu et al., 2020] Hu, Y., Xie, S., Zhan, J., Zhang, Y., Veilleux, S., and Dagenais, M. (2020). Integrated arbitrary filter with spiral gratings: Design and characterization. *Journal of Lightwave Technology*.

[Hu et al., 2018] Hu, Y.-W., Zhang, Y., Gatkine, P., Bland-Hawthorn, J., Veilleux, S., and Dagenais, M. (2018). Characterization of low loss waveguides using bragg gratings. *IEEE Journal of Selected Topics in Quantum Electronics*, 24(4):1–8.

[Irene, 1976] Irene, E. (1976). Residual stress in silicon nitride films. *Journal of Electronic Materials*, 5(3):287–298.

[Isobe and Feigelson, 1990] Isobe, T. and Feigelson, E. (1990). Asurv. the pennsylvania state university. report for the period sep 1987-jan 1990. In *Bulletin of the American Astronomical Society*, volume 22, pages 917–918.

[Isobe et al., 1986] Isobe, T., Feigelson, E., and Nelson, P. I. (1986). Statistical methods for astronomical data with upper limits. ii-correlation and regression. *The Astrophysical Journal*, 306:490–507.

[Jakobsson et al., 2005] Jakobsson, P., Björnsson, G., Fynbo, J., Jóhannesson, G., Hjorth, J., Thomsen, B., Møller, P., Watson, D., Jensen, B., Östlin, G., et al. (2005). Ly+ and ultraviolet emission from high-redshift gamma-ray burst hosts: to what extent do gamma-ray bursts trace star formation? *Monthly Notices of the Royal Astronomical Society*, 362(1):245–251.

[Janz et al., 2006] Janz, S., Čtyrokỳ, J., and Tanev, S. (2006). *Frontiers in Planar Lightwave Circuit Technology*. Springer.

[Japelj et al., 2016] Japelj, J., Vergani, S., Salvaterra, R., D'Avanzo, P., Mannucci, F., Fernandez-Soto, A., Boissier, S., Hunt, L., Atek, H., Rodríguez-Muñoz, L., et al. (2016). Are long gamma-ray bursts biased tracers of star formation? clues from the host galaxies of the swift/bat6 complete sample of bright lgrbs-ii. star formation rates and metallicities at z $<$ 1. *Astronomy & Astrophysics*, 590:A129.

[Jovanovic et al., 2016] Jovanovic, N., Cvetojevic, N., Schwab, C., Norris, B., Lozi, J., Gross, S., Betters, C., Singh, G., Guyon, O., Martinache, F., et al. (2016). Efficiently feeding single-mode fiber photonic spectrographs with an extreme adaptive optics system: on-sky characterization and preliminary spectroscopy. In *Ground-based and Airborne Instrumentation for Astronomy VI*, volume 9908, page 99080R. International Society for Optics and Photonics.

[Kajisawa et al., 2009] Kajisawa, M., Ichikawa, T., Tanaka, I., Konishi, M., Yamada, T., Akiyama, M., Suzuki, R., Tokoku, C., Uchimoto, Y., Yoshikawa, T., et al. (2009). Moircs deep survey. iv. evolution of galaxy stellar mass function back to z $\sim$ 3. *The Astrophysical Journal*, 702(2):1393.

[Karim et al., 2018] Karim, M. T., Fox, A. J., Jenkins, E. B., Bordoloi, R., Wakker, B. P., Savage, B. D., Lockman, F. J., Crawford, S. M., Jorgenson, R. A., and Bland-Hawthorn, J. (2018). Probing the southern fermi bubble in ultraviolet absorption using distant agns. *The Astrophysical Journal*, 860(2):98.

[Kelly et al., 2014] Kelly, P. L., Filippenko, A. V., Modjaz, M., and Kocevski, D. (2014). The host galaxies of fast-ejecta core-collapse supernovae. *The Astrophysical Journal*, 789(1):23.

[Kennicutt, 1998] Kennicutt, R. C. (1998). Star formation in galaxies along the hubble sequence. *Annual Review of Astronomy and Astrophysics*, 36(1):189–231.

[King and Pounds, 2015] King, A. and Pounds, K. (2015). Powerful outflows and feedback from active galactic nuclei. *Annual Review of Astronomy and Astrophysics*, 53:115–154.

[Kornei et al., 2012] Kornei, K. A., Shapley, A. E., Martin, C. L., Coil, A. L., Lotz, J. M., Schiminovich, D., Bundy, K., and Noeske, K. G. (2012). The properties and prevalence of galactic outflows at z $\sim$ 1 in the extended groth strip. *The Astrophysical Journal*, 758(2):135.

[Krühler et al., 2009] Krühler, T., Greiner, J., McBreen, S., Klose, S., Rossi, A., Afonso, P., Clemens, C., Filgas, R., Yoldaş, A. K., Szokoly, G., et al. (2009). Correlated optical and x-ray flares in the afterglow of xrf 071031. *The Astrophysical Journal*, 697(1):758.

[Krühler et al., 2011] Krühler, T., Greiner, J., Schady, P., Savaglio, S., Afonso, P., Clemens, C., Elliott, J., Filgas, R., Gruber, D., Kann, D., et al. (2011). The seds and host galaxies of the dustiest grb afterglows. *Astronomy & Astrophysics*, 534:A108.

[Krühler et al., 2013] Krühler, T., Ledoux, C., Fynbo, J., Vreeswijk, P., Schmidl, S., Malesani, D., Christensen, L., De Cia, A., Hjorth, J., Jakobsson, P., et al. (2013). Molecular hydrogen in the damped lyman $\alpha$ system towards grb 120815a at z= 2.36. *Astronomy & Astrophysics*, 557:A18.

[Krühler et al., 2015] Krühler, T., Malesani, D., Fynbo, J., Hartoog, O., Hjorth, J., Jakobsson, P., Perley, D., Rossi, A., Schady, P., Schulze, S., et al. (2015). Grb hosts through cosmic time-vlt/x-shooter emission-line spectroscopy of 96 $\gamma$-ray-burst-selected galaxies at $0.1 < z < 3.6$. *Astronomy & Astrophysics*, 581:A125.

[Kuijken et al., 2019] Kuijken, K., Heymans, C., Dvornik, A., Hildebrandt, H., de Jong, J., Wright, A., Erben, T., Bilicki, M., Giblin, B., Shan, H.-Y., et al. (2019). The fourth data release of the kilo-degree survey: ugri imaging and nine-band optical-ir photometry over 1000 square degrees. *Astronomy & Astrophysics*, 625:A2.

[Lagos et al., 2014] Lagos, C. d. P., Baugh, C. M., Zwaan, M., Lacey, C. G., Gonzalez-Perez, V., Power, C., Swinbank, A., and van Kampen, E. (2014). Which galaxies dominate the neutral gas content of the universe? *Monthly Notices of the Royal Astronomical Society*, 440(1):920–941.

[Lan and Mo, 2018] Lan, T.-W. and Mo, H. (2018). The circumgalactic medium of eboss emission line galaxies: signatures of galactic outflows in gas distribution and kinematics. *arXiv preprint arXiv:1806.05786*.

[Lawrence et al., 2012] Lawrence, J., Bland-Hawthorn, J., Bryant, J., Brzeski, J., Colless, M., Croom, S., Gers, L., Gilbert, J., Gillingham, P., Goodwin, M., et al. (2012). Hector: a high-multiplex survey instrument for spatially resolved galaxy spectroscopy. In *SPIE Astronomical Telescopes+ Instrumentation*, pages 844653–844653. International Society for Optics and Photonics.

[Lehner et al., 2015] Lehner, N., Howk, J. C., and Wakker, B. P. (2015). Evidence for a massive, extended circumgalactic medium around the andromeda galaxy. *The Astrophysical Journal*, 804(2):79.

[Lehner et al., 2014] Lehner, N., O'Meara, J. M., Fox, A. J., Howk, J. C., Prochaska, J. X., Burns, V., and Armstrong, A. A. (2014). Galactic and circumgalactic o vi and its impact on the cosmological metal and baryon budgets at $2 <$ z 3.5. *The Astrophysical Journal*, 788(2):119.

[Leon-Saval et al., 2010] Leon-Saval, S. G., Argyros, A., and Bland-Hawthorn, J. (2010). Photonic lanterns: a study of light propagation in multimode to single-mode converters. *Optics Express*, 18(8):8430–8439.

[Levesque et al., 2010] Levesque, E. M., Berger, E., Kewley, L. J., and Bagley, M. M. (2010). The host galaxies of gamma-ray bursts. i. interstellar medium properties of ten nearby long-duration gamma-ray burst hosts. *The Astronomical Journal*, 139(2):694.

[Li, 2020] Li, J.-T. (2020). An x-ray view of the hot circum-galactic medium. *Astronomische Nachrichten*, 341(2):177–183.

[Li et al., 2018] Li, L., Wang, Y., Shao, L., Wu, X.-F., Huang, Y.-F., Zhang, B., Ryde, F., and Yu, H.-F. (2018). A large catalog of multiwavelength grb afterglows. i. color evolution and its physical implication. *The Astrophysical Journal Supplement Series*, 234(2):26.

[Lindley et al., 2014] Lindley, E., Min, S.-S., Leon-Saval, S., Cvetojevic, N., Lawrence, J., Ellis, S., and Bland-Hawthorn, J. (2014). Demonstration of uniform multicore fiber bragg gratings. *Optics express*, 22(25):31575–31581.

[Littlejohns et al., 2015] Littlejohns, O., Butler, N., Cucchiara, A., Watson, A., Fox, O., Lee, W., Kutyrev, A., Richer, M., Klein, C., Prochaska, J., et al. (2015). A detailed study of the optical attenuation of gamma-ray bursts in the swift era. *Monthly Notices of the Royal Astronomical Society*, 449(3):2919–2936.

[Littlejohns et al., 2012] Littlejohns, O., Willingale, R., O'brien, P., Beardmore, A. P., Covino, S., Perley, D., Tanvir, N. R., Rol, E., Yuan, F., Akerlof, C., et al. (2012). The origin of the early-time optical emission of swift grb 080310. *Monthly Notices of the Royal Astronomical Society*, 421(3):2692–2712.

[Lopez et al., 2018] Lopez, S., Tejos, N., Ledoux, C., Barrientos, L. F., Sharon, K., Rigby, J. R., Gladders, M. D., Bayliss, M. B., and Pessa, I. (2018). A clumpy and anisotropic galaxy halo at redshift 1 from gravitational-arc tomography. *Nature*, 554(7693):493.

[Lu et al., 2003] Lu, S., Wong, W., Pun, E., Yan, Y., Wang, D., Yi, D., and Jin, G. (2003). Design of flat-field arrayed waveguide grating with three stigmatic points. *Optical and quantum electronics*, 35(8):783–790.

[Lu et al., 2005] Lu, S., Yang, C., Yan, Y., Jin, G., Zhou, Z., Wong, W., and Pun, E. (2005). Design and fabrication of a polymeric flat focal field arrayed waveguide grating. *Optics Express*, 13(25):9982–9994.

[Lyman et al., 2017] Lyman, J., Levan, A., Tanvir, N., Fynbo, J., McGuire, J., Perley, D., Angus, C., Bloom, J., Conselice, C. J., Fruchter, A., et al. (2017). The host galaxies and explosion sites of long-duration gamma-ray bursts: Hubble space telescope near-infrared imaging. *Monthly Notices of the Royal Astronomical Society*, 467(2):1795–1817.

[Markwardt, 2009] Markwardt, C. B. (2009). Non-linear least squares fitting in idl with mpfit. *arXiv preprint arXiv:0902.2850*.

[Martin, 2005] Martin, C. L. (2005). Mapping large-scale gaseous outflows in ultraluminous galaxies with keck ii esi spectra: variations in outflow velocity with galactic mass. *The Astrophysical Journal*, 621(1):227.

[Martin and Bouché, 2009] Martin, C. L. and Bouché, N. (2009). Physical conditions in the low-ionization component of starburst outflows: The shape of near-ultraviolet and optical absorption-line troughs in keck spectra of ulirgs. *The Astrophysical Journal*, 703(2):1394.

[Martin et al., 2012] Martin, C. L., Shapley, A. E., Coil, A. L., Kornei, K. A., Bundy, K., Weiner, B. J., Noeske, K. G., and Schiminovich, D. (2012). Demographics and physical properties of gas outflows/inflows at $0.4 < z < 1.4$. *The Astrophysical Journal*, 760(2):127.

[Massey et al., 2013] Massey, P., Dunham, E., Bida, T., Collins, P., Hall, J., Hunter, D., Lauman, S., Levine, S., Neugent, K., Nye, R., et al. (2013). As big and as good as it gets: The large monolithic imager for lowell observatory's 4.3-m discovery channel telescope. *AAS*, 221:345–02.

[McCauley and Melandri, 2015] McCauley, L. and Melandri, A. (2015). Grb 151021a: Swift/uvot detection. *GCN*, 18432:1.

[McLean et al., 1994] McLean, A., Mitchell, C., and Swanston, D. (1994). Implementation of an efficient analytical approximation to the voigt function for photoemission lineshape analysis. *Journal of Electron Spectroscopy and Related Phenomena*, 69(2):125–132.

[Meltz et al., 1989] Meltz, G., Morey, W., and Glenn, W. (1989). Formation of bragg gratings in optical fibers by a transverse holographic method. *Optics letters*, 14(15):823–825.

[Meurer et al., 1999] Meurer, G. R., Heckman, T. M., and Calzetti, D. (1999). Dust absorption and the ultraviolet luminosity density at z 3 as calibrated by local starburst galaxies. *The Astrophysical Journal*, 521(1):64.

[Milvang-Jensen et al., 2012] Milvang-Jensen, B., Fynbo, J. P., Malesani, D., Hjorth, J., Jakobsson, P., and Møller, P. (2012). The optically unbiased grb host (tough) survey. iv. ly$\alpha$ emitters. *The Astrophysical Journal*, 756(1):25.

[Mitchell et al., 2020] Mitchell, P. D., Schaye, J., Bower, R. G., and Crain, R. A. (2020). Galactic outflow rates in the eagle simulations. *Monthly Notices of the Royal Astronomical Society*, 494(3):3971–3997.

[Mo and White, 2002] Mo, H. and White, S. (2002). The abundance and clustering of dark haloes in the standard $\lambda$cdm cosmogony. *Monthly Notices of the Royal Astronomical Society*, 336(1):112–118.

[Morton, 2003] Morton, D. C. (2003). Atomic data for resonance absorption lines. iii. wavelengths longward of the lyman limit for the elements hydrogen to gallium. *The Astrophysical Journal Supplement Series*, 149(1):205.

[Moster et al., 2012] Moster, B. P., Naab, T., and White, S. D. (2012). Galactic star formation and accretion histories from matching galaxies to dark matter haloes. *Monthly Notices of the Royal Astronomical Society*, 428(4):3121–3138.

[Muñoz et al., 2017] Muñoz, P., Micó, G., Bru, L., Pastor, D., Pérez, D., Doménech, J., Fernández, J., Baños, R., Gargallo, B., Alemany, R., et al. (2017). Silicon nitride photonic integration platforms for visible, near-infrared and mid-infrared applications. *Sensors*, 17(9):2088.

[Muratov et al., 2017] Muratov, A. L., Kereš, D., Faucher-Giguère, C.-A., Hopkins, P. F., Ma, X., Anglés-Alcázar, D., Chan, T., Torrey, P., Hafen, Z. H., Quataert, E., et al. (2017). Metal flows of the circumgalactic medium, and the metal budget in galactic haloes. *Monthly Notices of the Royal Astronomical Society*, 468(4):4170–4188.

[Muratov et al., 2015] Muratov, A. L., Kereš, D., Faucher-Giguère, C.-A., Hopkins, P. F., Quataert, E., and Murray, N. (2015). Gusty, gaseous flows of fire: galactic winds in cosmological simulations with explicit stellar feedback. *Monthly Notices of the Royal Astronomical Society*, 454(3):2691–2713.

[Murphy et al., 2011] Murphy, E., Condon, J., Schinnerer, E., Kennicutt, R., Calzetti, D., Armus, L., Helou, G., Turner, J., Aniano, G., Beirão, P., et al. (2011). Calibrating extinction-free star formation rate diagnostics with 33 ghz free-free emission in ngc 6946. *The Astrophysical Journal*, 737(2):67.

[Murray et al., 2011] Murray, N., Ménard, B., and Thompson, T. A. (2011). Radiation pressure from massive star clusters as a launching mechanism for supergalactic winds. *The Astrophysical Journal*, 735(1):66.

[Murray et al., 2005] Murray, N., Quataert, E., and Thompson, T. A. (2005). Galaxies' maximum luminosity and central bhs. *The Astrophysical Journal*, 618:569–585.

[Nelson et al., 2019] Nelson, D., Pillepich, A., Springel, V., Pakmor, R., Weinberger, R., Genel, S., Torrey, P., Vogelsberger, M., Marinacci, F., and Hernquist, L. (2019). First results from the tng50 simulation: galactic outflows driven by supernovae and black hole feedback. *Monthly Notices of the Royal Astronomical Society*, 490(3):3234–3261.

[Nielsen et al., 2020] Nielsen, N. M., Kacprzak, G. G., Pointon, S. K., Murphy, M. T., Churchill, C. W., and Davé, R. (2020). The cgm at cosmic noon with kcwi: Outflows from a star-forming galaxy at $z = 2.071$. *arXiv preprint arXiv:2002.08516*.

[Okamoto, 2010] Okamoto, K. (2010). *Fundamentals of optical waveguides*. Academic press.

[Oppenheimer and Davé, 2006] Oppenheimer, B. D. and Davé, R. (2006). Cosmological simulations of intergalactic medium enrichment from galactic outflows. *Monthly Notices of the Royal Astronomical Society*, 373(4):1265–1292.

[Oppenheimer and Schaye, 2013] Oppenheimer, B. D. and Schaye, J. (2013). Non-equilibirum ionization and cooling of metal-enriched gas in the presence of a photoionization background. *Monthly Notices of the Royal Astronomical Society*, 434(2):1043–1062.

[Othonos, 1997] Othonos, A. (1997). Fiber bragg gratings. *Review of scientific instruments*, 68(12):4309–4341.

[O'Sullivan et al., 2020] O'Sullivan, D. B., Martin, C., Matuszewski, M., Hoadley, K., Hamden, E., Neill, J. D., Lin, Z., and Parihar, P. (2020). The flashes survey. i. integral field spectroscopy of the cgm around 48 z $\sim$ 2.3–3.1 qsos. *The Astrophysical Journal*, 894(1):3.

[Page et al., 2009] Page, K. L., Willingale, R., Bissaldi, E., Postigo, A. d. U., Holland, S. T., McBreen, S., O'Brien, P. T., Osborne, J. P., Prochaska, J. X., Rol, E., et al. (2009). Multiwavelength observations of the energetic grb 080810: detailed mapping of the broad-band spectral evolution. *Monthly Notices of the Royal Astronomical Society*, 400(1):134–146.

[Pallottini et al., 2014] Pallottini, A., Gallerani, S., and Ferrara, A. (2014). The circumgalactic medium of high-redshift galaxies. *Monthly Notices of the Royal Astronomical Society: Letters*, 444(1):L105–L109.

[Pathak et al., 2014] Pathak, S., Dumon, P., Van Thourhout, D., and Bogaerts, W. (2014). Comparison of awgs and echelle gratings for wavelength division multiplexing on silicon-on-insulator. *IEEE Photonics Journal*, 6(5):1–9.

[Peeples et al., 2018] Peeples, M. S., Corlies, L., Tumlinson, J., O'Shea, B. W., Lehner, N., O'Meara, J. M., Howk, J. C., Smith, B. D., Wise, J. H., and Hummels, C. B. (2018). Figuring out gas and galaxies in enzo (foggie). i. resolving simulated circumgalactic absorption at $2 < z < 2.5$. *arXiv preprint arXiv:1810.06566*.

[Peeples et al., 2014] Peeples, M. S., Werk, J. K., Tumlinson, J., Oppenheimer, B. D., Prochaska, J. X., Katz, N., and Weinberg, D. H. (2014). A budget and accounting of metals at z $\sim$ 0: Results from the cos-halos survey. *The Astrophysical Journal*, 786(1):54.

[Peng, 2003] Peng, C. Y. (2003). Galfit user's manual. *Retrieved from*.

[Perley et al., 2008] Perley, D., Bloom, J., and Li, W. (2008). Grb 080310: Pairitel detection and pairitel+ kait+ uvot sed. *GRB Coordinates Network*, 7406.

[Perley et al., 2016a] Perley, D., Krühler, T., Schulze, S., de Ugarte Postigo, A., Hjorth, J., Berger, E., Cenko, S., Chary, R., Cucchiara, A., Ellis, R., et al. (2016a). The swift gamma-ray burst host galaxy legacy survey. i. sample selection and redshift distribution. *The Astrophysical Journal*, 817(1):7.

[Perley et al., 2013] Perley, D., Levan, A., Tanvir, N., Cenko, S. B., Bloom, J. S., Hjorth, J., Krühler, T., Filippenko, A. V., Fruchter, A., Fynbo, J. P., et al. (2013). A population of massive, luminous galaxies hosting heavily dust-obscured gamma-ray bursts: implications for the use of grbs as tracers of cosmic star formation. *The Astrophysical Journal*, 778(2):128.

[Perley and Perley, 2013] Perley, D. and Perley, R. (2013). Radio constraints on heavily obscured star formation within dark gamma-ray burst host galaxies. *The Astrophysical Journal*, 778(2):172.

[Perley et al., 2015] Perley, D., Perley, R., Hjorth, J., Michałowski, M., Cenko, S., Jakobsson, P., Krühler, T., Levan, A., Malesani, D., and Tanvir, N. (2015). Connecting grbs and ulirgs: a sensitive, unbiased survey for radio emission from gamma-ray burst host galaxies at $0 < z < 2.5$. *The Astrophysical Journal*, 801(2):102.

[Perley et al., 2016b] Perley, D., Tanvir, N. R., Hjorth, J., Laskar, T., Berger, E., Chary, R., de Ugarte Postigo, A., Fynbo, J., Krühler, T., Levan, A., et al. (2016b). The swift grb host galaxy legacy survey. ii. rest-frame near-ir luminosity distribution and evidence for a near-solar metallicity threshold. *The Astrophysical Journal*, 817(1):8.

[Perley et al., 2016c] Perley, D., Tanvir, N. R., Hjorth, J., Laskar, T., Berger, E., Chary, R., de Ugarte Postigo, A., Fynbo, J., Krühler, T., Levan, A., et al. (2016c). The swift grb host galaxy legacy survey. ii. rest-frame near-ir luminosity distribution and evidence for a near-solar metallicity threshold. *The Astrophysical Journal*, 817(1):8.

[Perley et al., 2009] Perley, D. A., Cenko, S., Bloom, J., Chen, H.-W., Butler, N., Kocevski, D., Prochaska, J., Brodwin, M., Glazebrook, K., Kasliwal, M., et al. (2009). The host galaxies of swift dark gamma-ray bursts: observational constraints on highly obscured and very high redshift grbs. *The Astronomical Journal*, 138(6):1690.

[Perley et al., 2016d] Perley, D. A., Hjorth, J., Tanvir, N. R., and Perley, R. A. (2016d). Late-time vla reobservations rule out ulirg-like host galaxies for most pre-swift long-duration gamma-ray bursts. *Monthly Notices of the Royal Astronomical Society*, page stw2789.

[Pervez et al., 2010] Pervez, N. K., Cheng, W., Jia, Z., Cox, M. P., Edrees, H. M., and Kymissis, I. (2010). Photonic crystal spectrometer. *Optics express*, 18(8):8277–8285.

[Petitjean, 1995] Petitjean, P. (1995). Qso absorption line systems. In *Science with the VLT*, pages 339–348. Springer.

[Pizzati et al., 2020] Pizzati, E., Ferrara, A., Pallottini, A., Gallerani, S., Vallini, L., Decataldo, D., and Fujimoto, S. (2020). Outflows and extended [c ii] haloes in high-redshift galaxies. *Monthly Notices of the Royal Astronomical Society*, 495(1):160–172.

[Prochaska et al., 2007] Prochaska, J., Chen, H.-W., Bloom, J., Dessauges-Zavadsky, M., O'Meara, J., Foley, R., Bernstein, R., Burles, S., Dupree, A., Falco, E., et al. (2007). The interstellar medium of gamma-ray burst host galaxies. i. echelle spectra of swift grb afterglows. *The Astrophysical Journal Supplement Series*, 168(2):231.

[Prochaska et al., 2008a] Prochaska, J., Foley, R., Holden, B., Magee, D., Cooper, M., and Dutton, A. (2008a). Grb 080310: redshift from keck/deimos spectra. *GRB Coordinates Network*, 7397.

[Prochaska et al., 2006] Prochaska, J. X., Chen, H.-W., and Bloom, J. S. (2006). Dissecting the circumstellar environment of $\gamma$-ray burst progenitors. *The Astrophysical Journal*, 648(1):95.

[Prochaska et al., 2008b] Prochaska, J. X., Chen, H.-W., Dessauges-Zavadsky, M., Bloom, J. S., Galassi, M., Palmer, D., and Fenimore, E. (2008b). Resolving the ism surrounding grbs with afterglow spectroscopy. In *AIP Conference Proceedings*, volume 1000, pages 479–485. AIP.

[Prochaska et al., 2008c] Prochaska, J. X., Dessauges-Zavadsky, M., Ramirez-Ruiz, E., and Chen, H.-W. (2008c). A survey for nv absorption at z $\approx$ zgrb in grb afterglow spectra: Clues to gas near the progenitor star. *The Astrophysical Journal*, 685(1):344.

[Prochaska et al., 2014] Prochaska, J. X., Lau, M. W., and Hennawi, J. F. (2014). Quasars probing quasars. vii. the pinnacle of the cool circumgalactic medium surrounds massive z $\sim$ 2 galaxies. *The Astrophysical Journal*, 796(2):140.

[Prochaska et al., 2017] Prochaska, J. X., Werk, J. K., Worseck, G., Tripp, T. M., Tumlinson, J., Burchett, J. N., Fox, A. J., Fumagalli, M., Lehner, N., Peeples, M. S., et al. (2017). The cos-halos survey: metallicities in the low-redshift circumgalactic medium. *The Astrophysical Journal*, 837(2):169.

[Rahmati et al., 2016] Rahmati, A., Schaye, J., Crain, R. A., Oppenheimer, B. D., Schaller, M., and Theuns, T. (2016). Cosmic distribution of highly ionized metals and their physical conditions in the eagle simulations. *Monthly Notices of the Royal Astronomical Society*, 459(1):310–332.

[Reddy et al., 2012] Reddy, N. A., Pettini, M., Steidel, C. C., Shapley, A. E., Erb, D. K., and Law, D. R. (2012). The characteristic star formation histories of galaxies at redshifts z $\sim$ 2-7. *The Astrophysical Journal*, 754(1):25.

[Rigby et al., 2018] Rigby, J., Bayliss, M., Sharon, K., Gladders, M., Chisholm, J., Dahle, H., Johnson, T., Paterno-Mahler, R., Wuyts, E., and Kelson, D. (2018). The magellan evolution of galaxies spectroscopic and ultraviolet reference atlas (megasaura). i. the sample and the spectra. *The Astronomical Journal*, 155(3):104.

[Robitaille et al., 2013] Robitaille, T. P., Tollerud, E. J., Greenfield, P., Droettboom, M., Bray, E., Aldcroft, T., Davis, M., Ginsburg, A., Price-Whelan, A. M., Kerzendorf, W. E., et al. (2013). Astropy: A community python package for astronomy. *Astronomy & Astrophysics*, 558:A33.

[Roelkens et al., 2013] Roelkens, G., Dave, U., Gassenq, A., Hattasan, N., Hu, C., Kuyken, B., Leo, F., Malik, A., Muneeb, M., Ryckeboer, E., et al. (2013). Silicon-based heterogeneous photonic integrated circuits for the mid-infrared. *Optical Materials Express*, 3(9):1523–1536.

[Roming et al., 2005] Roming, P. W., Kennedy, T. E., Mason, K. O., Nousek, J. A., Ahr, L., Bingham, R. E., Broos, P. S., Carter, M. J., Hancock, B. K., Huckle, H. E., et al. (2005). The swift ultra-violet/optical telescope. *Space Science Reviews*, 120(3-4):95–142.

[Rousselot et al., 2000] Rousselot, P., Lidman, C., Cuby, J.-G., Moreels, G., and Monnet, G. (2000). Night-sky spectral atlas of oh emission lines in the near-infrared. *Astronomy and Astrophysics*, 354:1134–1150.

[Rubin et al., 2012] Rubin, K. H., Prochaska, J. X., Koo, D. C., and Phillips, A. C. (2012). The direct detection of cool, metal-enriched gas accretion onto galaxies at z $\sim$ 0.5. *The Astrophysical Journal Letters*, 747(2):L26.

[Rubin et al., 2014] Rubin, K. H., Prochaska, J. X., Koo, D. C., Phillips, A. C., Martin, C. L., and Winstrom, L. O. (2014). Evidence for ubiquitous collimated galactic-scale outflows along the star-forming sequence at z $\sim$ 0.5. *The Astrophysical Journal*, 794(2):156.

[Rudie et al., 2019] Rudie, G. C., Steidel, C. C., Pettini, M., Trainor, R. F., Strom, A. L., Hummels, C. B., Reddy, N. A., and Shapley, A. E. (2019). The column density, kinematics, and thermal state of metal-bearing gas within the virial radius of z $\sim$ 2 star-forming galaxies in the keck baryonic structure survey. *arXiv preprint arXiv:1903.00004*.

[Sakamaki et al., 2009] Sakamaki, Y., Kamei, S., Hashimoto, T., Kitoh, T., and Takahashi, H. (2009). Loss uniformity improvement of arrayed-waveguide grating with mode-field converters designed by wavefront matching method. *Journal of Lightwave Technology*, 27(24):5710–5715.

[Salvaterra, 2015] Salvaterra, R. (2015). High redshift gamma-ray bursts. *Journal of High Energy Astrophysics*, 7:35–43.

[Salvaterra et al., 2009] Salvaterra, R., Della Valle, M., Campana, S., Chincarini, G., Covino, S., D'avanzo, P., Fernández-Soto, A., Guidorzi, C., Mannucci, F., Margutti, R., et al. (2009). Grb 090423 at a redshift of z $\approx$ 8.1. *Nature*, 461(7268):1258.

[Sargent et al., 2010] Sargent, M. T., Schinnerer, E., Murphy, E., Aussel, H., Le Floc'h, E., Frayer, D., Martínez-Sansigre, A., Oesch, P., Salvato, M., Smolčić, V., et al. (2010). The vla-cosmos perspective on the infrared-radio relation. i. new constraints on selection biases and the non-evolution of the infrared/radio properties of star-forming and active galactic nucleus galaxies at intermediate and high redshift. *The Astrophysical Journal Supplement Series*, 186(2):341.

[Savage and Sembach, 1991] Savage, B. D. and Sembach, K. R. (1991). The analysis of apparent optical depth profiles for interstellar absorption lines. *The Astrophysical Journal*, 379:245–259.

[Savage et al., 1997] Savage, B. D., Sembach, K. R., and Lu, L. (1997). Absorption by highly ionized interstellar gas along extragalactic and galactic sight lines. *The Astronomical Journal*, 113:2158.

[Savaglio et al., 2009] Savaglio, S., Glazebrook, K., and Le Borgne, D. (2009). The galaxy population hosting gamma-ray bursts. *The Astrophysical Journal*, 691(1):182.

[Schady, 2017] Schady, P. (2017). Gamma-ray bursts and their use as cosmic probes. *Royal Society open science*, 4(7):170304.

[Schady et al., 2012] Schady, P., Dwelly, T., Page, M. J., Krühler, T., Greiner, J., Oates, S. R., De Pasquale, M., Nardini, M., Roming, P., Rossi, A., et al. (2012). The dust extinction curves of gamma-ray burst host galaxies. *Astronomy & Astrophysics*, 537:A15.

[Schaye et al., 2007] Schaye, J., Carswell, R. F., and Kim, T.-S. (2007). A large population of metal-rich, compact, intergalactic c iv absorbers–evidence for poor small-scale metal mixing. *Monthly Notices of the Royal Astronomical Society*, 379(3):1169–1194.

[Schaye et al., 2014] Schaye, J., Crain, R. A., Bower, R. G., Furlong, M., Schaller, M., Theuns, T., Dalla Vecchia, C., Frenk, C. S., McCarthy, I., Helly, J. C.,

et al. (2014). The eagle project: simulating the evolution and assembly of galaxies and their environments. *Monthly Notices of the Royal Astronomical Society*, 446(1):521–554.

[Schindler and Diaferio, 2008] Schindler, S. and Diaferio, A. (2008). Metal enrichment processes. *Space Science Reviews*, 134(1):363–377.

[Schlafly and Finkbeiner, 2011] Schlafly, E. F. and Finkbeiner, D. P. (2011). Measuring reddening with sloan digital sky survey stellar spectra and recalibrating sfd. *The Astrophysical Journal*, 737(2):103.

[Schmidt, 1963] Schmidt, M. (1963). 3c 273: a star-like object with large red-shift. *Nature*, 197(4872):1040–1040.

[Schmitt, 1985] Schmitt, J. (1985). Statistical analysis of astronomical data containing upper bounds-general methods and examples drawn from x-ray astronomy. *The Astrophysical Journal*, 293:178–191.

[Schulze et al., 2015] Schulze, S., Chapman, R., Hjorth, J., Levan, A., Jakobsson, P., Björnsson, G., Perley, D., Krühler, T., Gorosabel, J., Tanvir, N., et al. (2015). The optically unbiased grb host (tough) survey. vii. the host galaxy luminosity function: Probing the relationship between grbs and star formation to redshift $\sim$ 6. *The Astrophysical Journal*, 808(1):73.

[Selsing et al., 2018] Selsing, J., Malesani, D., Goldoni, P., Fynbo, J., Krühler, T., Antonelli, L., Arabsalmani, M., Bolmer, J., Cano, Z., Christensen, L., et al. (2018). The x-shooter grb afterglow legacy sample (xs-grb). *arXiv preprint arXiv:1802.07727*.

[Shaklan and Roddier, 1988] Shaklan, S. and Roddier, F. (1988). Coupling starlight into single-mode fiber optics. *Applied Optics*, 27(11):2334–2338.

[Shapley, 2011] Shapley, A. E. (2011). Physical properties of galaxies from z= 2–4. *Annual Review of Astronomy and Astrophysics*, 49:525–580.

[Shapley et al., 2003] Shapley, A. E., Steidel, C. C., Pettini, M., and Adelberger, K. L. (2003). Rest-frame ultraviolet spectra of z $\sim$ 3 lyman break galaxies. *The Astrophysical Journal*, 588(1):65.

[Sharma and Nath, 2012] Sharma, M. and Nath, B. B. (2012). Supernovae and agn driven galactic outflows. *The Astrophysical Journal*, 763(1):17.

[Shen et al., 2012] Shen, S., Madau, P., Aguirre, A., Guedes, J., Mayer, L., and Wadsley, J. (2012). The origin of metals in the circumgalactic medium of massive galaxies at z= 3. *The Astrophysical Journal*, 760(1):50.

[Shen et al., 2013] Shen, S., Madau, P., Guedes, J., Mayer, L., Prochaska, J. X., and Wadsley, J. (2013). The circumgalactic medium of massive galaxies at z $\sim$ 3: a test for stellar feedback, galactic outflows, and cold streams. *The Astrophysical Journal*, 765(2):89.

[Shull et al., 2014] Shull, J. M., Danforth, C. W., and Tilton, E. M. (2014). Tracing the cosmic metal evolution in the low-redshift intergalactic medium. *The Astrophysical Journal*, 796(1):49.

[Simcoe et al., 2011] Simcoe, R. A., Cooksey, K. L., Matejek, M., Burgasser, A. J., Bochanski, J., Lovegrove, E., Bernstein, R. A., Pipher, J. L., Forrest, W. J., McMurtry, C., et al. (2011). Constraints on the universal c iv mass density at z $\sim$ 6 from early infrared spectra obtained with the magellan fire spectrograph. *The Astrophysical Journal*, 743(1):21.

[Smette et al., 2013] Smette, A., Ledoux, C., Vreeswijk, P., De Cia, A., Petitjean, P., Fynbo, J., Malesani, D., and Fox, A. (2013). GRB 130610A: VLT/UVES redshift. *GRB Coordinates Network, Circular Service, No. 14848, #1 (2013)*, 14848.

[Smit and Van Dam, 1996] Smit, M. K. and Van Dam, C. (1996). Phasar-based wdm-devices: Principles, design and applications. *IEEE Journal of Selected Topics in Quantum Electronics, 2 (2)*.

[Smith and Collins, 1990] Smith, R. and Collins, S. (1990). Thick films of silicon nitride. *Sensors and Actuators A: Physical*, 23(1-3):830–834.

[Spaleniak et al., 2014] Spaleniak, I., Gross, S., Jovanovic, N., Williams, R. J., Lawrence, J. S., Ireland, M. J., and Withford, M. J. (2014). Multiband processing of multimode light: combining 3d photonic lanterns with waveguide bragg gratings. *Laser & Photonics Reviews*, 8(1).

[Sparre et al., 2014] Sparre, M., Hartoog, O., Krühler, T., Fynbo, J. P. U., Watson, D., Wiersema, K., D'Elia, V., Zafar, T., Afonso, P., Covino, S., et al. (2014). The metallicity and dust content of a redshift 5 gamma-ray burst host galaxy. *The Astrophysical Journal*, 785(2):150.

[Speagle et al., 2014] Speagle, J. S., Steinhardt, C. L., Capak, P. L., and Silverman, J. D. (2014). A highly consistent framework for the evolution of the star-forming "main sequence" from z $\sim$ 0-6. *The Astrophysical Journal Supplement Series*, 214(2):15.

[Spitzer Jr, 1956] Spitzer Jr, L. (1956). On a possible interstellar galactic corona. *The Astrophysical Journal*, 124:20.

[Stanek et al., 2003] Stanek, K. Z., Matheson, T., Garnavich, P., Martini, P., Berlind, P., Caldwell, N., Challis, P., Brown, W., Schild, R., Krisciunas, K., et al. (2003). Spectroscopic discovery of the supernova 2003dh associated with grb 030329. *The Astrophysical Journal Letters*, 591(1):L17.

[Stanway et al., 2014] Stanway, E. R., Levan, A. J., and Davies, L. J. (2014). Radio observations of grb host galaxies. *Monthly Notices of the Royal Astronomical Society*, 444(3):2133–2146.

[Steidel et al., 2010] Steidel, C. C., Erb, D. K., Shapley, A. E., Pettini, M., Reddy, N., Bogosavljević, M., Rudie, G. C., and Rakic, O. (2010). The structure and kinematics of the circumgalactic medium from far-ultraviolet spectra of z 2-3 galaxies. *The Astrophysical Journal*, 717(1):289.

[Stern et al., 2016] Stern, J., Hennawi, J. F., Prochaska, J. X., and Werk, J. K. (2016). A universal density structure for circumgalactic gas. *The Astrophysical Journal*, 830(2):87.

[Stocke et al., 2013] Stocke, J. T., Keeney, B. A., Danforth, C. W., Shull, J. M., Froning, C. S., Green, J. C., Penton, S. V., and Savage, B. D. (2013). Characterizing the circumgalactic medium of nearby galaxies with hst/cos and hst/stis absorption-line spectroscopy. *The Astrophysical Journal*, 763(2):148.

[Subramanian et al., 2015] Subramanian, A. Z., Ryckeboer, E., Dhakal, A., Peyskens, F., Malik, A., Kuyken, B., Zhao, H., Pathak, S., Ruocco, A., De Groote, A., et al. (2015). Silicon and silicon nitride photonic circuits for spectroscopic sensing on-a-chip [invited]. *Photonics Research*, 3(5):B47–B59.

[Sugahara et al., 2019] Sugahara, Y., Ouchi, M., Harikane, Y., Bouché, N., Mitchell, P. D., and Blaizot, J. (2019). Fast outflows identified in early star-forming galaxies at z= 5–6. *The Astrophysical Journal*, 886(1):29.

[Sugahara et al., 2017] Sugahara, Y., Ouchi, M., Lin, L., Martin, C. L., Ono, Y., Harikane, Y., Shibuya, T., and Yan, R. (2017). Evolution of galactic outflows at revealed with sdss, deep2, and keck spectra. *The Astrophysical Journal*, 850(1):51.

[Swinbank et al., 2015] Swinbank, A., Vernet, J., Smail, I., De Breuck, C., Bacon, R., Contini, T., Richard, J., Röttgering, H., Urrutia, T., and Venemans, B. (2015). Mapping the dynamics of a giant ly $\alpha$ halo at z= 4.1 with muse: the energetics of a large-scale agn-driven outflow around a massive, high-redshift galaxy. *Monthly Notices of the Royal Astronomical Society*, 449(2):1298–1308.

[Tacconi et al., 2018] Tacconi, L. J., Genzel, R., Saintonge, A., Combes, F., García-Burillo, S., Neri, R., Bolatto, A., Contini, T., Schreiber, N. F., Lilly, S., et al. (2018). Phibss: unified scaling relations of gas depletion time and molecular gas fractions. *The Astrophysical Journal*, 853(2):179.

[Takahashi et al., 1992] Takahashi, H., Hibino, Y., and Nishi, I. (1992). Polarization-insensitive arrayed-waveguide grating wavelength multiplexer on silicon. *Optics letters*, 17(7):499–501.

[Takahashi et al., 1995] Takahashi, H., Oda, K., Toba, H., and Inoue, Y. (1995). Transmission characteristics of arrayed waveguide n/spl times/n wavelength multiplexer. *Journal of Lightwave Technology*, 13(3):447–455.

[Tanvir et al., 2012] Tanvir, N., Fynbo, J., Melandri, A., Levan, A., Xu, D., and D'Elia, V. (2012). Grb 121024a: Vlt/x-shooter redshift. *GRB Coordinates Network, Circular Service, No. 13890,# 1 (2012)*, 13890.

[Tanvir et al., 2009] Tanvir, N. R., Fox, D. B., Levan, A., Berger, E., Wiersema, K., Fynbo, J., Cucchiara, A., Krühler, T., Gehrels, N., Bloom, J. S., et al. (2009). A $\gamma$-ray burst at a redshift of z $\approx$ 8.2. *Nature*, 461(7268):1254–1257.

[Thomson et al., 2011] Thomson, R. R., Birks, T. A., Leon-Saval, S., Kar, A. K., and Bland-Hawthorn, J. (2011). Ultrafast laser inscription of an integrated photonic lantern. *Optics express*, 19(6):5698–5705.

[Thöne et al., 2012] Thöne, C., Fynbo, J. P. U., Goldoni, P., de Ugarte, A. P., Campana, S., Vergani, S., Covino, S., Krühler, T., Kaper, L., Tanvir, N., et al. (2012). Grb 100219a with x-shooter–abundances in a galaxy at z= 4.7. *Monthly Notices of the Royal Astronomical Society*, 428(4):3590–3606.

[Toy et al., 2016] Toy, V. L., Cucchiara, A., Veilleux, S., Fumagalli, M., Rafelski, M., Rahmati, A., Cenko, S. B., Capone, J. I., and Pasham, D. R. (2016). Exploring damped ly$\alpha$ system host galaxies using gamma-ray bursts. *The Astrophysical Journal*, 832(2):175.

[Trenti et al., 2015] Trenti, M., Perna, R., and Jimenez, R. (2015). The luminosity and stellar mass functions of grb host galaxies: insight into the metallicity bias. *The Astrophysical Journal*, 802(2):103.

[Trinh et al., 2013] Trinh, C. Q., Ellis, S. C., Bland-Hawthorn, J., Lawrence, J. S., Horton, A. J., Leon-Saval, S. G., Shortridge, K., Bryant, J., Case, S., Colless, M., et al. (2013). GNOSIS: the first instrument to use fiber Bragg gratings for OH suppression. *The Astronomical Journal*, 145(2):51.

[Tumlinson et al., 2017] Tumlinson, J., Peeples, M. S., and Werk, J. K. (2017). The circumgalactic medium. *Annual Review of Astronomy and Astrophysics*, 55:389–432.

[Tumlinson et al., 2013] Tumlinson, J., Thom, C., Werk, J. K., Prochaska, J. X., Tripp, T. M., Katz, N., Davé, R., Oppenheimer, B. D., Meiring, J. D., Ford, A. B., et al. (2013). The cos-halos survey: rationale, design, and a census of circumgalactic neutral hydrogen. *The Astrophysical Journal*, 777(1):59.

[Tumlinson et al., 2011] Tumlinson, J., Thom, C., Werk, J. K., Prochaska, J. X., Tripp, T. M., Weinberg, D. H., Peeples, M. S., O'Meara, J. M., Oppenheimer, B. D., Meiring, J. D., et al. (2011). The large, oxygen-rich halos of star-forming galaxies are a major reservoir of galactic metals. *Science*, 334(6058):948–952.

[Turner et al., 2014] Turner, M. L., Schaye, J., Steidel, C. C., Rudie, G. C., and Strom, A. L. (2014). Metal-line absorption around z $\sim$ 2.4 star-forming galaxies in the keck baryonic structure survey. *Monthly Notices of the Royal Astronomical Society*, 445(1):794–822.

[Veilleux et al., 2005] Veilleux, S., Cecil, G., and Bland-Hawthorn, J. (2005). Galactic winds. *Annu. Rev. Astron. Astrophys.*, 43:769–826.

[Veilleux et al., 2020] Veilleux, S., Maiolino, R., Bolatto, A. D., Aalto, S., d'Alessandro, M. M., Tebaldini, S., Quegan, S., Scipal, K., Anderson, J., Kim, E.-J., et al. (2020). Cool outflows in galaxies and their implications. *A&ARv*, 28(1):2.

[Vergani et al., 2017] Vergani, S., Palmerio, J., Salvaterra, R., Japelj, J., Mannucci, F., Perley, D., D'Avanzo, P., Krühler, T., Puech, M., Boissier, S., et al. (2017). The chemical enrichment of long gamma-ray bursts nurseries up to z= 2. *Astronomy & Astrophysics*, 599:A120.

[Vergani et al., 2015] Vergani, S., Salvaterra, R., Japelj, J., Le Floc'h, E., D'avanzo, P., Fernandez-Soto, A., Krühler, T., Melandri, A., Boissier, S., Covino, S., et al. (2015). Are long gamma-ray bursts biased tracers of star formation? clues from the host galaxies of the swift/bat6 complete sample of lgrbs-i. stellar mass at z $<$ 1. *Astronomy & Astrophysics*, 581:A102.

[Voit et al., 2015] Voit, G., Donahue, M., Bryan, G., and McDonald, M. (2015). Regulation of star formation in giant galaxies by precipitation, feedback and conduction. *Nature*, 519(7542):203.

[Vreeswijk et al., 2008] Vreeswijk, P., Jakobsson, P., Jaunsen, A., and Ledoux, C. (2008). Grb 080310: Vlt/uves spectroscopy. *GRB Coordinates Network*, 7391.

[Vreeswijk et al., 2013] Vreeswijk, P., Ledoux, C., Raassen, A., Smette, A., De Cia, A., Woźniak, P., Fox, A., Vestrand, W., and Jakobsson, P. (2013). Time-dependent excitation and ionization modelling of absorption-line variability due to grb 080310. *Astronomy & Astrophysics*, 549:A22.

[Vreeswijk et al., 2007] Vreeswijk, P., Ledoux, C., Smette, A., Ellison, S., Jaunsen, A., Andersen, M., Fruchter, A., Fynbo, J. P. U., Hjorth, J., Kaufer, A., et al. (2007). Rapid-response mode vlt/uves spectroscopy of grb 060418-conclusive evidence for uv pumping from the time evolution of fe ii and ni ii excited-and metastable-level populations. *Astronomy & Astrophysics*, 468(1):83–96.

[Vreeswijk et al., 2006] Vreeswijk, P., Smette, A., Fruchter, A., Palazzi, E., Rol, E., Wijers, R., Kouveliotou, C., Kaper, L., Pian, E., Masetti, N., et al. (2006). Low-resolution vlt spectroscopy of grbs 991216, 011211 and 021211. *Astronomy & Astrophysics*, 447(1):145–156.

[Wainwright et al., 2007] Wainwright, C., Berger, E., and Penprase, B. (2007). A morphological study of gamma-ray burst host galaxies. *The Astrophysical Journal*, 657(1):367.

[Wechsler and Tinker, 2018] Wechsler, R. H. and Tinker, J. L. (2018). The connection between galaxies and their dark matter halos. *Annual Review of Astronomy and Astrophysics*, 56:435–487.

[Weiner et al., 2009] Weiner, B. J., Coil, A. L., Prochaska, J. X., Newman, J. A., Cooper, M. C., Bundy, K., Conselice, C. J., Dutton, A. A., Faber, S., Koo, D. C., et al. (2009). Ubiquitous outflows in deep2 spectra of star-forming galaxies at z= 1.4. *The Astrophysical Journal*, 692(1):187.

[Werk et al., 2016] Werk, J. K., Prochaska, J. X., Cantalupo, S., Fox, A. J., Oppenheimer, B., Tumlinson, J., Tripp, T. M., Lehner, N., and McQuinn, M. (2016). The cos-halos survey: Origins of the highly ionized circumgalactic medium of star-forming galaxies. *The Astrophysical Journal*, 833(1):54.

[Werk et al., 2013] Werk, J. K., Prochaska, J. X., Thom, C., Tumlinson, J., Tripp, T. M., O'Meara, J. M., and Peeples, M. S. (2013). The cos-halos survey: an empirical description of metal-line absorption in the low-redshift circumgalactic medium. *The Astrophysical Journal Supplement Series*, 204(2):17.

[Werk et al., 2014] Werk, J. K., Prochaska, J. X., Tumlinson, J., Peeples, M. S., Tripp, T. M., Fox, A. J., Lehner, N., Thom, C., O'Meara, J. M., Ford, A. B., et al. (2014). The cos-halos survey: physical conditions and baryonic mass in the low-redshift circumgalactic medium. *The Astrophysical Journal*, 792(1):8.

[Whitaker et al., 2017] Whitaker, K. E., Pope, A., Cybulski, R., Casey, C. M., Popping, G., and Yun, M. S. (2017). The constant average relationship between dust-obscured star formation and stellar mass from z= 0 to z= 2.5. *The Astrophysical Journal*, 850(2):208.

[Wiklind et al., 2019] Wiklind, T., Ferguson, H. C., Guo, Y., Koo, D. C., Kocevski, D., Mobasher, B., Brammer, G. B., Kassin, S., Koekemoer, A. M., Giavalisco, M., et al. (2019). Evolution of the gas mass fraction of progenitors to today's massive galaxies: Alma observations in the candels goods-s field. *arXiv preprint arXiv:1903.06962*.

[Wiseman et al., 2017a] Wiseman, P., Perley, D., Schady, P., Prochaska, J., de Ugarte Postigo, A., Krühler, T., Yates, R., and Greiner, J. (2017a). Gas inflow and outflow in an interacting high-redshift galaxy-the remarkable host environment of grb 080810 at z= 3.35. *Astronomy & Astrophysics*, 607:A107.

[Wiseman et al., 2017b] Wiseman, P., Schady, P., Bolmer, J., Krühler, T., Yates, R., Greiner, J., and Fynbo, J. (2017b). Evolution of the dust-to-metals ratio in high-redshift galaxies probed by grb-dlas. *Astronomy & Astrophysics*, 599:A24.

[Xu et al., 2014] Xu, D., Vreeswijk, P., Fynbo, J., D'Elia, V., Wiersema, K., Tanvir, N., de Ugarte Postigo, A., and Covino, S. (2014). X-shooter redshift of grb 141109a. *GCN*, 17040:1.

[Yun and Carilli, 2002] Yun, M. S. and Carilli, C. (2002). Radio-to-far-infrared spectral energy distribution and photometric redshifts for dusty starburst galaxies. *The Astrophysical Journal*, 568(1):88.

[Zafar et al., 2018] Zafar, T., Møller, P., Watson, D., Lattanzio, J., Hopkins, A., Karakas, A., Fynbo, J., Tanvir, N., Selsing, J., Jakobsson, P., et al. (2018). X-shooting grbs at high redshift: probing dust production history. *Monthly Notices of the Royal Astronomical Society*, 480(1):108–118.

[Zhu and Ménard, 2013] Zhu, G. and Ménard, B. (2013). Calcium h & k induced by galaxy halos. *The Astrophysical Journal*, 773(1):16.

[Zhu et al., 2016a] Zhu, T., Hu, Y., Gatkine, P., Veilleux, S., Bland-Hawthorn, J., and Dagenais, M. (2016a). Arbitrary on-chip optical filter using complex waveguide bragg gratings. *Applied Physics Letters*, 108(10):101104.

[Zhu et al., 2016b] Zhu, T., Hu, Y., Gatkine, P., Veilleux, S., Bland-Hawthorn, J., and Dagenais, M. (2016b). Ultrabroadband high coupling efficiency fiber-to-waveguide coupler using $Si_3N_4/SiO_2$ waveguides on silicon. *IEEE Photonics Journal*, 8(5):1–12.